COLLOIDAL FABRICATION TECHNIQUES FOR THE DEVELOPMENT OF SUPERCAPACITOR ELECTRODES AND DEVICES

COLLOIDAL FABRICATION TECHNIQUES FOR THE DEVELOPMENT OF SUPERCAPACITOR ELECTRODES AND DEVICES

By Ri Chen, B.Eng, M.Eng

A Thesis Submitted to the School of Graduate Studies in Partial Fulfillment of the Requirements for the Degree Doctor of Philosophy

TITLE: Colloidal Fabrication Techniques for the Development of Supercapacitor Electrodes and Devices

AUTHOR: Ri Chen,

M.Eng. (Guangdong University of Technology, China),

B.Eng. (Changchun University of Science and Technology, China).

SUPERVISORS:

Prof. Ishwar K. Puri and Prof. Igor Zhitomirsky

NUMBER OF PAGES: xxiv, 213.

Abstract

In this thesis, an advanced colloidal fabrication technique, called particle extraction through liquid-liquid interface (PELLI), has been developed to fabricate components of positive and negative electrodes of electrochemical capacitors (ECs). This new colloidal strategy is applied to create stable suspensions for the electrophoretic deposition (EPD) of thin films and advanced inks for screen printing applications.

Bottom-up and top-down PELLI strategies were developed to extract MnO_2 particles synthesized in an aqueous phase to the organic phases of 1-butanol and dichloromethane, respectively. During both extraction processes, hexadecylamine with amine functional group was used as the extractor for transferring the MnO_2 particles. Compared to the top-down PELLI technique, the bottom-up PELLI synthesized particles of relatively small sizes, which is beneficial for fabricating MnO_2-multiwalled carbon nanotube (MWCNT) binary composite EC electrodes with enhanced electrochemical performance. Hence, the subsequent work was carried out using the bottom-up strategy for PELLI.

Head-tail extractors with a single functional group, such as carboxylic acid and phosphonate, and head-tail-head (HTH) multifunctional extractors with functional groups of both carboxylic acid and phosphonate were used as the vehicles for transferring MnO_2 from the synthesis media to the device processing media to achieve a good suspension of MnO_2-MWCNT to fabricate positive EC electrodes. Advanced FeOOH-MWCNT negative electrodes were also prepared by PELLI strategies using HT and HTH extractors. The experimental results showed that both positive and negative electrodes prepared by HTH extractors exhibit the highest electrochemical performance. Moreover, stable suspensions of MnO_2 particles synthesized by PELLI with multifunctional HTH extractors were prepared to fabricate advanced thin films by EPD and also MnO_2-carbon black printing inks for screen printing of thin EC electrodes.

Subsequently, to fabricate efficient polypyrrole (PPy) based composite negative electrodes, for the first time, non-agglomerated FeOOH particles were prepared with PELLI using tetradecylamine as extractor. Introduction of PPy enhances the electrochemical performance of the binary composite of PPy coated MWCNT in a potential range of -0.8 - +0.1V. Advanced asymmetric ECs devices with MnO_2-MWCNT positive electrodes and PPy-FeOOH-MWCNT negative electrodes were fabricated. These devices with comparable capacitance for both the positive and negative electrodes and high active mass loading were found to have high electrochemical performance in a wide working voltage window of 1.6V in aqueous electrolyte.

Key words: particle, extraction, heterocoagulation, electrochemical capacitor, electrophoretic deposition, ink, screen printing.

Acknowledgement

Frankly speaking, this dissertation has been completed successfully with a lot of unselfish support from my supervisors, group members, my friends, my family, Overseas Study of Guangzhou Elite Project and Natural Sciences and Engineering Research Council of Canada.

First and foremost, my deepest gratitude goes for my supervisors, Prof. Ishwar K. Puri and Prof. Igor Zhitomirsky for their selfless supports, patient discussions, kind guidance as well as priceless advices. Herein, I express my sincere thanks to you for your great encouragement, tolerance and patience during the period of my Ph.D. study! To be sincere, it is my great honor to join your research groups and work with you. Your enthusiasm, strictness and endless quest on pursuit of perfection on development of high-quality research to serve the world have deeply influenced and set up a role model for me to follow in my future career. Subsequently, I would also like to express my sincere thanks to my committee members Prof. Stephen C. Veldhuis and Prof. Tohid Didar, for their patient discussion and useful suggestions. I would also express my gratitude to Prof. Oleg Rubel for becoming the external examiner of my Ph.D. comprehensive exam and giving me good advice.

I would like to thank the coauthors and collaborators: Dr. Rakesh P. Sahu, Tahereh Majdi, Dr. Ahmed Abdalla, Alexandra Korp, Abhinav Jain, Mohamed Nawwar, Ryan Poon, Dr. Mustafa S. Ata, Miao Yu, Xinya Zhao, Zhengzheng Wang, Haoyu Fan, Amanda Clifford, Cameron J. Wallar, Wenyu Liang, Chaoyu Xiang, Dr. Abdel Rahman Abdel Fattah, Dr.

Suvojit Ghosh, Dr. Souvik Pal. To be frank, my research is hard to go smoothly without their kind help, contribution and cooperation. I am also thankful for my colleagues: Dr. Fei Geng, Dr. Peiying Jennifer Tsai, Sarah Mishriki, Dr. Srivatsa Aithal, Tamaghna Gupta, Arash Fattahi, Krishna Jangid, Jordan Milne, Ricardo M. Silva, Aseeb M. Syed, Xinqian Liu and Qinfu Zhao. I would also like to express my gratitude to the following people for their technical support for my Ph.D. study: Chris Butcher, Jhoynner Martinez, Hui Yuan, Victoria Jarvis, Frank Gibbs and Danielle Covelli. My special gratitude goes for my friends: Xiangyi Chen, Dr. Jinbiao Ning, Xiaoxia Lin, Weiwei Zhang, Longxing Chi, Jing Chen, Ruoyi Wang and Rashid Mahmood. Additionally, I greatly appreciate Dr. Kaiyuan Shi at National Research Council Canada for his kind help, training and valuable suggestions for my research.

Lastly, but the most importantly, I would like to express my heartfelt appreciation for my family, especially for my parents and sister, for their continuous encouragement, unconditional support and endless help. The Ph.D. thesis is initially from your biggest motivation.

Declaration of Academic Achievements

This dissertation was used to fulfill the requirements of Ph.D. degree. All the research was conducted from September 2015 to May 2019. During the period of thesis study, advanced colloidal fabrication techniques, called PELLI and heterocoagulation, were successfully developed to fabricate individual components, binary composites and ternary composites for both the positive and negative electrodes of ECs. These new colloidal strategies were also applied to prepare stable suspensions for EPD of thin films and to synthesize inks for screen printing application. I am the major contributor towards this thesis work.

This thesis has resulted in seven peer-reviewed journal articles and I am the first author on 6 of these papers. These papers are listed below:

1. **Ri Chen**, Ishwar K. Puri and Igor Zhitomirsky, Polypyrrole-carbon nanotube-FeOOH composites for negative electrodes of asymmetric supercapacitors, ***Journal of Electrochemical Society***, 166 (6), A935-A940, 2019.
2. **Ri Chen**, Zhengzheng Wang, Rakesh P. Sahua, Ishwar K. Puri and Igor Zhitomirsky, Influence of molecular structure of extractor molecules on liquid-liquid extraction of oxide particles and properties of composites, ***Ceramics International***, 44, 15714-15720, 2018,
3. **Ri Chen**, Ishwar K. Puri and Igor Zhitomirsky, High areal capacitance of FeOOH-carbon nanotube negative electrodes for asymmetric supercapacitors, ***Ceramics International***, 44, 18007-18015, 2018.

4. **<u>Ri Chen</u>**, Ryan Poon, Rakesh P. Sahu, Ishwar K. Puri and Igor Zhitomirsky, MnO_2-carbon nanotube electrodes for supercapacitors with high active mass loadings, ***Journal of Electrochemical Society***, 164(9), A1673-A167, 2017.
5. **<u>Ri Chen</u>**, Mustafa S. Ata, Xinya Zhao, Amanda Clifford, Ishwar K. Puri and Igor Zhitomirsky, Strategies for liquid-liquid extraction of oxide particles for applications in supercapacitor electrodes and thin films, ***Journal of Colloid and Interface Science***, 499, 1-8, 2017.
6. **<u>Ri Chen</u>**, Mustafa S. Ata, Xinya Zhao, Ishwar K. Puri and Igor Zhitomirsky, Liquid-liquid extraction of oxide particles and application in supercapacitors, ***Journal of Materials Research***, 92, 1-9, 2017.
7. Ahmed M Abdalla, Rakesh P Sahu, Cameron J Wallar, **<u>Ri Chen</u>**, Igor Zhitomirsky and Ishwar K Puri, Nickel oxide nanotube synthesis using multiwalled carbon nanotubes as sacrificial templates for supercapacitor application, ***Nanotechnology***, 28, 1-10, 20

Table of Contents

Abstract i

Acknowledgement iii

Declaration of Academic Achievements v

List of Figures xii

List of Abbreviations and Symbols xxiii

1 Introduction 1

  1.1 References 4

2 Literature review 6

  2.1 Conventional capacitors 6

  2.2 Categories of electrochemical capacitors (ECs) 9

    2.2.1 Electric double layer capacitors (EDLCs) 9

    2.2.2 Pseudocapacitors 10

    2.2.3 Asymmetric supercapacitors 12

  2.3 Electrode materials 13

    2.3.1 Carbon based electrode materials 14

    2.3.2 Transition metal oxides/oxide-hydroxides 14

    2.3.3 Conductive polymers 15

2.3.4 Composite electrodes 16

2.4 Electrolytes 17

2.4.1 Aqueous electrolytes 17

2.4.2 Organic electrolytes 18

2.5 Manufacturing methodologies 19

2.5.1 Colloidal techniques for fabrication of bulk electrodes and thin films 19

2.5.1.1 Co-dispersion method 20

2.5.1.2 Heterocoagulation technique 21

2.5.1.3 Particle extraction through liquid-liquid interface (PELLI) method 22

2.5.1.4 Electrophoretic deposition (EPD) 24

2.5.1.5 Screen printing 25

2.6 References 27

3 Research objective 41

3.1 Liquid liquid extraction of oxide particles by head-tail extractor hexadecylphosphonic acid 41

3.2 Bottom-up and top-down PELLI of oxide particles and electrophoretic deposition of thin films 42

3.3 Effect of extractors and active mass loading on the electrochemical performance of electrochemical capacitors 42

3.4 Multifunctional extractor for liquid-liquid extraction of oxide particles and applications in supercapacitors, electrophoretic deposition and screen printing 43

3.5 High areal capacitance of FeOOH-carbon nanotube negative electrodes for asymmetric supercapacitors 44

3.6 Polypyrrole-carbon nanotube-FeOOH composites for negative electrodes of asymmetric supercapacitors 44

4 Liquid liquid extraction of oxide particles by head-tail extractor hexadecylphosphonic acid 46

4.1 Abstract 46

4.2 Introduction 47

4.3 Experimental procedures 51

4.4 Results and discussion 54

4.5 Conclusions 62

4.6 References 63

5 Bottom-up and top-down PELLI of oxide particles and electrophoretic deposition of thin films 71

5.1 Abstract 71

5.2 Introduction 72

5.3 Experimental procedures 75

5.4 Results and discussion 77

5.5 Conclusions 89

5.6 References 90

6 Effect of extractors and active mass loading on the electrochemical performance of electrochemical capacitors 98

6.1 Abstract 98

6.2 Introduction 99

6.3 Experimental procedures 103

6.4 Results and discussion 106

6.5 Conclusions 118

6.6 References 119

7 Multifunctional extractor for liquid-liquid extraction of oxide particles and applications in supercapacitors, electrophoretic deposition and screen printing 126

7.1 Abstract 126

7.2 Introduction 127

7.3 Experimental procedures 130

7.4 Results and discussion 132

7.5 Conclusions 144

7.6 References 145

8 High areal capacitance of FeOOH-carbon nanotube negative electrodes for asymmetric supercapacitors 151

8.1 Abstract 151

8.2 Introduction 152

8.3 Experimental procedures 155

8.4 Results and discussion 157

8.5 Conclusions 175

8.6 References 176

9 Polypyrrole-carbon nanotube-FeOOH composites for negative electrodes of asymmetric supercapacitors 183

9.1 Abstract 183

9.2 Introduction 184

9.3 Experimental procedures 187

9.4 Results and discussion 189

9.5 Conclusions 200

9.6 Reference 201

10 Conclusions and future directions 211

10.1 Conclusions 211

10.2 Future directions 212

List of Figures

Figure 2.1 Schematic of electrostatic capacitors..7

Figure 2.2 Schematic structure and principles of a single cell EDLCs[2]..........................10

Figure 2.3 Various reversible redox mechanisms for pseudocapacitance 12

Figure 2.4 Ragone plot of three major electrochemical energy storage devices and time constants are shown in dashed line, by dividing the specific energy with specific power[33] 13

Figure 2.5 Co-dispersion of PPy-MWCNT by SAF[73]. 20

Figure 2.6 MnO_2-MWCNT composite fabricated by heterocoagulation based on electrostatic interaction[74]. 21

Figure 2.7 MnO_2-MWCNT composite fabricated by heterocoagulation based on Schiff based reaction between (A) new fuchsin (NF) and (B) 3,4-Dihydroxybenzaldehyde (DHB)[67]..22

Figure 2.8 (A) MnO_2 precipitation, (B) MnO_2 extracted by LG in 1-butanol, (C) MWCNT dispersion in 1-butanol, (D) MnO_2-MWCNT extracted in 1-butanol and (E) Ag extracted by LG in 1-butonal[14]. 23

Figure 2.9 Co-dispersion of MWCNT-graphene and PPy-graphene and their applications for film formation by EPD[71]. 25

Figure 2.10 Schematic of screen printing[90]...26

Figure 4.1 (A) Chemical structure of HDPA (B) adsorption mechanisms of HDPA, involving (a) chelating bidentate bonding, (b) chelating tridentate bonding, (c) bridging bidentate bonding, (d) bridging tridentate bonding, (C) schematic of the PELLI method: (a) particles, precipitated in aqueous phase, (b) transfer through liquid–liquid interface, (c) formation of a stable suspension of particles in n-butanol. 50

Figure 4.2 (a) $NaMnO_4$ solution, (b) precipitation of MnO_2 after mixing of $NaMnO_4$ with n-butanol, (c) extraction of MnO_2 to the n-butanol solvent after addition of HDPA solution in n-butanol and mixing, (d) as-precipitated titania in water, (e) extraction of titania to the n-butanol solvent after addition of HDPA solution in n-butanol and mixing, red arrows show the interface of water and n-butanol. 52

Figure 4.3 FTIR spectra of (a) HDPA and of extracted materials: (b) MnO_2 and (c) titania. 55

Figure 4.4 XRD patterns of (a) MnO_2 (●-JCPDS file 87-1497) and (b) titania. 57

Figure 4.5 SEM images of (a) MnO_2 and (b) titania, prepared from suspensions, shown in Figs. 2(b) and 2(d), respectively, after filtration, washing with water, and drying in air for 72 h..58

Figure 4.6 Particle size distributions for (a) MnO_2 and (b) titania, extracted using HDPA and (c) SEM image of MnO_2-MWCNT composite. 59

Figure 4.7 (A) CVs at scan rates of (a) 2, (b) 10, and (c) 20 mV s^{-1}, (B) C_S and C_m, calculated from the CVs data at different scan rates. 61

Figure 4.8 (a) Nyquist plot for complex impedance and frequency dependences of (b) C_S' and (c) C_S'' calculated from the impedance data for MnO_2-MWCNT electrodes.............62

Figure 5.1 X-ray diffraction pattern of manganese dioxide (▼- JCPDS file 87-1497). ...78

Figure 5.2 SEM images of (A) manganese dioxide and (B) titania powders. 79

Figure 5.3 (A) Chemical structure of $NH_2R^{'}$, (B) adsorption mechanisms of $NH_2R^{'}$ on oxide surface: (a) chemisorption and (b) electrostatic interactions, involving surface OH groups (C) Schiff base reaction of $R^{''}$-CHO and $NH_2R^{'}$, (D) chemical structure of $R^{''}$-CHO, (E-G) schematics of the Schiff base reaction for $R^{''}$-CHO, adsorbed on particle surface by different mechanism: (E) chelation, (F) bridging inner sphere complex and (E) bridging outer sphere complex. 80

Figure 5.4 (A) Schematic of (a) precipitation and different steps in extraction in EM1, (B) manganese dioxide suspension (a) before and (b) after extraction. 81

Figure 5.5 (A) Schematic of (a) precipitation and (b,c) different steps in extraction in EM2, (B) manganese dioxide suspension (a) before and (b) after extraction 82

Figure 5.6 FTIR spectra of (a) as-received $NH_2R^{'}$ and (b-d) particles, extracted by methods (a) EM1, (b) EM2 and (c) EM3 83

Figure 5.7 Particles size distributions for (a) manganese dioxide particles, extracted by EM1, (b) manganese dioxide particles, extracted by EM2, (c) titania particles, extracted by EM3 84

Figure 5.8 (A,B) CVs for manganese dioxide-MWCNT electrodes, prepared using (A) EM1 and (B) EM2 at scan rates of (a) 2, (b) 10 and (c) 20 mV s^{-1}, (C) C_S and C_m for manganese dioxide-MWCNT electrodes, prepared using (a) EM1 and (b) EM2. 85

Figure 5.9 (A) Nyquist plot of complex impedance, (B,C) frequency dependences of (B) $C_S^{'}$ and (C) $C_S^{''}$ for manganese dioxide-MWCNT electrodes, prepared using (a) EM1 and (b) EM2. 86

Figure 5.10 (A) Schematic of (a) precipitation in the presence of R''-CHO, involving R''-CHO adsorption on particles (b) particle extraction in EM3, involving Schiff base reaction at the liquid-liquid interface, (B) titania suspension (a) before and (b) after extraction ... 87

Figure 5.11 SEM image of a titania–PVB film. ... 89

Figure 6.1 (A) Schematic of (a) precipitation and (b,c) different steps in extraction, (B) MnO_2 suspensions (a) before and (b) after extraction using DPA and (C) MnO_2 suspensions (a) before and (b) after extraction using TDA for $C_m = 5$ g L^{-1} and Rep = 0.25. ... 104

Figure 6.2 X-ray diffraction pattern of precipitated MnO_2 (▼- JCPDS file 87-1497). ... 107

Figure 6.3 (A,B) SEM images of MnO_2 powder. ... 107

Figure 6.4 (A) Chemical structure of DPA, (B) DPA adsorption on particle surface: (a,b) bridging, (c,d) chelation of metal atoms (M) on the particle surface, (C) chemical structure of TDA, (D) TDA adsorption mechanisms: (a) chemisorption and (b) electrostatic interaction, involving a surface OH group. ... 108

Figure 6.5 FTIR spectrum of (a) DPA, (b) MnO_2, extracted using DPA, (c) TDA and (d) MnO_2, extracted using TDA. ... 109

Figure 6.6 Particle size distribution for MnO_2 particles, extracted using (A) DPA and (B) TDA for $C_m = 5$ g L^{-1} and Rep = 0.25. ... 111

Figure 6.7 Particle size distribution for MnO_2 particles, extracted using TDA for different Rep: (A) 0.33, (B) 0.5, (C) 1.0 and (D) 2.5. ... 112

Figure 6.8 SEM images of the MnO_2-MWCNT composites, prepared by the extraction methods using (A) DPA and (B) TDA for $C_m = 5$ g L^{-1} and Rep = 0.25. ... 113

Figure 6.9 (A,B) CVs for MnO_2-MWCNT electrodes with active mass loading of 35 mg cm^{-2}, prepared using (A) DPA and (B) TDA at scan rates of (a) 2, (b) 10 and (c) 20 mV s^{-1}, (C) C_S and C_m for MnO_2-MWCNT electrodes, prepared using (a) DPA and (b) TDA. .113

Figure 6.10 (A)Nyquist plot of complex impedance, inset shows a high frequency range, (B) C_S' versus frequency and (C) C_S'' versus frequency for MnO_2-MWCNT electrodes with active mass loading of 35 mg cm^{-2}, prepared using (a) DPA and (b) TDA. 115

Figure 6.11 (A) CVs at scan rates of (a) 2, (b) 10 and (c) 20 mV s^{-1} and (B) capacitance versus scan rate for MnO_2-MWCNT electrodes with active mass loading of 47 mg cm^{-2}, prepared using TDA. 116

Figure 6.12 (A) Nyquist plot of complex impedance, inset shows a high frequency range, (B) C_S' versus frequency and (C) C_S'' versus frequency for MnO_2-MWCNT electrodes with active mass loading of 47 mg cm^{-2}, prepared using TDA. 117

Figure 6.13 Capacitance versus active mass loading for MnO_2-MWCNT electrodes at scan rates of (a) 2, (b) 5, (c) 50 and (d) 100 mV s^{-1}. 118

Figure 7.1 X-ray diffraction pattern of as-precipitated (a) MnO_2 (▼- JCPDS file 87-1497), (b) CeO_2 (•-JCPDS file 34-0394) and (c) ZnO (♦ -JCPDS file 36-1451). 132

Figure 7.2 (A–C) Chemical structures of (A) 16PHA, (B) ODPA and (C) SA; (D) adsorption mechanisms, involving metal (M) atoms on the particle surface and (a–d) phosphonic acid group of ODPA or (e, f) carboxylic acid group of SA: (a, b, e) bridging, (c, d, f) chelation. 134

Figure 7.3 Schematic of PELLI method: (A) particles, precipitated in aqueous phase, (B) transfer through liquid-liquid interface, (C) formation of a stable suspension of particles in n-butanol, (D) (a) as-prepared MnO_2, (b–e) extraction of MnO_2 to the 1-butanol solvent, using (b) 16PHA, (c) ODPA, (d, e) SA for mass ratio of extractor:MnO_2 of (b, c, d) 1:3 and (e) (1:1). 135

Figure 7.4 (a–l) FTIR spectra for (a) 16PHA, (c) ODPA, (e) SA, (b, d, f) MnO_2, extracted using 16PHA, ODPA and SA, respectively, (g, h, i) CeO_2, extracted using 16PHA, ODPA, and SA, respectively, (j, k, l) ZnO, extracted using 16PHA, ODPA, and SA, respectively. 136

Figure 7.5 SEM images of (A) MnO_2, (B) CeO_2 and (C) ZnO films, which were electrophoretically deposited from suspensions, prepared using PELLI and 16PHA extractor. 137

Figure 7.6 CVs at scan rates of (a) 2, (b) 10 and (c) 20 $mV\ s^{-1}$ for bulk MnO_2-MWCNT electrodes, prepared (A) without extraction, and (B–D) by PELLI using (B) 16PHA, (C) ODPA and (D) SA extractors. 139

Figure 7.7 Capacitances C_S and C_m calculated from the CVs for bulk MnO_2-MWCNT electrodes, prepared (a) without extraction, and (b–d) by PELLI using (b) 16PHA, (c) ODPA and (d) SA extractors. 140

Figure 7.8 (A) Nyquist plots of complex impedance and frequency dependences of (B) real C_S' and (C) imaginary C_S'' components of complex capacitance, calculated from the impedance data for MnO_2-MWCNT electrodes, prepared (a) without extraction and (b–d) by PELLI using (b) 16PHA, (c) ODPA and (d) SA extractors. 142

Figure 7.9 SEM image of MnO_2-MWCNT composite, prepared by PELLI using 16PHA extractor. 143

Figure 7.10 (A) CVs at scan rates of (a) 2, (b) 10 and (c) 20 mV s^{-1}, (B) C_S and C_m for thin film MnO_2-CB electrode, prepared by screen printing. 144

Figure 7.11 (A) Nyquist plot of complex impedance, (B) C_S' and (C) C_S'' versus frequency for thin film MnO_2-CB electrodes, prepared using screen printing method. 144

Figure 8.1 X-ray diffraction patterns of as-precipitated (a) α-FeOOH (▼ - peaks corresponding to JCPDS file 29–713, a' - diagram of standard peaks of JCPDS file 29–713), and (b) β-FeOOH (•- peaks, corresponding to JCPDS file 34–1266, b' - diagram of standard peaks of JCPDS file 34–1266). 158

Figure 8.2 TGA data for (a) α-FeOOH and (b) β-FeOOH. 159

Figure 8.3 SEM images of (A) α-FeOOH and (B) β-FeOOH powders. 160

Figure 8.4 (A–C) Chemical structures of (A) 16PHA, (B) HDPA and (C) PA; (D) adsorption mechanisms, involving Fe atoms on the particle surface and (a–d) phosphonic acid group of HDPA or (e, f) carboxylic acid group of PA: (a, b,e) bridging, (c,d,f) chelation. 161

Figure 8.5 (A) as-prepared α-FeOOH, (B–D) extraction of α-FeOOH to the 1-butanol solvent, using (B) 16PHA, (C) HDPA and (D) PA. 162

Figure 8.6 FTIR spectra of (a) 16PHA, (b) α-FeOOH, extracted using 16PHA, (c) HDPA and (d) α-FeOOH, extracted using HDPA, (e) PA, (f) α-FeOOH, extracted using PA... 162

Figure 8.7 Schematic of the extraction mechanisms A-B1-B2-D and A-C1-C2-D in the extraction method 1: (A) as-prepared FeOOH particles in an aqueous phase, (B1,C1) the solution of extractor molecules in 1-butanol is added and extractor molecules (B1) accumulated at or (C1) penetrated the liquid-liquid interface, (B2,C2) extractor molecules are adsorbed on the particles (B2) at the liquid-liquid interface or (C2) in the bulk of an aqueous phase, (D) particles are extracted to 1-butanol. 164

Figure 8.8 Schematic of the extraction method 2: (A) 16PHA is dissolved in alkali and added to (B) $FeCl_3$ solution, (C) FeOOH particles, modified with 16PHA are formed and (D) after addition of 1-butanol the modified particles are transferred to the 1-butanol phase. 166

Figure 8.9 (A–C) CVs at scan rates of (a) 2, (b) 10 and (c) 20 mV s^{-1} and (D) C_S and C_m for (A, D(a)) β-FeOOH-MWCNT, prepared using 16PHA and extraction method 1, (B, D(b)) α-FeOOH-MWCNT, prepared using 16PHA and extraction method 1, (C, D(c)) α-FeOOH-MWCNT, prepared using 16PHA and extraction method 2. 168

Figure 8.10 (A) Nyquist plot of complex impedance and frequency dependences of (B) real C_S' and (C) imaginary C_S'' components of complex capacitance, calculated from the impedance data for (a) β-FeOOH-MWCNT, prepared using 16PHA and extraction method 1, (b) α-FeOOH-MWCNT, prepared using 16PHA and extraction method 1, (c) α-FeOOH-MWCNT, prepared using 16PHA and extraction method 2. 169

Figure 8.11 (A–C) CVs at scan rates of (a) 2, (b) 10 and (c) 20 mV s^{-1} and (D) C_S and C_m for α-FeOOH-MWCNT, prepared (A, D(a)) without extraction, (B, D(b)) using HDPA and extraction method 1, (C, D(c)) using PA and extraction method 1. 170

Figure 8.12 (A) Nyquist plot of complex impedance and frequency dependences of (B) real C_S' and (C) imaginary C_S'' components of complex capacitance, calculated from the impedance data for α-FeOOH-MWCNT, prepared (a) without extraction, (b) using HDPA and extraction method 1, (c) using PA and extraction method 1. 171

Figure 8.13 SEM image of α-FeOOH-MWCNT composite, prepared (A) without PELLI and (B) by the PELLI method 1 using 16PHA. 172

Figure 8.14 (A) CVs at scan rates of (a) 2, (b) 10 and (c) 20 mV s^{-1} (B) C_S and C_m versus scan rate for an asymmetric supercapacitor cell, containing MnO_2-MWCNT positive electrode and α-FeOOH-MWCNT negative electrode. 173

Figure 8.15 (A)Nyquist plot of complex impedance, and frequency dependences of (B) real C_S' and (C) imaginary C_S'' components of complex capacitance, calculated from the impedance data for an asymmetric supercapacitor cell, containing MnO_2-MWCNT positive electrode and α-FeOOH-MWCNT negative electrode. 174

Figure 8.16 (A) Charge-discharge curves at current densities of (a) 3, (b) 5, (c)7, (d) 10, (e) 20, (f) 30, (g) 40 and (h) 50 mA cm^{-2}, (B) C_S and C_m calculated from the charge-discharge curves versus current density and (C) Ragone plot for an asymmetric supercapacitor cell, containing MnO_2-MWCNT positive electrode and α-FeOOH-MWCNT negative electrode. 175

Figure 9.1 (A) Chemical structure of TDA, (B) TDA adsorption mechanisms involving a surface OH group: (a) chemisorption and (b) electrostatic interaction, (C) precipitated FeOOH (D,E) schematic of extraction: (D) addition of TDA extractor to precipitated FeOOH, (E) extraction of FeOOH to n-butanol phase, (F) extracted FeOOH. 190

Figure 9.2 FTIR spectrum of (a) TDA, (b) FeOOH, extracted using TDA. 191

Figure 9.3 CVs at scan rates of (a) 2, (b) 5 and (c) 10 mV s^{-1} for different electrodes: (A) PPy-CNT, (B) FeOOH-CNT, prepared without PELLI, (C) FeOOH-CNT, prepared using PELLI, and (D) PPy-CNT-FeOOH, prepared using PELLI. 192

Figure 9.4 C_S and C_m for different electrodes: (a) PPy-CNT, (b) FeOOH-CNT, prepared without PELLI, (c) FeOOH-CNT, prepared using PELLI and (d) PPy-CNT-FeOOH, prepared using PELLI. 193

Figure 9.5 (A) Nyquist plot of complex impedance, (B) $C_S^{'}$ versus frequency and (C) $C_S^{''}$ versus frequency for PPy-CNT at different electrode potentials: (a) 0.1, (b) −0.2, (c) −0.5 and (d) −0.8 V. 194

Figure 9.6 (A) Nyquist plot of complex impedance, (B) $C_S^{'}$ versus frequency and (C) $C_S^{''}$ versus frequency for FeOOH-CNT, prepared without PELLI, (D) Nyquist plot of complex impedance, (E) $C_S^{'}$ versus frequency and (F) $C_S^{''}$ versus frequency for FeOOH-CNT, prepared using PELLI at different electrode potentials: (a) 0.1, (b) −0.2, (c) −0.5 and (d) −0.8 V. 196

Figure 9.7 (A) Nyquist plot of complex impedance, (B) $C_S^{'}$ versus frequency and (C) $C_S^{''}$ versus frequency for PPy-CNT-FeOOH, prepared using PELLI at different electrode potentials: (a) 0.1, (b) −0.2, (c) −0.5 and (d) −0.8 V. 197

Figure 9.8 CVs for (a) negative PPy-CNT-FeOOH electrodes and (b) positive MnO_2-CNT electrodes at a scan rate of 10mV s^{-1}. 198

Figure 9.9 (A) CVs at scan rates of (a) 2, (b) 5 and (c) 10 mV s^{-1} (B) C_S and C_m versus scan rate for an asymmetric supercapacitor cell, containing a negative PPy-CNT-FeOOH electrode and a positive MnO_2-CNT electrode. 199

Figure 9.10 (A) Nyquist plot of complex impedance, (B) C_S' versus frequency and (C) C_S'' versus frequency for an asymmetric supercapacitor cell, containing a negative PPy-CNT-FeOOH electrode and a positive MnO_2-CNT electrode. 199

Figure 9.11 (A) Charge-discharge curves at currents of (a) 3, (b) 5, (c) 7, (d) 10, (e) 20, (f) 30, (g) 40 and (h) 50 mA cm^{-2}, (B) C_S and C_m calculated from the charge-discharge data versus current density for an asymmetric supercapacitor cell, containing a negative PPy-CNT-FeOOH electrode and a positive MnO_2-CNT electrode. 200

List of Abbreviations and Symbols

EPD	Electrophoretic Deposition
PELLI	Particles extraction through liquid-liquid interface
EC	Electrochemical capacitor
SC	Supercapacitor
EDLC	Electrochemical double layer capacitor
TGA	Thermogravimetric analysis
FTIR	Fourier transform infrared spectroscopy
DLS	Dynamic light scattering
CV	Cyclic voltammetry
EIS	Electrochemical Impedance Spectroscopy
SCE	Saturated calomel electrode
XRD	X-ray diffraction
SEM	Scanning electron microscope
MWCNT	Multiwalled carbon nanotube
PPy	Polypyrrole
C_m	Mass normalized specific capacitance

C_S	Area normalized specific capacitance
F (unit)	Farad

1 Introduction

In mid-1970s, the energy crisis caused by the potential risk of using up the conventional fossil fuel arose people's attentions on development of renewable energy sources. Although different kinds of renewable energy sources, such as solar, wind and tidal wave, are abundant in the nature, they depend on the natural condition and are not continual and even. As a result, these kinds of energy cannot meet the demand of modern technical equipment, which need an uninterrupted and stable power supply[1-5]. Therefore, aiming to address these issues, many effective and practical technologies of electrochemical energy storage and conversion, such as batteries, fuel cells and supercapacitors, attract more and more people's attentions[2, 6, 7]. However, in many practical areas, such as portable electrochemical devices, hybrid electric vehicles and large industrial equipment, most of the present electrical energy storage systems cannot meet their requirements of high performance. Therefore, it's extremely significant for us to develop advanced materials and advance our understanding of electrochemical energy storage mechanisms at the nanoscale[2].

Electrochemical capacitors (ECs), also called ultracapacitors or supercapacitors (SCs), play an important role in these kind of areas because of their high power density (about 10 kW/ kg), which can be fully charged or discharged within a few seconds. Although ECs are limited by their low energy delivery (about 5Wh/kg), they are considered as the most promising products to complement or replace the batteries in the energy storage systems, such as for uninterruptible power supplies for protection against power disruptions, stores energy for acceleration in electric vehicles and harvesting braking energy when the engine shut-off as well as rapid loading. The recent application of electrochemical double layer capacitors (EDLCs) in emergency doors on an Airbus A380 proved that their performance and stability are good enough for large scale implementation. Therefore, in the US Department of Energy, ECs have been considered as important as batteries in future energy storage systems[8, 9].

ECs can be classified into three types, EDLCs, pseudocapacitors and hybrid supercapacitors[2]. This classification is based on their charge storage mechanism as well as the active materials used. Among these ECs, EDLCs is the first kind of commercial and most commonly used devices, currently fabricated by carbon-based active material with high surface area and high conductivity, such as carbon nanotube, activated carbon and carbon black. Pseudocapacitors is the second kind of ECs, which normally uses the redox material with high specific capacitance and large energy storage capacity (conductive polymer, transition metal oxide, etc.) as the active material. To increase the energy density and power density of ECs, the devices are fabricated as an asymmetric hybrid capacitor, which combines both the advantages of EDLCs and pseudo-capacitors. In hybrid capacitor systems, combination of two different electrode materials with different operating potentials are used for the positive and negative materials, such as transition metal oxide (oxide-hydroxide)-carbon based material, conductive polymer-carbon based material and conductive polymer-transition metal oxide(oxide-hydroxide) composite. As a result, this strategy increases the overall cell potential and results in higher energy density as well as power density[2, 10]. Among these electrode materials, manganese dioxide (MnO_2) and iron oxide-hydroxide are good candidates for the fabrication of positive and negative electrodes for ECs, respectively[7, 11]. This is attributed to their high specific capacitance, their natural abundance, friendly environmental nature and low cost. However, the specific capacitance decreases drastically with increasing active mass loading, especially at high charge-discharge rates, due to the low electronic conductivity of active material and poor electrolyte access to their surface. It is important to fabricate small particles with high surface area without agglomeration to provide more active sites for ions absorption. Meanwhile, conductive additives should be dispersed well and uniformly mixed with active material to generate conductive network which can enhance the electronic conductivity[5, 12-14].

In this investigation, an advanced colloidal fabrication technique, called particle extraction through liquid-liquid interface technique (PELLI), has been developed for the fabrication of individual component, binary composite and ternary composite for both the positive and negative electrodes of electrochemical capacitors (ECs). Furthermore, the new colloidal strategies were applied to fabrication of stable suspension for electrophoretic deposition (EPD) of thin film and fabrication of environmentally friendly printing inks for screen printing application. We focus on the development of advanced composite electrodes and efficient electronic devices with high active mass loadings, a high ratio of the active material mass to the current collector mass, high capacitance, good capacitance retention at high charge-discharge rates and low impedance.

1.1 References

[1] J. A. Turner, "A realizable renewable energy future," *Science,* vol. 285, pp. 687-689, 1999.

[2] P. Simon and Y. Gogotsi, "Materials for electrochemical capacitors," in *Nanoscience And Technology: A Collection of Reviews from Nature Journals*, ed: World Scientific, 2010, pp. 320-329.

[3] A. Evans, V. Strezov, and T. J. Evans, "Assessment of utility energy storage options for increased renewable energy penetration," *Renewable and Sustainable Energy Reviews,* vol. 16, pp. 4141-4147, 2012.

[4] M. Steinberg, "Fossil fuel decarbonization technology for mitigating global warming," *International Journal of Hydrogen Energy,* vol. 24, pp. 771-777, 1999.

[5] K. Shi and K. P. Giapis, "Scalable fabrication of supercapacitors by nozzle-free electrospinning," *ACS Applied Energy Materials,* vol. 1, pp. 296-300, 2018.

[6] M. Winter and R. J. Brodd, "What are batteries, fuel cells, and supercapacitors?," ed: ACS Publications, 2004.

[7] W. Wei, X. Cui, W. Chen, and D. G. Ivey, "Manganese oxide-based materials as electrochemical supercapacitor electrodes," *Chemical society reviews,* vol. 40, pp. 1697-1721, 2011.

[8] G. Wang, L. Zhang, and J. Zhang, "A review of electrode materials for electrochemical supercapacitors," *Chemical Society Reviews,* vol. 41, pp. 797-828, 2012.

[9] Y. Gogotsi and P. Simon, "True performance metrics in electrochemical energy storage," *Science,* vol. 334, pp. 917-918, 2011.

[10] S.-B. Ma, K.-W. Nam, W.-S. Yoon, X.-Q. Yang, K.-Y. Ahn, K.-H. Oh, *et al.*, "A novel concept of hybrid capacitor based on manganese oxide materials," *Electrochemistry Communications,* vol. 9, pp. 2807-2811, 2007.

[11] B. Xu, M. Zheng, H. Tang, Z. Chen, Y. Chi, L. Wang, *et al.*, "Iron oxide-based nanomaterials for supercapacitors," *Nanotechnology,* vol. 30, p. 204002, 2019.

[12] Y. Wang, Y. Liu, and I. Zhitomirsky, "Surface modification of MnO_2 and carbon nanotubes using organic dyes for nanotechnology of electrochemical supercapacitors," *Journal of Materials Chemistry A,* vol. 1, pp. 12519-12526, 2013.

[13] H. Fan, R. Chen, and I. Zhitomirsky, "Manufacturing of polypyrrole-FeOOH supercapacitors," *Materials and Manufacturing Processes,* pp. 1-4, 2019.

[14] Y. Liu, D. Luo, K. Shi, X. Michaud, and I. Zhitomirsky, "Asymmetric supercapacitor based on MnO_2 and Fe_2O_3 nanotube active materials and graphene current collectors," *Nano-Structures & Nano-Objects,* vol. 15, pp. 98-106, 2018.

2 Literature review

2.1 Conventional capacitors

In 1745, German Ewald Georg von Kleist discovered that charge could be stored in glass jar containing a volume of water when a high voltage was applied[1]. In 1746, scientist Pieter van Musschenbroek from University of Leiden invented a capacitor, called Leyden jar. The storage mechanism of capacitors in early time were mainly developed by scientists Benjamin Franklin and Faraday[1]. The first generation of capacitors, called electrostatic capacitors, shown schematically in Figure 2.1, are composed of two conducting electrodes separated by an insulating dielectric material. When a certain voltage is applied to a capacitor, the dielectric material would be polarized and then the positive and negative charges accumulate on the positive electrode and the negative electrode, respectively. As the charges are separated by the dielectric material, a static electric field is built between the two electrodes to store energy. These kinds of capacitors are mainly used for small energy storage devices and to reduce the ripple of power supply.

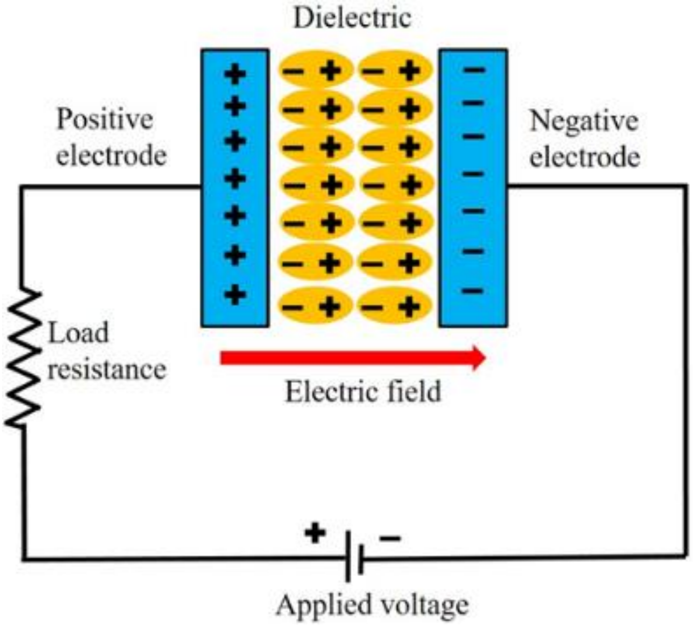

Figure 2.1 Schematic of electrostatic capacitors

The capacitance C is supposed to be a constant value for an ideal electrostatic capacitor. This value is defined by the relationship of accumulated charge Q on a certain electrode and the applied voltage V between the two electrodes:

$$C = \frac{Q}{V} \tag{2-1}$$

For a conventional capacitor, *C* is directly proportional to the surface area *A* of each electrode and dielectric property of the dielectric material and inversely proportional to the distance between the electrodes *d*:

$$C = \varepsilon_0 \varepsilon_r \frac{A}{d} \tag{2-2}$$

Herein, ε_0 represents the permittivity of free space and ε_r represents the permittivity of insulating material between the electrodes. The performance of a capacitor can be characterized by its power density and energy density, which can be expressed in either per unit mass, per unit surface area, or per unit volume. The stored energy E of a capacitor can be expressed by the following equation:

$$E = \frac{1}{2}CV^2 \tag{2-3}$$

From this equation, it is evident that the stored energy in a capacitor is proportional to the capacitance and the square of the applied voltage between the two electrodes. The power of a capacitor could be calculated from an electric circuit, containing a capacitor with an external loading resistance R in series. The internal resistance, coming from different parts of a capacitor, such as electrode, current collector and dielectric material, can be considered as equivalent series resistance (*ESR*). When R is equal to *ESR*, the maximum power P can be achieved and expressed as the following equation:

$$P = \frac{V^2}{4 \times ESR} \tag{2-4}$$

Although conventional capacitors have high power density, their applications are limited by their low energy density. Therefore, electrochemical capacitors with higher energy density than that of conventional capacitors attract more attentions.

Based on the working mechanism during charging and discharging, supercapacitors typically can be divided into three groups: (i) electric double layer capacitors (EDLCs), (ii) pseudocapacitors and (iii) hybrid supercapacitors.

2.2 Categories of electrochemical capacitors (ECs)

2.2.1 Electric double layer capacitors (EDLCs)

Figure 2.2 shows the schematic diagram of electric double layer capacitors (EDLCs), consisting of two high surface area porous electrodes separated by a separator in the middle and immersed in an electrolyte. The charge accumulates at the interface between the electrode and electrolyte. As a result, an electric double layer is built up at the interface of electrolyte and electrode surface and the thickness of each layer is just in the order of a few Angstroms[2]. It is important to point out that the surface area of porous activate carbon material using in EDLCs is around 0.1 million times larger than that of smooth surface. Based on equation (2-2), d is the thickness of the double layer capacitor with a high surface area A. In this situation, the corresponding electric field of the electrochemical double layer is extremely high and its value can reach 10^6 V cm^{-1} easily. Therefore, the capacitance and energy density of EDLCs are much higher than that of conventional capacitor where the capacitance is just in the order of pF or μF. Due to the electrostatic charge mechanism of EDLCs, which does not involve redox reaction, there is no limitation on the electrochemical kinetic during charging or discharging process. As a result, EDLCs can have a much higher power density than pseudocapacitors involving redox reaction, as well as a much higher energy density than conventional capacitors.

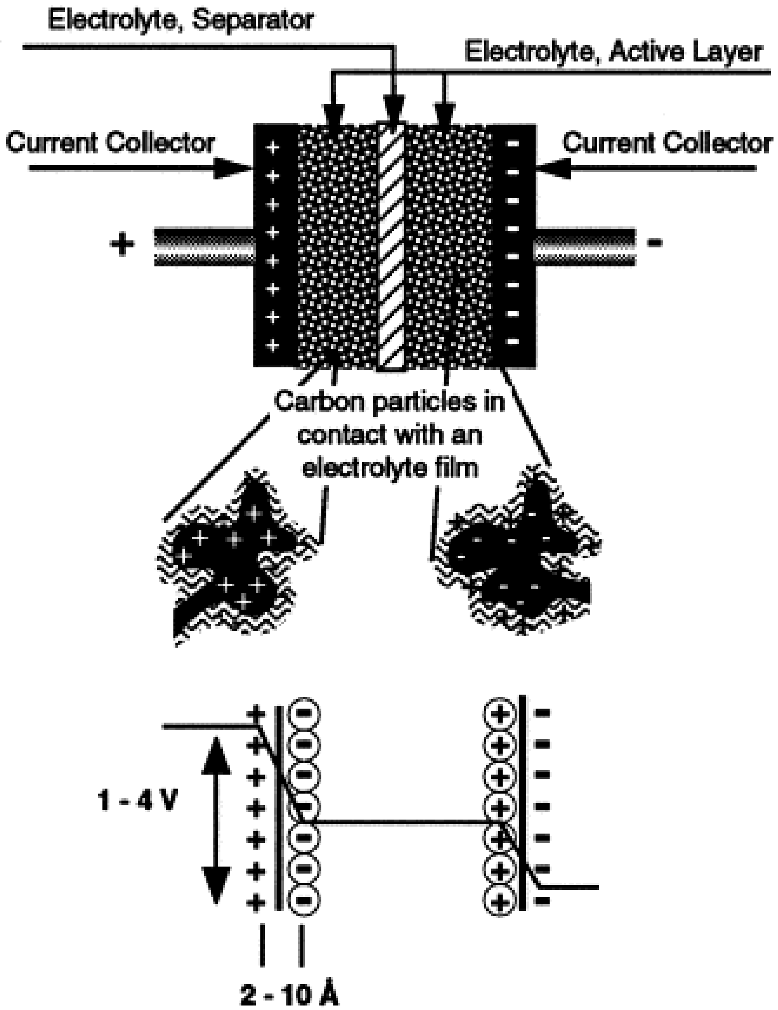

Figure 2.2 Schematic structure and principles of a single cell EDLCs[2].

2.2.2 Pseudocapacitors

Different from EDLCs, which are only based on electrostatic charge storage mechanism (non-faradaic), pseudocapacitors involve reversible redox reaction (faradaic) combined with electrostatic effect during charging or discharging process. For the same surface area, the value of pseudocapacitance could be 100 times larger than that of electric double layer capacitance because of the contribution of faradaic reaction[3]. In this faradaic process, the charges pass through the electrode/electrolyte interface whereas the charges just accumulate at the electrode/electrolyte interface in EDLCs.

Figure 2.3 shows several faradaic mechanisms, proposed by Conway, which can result in psedocapacitive behavior in capacitors[4-9]. The first one is underpotential deposition (UPD), which occurs when metal ions form an adsorbed monolayer at a different metal surface well above their redox potential. The deposition of lead on the gold surface is a representative example of UPD. The second one is redox pseudocapacitance. This occurs during the process of the electrochemical absorption of ion on the surface or near the surface of a material accompanied by a faradaic charge transfer. Transitional metal oxides/oxide-hydroxides, such as RuO_2[10, 11], MnO_2[12-14], Mn_3O_4[15, 16], NiO[17], Co_3O_4[18, 19], $Ni(OH)_2$[20, 21], $Co(OH)_2$[22, 23], FeOOH[24, 25], etc, as well as conductive polymers, such as poly(3,4-ethylenedioxythiophene) (PEDOT)[26, 27], polyaniline (PANI)[28, 29] and polypyrrole (PPy)[30-32], are classified as the redox pseudocapacitive materials. The third one is intercalation pseudocapacitance. This results from intercalation of ions into the tunnels or layers of a redox active material with a concomitant faradaic charge transfer but without crystallographic phase change.

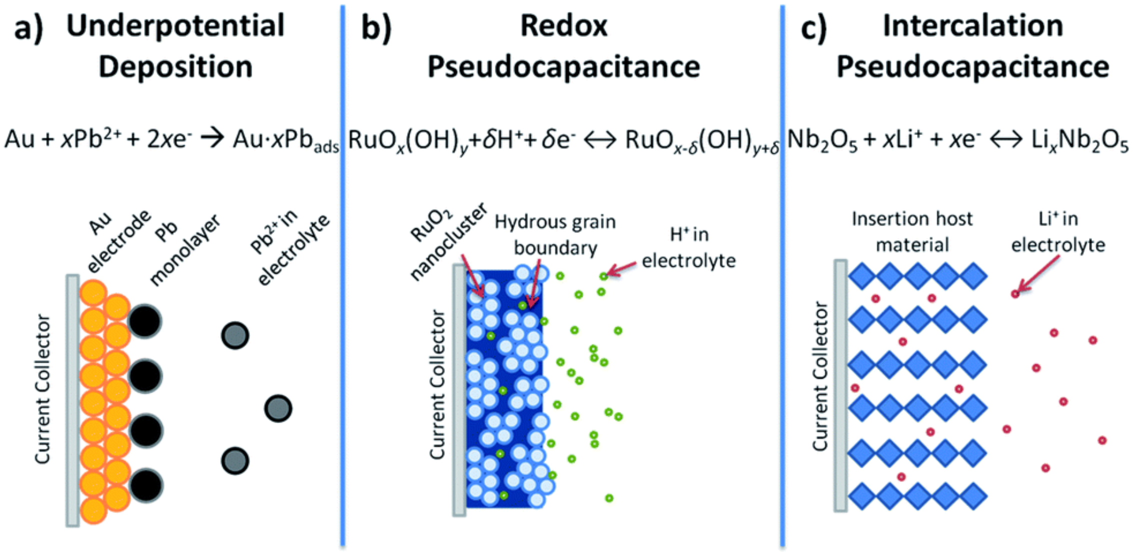

Figure 2.3 Various reversible redox mechanisms for pseudocapacitance

2.2.3 Asymmetric supercapacitors

Typically, electric double layer capacitors (EDLCs) and pseudocapacitors can be classified as symmetric supercapacitors as both the positive and negative electrodes uses the same kind of material. However, in order to maximize the electrochemical performance of the capacitors, hybrid supercapacitors, coupled with one electric double electrode with another pseudocapacitive electrode or assembled by two different pseudocapacitive electrode, have received a great deal of attentions recently. This kind of hybrid cells combine the high power density of EDLCs with the high energy density of pseudocapacitors. As it is shown in Figure 2.4, the hybrid supercapacitors with relatively high specific energy as well as high specific power fill the gap between symmetric supercapacitors and Li-ion batteries.

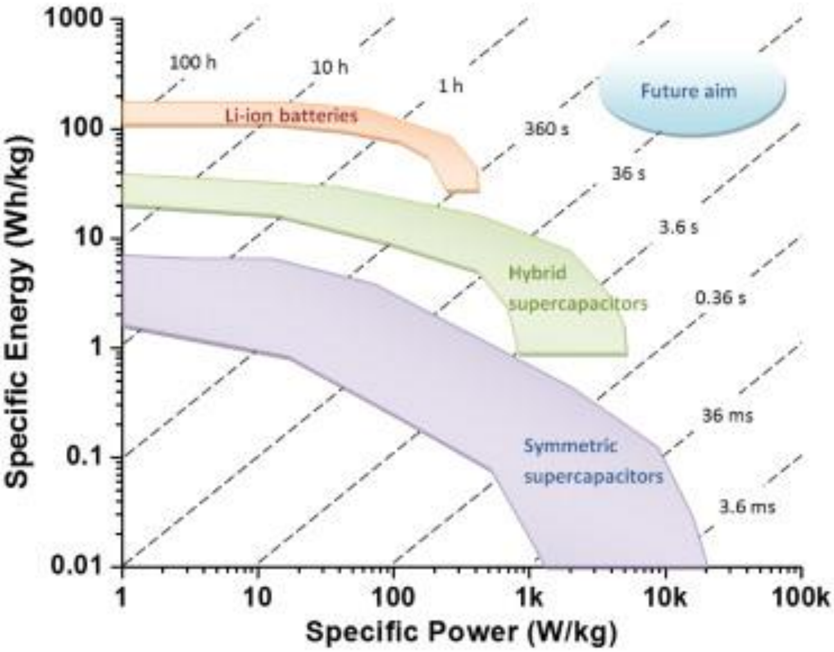

Figure 2.4 Ragone plot of three major electrochemical energy storage devices and time constants are shown in dashed line, by dividing the specific energy with specific power[33]

2.3 Electrode materials

The type of electrode materials has a great influence on the electrochemical performance of electrochemical capacitors. Normally, carbon based electrode materials, whose energy storage is based on electrostatic mechanism, are used in EDLCs, whereas metal oxide/oxide-hydroxide and conductive polymer are used as pseudocapacitive materials in pseudocapacitors where the charge storage is based on redox reaction. In order to fully utilize the merits of both the carbon based electrode materials and pseudocapacitive materials, composite electrodes combining these two kinds of material attract a lot of attention. Significant advancement in the development of composite electrodes has been achieved recently.

2.3.1 Carbon based electrode materials

Carbon based electrode materials offer several significant advantages, such as high chemical stability, abundant source in nature, non-toxic for environment, relatively low cost and wide operating temperature range. Therefore, researchers focus on investigating different kinds of carbon based electrode materials, like carbon nanotubes[34, 35], graphene[36, 37], activated carbons[38], carbon aerogels[39, 40], graphite[41] and other related nano-structured carbon materials[42-44].

In EDLCs, as the charges are stored at the electrode/electrolyte interface, the specific surface area, pore size distribution as well as the shape and structure of pore result in different electrochemical performance[45]. Especially, the specific surface area and pore size distribution affect the electrochemical performance greatly.

2.3.2 Transition metal oxides/oxide-hydroxides

Compared to carbon-based material, transition metal oxides/oxide-hydroxides are more attractive for ECs application because of their high specific capacitance. Normally, transition metal oxides/oxide-hydroxides offer two or more oxidation states for charge transfer without involving phase change. These oxidation states allow for energy storage not only electrostatically but also via faradaic reaction[46]. In the transition metal oxide, RuO_2 is widely recognized as the most promising candidate for ECs because of its high conductivity, high specific capacitance as well as good reversible electrochemical properties[3, 47]. However, its limited availability, high cost and toxic nature significantly limits its application in our real life. Therefore, RuO_2 was normally extensively investigated for military applications where the cost is not the major concern. Other metal oxides/oxide-hydroxides materials, such as MnO_2, Mn_3O_4, Co_3O_4, NiO, V_2O_5, $Co(OH)_2$, $Ni(OH)_2$, FeOOH, etc, have been explored to replace RuO_2 in the application of ECs. However, many metal oxides/oxide-hydroxides, such as Co_3O_4, NiO, V_2O_5, $Co(OH)_2$, $Ni(OH)_2$, etc, are not environmentally friendly and low capacitance of Mn_3O_4 particles limits their applications. Among all these metal oxides/oxide-hydroxides materials, MnO_2 and FeOOH with a relative high theoretical capacitance abundant source and environmental friendly properties, have been considered as the promising candidates for fabrication of positive and negative electrodes for ECs[4, 48-50] . However, their nature of low electronic conductivity needs to be enhanced by combining with different kinds of conductive media, such as carbon nanotube, carbon black, graphene, etc.

2.3.3 Conductive polymers

Another family of potential electrode material based on faradaic charge mechanism for pseudocapacitors are conductive polymers, such as Poly(3,4-ethylenedioxythiophene) (PEDOT)[27, 51], polyaniline (PANI)[52, 53] and polypyrrole (PPy)[30, 54, 55]. In 1990s, conductive polymers were first introduced to fabricate pseudocapacitive electrodes because of their high conductivity, low cost, light weight, relatively high theoretical capacitance, and simple fabrication methods. Moreover, it was reported that conductive polymer was beneficial for fabricating portable, flexible, pressable and lightweight modern electronic devices which have promising market demands in our real life. Currently, lots of ECs devices with relative high energy density as well as high power density have been fabricated using conductive polymer based electrodes[56]. Among these conductive polymers, PPy shows a promising future because it could be operated in mild electrolyte, whereas PANI and PEDOT needs acidic electrolytes which are not environmental friendly, more corrosive and less safe. Significant progress on the development of PPy electrodes using different kinds of dopants and synthesized methods has been reported. In this research, PPy was selected as the electrode material by combining with FeOOH for fabrication of negative electrodes.

2.3.4 Composite electrodes

Generally, carbon based electrode materials, which store energy through electrostatic mechanism without involving faradaic reaction, can achieve ultra-long cycle life and high power density due to their high conductivity, high surface area and good chemical stability. However, these electrodes have a limitation of low energy density that greatly restricts their applications. On the contrary, pseudocapacitive electrode materials (transition metal oxides/oxide-hydroxides and conductive polymers) based on faradaic reaction charge mechanism, can achieve high energy density because of their high theoretical specific capacitance. However, these materials also have their limitations, such as low conductivity of transition metal oxides and low mechanical stability of conductive polymers.

Therefore, aiming to address the limitations of the aforementioned materials, composite electrodes based on carbon based materials and pseudocapacitive materials are widely utilized in electrochemical capacitors, which can achieve a high power density, high energy density, good mechanical stability as well as good cyclic stability[57-59]. Significant progress on the development of composite electrodes, such as MnO_2-MWCNT, MnO_2-carbon black, Mn_3O_4-MWCNT, V_2O_5-MWCNT, NiO-MWCNT, PPy-MWCNT, PPy-Graphene, FeOOH-MWCNT, PPy-FeOOH-MWCNT, has been achieved recently.

2.4 Electrolytes

Electrolytes play an important role on electrochemical performance of ECs, involving EDLCs, pseudocapacitors and hybrid ECs. Significant efforts have been contributed to investigate the ionic conductivity, ion mobility, viscosity, ion size, potential window, concentration, stabilization and temperature of electrolytes on the effect of electrochemical performance of ECs, such as ESR, capacitance, power density, etc. Electrolytes could be mainly divided into following groups: (1) aqueous electrolytes, (2) organic electrolytes and (3) ionic liquids based electrolytes. Aqueous electrolytes and the organic electrolytes are the most common electrolytes for ECs applications.

2.4.1 Aqueous electrolytes

Compared to organic electrolytes, aqueous electrolytes are commonly used in energy storage devices owing to their advantages of low cost and facile handling [60]. Normally, the conductivity of organic electrolytes is at least one order of magnitude lower than that of aqueous electrolytes. For instance, 1M H_2SO_4 has a conductivity of 0.8 S cm^{-2} at 25 °C[61]. The main drawbacks of aqueous electrolytes are attributed to their small electrochemical stable potential window, which easily results in the issue of water decomposition[62]. Aqueous electrolytes can primarily be divided into three groups, including acidic electrolytes, alkaline electrolytes and neutral electrolytes. H_2SO_4, KOH and Na_2SO_4, which are commonly used, are the representatives for acidic electrolytes, alkaline electrolytes and neutral electrolytes, respectively. Compared to other acidic electrolytes, H_2SO_4 is commonly used in the academic investigations owing to its relatively high ionic conductivity, providing lower ESR of ECs with regards to neutral electrolytes[60]. It was found that the ionic conductivity of H_2SO_4 is dependent on its concentration and temperature. The maximum value should be achieved at a certain concentration and temperature. For similar reason, KOH represents the basic electrolytes owing to its relatively higher ion conductivity with regards to other basic electrolytes, such as LiOH and NaOH[60]. It has been reported that the capacitance of EDLCs electrodes was increased when the basic electrolytes was used compared to neutral electrolyte. This is because the pseudocapacitance was contributed to the charge storage in alkaline electrolyte environment. Although acidic and basic electrolytes show great ionic conductivity, their drawbacks of corrosion and safety limit their further development especially at a high temperature condition[63-65]. Therefore, neutral electrolytes play an important role in these fields. Extensive efforts have been focused on development of various neutral electrolytes for ECs, such as K_2SO_4, Li_2SO_4, Na_2SO_4, KCl, LiCl, NaCl, etc[60]. Among these electrolytes, Na_2SO_4 has been considered as the promising candidates for pseudocapacitors electrodes, especially for MnO_2. Neutral electrolytes are not only beneficial for pseudocapacitive materials but also for hybrid ECs with a higher operation voltage window owing to their electrochemical stability for many materials. Moreover, neutral electrolytes have advantages of environmental friendless and low cost.

2.4.2 Organic electrolytes

Although aqueous electrolytes are popularly investigated in academic work, their low operating voltage window (1.4-2V) results in low energy density of the devices. Therefore, the ECs assembled with organic electrolytes, providing typically higher operation voltage window (2.5-2.8V), shows great demands in the commercial markets[60, 66]. The energy density of ECs is enhanced when using organic electrolytes with larger operative voltage window. Moreover, organic electrolytes based ECs can be packaged in cheaper ways, such as using cheaper packages and current collectors. However, organic electrolytes based ECs also show their limitations of lower conductivity, smaller capacitance, higher cost, flammable property, and toxic effects. Moreover, they can easily suffer from the problems of large self-discharge rate and significant degradation of performances because of the impurity effect caused by complex purification processing. The electrochemical performance of organic electrolytes based ECs are dependent on the ion size, viscosity, conductivity, electrochemical stable potential windows of the organic electrolytes used in the systems[3].

2.5 Manufacturing methodologies

2.5.1 Colloidal techniques for fabrication of bulk electrodes and thin films

Composite materials are necessary for achieving desired electrochemical performance of ECs electrodes, which require high electrical conductivity, high surface area and high capacitance. Normally, active materials, such as MnO_2[67], Mn_3O_4[15], NiO[17], V_2O_3[68] MoO_3[69], FeOOH[25], PPy[70], etc, have very low electronic conductivity, which is far away for ECs electrodes applications, especially at a high active mass loading condition and high charge-discharge rates. Therefore, combining with conductive additive, such as MWCNT and graphene, are required to enhance their performance[70, 71]. For ECs applications, colloidal techniques are common strategies for fabrication of advanced composite which are achieved by efficient dispersion of different individual components.

2.5.1.1 Co-dispersion method

Co-dispersion method is a simple strategy to disperse the active materials and the conductive additives at the same time in one pot using only one dispersing agent. For example, it was found that celestine blue dye is an efficient co-dispersing agent for $BiMn_2O_5$ and MWCNT[72]. The dispersion of MWCNT is attributed to the electrosteric interactions and π-π interactions between MWCNT and celestine blue dye whereas the dispersion of $BiMn_2O_5$ is attributed to the strong adsorption of celestine blue on $BiMn_2O_5$ particles surface providing the electrosteric stabilization. Therefore, the $BiMn_2O_5$-MWCNT composite electrodes with a high capacitance of 6 F cm^{-2} (2mV s^{-1}) was reported at a very low resistance. Shi et al. reported that safranin (SAF) is an efficient dispersing agent for co-dispersing MWCNT and PPy (Figure 2.5)[73]. These PPy-MWCNT composite electrodes with a high active mass loading of 27 mg cm^{-2} showed a high capacitance of 7.8 F cm^{-2}. These co-dispersing suspensions showed a promising potential in the deposition of thin films by electrophoretic deposition (EPD).

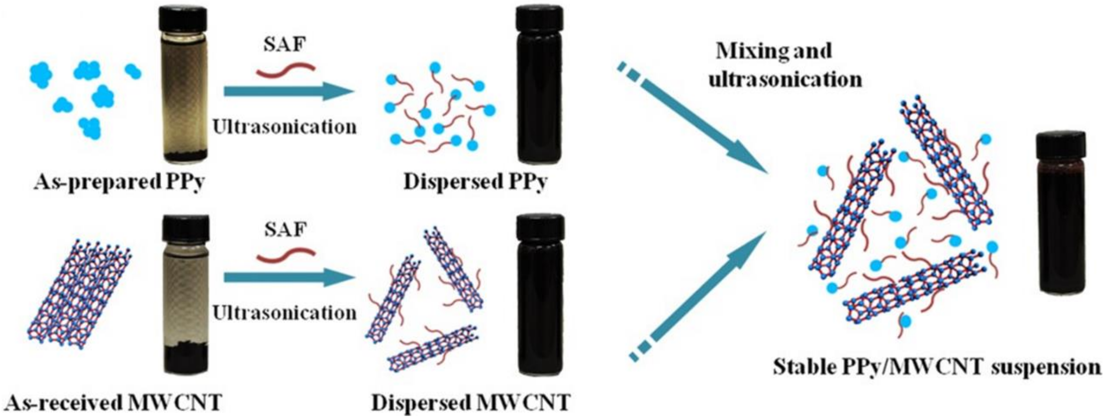

Figure 2.5 Co-dispersion of PPy-MWCNT by SAF[73].

2.5.1.2 Heterocoagulation technique

Heterocoagulation technique is one of the facile strategies to create strong linking between the active materials and the conductive additives for improving the contact of the individual components in these composites. They are mainly classified into following two groups: (1) heterocoagulation based on electrostatic interaction[74, 75] and (2) heterocoagulation based on Schiff based reaction[16, 67].

For example, Figure 2.6 shows the MnO_2-MWCNT composite fabricated by heterocoagulation based on electrostatic interaction[74]. In this strategy, phosphate ester and m-cresolsulfonphthalein dye were used as the dispersing agents for MWCNT and MnO_2 particles, respectively. Therefore, MWCNT and MnO_2 imparted positive and negative charge on their surface, respectively, which created links between MWCNT and MnO_2 by electrostatic interaction. Advanced MnO_2-MWCNT composite has been successfully fabricated. The electrodes showed a high areal capacitance of 5.3 F cm^{-2} at a scan rate of 2 mV s^{-1}.

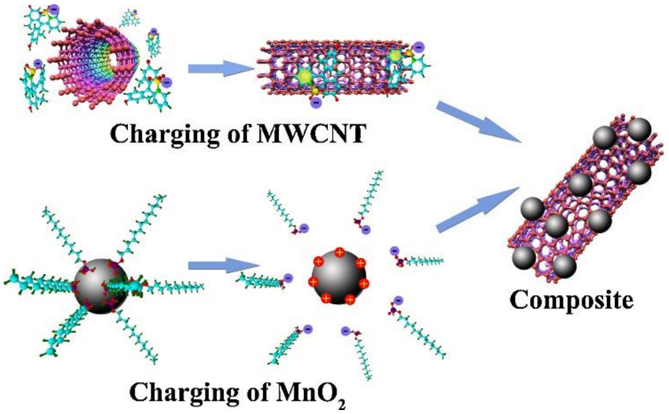

Figure 2.6 MnO_2-MWCNT composite fabricated by heterocoagulation based on electrostatic interaction[74].

Figure 2.7 shows that MnO_2-MWCNT composite can be fabricated by heterocoagulation based on Schiff base reaction between 3,4-Dihydroxybenzaldehyde (DHB) and new fuchsin (NF), which were used for dispersion of MnO_2 and MWCNT, respectively. The strong link created by the Schiff base reaction mechanism facilitated a good contact of the active materials MnO_2 particles and conductive MWCNTs additives. Therefore, these MnO_2-MWCNT composite showed good electrochemical performance.

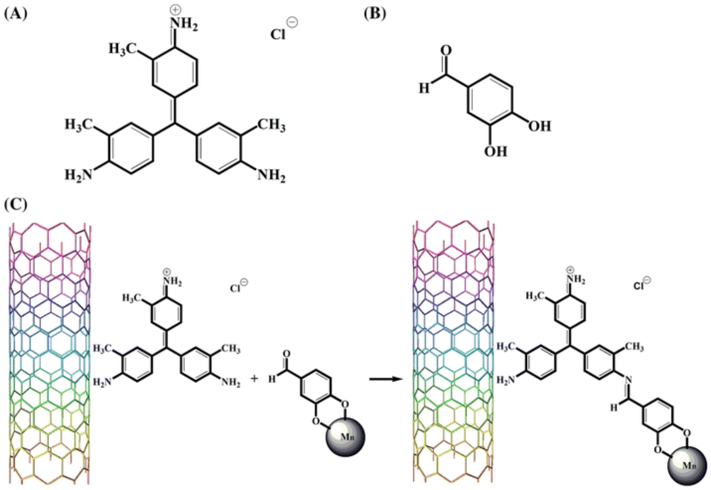

Figure 2.7 MnO_2-MWCNT composite fabricated by heterocoagulation based on Schiff based reaction between (A) new fuchsin (NF) and (B) 3,4-Dihydroxybenzaldehyde (DHB)[67].

2.5.1.3 Particle extraction through liquid-liquid interface (PELLI) method

PELLI method is one of the most important colloidal strategies for transferring different materials, such as metal oxides, metal hydroxides, metal oxide-hydroxides and metal particles between two immiscible phases. PELLI techniques allow extraction of particles form the synthesized media to the organic media which are beneficial for device processing. PELLI techniques attracts more and more attention because of their ability for fabricating high electrochemical performance composite electrodes, such as MnO_2-MWCNT[14, 76] and Mn_3O_4-MWCNT[16]. These were achieved by reducing agglomeration of particles and improving contact between the active materials and the conductive media. Poon et al.[16] demonstrated that Mn_3O_4 could be extracted from aqueous phase to the organic phase using lauryl gallate. Advanced Mn_3O_4-MWCNT composite has been fabricated for ECs applications. Wallar et al.[14] also reported that lauryl gallate (LG) could be used as an extractor for extraction of Ag particles and MnO_2 for further processing with MWCNT, which were well dispersed in the organic phase, to fabricate advanced Ag-MnO_2-MWCNT ternary composite electrodes for ECs (Figure 2.8). Moreover, Clifford et al. demonstrated that agglomeration-free hydroxyapatite nanorods prepared by PELLI method could be used for fabrication of thin films by EPD.

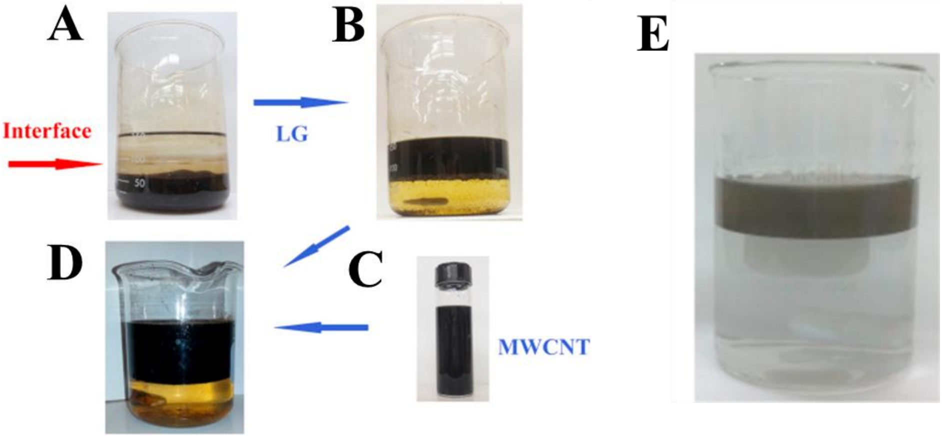

Figure 2.8 (A) MnO_2 precipitation, (B) MnO_2 extracted by LG in 1-butanol, (C) MWCNT dispersion in 1-butanol, (D) MnO_2-MWCNT extracted in 1-butanol and (E) Ag extracted by LG in 1-butonal[14].

2.5.1.4 Electrophoretic deposition (EPD)

Electrophoretic deposition (EPD) technique is widely used in the field of surface engineering for fabrication of composite and ceramic films with designed functions for specific applications, such as corrosion protection[77], flame-retardant[78, 79], biomedical applications[80-83], sensors[84] and energy storage[71, 85, 86]. EPD technique has emerged as promising manufacturing method owing to the advantages of facile control processing, low cost and high quality of film formation.

Figure 2.9 demonstrates the schematics of electrophoretic deposition of thin films for ECs applications. Firstly, the stable suspensions were prepared using safranin (SAF) as the co-dispersing and charging agent for dispersing and charging MWCNT, graphene and PPy particles[71]. Subsequently, two electrodes, one reference electrode and other working electrode for deposition, were immersed in the suspension separated by a certain distance. When a specific voltage is applied to these two electrodes, an electric field is formed between them. The charging particles in the suspension would allow them to be deposited on the working electrodes by the electric force introduced by the electric field. High quality composite thin films with improved electrochemical performance compared to the films formed by the single component, were obtained by EPD for ECs applications. Moreover, Clifford et al. [87] demonstrated that agglomeration-free hydroxyapatite nanorods prepared by PELLI could be used for preparation of stable suspension for depositing thin film by EPD for biomedical applications.

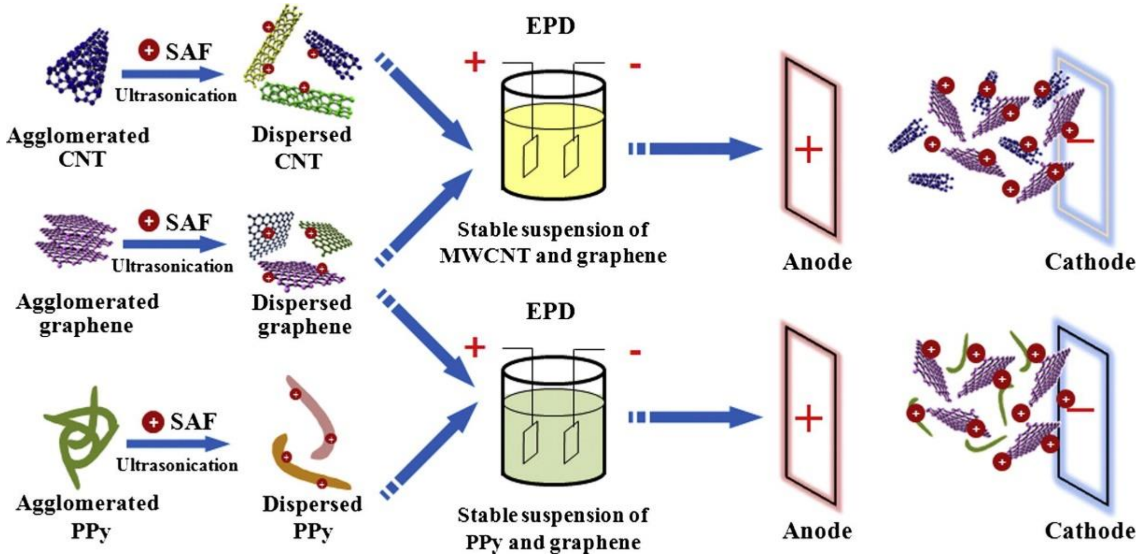

Figure 2.9 Co-dispersion of MWCNT-graphene and PPy-graphene and their applications for film formation by EPD[71].

2.5.1.5 Screen printing

Flexible, compressible, wearable and portable electronic devices are emerged as necessary products for human being in modern society[54, 88-90]. In order to scale-up the fabrication of these devices, facile techniques with low cost could be found to meet the market demands. Various printing techniques, such as screen printing[91, 92], inkjet printing[93] and roll-to-roll printing[90], shows their promising potential for fabrication of electronic devices. These printing techniques are mainly based on the transferring of the printing inks to the given substrates for assembly of electronic devices. Among all the printing techniques, screen printing is one of the most facile and inexpensive printing techniques for the fabrication of electronic devices.

Figure 2.10 shows the schematic of screen printing. The setup mainly consists of squeegee, screen plate, stencil and substrate. During the push-release process, the printable inks will be transferred from the screen plate to the substrate by squeegee through the mess openings of the stencil. Similar patterns could be achieved on the substrate according to the designable patterns of mesh opening on the stencil. Currently, screen printing techniques have been widely used for fabrication of different kinds electronic devices, such as solar cell, battery and electrochemical capacitors. In the process of screen printing, fabrication of printing inks is significantly important for printing electronic devices with desired properties. Normally, toxic solvents are required for fabrication of stable printing inks. Therefore, extensive efforts should be devoted to the development of environmental friendliness printing inks in near future.

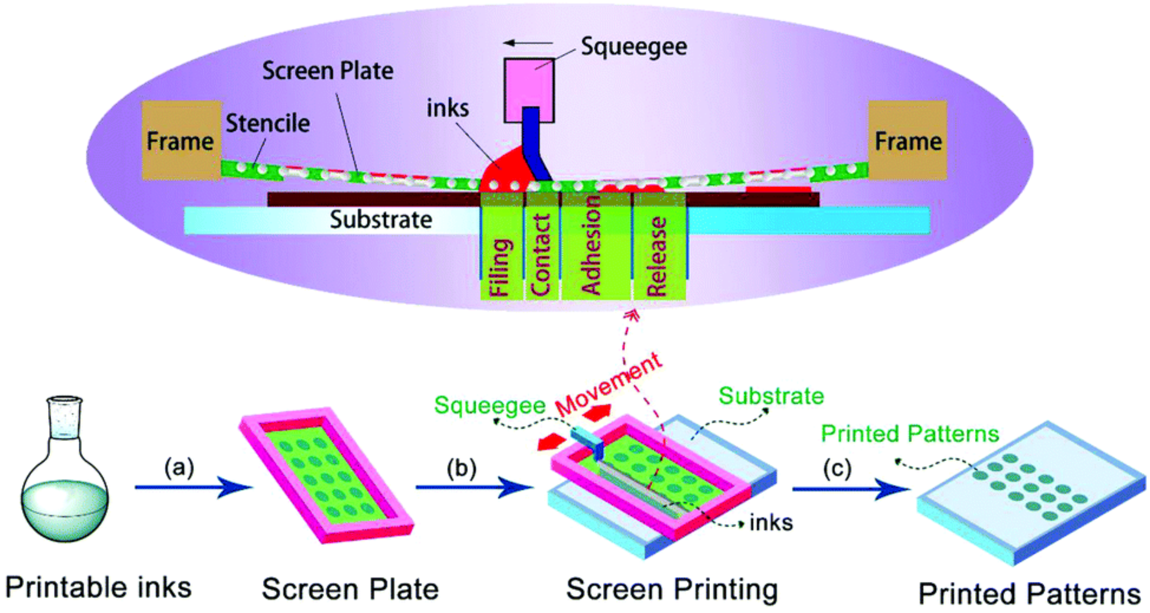

Figure 2.10 Schematic of screen printing[90].

2.6 References

[1] J. Ho, T. R. Jow, and S. Boggs, "Historical Introduction to Capacitor Technology," *Ieee Electrical Insulation Magazine,* vol. 26, pp. 20-25, Jan-Feb 2010.

[2] R. Kötz and M. Carlen, "Principles and applications of electrochemical capacitors," *Electrochimica acta,* vol. 45, pp. 2483-2498, 2000.

[3] B. E. Conway, *Electrochemical supercapacitors: scientific fundamentals and technological applications*: Springer Science & Business Media, 2013.

[4] V. Augustyn, P. Simon, and B. Dunn, "Pseudocapacitive oxide materials for high-rate electrochemical energy storage," *Energy & Environmental Science,* vol. 7, pp. 1597-1614, 2014.

[5] G. Kokkinidis, "Underpotential deposition and electrocatalysis," ed: Elsevier, 1986.

[6] C. L. Green and A. Kucernak, "Determination of the platinum and ruthenium surface areas in platinum− ruthenium alloy electrocatalysts by underpotential deposition of copper. I. Unsupported catalysts," *The Journal of Physical Chemistry B,* vol. 106, pp. 1036-1047, 2002.

[7] W. Lorenz, H. Hermann, N. Wüthrich, and F. Hilbert, "The formation of monolayer metal films on electrodes," *Journal of The Electrochemical Society,* vol. 121, pp. 1167-1177, 1974.

[8] Y. Liu, "FABRICATION OF COMPOSITE ELECTRODES AND SUPERCAPACITOR DEVICES," McMaster University, 2016.

[9] K. Shi, "Advanced Materials for Energy Storage in Supercapacitors and Capacitive Water Purification," McMaster University, 2016.

[10] C. M. Chuang, C. W. Huang, H. S. Teng, and J. M. Ting, "Hydrothermally synthesized RuO_2/Carbon nanofibers composites for use in high-rate supercapacitor electrodes," *Composites Science and Technology,* vol. 72, pp. 1524-1529, Aug 22 2012.

[11] Y. Y. Yang, Y. R. Liang, Y. D. Zhang, Z. Y. Zhang, Z. M. Li, and Z. Q. Hu, "Three-dimensional graphene hydrogel supported ultrafine RuO_2 nanoparticles for supercapacitor electrodes," *New Journal of Chemistry,* vol. 39, pp. 4035-4040, 2015.

[12] R. Poon and I. Zhitomirsky, "Supercapacitor electrodes with high active mass loading," *Mrs Communications,* vol. 8, pp. 1135-1138, Sep 2018.

[13] Y. Wang, Y. Liu, and I. Zhitomirsky, "Surface modification of MnO_2 and carbon nanotubes using organic dyes for nanotechnology of electrochemical supercapacitors," *Journal of Materials Chemistry A,* vol. 1, pp. 12519-12526, 2013.

[14] C. Wallar, T. Zhang, K. Shi, and I. Zhitomirsky, "Synthesis of metal and metal oxide nanoparticles, liquid-liquid extraction and application in supercapacitors," *Colloids and Surfaces a-Physicochemical and Engineering Aspects,* vol. 500, pp. 195-202, Jul 5 2016.

[15] R. Poon and I. Zhitomirsky, "High areal capacitance of Mn_3O_4-carbon nanotube electrodes," *Materials Letters,* vol. 215, pp. 4-7, Mar 15 2018.

[16] R. Poon, X. Zhao, M. S. Ata, A. Clifford, and I. Zhitomirsky, "Phase transfer of oxide particles for application in thin films and supercapacitors," *Ceramics International,* vol. 43, pp. 8314-8320, Aug 1 2017.

[17] A. M. Abdalla, R. P. Sahu, C. J. Wallar, R. Chen, I. Zhitomirsky, and I. K. Puri, "Nickel oxide nanotube synthesis using multiwalled carbon nanotubes as sacrificial templates for supercapacitor application," *Nanotechnology,* vol. 28, Feb 17 2017.

[18] A. A. Yadav, Y. M. Hunge, and S. B. Kulkarni, "Chemical synthesis of Co_3O_4 nanowires for symmetric supercapacitor device," *Journal of Materials Science-Materials in Electronics,* vol. 29, pp. 16401-16409, Oct 2018.

[19] D. F. Qiu, X. Ma, J. D. Zhang, B. Zhao, and Z. X. Lin, "In situ synthesis of mesoporous Co_3O_4 nanorods anchored on reduced graphene oxide nanosheets as supercapacitor electrodes," *Chemical Physics Letters,* vol. 710, pp. 188-192, Oct 16 2018.

[20] P. Xu, C. Miao, K. Cheng, K. Ye, J. Yin, D. Cao*, et al.*, "Preparation of binder-free porous ultrathin $Ni(OH)_2$ nanoleafs using ZnO as pore forming agent displaying both high mass loading and excellent electrochemical energy storage performance," *Electrochimica Acta,* vol. 216, pp. 499-509, 2016.

[21] X. Zhou, D. Cao, J. Huang, K. Ye, S. Yang, T. Liu*, et al.*, "Capacitance performance of nanostructured β-$Ni(OH)_2$ with different morphologies grown on nickel foam," *Journal of Electroanalytical Chemistry,* vol. 720, pp. 115-120, 2014.

[22] F. Zhou, Q. Liu, J. Gu, W. Zhang, and D. Zhang, "Microwave-assisted anchoring of flowerlike $Co(OH)_2$ nanosheets on activated carbon to prepare hybrid electrodes for high-rate electrochemical capacitors," *Electrochimica Acta,* vol. 170, pp. 328-336, 2015.

[23] Z. Gao, W. Yang, Y. Yan, J. Wang, J. Ma, X. Zhang, *et al.*, "Synthesis and Exfoliation of Layered α-Co(OH)$_2$ Nanosheets and Their Electrochemical Performance for Supercapacitors," *European Journal of Inorganic Chemistry*, vol. 2013, pp. 4832-4838, 2013.

[24] J. Milne, R. M. Silva, and I. Zhitomirsky, "Surface modification and dispersion of ceramic particles using liquid-liquid extraction method for application in supercapacitor electrodes," *Journal of the European Ceramic Society*, 2018.

[25] J. Milne, R. Silva, Z. Wang, and I. Zhitomirsky, "Phase transfer of oxide particles using hydroxamic acid derivatives and application for supercapacitors," *Ceramics International*, vol. 45, pp. 2498-2503, 2019.

[26] Y. Han, M. Shen, Y. Wu, J. Zhu, B. Ding, H. Tong, *et al.*, "Preparation and electrochemical performances of PEDOT/sulfonic acid-functionalized graphene composite hydrogel," *Synthetic Metals*, vol. 172, pp. 21-27, 2013.

[27] Y. Han, M. Shen, J. Zhu, Y. Wu, and X. Zhang, "Preparation and capacitive performances of PEDOT/indigo carmine composite hydrogel," *Polymer Composites*, vol. 34, pp. 989-996, 2013.

[28] W.-x. Liu, L. Na, H.-h. Song, and X.-h. Chen, "Properties of polyaniline/ordered mesoporous carbon composites as electrodes for supercapacitors," *New carbon materials*, vol. 26, pp. 217-223, 2011.

[29] N. Song, H. Tan, and Y. Zhao, "Carbon fiber-bridged polyaniline/graphene paper electrode for a highly foldable all-solid-state supercapacitor," *Journal of Solid State Electrochemistry*, vol. 23, pp. 9-17, 2019.

[30] K. Shi, X. Pang, and I. Zhitomirsky, "Fabrication of T iron-doped polypyrrole/MWCNT composite electrodes with high mass loading and enhanced performance for supercapacitors," *Journal of Applied Polymer Science*, vol. 132, 2015.

[31] K. Shi, X. Yang, E. D. Cranston, and I. Zhitomirsky, "Efficient lightweight supercapacitor with compression stability," *Advanced Functional Materials*, vol. 26, pp. 6437-6445, 2016.

[32] K. Shi and I. Zhitomirsky, "Polypyrrole nanofiber–carbon nanotube electrodes for supercapacitors with high mass loading obtained using an organic dye as a co-dispersant," *Journal of Materials Chemistry A*, vol. 1, pp. 11614-11622, 2013.

[33] X. Li and B. Q. Wei, "Supercapacitors based on nanostructured carbon," *Nano Energy*, vol. 2, pp. 159-173, Mar 2013.

[34] T. Katakabe, T. Kaneko, W. Watanabe, T. Fukushima, and T. Aida, "Electric double-layer capacitors using "bucky gels" consisting of an ionic liquid and carbon nanotubes," *Journal of the Electrochemical Society*, vol. 152, pp. A1913-A1916, 2005.

[35] Y. Honda, T. Haramoto, M. Takeshige, H. Shiozaki, T. Kitamura, and M. Ishikawa, "Aligned MWCNT sheet electrodes prepared by transfer methodology providing high-power capacitor performance," *Electrochemical and Solid State Letters*, vol. 10, pp. A106-A110, 2007.

[36] D. A. C. Brownson, D. K. Kampouris, and C. E. Banks, "An overview of graphene in energy production and storage applications," *Journal of Power Sources,* vol. 196, pp. 4873-4885, Jun 1 2011.

[37] J. R. Miller, R. A. Outlaw, and B. C. Holloway, "Graphene Double-Layer Capacitor with ac Line-Filtering Performance," *Science,* vol. 329, pp. 1637-1639, Sep 24 2010.

[38] H. Y. Wang, M. Yoshio, A. K. Thapa, and H. Nakamura, "From symmetric AC/AC to asymmetric AC/graphite, a progress in electrochemical capacitors," *Journal of Power Sources,* vol. 169, pp. 375-380, Jun 20 2007.

[39] B. Z. Fang and L. Binder, "Enhanced surface hydrophobisation for improved performance of carbon aerogel electrochemical capacitor," *Electrochimica Acta,* vol. 52, pp. 6916-6921, Aug 1 2007.

[40] X. M. Liu, R. Zhang, L. Zhan, D. H. Long, W. M. Qiao, J. H. Yang, *et al.*, "Impedance of carbon aerogel/activated carbon composites as electrodes of electrochemical capacitors in aprotic electrolyte," *New Carbon Materials,* vol. 22, pp. 153-158, Jun 2007.

[41] H. Y. Wang and M. Yoshio, "Graphite, a suitable positive electrode material for high-energy electrochemical capacitors," *Electrochemistry Communications,* vol. 8, pp. 1481-1486, Sep 2006.

[42] B. Xu, F. Wu, S. Chen, C. Z. Zhang, G. P. Cao, and Y. S. Yang, "Activated carbon fiber cloths as electrodes for high performance electric double layer capacitors," *Electrochimica Acta*, vol. 52, pp. 4595-4598, Mar 20 2007.

[43] S. U. Kim and K. H. Lee, "Carbon nanofiber composites for the electrodes of electrochemical capacitors," *Chemical Physics Letters,* vol. 400, pp. 253-257, Dec 11 2004.

[44] S. R. Sivakkumar, J. M. Ko, D. Y. Kim, B. C. Kim, and G. G. Wallace, "Performance evaluation of CNT/polypyrrole/MnO_2 composite electrodes for electrochemical capacitors," *Electrochimica Acta,* vol. 52, pp. 7377-7385, Sep 2007.

[45] G. Wang, L. Zhang, and J. Zhang, "A review of electrode materials for electrochemical supercapacitors," *Chemical Society Reviews,* vol. 41, pp. 797-828, 2012.

[46] D. D. Zhao, S. J. Bao, W. H. Zhou, and H. L. Li, "Preparation of hexagonal nanoporous nickel hydroxide film and its application for electrochemical capacitor," *Electrochemistry Communications,* vol. 9, pp. 869-874, May 2007.

[47] I. H. Kim and K. B. Kim, "Electrochemical characterization of hydrous ruthenium oxide thin-film electrodes for electrochemical capacitor applications," *Journal of the Electrochemical Society,* vol. 153, pp. A383-A389, 2006.

[48] W. Wei, X. Cui, W. Chen, and D. G. Ivey, "Manganese oxide-based materials as electrochemical supercapacitor electrodes," *Chemical society reviews,* vol. 40, pp. 1697-1721, 2011.

[49] L.-F. Chen, Z.-Y. Yu, J.-J. Wang, Q.-X. Li, Z.-Q. Tan, Y.-W. Zhu, *et al.*, "Metal-like fluorine-doped β-FeOOH nanorods grown on carbon cloth for scalable high-performance supercapacitors," *Nano Energy,* vol. 11, pp. 119-128, 2015.

[50] Q. Lu, L. Liu, S. Yang, J. Liu, Q. Tian, W. Yao, *et al.*, "Facile synthesis of amorphous FeOOH/MnO_2 composites as screen-printed electrode materials for all-printed solid-state flexible supercapacitors," *Journal of Power Sources,* vol. 361, pp. 31-38, 2017.

[51] X. He, W. Yang, X. Mao, L. Xu, Y. Zhou, Y. Chen*, et al.*, "All-solid state symmetric supercapacitors based on compressible and flexible free-standing 3D carbon nanotubes (CNTs)/poly (3, 4-ethylenedioxythiophene)(PEDOT) sponge electrodes," *Journal of Power Sources,* vol. 376, pp. 138-146, 2018.

[52] R. Liu, L. Ma, S. Huang, J. Mei, J. Xu, and G. Yuan, "Large areal mass, flexible and freestanding polyaniline/bacterial cellulose/graphene film for high-performance supercapacitors," *RSC Advances,* vol. 6, pp. 107426-107432, 2016.

[53] N. Song, Y. Wu, W. Wang, D. Xiao, H. Tan, and Y. Zhao, "Layer-by-layer in situ growth flexible polyaniline/graphene paper wrapped by MnO2 nanoflowers for all-solid-state supercapacitor," *Materials Research Bulletin,* vol. 111, pp. 267-276, 2019.

[54] X. Yang, K. Y. Shi, I. Zhitomirsky, and E. D. Cranston, "Cellulose Nanocrystal Aerogels as Universal 3D Lightweight Substrates for Supercapacitor Materials," *Advanced Materials,* vol. 27, pp. 6104-6109, Oct 28 2015.

[55] Y. Zhu, K. Shi, and I. Zhitomirsky, "Polypyrrole coated carbon nanotubes for supercapacitor devices with enhanced electrochemical performance," *Journal of Power Sources,* vol. 268, pp. 233-239, 2014.

[56] K. Lota, V. Khomenko, and E. Frackowiak, "Capacitance properties of poly(3,4-ethylenedioxythiophene)/carbon nanotubes composites," *Journal of Physics and Chemistry of Solids,* vol. 65, pp. 295-301, Feb-Mar 2004.

[57] L. Z. Fan, Y. S. Hu, J. Maier, P. Adelhelm, B. Smarsly, and M. Antonietti, "High electroactivity of polyaniline in supercapacitors by using a hierarchically porous carbon monolith as a support," *Advanced Functional Materials,* vol. 17, pp. 3083-3087, Nov 5 2007.

[58] H. Zhang, G. P. Cao, Z. Y. Wang, Y. S. Yang, Z. J. Shi, and Z. N. Gu, "Tube-covering-tube nanostructured polyaniline/carbon nanotube array composite electrode with high capacitance and superior rate performance as well as good cycling stability," *Electrochemistry Communications,* vol. 10, pp. 1056-1059, Jul 2008.

[59] H. F. Li, R. D. Wang, and R. Cao, "Physical and electrochemical characterization of hydrous ruthenium oxide/ordered mesoporous carbon composites as supercapacitor," *Microporous and Mesoporous Materials,* vol. 111, pp. 32-38, Apr 15 2008.

[60] C. Zhong, Y. D. Deng, W. B. Hu, J. L. Qiao, L. Zhang, and J. J. Zhang, "A review of electrolyte materials and compositions for electrochemical supercapacitors," *Chemical Society Reviews,* vol. 44, pp. 7484-7539, 2015.

[61] M. Galinski, A. Lewandowski, and I. Stepniak, "Ionic liquids as electrolytes," *Electrochimica Acta,* vol. 51, pp. 5567-5580, Aug 15 2006.

[62] A. P. Yu, Z. W. Chen, R. Maric, L. Zhang, J. J. Zhang, and J. Y. Yan, "Electrochemical supercapacitors for energy storage and delivery: Advanced materials, technologies and applications," *Applied Energy,* vol. 153, pp. 1-2, Sep 1 2015.

[63] U. M. Patil, R. R. Salunkhe, K. V. Gurav, and C. D. Lokhande, "Chemically deposited nanocrystalline NiO thin films for supercapacitor application," *Applied Surface Science,* vol. 255, pp. 2603-2607, Dec 30 2008.

[64] L. H. Su, L. Y. Gong, H. T. Lu, and Q. Xu, "Enhanced low-temperature capacitance of MnO_2 nanorods in a redox-active electrolyte," *Journal of Power Sources,* vol. 248, pp. 212-217, Feb 15 2014.

[65] X. L. Wang, A. B. Yuan, and Y. Q. Wang, "Supercapacitive behaviors and their temperature dependence of sol-gel synthesized nanostructured manganese dioxide in lithium hydroxide electrolyte," *Journal of Power Sources,* vol. 172, pp. 1007-1011, Oct 25 2007.

[66] F. Beguin, V. Presser, A. Balducci, and E. Frackowiak, "Carbons and Electrolytes for Advanced Supercapacitors," *Advanced Materials,* vol. 26, pp. 2219-2251, Apr 2014.

[67] C. Wallar, D. Luo, R. Poon, and I. Zhitomirsky, "Manganese dioxide-carbon nanotube composite electrodes with high active mass loading for electrochemical supercapacitors," *Journal of Materials Science,* vol. 52, pp. 3687-3696, Apr 2017.

[68] C. J. Wallar, R. Poon, and I. Zhitomirsky, "High Areal Capacitance of V_2O_3-Carbon Nanotube Electrodes," *Journal of the Electrochemical Society*, vol. 164, pp. A3620-A3627, 2017.

[69] K. Zhou, W. J. Zhou, X. J. Liu, Y. H. Sang, S. Z. Ji, W. Li, *et al.*, "Ultrathin MoO_3 nanocrystalsself-assembled on graphene nanosheets via oxygen bonding as supercapacitor electrodes of high capacitance and long cycle life," *Nano Energy*, vol. 12, pp. 510-520, Mar 2015.

[70] K. Y. Shi and I. Zhitomirsky, "Fabrication of Polypyrrole-Coated Carbon Nanotubes Using Oxidant-Surfactant Nanocrystals for Supercapacitor Electrodes with High Mass Loading and Enhanced Performance," *Acs Applied Materials & Interfaces*, vol. 5, pp. 13161-13170, Dec 25 2013.

[71] K. Y. Shi and I. Zhitomirsky, "Electrophoretic nanotechnology of graphene-carbon nanotube and graphene-polypyrrole nanofiber composites for electrochemical supercapacitors," *Journal of Colloid and Interface Science*, vol. 407, pp. 474-481, Oct 1 2013.

[72] Y. S. Liu and I. Zhitomirsky, "Electrochemical supercapacitor based on multiferroic BiMn2O5," *Journal of Power Sources*, vol. 284, pp. 377-382, Jun 15 2015.

[73] K. Y. Shi, X. Pang, and I. Zhitomirsky, "Fabrication of Tiron-doped polypyrrole/MWCNT composite electrodes with high mass loading and enhanced performance for supercapacitors," *Journal of Applied Polymer Science*, vol. 132, Aug 20 2015.

[74] Y. Liu, K. Shi, and I. Zhitomirsky, "New colloidal route for electrostatic assembly of oxide nanoparticle–carbon nanotube composites," *Colloids and Surfaces A: Physicochemical and Engineering Aspects,* vol. 446, pp. 15-22, 2014.

[75] Y. Liu and I. Zhitomirsky, "Aqueous electrostatic dispersion and heterocoagulation of multiwalled carbon nanotubes and manganese dioxide for the fabrication of supercapacitor electrodes and devices," *RSC Advances,* vol. 4, pp. 45481-45489, 2014.

[76] J. Milne and I. Zhitomirsky, "Application of octanohydroxamic acid for liquid-liquid extraction of manganese oxides and fabrication of supercapacitor electrodes," *Journal of Colloid and Interface Science,* vol. 515, pp. 50-57, Apr 1 2018.

[77] X. Pang, T. Casagrande, and I. Zhitomirsky, "Electrophoretic deposition of hydroxyapatite-$CaSiO_3$-chitosan composite coatings," *Journal of Colloid and Interface Science,* vol. 330, pp. 323-329, Feb 15 2009.

[78] T. S. Zhang, D. Luo, P. Wojtal, and I. Zhitomirsky, "Electrophoretic deposition of flame retardant polymer-huntite coatings," *Materials Letters,* vol. 159, pp. 106-109, Nov 15 2015.

[79] P. Wojtal, S. L. Chen, K. Y. Shi, R. Mathews, and I. Zhitomirsky, "Electrophoretic deposition of a memory-type flame retardant material," *Materials Letters,* vol. 153, pp. 106-109, Aug 15 2015.

[80] A. Clifford, B. E. J. Lee, K. Grandfield, and I. Zhitomirsky, "Biomimetic modification of poly-L-lysine and electrodeposition of nanocomposite coatings for

orthopaedic applications," *Colloids and Surfaces B-Biointerfaces,* vol. 176, pp. 115-121, Apr 1 2019.

[81] A. Clifford, D. Luo, and I. Zhitomirsky, "Colloidal strategies for electrophoretic deposition of organic-inorganic composites for biomedical applications," *Colloids and Surfaces a-Physicochemical and Engineering Aspects,* vol. 516, pp. 219-225, Mar 5 2017.

[82] A. Clifford, X. Pang, and I. Zhitomirsky, "Biomimetically modified chitosan for electrophoretic deposition of composites," *Colloids and Surfaces a-Physicochemical and Engineering Aspects,* vol. 544, pp. 28-34, May 5 2018.

[83] A. Clifford and I. Zhitomirsky, "Aqueous electrophoretic deposition of drugs using bile acids as solubilizing, charging and film-forming agents," *Materials Letters,* vol. 227, pp. 1-4, Sep 15 2018.

[84] F. Hossein-Babaei and F. Taghibakhsh, "Electrophoretically deposited zinc oxide thick film gas sensor," *Electronics Letters,* vol. 36, pp. 1815-1816, Oct 12 2000.

[85] Y. Liu, M. S. Ata, K. Shi, G. Z. Zhu, G. A. Botton, and I. Zhitomirsky, "Surface modification and cathodic electrophoretic deposition of ceramic materials and composites using celestine blue dye," *Rsc Advances,* vol. 4, pp. 29652-29659, 2014.

[86] Y. S. Liu, K. Y. Shi, and I. Zhitomirsky, "Azopolymer triggered electrophoretic deposition of MnO_2-carbon nanotube composites and polypyrrole coated carbon nanotubes for supercapacitors," *Journal of Materials Chemistry A,* vol. 3, pp. 16486-16494, 2015.

[87] A. Clifford, M. S. Ata, and I. Zhitomirsky, "Synthesis, liquid - Liquid extraction and deposition of hydroxyapatite nanorod composites," *Materials Letters,* vol. 201, pp. 140-143, Aug 15 2017.

[88] K. Y. Shi, X. Yang, E. D. Cranston, and I. Zhitomirsky, "Efficient Lightweight Supercapacitor with Compression Stability," *Advanced Functional Materials*, vol. 26, pp. 6437-6445, Sep 2016.

[89] C. Z. Meng, C. H. Liu, L. Z. Chen, C. H. Hu, and S. S. Fan, "Highly Flexible and All-Solid-State Paper like Polymer Supercapacitors," *Nano Letters,* vol. 10, pp. 4025-4031, Oct 2010.

[90] W. Wu, "Inorganic nanomaterials for printed electronics: a review," *Nanoscale,* vol. 9, pp. 7342-7372, Jun 14 2017.

[91] K. Arapov, E. Rubingh, R. Abbel, J. Laven, G. de With, and H. Friedrich, "Conductive Screen Printing Inks by Gelation of Graphene Dispersions," *Advanced Functional Materials,* vol. 26, pp. 586-593, Jan 26 2016.

[92] W. J. Yao, Q. Y. Tian, J. Liu, Z. H. Wu, S. Y. Cui, J. Ding, *et al.*, "Large-scale synthesis and screen printing of upconversion hexagonal-phase NaYF4:Yb3+,Tm3+/Er3+/Eu3+ plates for security applications," *Journal of Materials Chemistry C,* vol. 4, pp. 6327-6335, 2016.

[93] M. Singh, H. M. Haverinen, P. Dhagat, and G. E. Jabbour, "Inkjet Printing-Process and Its Applications," *Advanced Materials,* vol. 22, pp. 673-685, Feb 9 2010.

3 Research objective

New colloidal techniques are necessary for manufacturing of advanced composites for achieving desired properties for applications of electrochemical capacitors and thin film fabrication. For ECs applications, composite electrodes are important to be designed with properties of high electronic conductivity for electron transfer, high surface area for ions absorption and high capacitance of non-agglomerated active material.

The main objective is to fabricate advanced composite electrodes and supercapacitor devices with high active mass loadings, high ratio of the active material mass to the current collector mass, high capacitance, good capacitance retention at high charge-discharge rates and low impedance. The main objective is based on short-term objectives 3.1-3.6.

3.1 Liquid liquid extraction of oxide particles by head-tail extractor hexadecylphosphonic acid

In Chapter 4, the background information of particle extraction through liquid-liquid interface (PELLI) and experimental works are presented to demonstrate the benefits of PELLI for synthesis of reduced agglomeration particles with head-tail extractor hexadecylphosphonic acid and improved mixing with conductive media for electrochemical supercapacitors with high active mass loading and high active material to current collector mass ratio. The results discussed in this chapter are reproduced from Liquid-liquid extraction of oxide particles and application in supercapacitors, 92, 1-9, 2017, Journal of Materials Research, ***Ri Chen***, Mustafa S. Ata, Xinya Zhao, Ishwar K. Puri and Igor Zhitomirsky, *https://doi.org/10.1557/jmr.2017.92, Copyright 2019, with permission* *from Materials Research Society*. The author of this thesis is the first author and the main contributor of this publication.

3.2 Bottom-up and top-down PELLI of oxide particles and electrophoretic deposition of thin films

In Chapter 5, Bottom-up and top-down liquid-liquid extraction methods have been developed for the transfer of colloidal metal oxide particles, synthesized in an aqueous phase, to organic phases by head tail extractors. The extracted non-agglomerated particles have been developed for fabrication of supercapacitor electrodes and thin films by electrophoretic deposition. The results discussed in this chapter are reproduced from Strategies for liquid-liquid extraction of oxide particles for applications in supercapacitor electrodes and thin films, 499, 1-8, 2017, Journal of Colloid and Interface Science, ***Ri Chen***, Mustafa S. Ata, Xinya Zhao, Amanda Clifford, Ishwar K. Puri and Igor Zhitomirsky, *https://doi.org/10.1016/j.jcis.2017.03.095, Copyright 2019, with permission from Elsevier*. The author of this thesis is the first author and the main contributor of this publication.

3.3 Effect of extractors and active mass loading on the electrochemical performance of electrochemical capacitors

In Chapter 6, head tail extractors with different functional groups have been developed to synthesize small size particles by PELLI for fabrication of supercapacitor electrodes. The goal is to achieve a high area normalized capacitance, low impedance and enhanced capacitance retention at high charge-discharge rates. The results discussed in this chapter are reproduced from MnO_2-carbon nanotube electrodes for supercapacitors with high active mass loadings, 164(9), A1673-A167, 2017, Journal of Electrochemical Society, **Ri Chen**, Ryan Poon, Rakesh P. Sahu, Ishwar K. Puri and Igor Zhitomirsky, *doi: 10.1149/2.1491707jes, Copyright 2019, with permission from ECS -- The Electrochemical Society*. The author of this thesis is the first author and the main contributor of this publication.

3.4 Multifunctional extractor for liquid-liquid extraction of oxide particles and applications in supercapacitors, electrophoretic deposition and screen printing

In Chapter 7, head tail head extractor and head tail extractor have been developed for extraction of oxide particles with reduced agglomeration for fabrication of supercapacitors bulk electrodes. Stable colloidal suspension prepared by PELLI with head tail head extractor has been developed for electrophoretic deposition thin film and screen printing of thin electrodes. The results discussed in this chapter are reproduced from Influence of molecular structure of extractor molecules on liquid-liquid extraction of oxide particles and properties of composites, 44, 15714-15720, 2018, Ceramics International, **Ri Chen**, Zhengzheng Wang, Rakesh P. Sahu, Ishwar K. Puri and Igor Zhitomirsky, *https://doi.org/10.1016/j.ceramint.2018.05.244, Copyright 2019, with permission from Elsevier*. The author of this thesis is the first author and the main contributor of this publication.

3.5 High areal capacitance of FeOOH-carbon nanotube negative electrodes for asymmetric supercapacitors

In Chapter 8, FeOOH-CNT negative electrodes have been developed by PELLI with head tail head extractor and head tail extractor. Comparable capacitance of negative electrodes and positive electrode has been achieved at similar mass loading and efficient asymmetric supercapacitors has been developed. The results discussed in this chapter are reproduced from High areal capacitance of FeOOH-carbon nanotube negative electrodes for asymmetric supercapacitors, 44, 18007-18015, 2018, Ceramics International, ***Ri Chen***, Ishwar K. Puri and Igor Zhitomirsky, *https://doi.org/10.1016/j.ceramint.2018.07.002, Copyright 2019, with permission from Elsevier*. The author of this thesis is the first author and the main contributor of this publication.

3.6 Polypyrrole-carbon nanotube-FeOOH composites for negative electrodes of asymmetric supercapacitors

In Chapter 9, polypyrrole (PPy) coated carbon nanotubes (CNT) were combined with FeOOH to fabricate advanced negative supercapacitor electrodes. High efficient asymmetric supercapacitor devices have been fabricated using PPy-FeOOH-CNT ternary composite and MnO_2-CNT binary composite as the negative and positive electrodes, respectively. The results discussed in this chapter are reproduced from Polypyrrole-carbon nanotube-FeOOH composites for negative electrodes of asymmetric supercapacitors, 166 (6), A935-A940, 2019, Journal of Electrochemical Society, ***Ri Chen***, Ishwar K. Puri and Igor Zhitomirsky, *doi: 10.1149/2.0281906jes, Copyright 2019, with permission from ECS*

-- *The Electrochemical Society*. The author of this thesis is the first author and the main contributor of this publication.

4 Liquid liquid extraction of oxide particles by head-tail extractor hexadecylphosphonic acid

This chapter is reproduced from *Liquid-liquid extraction of oxide particles and application in supercapacitors, 92, 1-9, 2017, Journal of Materials Research,* ***Ri Chen****, Mustafa S. Ata, Xinya Zhao, Ishwar K. Puri and Igor Zhitomirsky, https://doi.org/10.1557/jmr.2017.92, Copyright 2019, with permission from Materials Research Society*. The author of this thesis is the first author and the main contributor of this publication.

4.1 Abstract

Many manufacturing techniques require the use of non-aqueous colloidal suspensions, containing well dispersed oxide particles and various water insoluble functional components. We report an efficient method for the direct transfer of MnO_2 and titania particles, synthesised in water, to an organic solvent through the interface of two immiscible liquids. Particle agglomeration during the drying stage was avoided and stable suspensions of non-agglomerated particles in the organic phase were obtained. The advantages of this method were demonstrated by the fabrication of advanced composite MnO_2-multiwalled carbon nanotube electrodes, containing a polymer binder, for electrochemical supercapacitors with high active mass loading and high active material to current collector mass ratio. The electrodes showed a capacitance of 5.13 F cm^{-2} and low impedance. High extraction efficiency from concentrated suspensions was achieved by the use of an advanced extractor, which allowed strong adsorption on the particles by the polydentate bonding. The extraction mechanism is discussed.

4.2 Introduction

Particle extraction through liquid-liquid interface (PELLI) is emerging as a new method of technological and scientific interest. PELLI has been utilized for the separation of rare earth fluorescent powders[1], alumina and zircon[2]. Size-dependent transfer of gold particles allowed obtaining suspensions with narrow particle size distribution[3]. PELLI has been utilized in the hydrometallurgy of cassiterite[4] and other mineral particles[5]. Luminescent CdTe and HgTe quantum dots, synthesized in an aqueous media were transferred to non-polar organic solvents for the fabrication of photovoltaic and optoelectronic devices[6].

Various organic molecules were used as extractors for PELLI applications. The chemical structures of such molecules contained hydrophobic hydrocarbon chains and functional groups, which provided electrostatic or chemical interactions with inorganic particles. Investigations were focused on the use of ionic surfactants[1-5], which had an electric charge, opposite to that of inorganic particles. In this case, the surfactant adsorption was governed by electrostatic interactions with inorganic particles. Ion-pair interactions of carboxylate-modified gold nanoparticles and cationic surfactants resulted in the particle transfer from water to toluene[7]. The adsorption of other extractors, such as thiol based molecules and fatty acids, on inorganic particles involved chemical interactions. The molecules, containing thiol groups allowed for partial extraction of CdTe and HgTe quantum dots[6]. The chemical interactions of carboxylic groups of fatty acids with iron atoms on the particle surface allowed for magnetite particle extraction[8]. Long chain surfactants, containing amino groups were investigated for extraction of gold[9-11] and silver[12] nanoparticles. It was found that polymer molecules can also be used as extractors[13]. The extraction efficiency was enhanced in the presence of co-solvents, such as sub-oil phase[5] or acetone[6]. In another strategy[14], PELLI was triggered by changes of the temperature. The temperature increase from the room temperature to 80ºC resulted in the reduction of the solubility of the polymer extractor in an aqueous phase and transfer of the adsorbed particles to an organic phase[14].

Previous PELLI research has been mainly focused on nanoparticles of metals and semiconductor quantum dots. The development of PELLI methods for oxide nanoparticles offers benefits for many applications. Various applications of oxide materials in thin film electronic devices, protective coatings, sensors, biomedical implants, aqueous batteries and supercapacitors require the use of water insoluble organic components, such as binders, film forming agents and functional organic molecules[15, 16]. In many manufacturing procedures, oxide nanoparticles must be dispersed in an organic solvent, containing dissolved functional organic molecules or macromolecules, which are insoluble in water. It is important to note that many important techniques for the oxide nanoparticle synthesis are based on aqueous processing. The synthesized nanoparticles are usually dried and then re-dispersed in an organic solvent. However, the drying of the oxide or hydroxide particles results in their agglomeration. The reduction of particle surface area and condensation of surface OH groups are major driving forces for particle agglomeration. The important task is the development of PELLI methods for the transfer of synthesized oxide nanoparticles directly from an aqueous phase to an organic phase, avoiding the drying procedure. However, poor adsorption of extractor molecules on oxide particles and low extraction efficiency are still major obstacles in achieving this goal.

The selection of extractor molecules with strong adsorption on particle surface is of critical importance for the development of PELLI methods. The approach, based on electrostatic interaction of surfactants and particles has limitations related to the control of particle charge in water as well as in organic phases and low recovery efficiency, attributed to weak surfactant adsorption on particles. The extractor molecules, containing carboxylate, amino and thiol groups allow for relatively weak bonding and poor adsorption on the oxide particles.

The goal of this investigation was the development of efficient PELLI method for oxide particles. The approach is based on the use of hexadecylphosphonic acid (HDPA) as an advanced extractor molecule. The chemical structure of HDPA (Figure 4.1A) contains a phosphonate group. Literature data indicates that phosphonates exhibit strong adsorption in water on various inorganic materials[17-23], such as hydroxyapatite, Fe_3O_4, SiO_2, ZnO, Al_2O_3 and TiO_2, clay, calcium carbonate, indium tin oxide. The oxygen atoms of the phosphonate ligand allow for bi- or tri-dentate bonding (Figure 4.1B), which results in significantly stronger adsorption, compared to monodentate bonding[24] of many extractor and dispersant molecules. The chelation bonding (Figure 4.1B(a,b)) involves the formation of the coordination bonds between two or three oxygen atoms of HDPA and a metal atom on the particle surface. The oxygen atoms of the phosphonate ligand can also be bonded to different metal atoms (Figure 4.1B(c,d)).

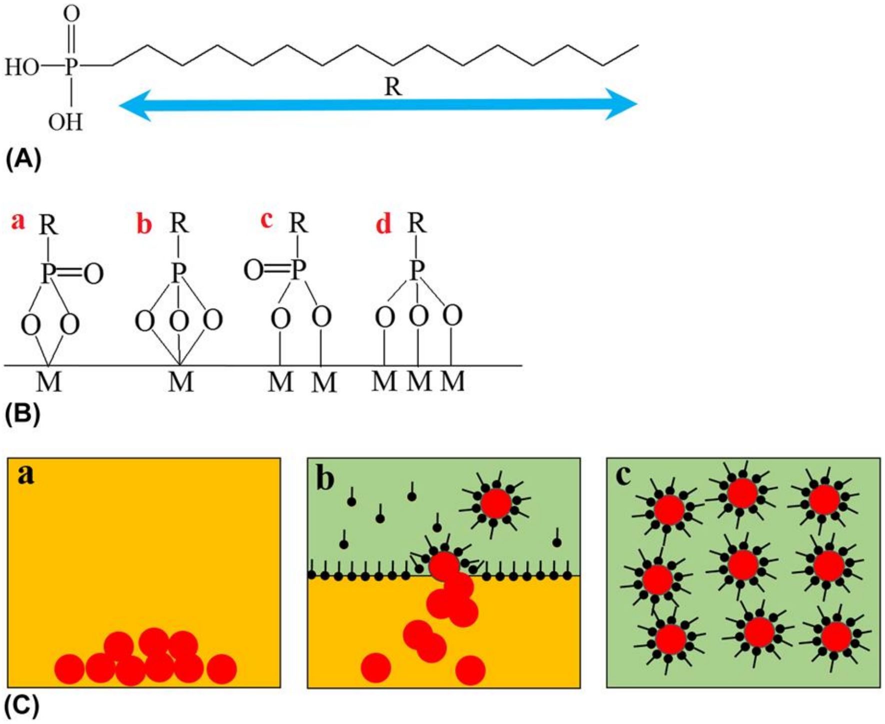

Figure 4.1 (A) Chemical structure of HDPA (B) adsorption mechanisms of HDPA, involving (a) chelating bidentate bonding, (b) chelating tridentate bonding, (c) bridging bidentate bonding, (d) bridging tridentate bonding, (C) schematic of the PELLI method: (a) particles, precipitated in aqueous phase, (b) transfer through liquid–liquid interface, (c) formation of a stable suspension of particles in n-butanol.

We report the synthesis of MnO_2 and titania particles in aqueous solutions and their extraction to the n-butanol phase (Figure 4.1C), containing dissolved HDPA. In this strategy, water insoluble HDPA molecules adsorbed on oxide particles at the water-n-butanol interface. The results presented below indicated high extraction efficiency and reduced particle agglomeration. An important outcome of this study was the fabrication of MnO_2-multiwalled carbon nanotube (MWCNT) composites for application in electrodes of electrochemical supercapacitors, which showed promising capacitive properties

4.3 Experimental procedures

Hexadecylphosphonic acid (HDPA), poly(vinyl butyral-co-vinyl alcohol-co-vinyl acetate) (PVB, average Mw=50,000-80,000), $NaMnO_4$, $TiOSO_4$, NaOH, Na_2SO_4, n-butanol (Aldrich) and multiwalled carbon nanotubes (MWCNT, ID 4 nm, OD 13 nm, length 1–2 μm, Bayer, Germany) were used. Ni foams with 95 % porosity were provided by Vale Company.

The synthesis of MnO_2 particles was performed by a chemical precipitation method using aqueous $NaMnO_4$ solutions and n-butanol as a reducing agent. Previous investigations[25-27] showed that various alcohols, such as ethanol, isopropanol, methanol and other alcohols, miscible with water, can be used as reducing agents for the synthesis of MnO_2 from permanganate solutions. In this investigation, water-immiscible n-butanol was used as a reducing agent for $NaMnO_4$. The addition of n-butanol to aqueous solutions and stirring during 1 h resulted in the precipitation of MnO_2 in an aqueous phase (Figure 4.2a,b). Further addition of HDPA solution in n-butanol and stirring resulted in the extraction of MnO_2 from the aqueous phase to n-butanol phase (Figure 4.2c). The MnO_2 particles formed a stable suspension in the n-butanol phase. The synthesis of titania was performed using aqueous $TiOSO_4$ solutions. The pH of the solutions was adjusted pH=6 by NaOH. The addition of HDPA solution in n-butanol and stirring resulted in the extraction of titania from the aqueous phase to n-butanol phase (Figure 4.2d,e). The extracted titania formed a stable suspension in n-butanol. The mass of extracted MnO_2 or titania particles was varied in the range of 0.3-1.0 g. The mass ratio of HDPA:oxide was 0.2-0.3. The extraction efficiency was above 95%.

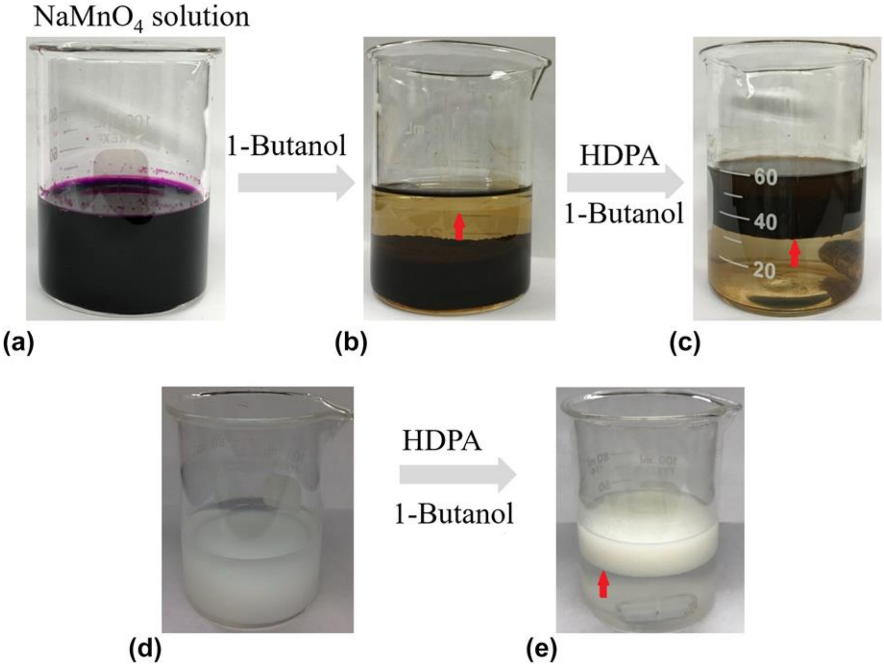

Figure 4.2 (a) NaMnO$_4$ solution, (b) precipitation of MnO$_2$ after mixing of NaMnO$_4$ with n-butanol, (c) extraction of MnO$_2$ to the n-butanol solvent after addition of HDPA solution in n-butanol and mixing, (d) as-precipitated titania in water, (e) extraction of titania to the n-butanol solvent after addition of HDPA solution in n-butanol and mixing, red arrows show the interface of water and n-butanol.

Electron microscopy investigations were performed using a JEOL JSM-7000F scanning electron microscope (SEM). X-ray diffraction (XRD) studies were performed using a powder diffractometer (Nicolet I2, monochromatized CuKα radiation). The materials for the XRD and SEM studies were prepared using suspensions, shown in Figure 4.2b,d. The suspensions were filtrated, washed with water and ethanol and then dried in air for 72 h. FTIR studies were performed on Bruker Vertex 70 spectrometer. For the preparation of samples for the FTIR studies, the suspensions, shown in Fig.2c,e were filtrated and the obtained materials were dried in air. Dynamic light scattering (DLS, DelsaMax Pro: Beckman Coulter) was used for the particle size distribution analysis. The suspensions of particles in n-butanol, separated from the aqueous phase, were diluted with ethanol for the particle distribution analysis.

The suspension of MWCNT in n-butanol was added to MnO_2 suspension in order to obtain the MnO_2: MWCNT mass ratio of 4:1. The organic suspension was separated from the aqueous phase, ultrasonicated and then the solution of PVB binder in ethanol was added. Obtained suspension was used for the fabrication of MnO_2-MWCNT electrodes by impregnation of the Ni foam current collectors. The active mass loading of the electrodes was 35.5 mg cm^{-2}.

Cyclic voltammetry and impedance spectroscopy investigations were performed using a potentiostat (PARSTAT 2273, Princeton Applied Research, USA). Capacitive behavior of the electrodes was studied in three-electrode cells using 0.5 M Na_2SO_4 aqueous solutions. The area of the working electrode was 1 cm^2. The counter electrode was a platinum gauze, and the reference electrode was a standard calomel electrode (SCE). Cyclic voltammetry (CV) studies were performed at scan rates of 2-100 mV s^{-1}. The integral capacitances $C_S=Q/\Delta VS$ and $C_m= Q/\Delta Vm$ were calculated using half the integrated area of the CV curve to obtain the charge Q, and subsequently dividing the charge Q by the width of the potential window ΔV and electrode area S or active mass m. The alternating current measurements of complex impedance $Z^*=Z'-iZ''$ were performed in the frequency range of 10 mHz to 100 kHz at the amplitude of the signal of 5 mV. The complex differential capacitance $C_S^*=C_S'-iC_S''$ was calculated[28] from the impedance data as $C_S'=Z''/\omega|Z|^2S$ and $C_S''=Z'/\omega|Z|^2S$, where $\omega=2\pi f$ (f-frequency).

4.4 Results and discussion

The successful extraction of MnO_2 and titania from water to n-butanol was achieved using HDPA as an advanced extractor. The polydentate bonding of the phosphonate groups of HDPA to the metal atoms on the particle surface allowed for strong adsorption, which was confirmed in several experiments, discussed below. After synthesis, the MnO_2 particles accumulated in the aqueous phase (Figure 4.2b) and precipitated. Figure 4.2b shows clear supernatant n-butanol solvent without MnO_2 particles. However, the addition of HDPA solution in n-butanol allowed for the bottom–up extraction of MnO_2 particles from the bottom aqueous phase to the top organic phase against the force of gravity (Figure 4.2c). The titania particles showed a similar behavior (Figure 4.2e). Our approach is different from the top-down strategy[29], where gravitation force promoted transfer of destabilized agglomerated particles from water to an organic liquid with higher density. The colloidal stabilization of the particles in the n-butanol solvent indicated that adsorbed HDPA provided a steric stabilization. The extracted particles have also been analyzed by the FTIR method. Figure 4.3 compares the FTIR spectra of the extracted particles and HDPA. The absorptions in the range of 2800-3000 cm^{-1} in the spectra of MnO_2 and titania particles are attributed to stretching vibrations[30, 31] of CH_2 and CH_3 groups of adsorbed HDPA. The FTIR spectrum of pure HDPA showed similar absorptions. The adsorptions at 1469 cm^{-1} in the spectra of particles and corresponding adsorption at 1471 cm^{-1} in the spectrum of pure HDPA resulted from the deformation C-H vibrations[31] of HDPA. The strong adsorption of HDPA was critical for the extraction. The insolubility of HDPA in water is another important factor, which was considered for the selection of this molecule as an extractor.

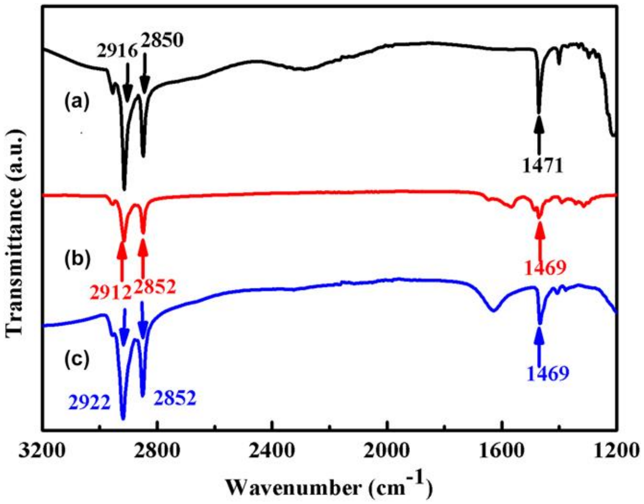

Figure 4.3 FTIR spectra of (a) HDPA and of extracted materials: (b) MnO_2 and (c) titania.

The extraction mechanism involved the adsorption of HDPA on the particles at the interface of the two immiscible liquids and transfer of the inorganic particles to the n-butanol phase by the adsorbed HDPA. In our investigation, n-butanol was used as a reducing agent for the synthesis of MnO_2 and as a receiving liquid in the PELLI method. However, the influence of the nature of the receiving liquid and liquid-liquid interface on the extraction process is not well understood. It should be noted that the adsorption of organic molecules on the particle surface is influenced by a solvent[32, 33]. Other observations indicated that the modification of water-oil mixtures by the sub-oil phases was beneficial for the particle transfer through the interface[5]. It is known that the surfactant concentration increases at the liquid-liquid interface[29]. From this point of view the accumulation of HDPA at the interface was beneficial for interaction with particles and their extraction. In many investigations, the liquid-liquid interface was used as a platform for the 2D assembly of particles[34, 35]. It was found that the driving force for particle accumulation at the interface is the reduction of the interface surface energy between two liquids[34, 36]. However, in our experiments, MnO_2 particles precipitated in the aqueous phase (Figure 4.2b). The stirring and ultrasonication promoted their transfer to the liquid-liquid interface, where HDPA molecules adsorbed on the particles. It is known that the adsorption of surfactant molecules on the particle surface at the liquid-liquid interface[34] can result in reduced interfacial energy. It is in this regard that liquid-liquid interface provides unique conditions, which facilitate various chemical reactions[34, 36, 37]. The modification of particles at the liquid-liquid interface with adsorbed HDPA promoted particle transfer from water to n-butanol in the PELLI method.

It is important to note that many PELLI applications were limited by the use of relatively dilute suspensions[3, 10, 12]. In our investigation, the application of HDPA as an advanced extractor allowed the use of suspensions of significantly higher concentrations. The typical particle concentration in the n-butanol phase was 15-50 g L^{-1}. The experimental results presented below indicated that concentrated suspensions are beneficial for practical applications for the fabrication of supercapacitor electrodes by impregnation of current collectors with an active material.

The MnO_2 and titania particles, synthesized in aqueous phases showed poor colloidal stability and precipitated immediately after stirring or ultrasonic agitation. In contrast, the extracted particles showed good colloidal stability in the n-butanol phase. The good dispersion of particles and suspension stability are critical for colloidal processing of oxide materials and composites[38].

The suspensions, shown in Figure 4.2b,d were filtrated, washed in water, dried in air for 72 h and studied by XRD and SEM. The XRD patterns (Figure 4.4) showed that MnO_2 and titania were mainly amorphous. However, small broad peaks of the birnessite phase were observed in the XRD pattern of MnO_2. The peak broadening resulted from the small particle size. The formation of mainly amorphous MnO_2, containing a small amount of a birnessite phase was also observed in other investigations, where $KMnO_4$ was reduced with different alcohols, such as ethanol[39] or isopropanol[40].

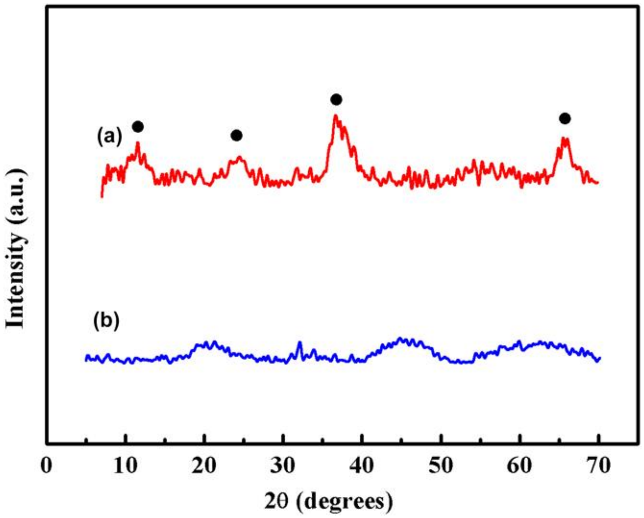

Figure 4.4 XRD patterns of (a) MnO_2 (•-JCPDS file 87-1497) and (b) titania.

The SEM studies (Figure 4.5a) showed that MnO_2 powder contained relatively small particles with a typical size of 0.1 μ m and agglomerates. The size of the agglomerates was in the range of 0.2-5 μ m. The SEM images of the titania powder (Figure 4.5b) showed relatively large agglomerates with a typical size of 2-20 μ m. In contrast, the investigation of extracted particles by dynamic light scattering method showed that the average radius of MnO_2 and titania particles was 90.6 and 188.1 nm, respectively (Figure 4.6). The extracted particles showed relatively small polydispersity indexes of 11.3 and 11.7% for MnO_2 and titania, respectively. Multiple testing experiments showed well repeatable results due to the use of stable suspensions. In contrast, the re-dispersion of dried powders, shown in Fig. 5 in ethanol, resulted in unstable suspensions. The analysis of particles in such suspensions by the dynamic light scattering method presented difficulties due to rapid sedimentation of the particles. The sedimentation resulted in significant variations of the measured particle average sizes and the polydispersity indexes with time.

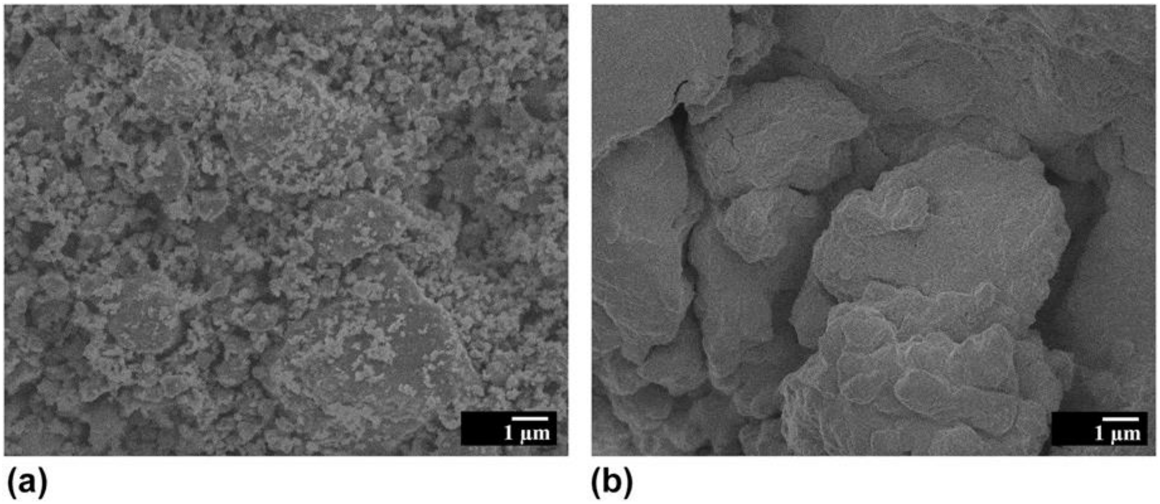

Figure 4.5 SEM images of (a) MnO_2 and (b) titania, prepared from suspensions, shown in Figs. 2(b) and 2(d), respectively, after filtration, washing with water, and drying in air for 72 h.

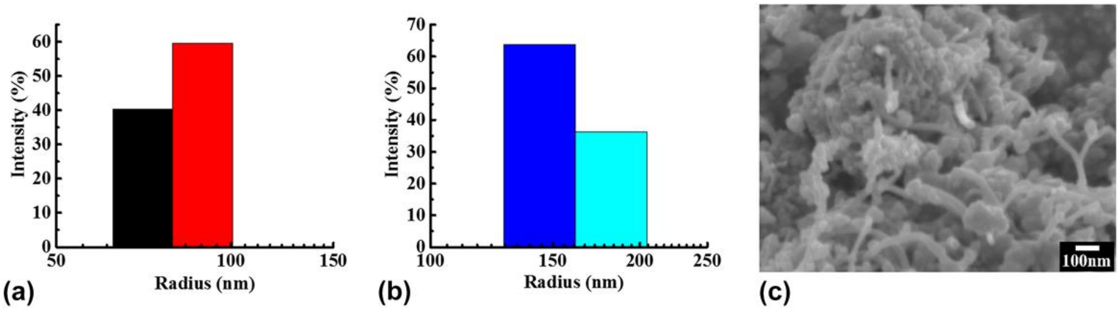

Figure 4.6 Particle size distributions for (a) MnO_2 and (b) titania, extracted using HDPA and (c) SEM image of MnO_2-MWCNT composite.

The ability to transfer MnO_2 and titania particles to an organic solvent and avoid particle agglomeration during the drying stage offers benefits for many applications, utilizing advanced properties of such materials. Of particular importance is the application of the PELLI method for the fabrication of advanced electrodes for electrochemical supercapacitors. As a step in this direction, we investigated MnO_2 particles, prepared using the PELLI method.

The charge storage properties of MnO_2 are related to the redox reaction[41]:

$$MnO_2 + A^+ + e^- \leftrightarrow MnO_2A \tag{4-1}$$

where $A^+ = Na^+$, K^+, H^+. The use of MnO_2 as a charge storage material offers the advantages[41-43] of high theoretical specific capacitance (1370 F g^{-1}) and nearly ideal capacitive behavior in a voltage window of ~0.9 V in mild aqueous electrolytes, such as K_2SO_4 or Na_2SO_4. The Equation (4-1) indicates that high electronic and ionic conductivities of the electrode material are important for the efficient charge-discharge behavior. Conductive additives, such as MWCNT are usually added to MnO_2 in order to improve electronic conductivity. However, the specific capacitance of MWCNT is low. Therefore, the amount of MWCNT in the composite electrode must be optimized. An important task is to avoid MnO_2 particle agglomeration and achieve good electrolyte access to the active material. Good dispersion and mixing of MnO_2 and MWCNT is extremely important for the electrode performance. The ability to achieve high capacitance at high active mass loadings is one of the challenges in the supercapacitor technology. Literature data indicates that gravimetric capacitance decreased by one order of magnitude with an increase of electrode mass due to poor utilization of the capacitive properties of MnO_2[44-47]. Another important parameter is the ratio of active material mass to the current collector mass (R_m). Relatively high specific capacitances were achieved in thin films with active mass of 0.005-2 mg cm^{-2}, deposited on foil substrates[45-48]. However, R_m for such films is only 5×10^{-5} to 5×10^{-2}. Relatively small areal capacitance can be achieved at such small mass loadings.

The extracted MnO_2 formed stable concentrated suspensions, suitable for the impregnation of Ni foam current collectors and fabrication of the supercapacitor electrodes. MWCNT were added to the suspensions with mass ratio of MnO_2: MWCNT=4:1. The PVB binder was added in order achieve 3% mass content of PVB in the composite electrode. The suspension was impregnated into the Ni foam. The total mass of the impregnated materials after drying was 35.5 mg cm^{-2} and R_m was 0.5.

Figure 4.7a shows CVs at different scan rates for the composite MnO_2-MWCNT electrodes. The nearly ideal box shape CVs and increase of current with increasing scan rate indicated good capacitive behavior. The electrodes showed relatively high gravimetric capacitance (Figure 4.7b) at high active mass loading (35.5 mg cm^{-2}), which was comparable with capacitance, achieved in literature at small mass loadings (0.1-2 mg cm^{-2})[46, 47, 49]. The highest capacitance C_m of 144.5 F g^{-1} was obtained at a scan rate of 2 mV s^{-1}. However, due to the use of high active material loading we were able to achieve high areal capacitance C_S of 5.13 F cm^{-2} at a scan rate of 2 mV s^{-1}. At high scan rates we observed significant improvement in capacitance retention, compared to the electrodes, prepared using advanced co-dispersants for MnO_2 and MWCNT[50]. The use of the PELLI method allowed ~2 times higher C_S at 50 and 100 mV s^{-1}, compared to C_S achieved at the same scan rates at higher mass loading[50] of 40 mg cm^{-2}.

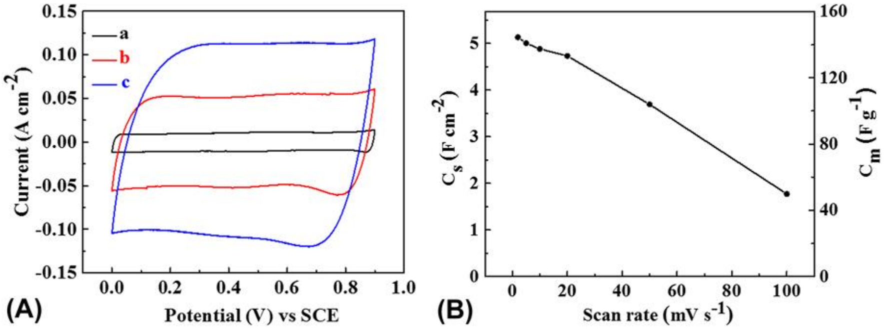

Figure 4.7 (A) CVs at scan rates of (a) 2, (b) 10, and (c) 20 mV s^{-1}, (B) C_S and C_m, calculated from the CVs data at different scan rates.

The analysis of the impedance data (Figure 4.8a) revealed good capacitive behavior, as indicated by nearly 90º slope of the Nyquist plot. The electrodes showed an advantage of low resistance R= Z'. The low Z" values resulted from high capacitance. The frequency dependences of the components of complex capacitance, calculated from the impedance data are presented in Figure 4.8b,c. The real component of the differential capacitance C_S' at low frequencies was slightly lower than the integral capacitance C_S at low scan rates. It should be noted that differential capacitance was measured at significantly lower voltages (5 mV). It was mentioned in the previous investigation[51] that lower differential capacitance can result from limited electrolyte access to some active sites of the capacitive material at low voltages. It is important to note, that integral capacitance depends of scan rate, whereas the differential capacitance is a function of frequency. The frequency dependences of the components of differential capacitance showed a relaxation type dispersion, as indicated by the reduction of C_S' with frequency and a maximum in the frequency dependence of C_S''. The relatively high relaxation frequency, corresponding to the C_S'' maximum, indicates good capacitive behavior at high charge-discharge rates.

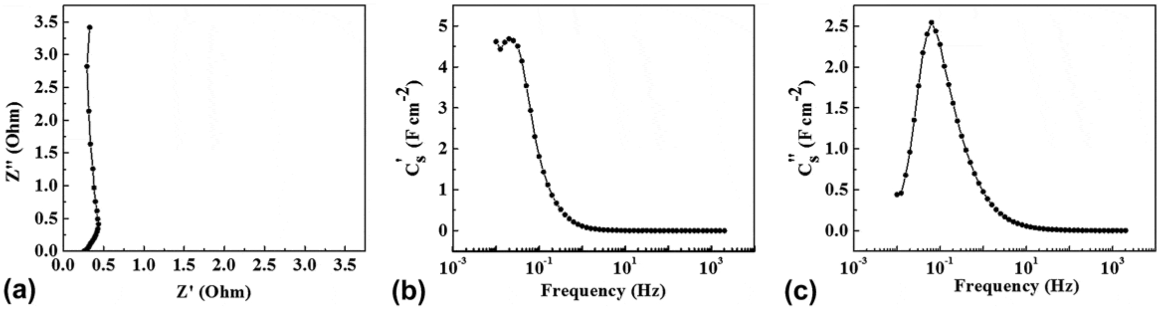

Figure 4.8 (a) Nyquist plot for complex impedance and frequency dependences of (b) C_S' and (c) C_S'' calculated from the impedance data for MnO_2-MWCNT electrodes.

4.5 Conclusions

New PELLI method has been developed for the fabrication of stable MnO_2 and titania suspensions in n-butanol. The extraction efficiency above 95% was achieved from concentrated suspensions using HDPA as an advanced extractor. The important factors for the efficient extraction are water insolubility of HDPA and its strong adsorption on the inorganic nanoparticles, involving the polydentate bonding. The extraction mechanism was based on the interaction of HDPA and the inorganic particles at the liquid-liquid interface. The problems, related to the particle agglomeration during the drying stage were avoided in the PELLI method. The ability to transfer synthesized particles from water to the organic solvent and obtain concentrated and stable suspensions allowed for the impregnation of Ni foam current collectors using slurries of MnO_2 and MWCNT, containing a solution of water insoluble PVB binder. The reduced agglomeration and efficient mixing of MnO_2 and MWCNT allowed for the fabrication of advanced electrodes with high active mass loading and high active material to current collector mass ratio, which showed good capacitive performance and low impedance. The capacitance of 5.13 F cm^{-2} was achieved at a scan rate of 2 mV s^{-1}. The electrodes prepared by the PELLI method are promising for energy storage in electrochemical supercapacitors. The PELLI method can be used for other applications, which require agglomerate-free colloidal processing of oxide materials and composites.

4.6 References

[1] A. Otsuki, G. Dodbiba, A. Shibayama, J. Sadaki, G. Mei, and T. Fujita, "Separation of rare earth fluorescent powders by two-liquid flotation using organic solvents," *Japanese Journal of Applied Physics,* vol. 47, p. 5093, 2008.

[2] L. P. Wang, Y. Kanemitsu, G. Dodbiba, T. Fujita, Y. Oya, and H. Yokoyama, "Separation of ultrafine particles of alumina and zircon by liquid–liquid extraction using kerosene as the organic phase and sodium dodecylsulfate (SDS) as the surfactant collector for abrasive manufacturing waste recycling," *Separation and Purification Technology,* vol. 108, pp. 133-138, 2013.

[3] W. Cheng and E. Wang, "Size-dependent phase transfer of gold nanoparticles from water into toluene by tetraoctylammonium cations: a wholly electrostatic interaction," *The Journal of Physical Chemistry B,* vol. 108, pp. 24-26, 2004.

[4] G. Zambrana, R. Medina, G. Gutierrez, and R. Vargas, "Recovery of minus ten micron cassiterite by liquid-liquid extraction," *International Journal of Mineral Processing,* vol. 1, pp. 335-345, 1974.

[5] B. Hu, Y. Nakahiro, and T. Wakamatsu, "The effect of organic solvents on the recovery of fine mineral particles by liquid-liquid extraction," *Minerals engineering,* vol. 6, pp. 731-742, 1993.

[6] N. Gaponik, D. V. Talapin, A. L. Rogach, A. Eychmüller, and H. Weller, "Efficient phase transfer of luminescent thiol-capped nanocrystals: from water to nonpolar organic solvents," *Nano Letters,* vol. 2, pp. 803-806, 2002.

[7] H. Yao, O. Momozawa, T. Hamatani, and K. Kimura, "Phase transfer of gold nanoparticles across a water/oil interface by stoichiometric ion-pair formation on particle surfaces," *Bulletin of the Chemical Society of Japan,* vol. 73, pp. 2675-2678, 2000.

[8] J. Erler, S. Machunsky, P. Grimm, H.-J. Schmid, and U. A. Peuker, "Liquid–liquid phase transfer of magnetite nanoparticles—evaluation of surfactants," *Powder technology,* vol. 247, pp. 265-269, 2013.

[9] M. Karg, N. Schelero, C. Oppel, M. Gradzielski, T. Hellweg, and R. von Klitzing, "Versatile phase transfer of gold nanoparticles from aqueous media to different organic media," *Chemistry–A European Journal,* vol. 17, pp. 4648-4654, 2011.

[10] A. Kumar, P. Mukherjee, A. Guha, S. Adyantaya, A. Mandale, R. Kumar, *et al.*, "Amphoterization of colloidal gold particles by capping with valine molecules and their phase transfer from water to toluene by electrostatic coordination with fatty amine molecules," *Langmuir*, vol. 16, pp. 9775-9783, 2000.

[11] K. S. Mayya and F. Caruso, "Phase transfer of surface-modified gold nanoparticles by hydrophobization with alkylamines," *Langmuir*, vol. 19, pp. 6987-6993, 2003.

[12] A. Kumar, H. Joshi, R. Pasricha, A. Mandale, and M. Sastry, "Phase transfer of silver nanoparticles from aqueous to organic solutions using fatty amine molecules," *Journal of Colloid and Interface Science*, vol. 264, pp. 396-401, 2003.

[13] S. Underwood and P. Mulvaney, "Effect of the solution refractive index on the color of gold colloids," *Langmuir*, vol. 10, pp. 3427-3430, 1994.

[14] X. Feng, H. Ma, S. Huang, W. Pan, X. Zhang, F. Tian, *et al.*, "Aqueous− organic phase-transfer of highly stable gold, silver, and platinum nanoparticles and new route for fabrication of gold Nanofilms at the oil/water Interface and on solid supports," *The Journal of Physical Chemistry B*, vol. 110, pp. 12311-12317, 2006.

[15] T. Casagrande, G. Lawson, H. Li, J. Wei, A. Adronov, and I. Zhitomirsky, "Electrodeposition of composite materials containing functionalized carbon nanotubes," *Materials Chemistry and Physics*, vol. 111, pp. 42-49, 2008.

[16] Y. Su and I. Zhitomirsky, "Hybrid MnO_2/carbon nanotube-VN/carbon nanotube supercapacitors," *Journal of Power Sources*, vol. 267, pp. 235-242, 2014.

[17] S. P. Pujari, L. Scheres, A. T. Marcelis, and H. Zuilhof, "Covalent surface modification of oxide surfaces," *Angewandte Chemie International Edition,* vol. 53, pp. 6322-6356, 2014.

[18] R. Boissezon, J. Muller, V. Beaugeard, S. Monge, and J.-J. Robin, "Organophosphonates as anchoring agents onto metal oxide-based materials: synthesis and applications," *Rsc Advances,* vol. 4, pp. 35690-35707, 2014.

[19] B. Kalska-Szostko, M. Rogowska, and D. Satuła, "Organophosphorous functionalization of magnetite nanoparticles," *Colloids and Surfaces B: Biointerfaces,* vol. 111, pp. 656-662, 2013.

[20] F. Li, H. Zhong, G. Zhao, S. Wang, and G. Liu, "Adsorption of α-hydroxyoctyl phosphonic acid to ilmenite/water interface and its application in flotation," *Colloids and Surfaces A: Physicochemical and Engineering Aspects,* vol. 490, pp. 67-73, 2016.

[21] C. S. Pauly, A.-C. Genix, J. G. Alauzun, M. Sztucki, J. Oberdisse, and P. H. Mutin, "Surface modification of alumina-coated silica nanoparticles in aqueous sols with phosphonic acids and impact on nanoparticle interactions," *Physical Chemistry Chemical Physics,* vol. 17, pp. 19173-19182, 2015.

[22] G. Thomas, F. Demoisson, J. Boudon, and N. Millot, "Efficient functionalization of magnetite nanoparticles with phosphonate using a one-step continuous hydrothermal process," *Dalton Transactions,* vol. 45, pp. 10821-10829, 2016.

[23] P. Kar, A. Pandey, J. J. Greer, and K. Shankar, "Ultrahigh sensitivity assays for human cardiac troponin I using TiO_2 nanotube arrays," *Lab on a Chip*, vol. 12, pp. 821-828, 2012.

[24] M. Ata, Y. Liu, and I. Zhitomirsky, "A review of new methods of surface chemical modification, dispersion and electrophoretic deposition of metal oxide particles," *Rsc Advances*, vol. 4, pp. 22716-22732, 2014.

[25] V. Subramanian, H. Zhu, and B. Wei, "Alcohol-assisted room temperature synthesis of different nanostructured manganese oxides and their pseudocapacitance properties in neutral electrolyte," *Chemical Physics Letters*, vol. 453, pp. 242-249, 2008.

[26] M. Cheong and I. Zhitomirsky, "Electrophoretic deposition of manganese oxide films," *Surface Engineering*, vol. 25, pp. 346-352, 2009.

[27] J. Li and I. Zhitomirsky, "Electrophoretic deposition of manganese oxide nanofibers," *Materials Chemistry and Physics*, vol. 112, pp. 525-530, 2008.

[28] P. Taberna, P. Simon, and J.-F. Fauvarque, "Electrochemical characteristics and impedance spectroscopy studies of carbon-carbon supercapacitors," *Journal of The Electrochemical Society*, vol. 150, pp. A292-A300, 2003.

[29] S. Machunsky and U. A. Peuker, "Liquid-liquid interfacial transport of nanoparticles," *Physical separation in science and engineering*, vol. 2007, 2007.

[30] E. S. Džunuzović, J. V. Džunuzović, A. D. Marinković, M. T. Marinović-Cincović, K. B. Jeremić, and J. M. Nedeljković, "Influence of surface modified TiO_2

nanoparticles by gallates on the properties of PMMA/TiO_2 nanocomposites," *European Polymer Journal,* vol. 48, pp. 1385-1393, 2012.

[31] M. Giza, P. Thissen, and G. Grundmeier, "Adsorption kinetics of organophosphonic acids on plasma-modified oxide-covered aluminum surfaces," *Langmuir,* vol. 24, pp. 8688-8694, 2008.

[32] I. Zhitomirsky and A. Petric, "Electrophoretic deposition of ceramic materials for fuel cell applications," *Journal of the European Ceramic Society,* vol. 20, pp. 2055-2061, 2000.

[33] I. Zhitomirsky and A. Petric, "Electrophoretic deposition of electrolyte materials for solid oxide fuel cells," *Journal of materials science,* vol. 39, pp. 825-831, 2004.

[34] A. Toor, T. Feng, and T. P. Russell, "Self-assembly of nanomaterials at fluid interfaces," *The European Physical Journal E,* vol. 39, p. 57, 2016.

[35] D. M. Andala, S. H. R. Shin, H.-Y. Lee, and K. J. Bishop, "Templated synthesis of amphiphilic nanoparticles at the liquid–liquid interface," *ACS nano,* vol. 6, pp. 1044-1050, 2012.

[36] W. P. Lee, H. Chen, R. Dryfe, and Y. Ding, "Kinetics of nanoparticle synthesis by liquid–liquid interfacial reaction," *Colloids and Surfaces A: Physicochemical and Engineering Aspects,* vol. 343, pp. 3-7, 2009.

[37] X. Liang, L. Xing, J. Xiang, F. Zhang, J. Jiao, L. Cui, *et al.*, "The role of the liquid–liquid interface in the synthesis of nonequilibrium crystalline Wurtzite ZnS at room temperature," *Crystal Growth & Design,* vol. 12, pp. 1173-1179, 2012.

[38] Y. Li, K. Wu, and I. Zhitomirsky, "Electrodeposition of composite zinc oxide–chitosan films," *Colloids and Surfaces A: Physicochemical and Engineering Aspects,* vol. 356, pp. 63-70, 2010.

[39] J. Li and I. Zhitomirsky, "Cathodic electrophoretic deposition of manganese dioxide films," *Colloids and Surfaces A: Physicochemical and Engineering Aspects,* vol. 348, pp. 248-253, 2009.

[40] G. M. Jacob, Q. M. Yang, and I. Zhitomirsky, "Electrodes for electrochemical supercapacitors," *Materials and Manufacturing Processes,* vol. 24, pp. 1359-1364, 2009.

[41] S. Devaraj and N. Munichandraiah, "High capacitance of electrodeposited MnO_2 by the effect of a surface-active agent," *Electrochemical and Solid-State Letters*, vol. 8, pp. A373-A377, 2005.

[42] L. Athouël, F. Moser, R. Dugas, O. Crosnier, D. Bélanger, and T. Brousse, "Variation of the MnO_2 birnessite structure upon charge/discharge in an electrochemical supercapacitor electrode in aqueous Na_2SO_4 electrolyte," *The Journal of Physical Chemistry C,* vol. 112, pp. 7270-7277, 2008.

[43] D. Bélanger, L. Brousse, and J. W. Long, "Manganese oxides: battery materials make the leap to electrochemical capacitors," *The Electrochemical Society Interface,* vol. 17, p. 49, 2008.

[44] R. Jiang, T. Huang, Y. Tang, J. Liu, L. Xue, J. Zhuang, *et al.*, "Factors influencing MnO_2/multi-walled carbon nanotubes composite's electrochemical performance as supercapacitor electrode," *Electrochimica acta,* vol. 54, pp. 7173-7179, 2009.

[45] M. Toupin, T. Brousse, and D. Bélanger, "Charge storage mechanism of MnO_2 electrode used in aqueous electrochemical capacitor," *Chemistry of Materials,* vol. 16, pp. 3184-3190, 2004.

[46] K.-W. Nam and K.-B. Kim, "Manganese oxide film electrodes prepared by electrostatic spray deposition for electrochemical capacitors," *Journal of the Electrochemical Society,* vol. 153, pp. A81-A88, 2006.

[47] H. Xia and C. Huo, "Electrochemical properties of MnO_2/CNT nanocomposite in neutral aqueous electrolyte as cathode material for asymmetric supercapacitors," *International Journal of Smart and Nano Materials,* vol. 2, pp. 283-291, 2011.

[48] G. M. Jacob and I. Zhitomirsky, "Microstructure and properties of manganese dioxide films prepared by electrodeposition," *Applied Surface Science,* vol. 254, pp. 6671-6676, 2008.

[49] J. Li and I. Zhitomirsky, "Electrophoretic deposition of manganese dioxide–carbon nanotube composites," *Journal of Materials Processing Technology,* vol. 209, pp. 3452-3459, 2009.

[50] Y. Wang, Y. Liu, and I. Zhitomirsky, "Surface modification of MnO_2 and carbon nanotubes using organic dyes for nanotechnology of electrochemical supercapacitors," *Journal of Materials Chemistry A,* vol. 1, pp. 12519-12526, 2013.

[51] Y. Zhu, K. Shi, and I. Zhitomirsky, "Anionic dopant–dispersants for synthesis of polypyrrole coated carbon nanotubes and fabrication of supercapacitor electrodes with high active mass loading," *Journal of Materials Chemistry A,* vol. 2, pp. 14666-14673, 2014.

5 Bottom-up and top-down PELLI of oxide particles and electrophoretic deposition of thin films

This chapter is reproduced from *Strategies for liquid-liquid extraction of oxide particles for applications in supercapacitor electrodes and thin films, 499, 1-8, 2017, Journal of Colloid and Interface Science,* ***Ri Chen****, Mustafa S. Ata, Xinya Zhao, Amanda Clifford, Ishwar K. Puri and Igor Zhitomirsky, https://doi.org/10.1016/j.jcis.2017.03.095, Copyright 2019, with permission from Elsevier*. The author of this thesis is the first author and the main contributor of this publication.

5.1 Abstract

Bottom-up and top-down liquid-liquid extraction methods have been developed for the transfer of colloidal metal oxide particles, synthesized in an aqueous phase, to organic phases. In such methods the agglomeration of the particles during the drying stage was avoided. Hexadecylamine was used as an extractor for MnO_2 particles in the bottom-up extraction to the 1-butanol phase and top-down extraction to the dichloromethane phase. The reduction of particle agglomeration facilitated the fabrication of MnO_2-carbon nanotube composite electrodes for electrochemical supercapacitors with enhanced mixing of the individual components and active mass as high as 35 mg cm^{-2}. Electrochemical testing results showed superior performance of the composite MnO_2-carbon nanotube electrodes, prepared by the bottom-up strategy. The new strategies allowed the fabrication of advanced electrodes, which showed a capacitance of 5.48 F cm^{-2} at a scan rate of 2 mV s^{-1}, good capacitance retention at high scan rates and low resistance. In another

conceptually new bottom-up strategy colloidal titania particles were modified during synthesis with 2,3,4-trihydroxybenzaldehyde, which allowed strong catecholate-type bonding to the Ti atoms on the particle surface. The Schiff base reaction with hexadecylamine at the liquid-liquid interface allowed for particle extraction. The extraction strategies developed in this investigation pave the way for agglomerate-free processing of advanced films, coatings and devices by colloidal methods.

5.2 Introduction

Colloidal processing in organic solvents is widely used for the fabrication of moisture-stable composite films, coatings and devices, combining functional properties of inorganic and organic materials. Typical slurry formulations for the fabrication methods usually include inorganic particles, dispersed in organic solvents, which contain dissolved polymers and other functional organic materials[1] that are insoluble in water. Various non-aqueous colloidal techniques, such as spin casting[1, 2], spray deposition[3], dip coating[4], electrophoretic deposition [5]and other techniques[6] have been used to manufacture thin films and coatings. Organic solvents offer processing advantages for many colloidal methods, such as electrophoretic deposition[7] and tape casting[8]. The use of organic solvents for electrophoretic deposition allows for reduced gas evolution at the electrodes and low porosity of the films and coatings[9]. Non-aqueous slurries offer many advantages for the tape casting technology[8] due to the superior properties of the polymer binders, which are soluble in organic solvents, as compared to water soluble binders. The use of organic solvents is critical for the development of electrodes of aqueous supercapacitors

[10, 11], batteries[12], biomedical scaffolds[13] and other devices that contain water-insoluble functional polymers or polymer binders.

Many techniques for the synthesis of semiconductor quantum dots and particles of metals, oxides, hydroxides and other functional inorganic materials are based on aqueous processing. Following synthesis, washing and drying, these particles must be re-dispersed in an organic solvent. However, the drying can result in particle agglomeration, which is detrimental for many applications. Particle agglomeration is governed by the reduction in particle surface area and condensation of the surface OH groups. The drying procedure and particle agglomeration can be avoided by extracting the particles from an aqueous phase to an organic phase. Particle extraction through the liquid-liquid interface (PELLI) is a promising method for the colloidal processing of materials and composites. Previous investigations successfully extracted metals[14, 15] and quantum dots[16] through the interface lying between two immiscible liquids. Various interactions of organic extractor molecules and inorganic particles have been explored for the extraction, such as electrostatic[14], covalent[17, 18] and ion-pair[15] interactions. Different organic solvents have been used for the particle extraction[17]. Gold nanoparticles were extracted from an underneath aqueous phase into top lower density organic liquids such as toluene, hexane and diethyl ether[17]. In the case of chloroform solvent, which has higher density than water, the extraction was performed from the top aqueous phase into the bottom organic phase[17]. The extraction efficiency was enhanced by including co-solvents[16, 19]. In another approach[20], the extraction was triggered by a temperature increase from the room temperature to 80 °C, which resulted in the reduction of the solubility of the polymer extractor in an aqueous phase and transfer of the adsorbed particles to an organic phase. The extraction efficiency of gold nanoparticles has been found to be influenced by the alkyl chain length of the extractor molecules[17]. Larger particles required longer extractor molecules for the phase transfer[17]. There is increasing interest in new applications of the PELLI method for photoelectronic and optoelectronic devices[16], separation of rare earth fluorescent powders[21] and magnetic devices[22]. It has been found that the adsorption of the extractor molecules on particles at the liquid-liquid interface can provide partial de-agglomeration of the particles, synthesized in an aqueous phase[22].

Previous investigations have primarily focused on the use of very dilute suspensions of metal nanoparticles. Thus, an important task is the development of efficient extractors for the particles of functional oxides in concentrated suspensions. However, the major difficulty in particle extraction is poor adsorption of the extractor molecules on the oxide particles.

The goal of this investigation was the development of PELLI strategies for the extraction of oxide materials. MnO_2 and titania, which exhibit a variety of functional properties, were used as model oxide materials for this study. Bottom-up and top-down strategies were explored for the extraction of MnO_2 using a 1-hexadecylamine (NH_2R') as an extractor molecule. The benefits of the PELLI method were demonstrated using the extracted MnO_2 particles to fabricate electrodes of electrochemical supercapacitors, which showed high areal capacitance and good capacitance retention at high charge-discharge rates. Electrochemical testing results correlated with particle size measurements and revealed the advantages of bottom-up extraction. Due to the poor adsorption of NH_2R' on titania, we developed another extraction strategy. The titania particles were modified in-situ by a catecholate type 2,3,4-trihydroxybenzaldehyde (R″-CHO) molecule in the aqueous phase, which allowed for strong bonding to the titania surface. The Schiff base reaction of R″-CHO, adsorbed on the particle surface and NH_2R', dissolved in the organic phase allowed for the liquid-liquid extraction. The advantages of this method were demonstrated by the fabrication of composite films. The PELLI strategies were applied to suspensions of relatively high concentrations and can be used for extraction of other functional oxides.

5.3 Experimental procedures

$NaMnO_4$, $TiOSO_4$, NaOH, Na_2SO_4, 1-hexadecylamine (NH_2R'), 2,3,4-trihydroxybenzaldehyde (R″-CHO), poly(vinyl butyral-co-vinyl alcohol-co-vinyl acetate) (PVB, average Mw = 50,000 – 80,000), 1-butanol, dichloromethane, (Aldrich) and multiwalled carbon nanotubes (MWCNT, ID 4 nm, OD 13 nm, length 1–2 μm, Bayer, Germany) were used. Ni foams with 95% porosity were provided by Vale Limited. Ni foams were cleaned by ultrasonication in water, acetone and finally in ethanol.

The synthesis of MnO_2 particles was performed by a chemical precipitation method using aqueous $NaMnO_4$ solutions and 1-butanol as a reducing agent. The reduction of Mn^{7+} was achieved at the liquid-liquid interface, because 1-butanol is a water immiscible solvent. The addition of 1-butanol to the aqueous $NaMnO_4$ solution and stirring during 1 h resulted in the precipitation of MnO_2 in an aqueous phase. After stirring, phase separation of the aqueous phase and 1-butanol was observed. The synthesis of titania was performed using aqueous $TiOSO_4$ solutions. The pH of the solutions was adjusted to pH = 6 by NaOH.

In the bottom-up extraction strategy 1-butanol was used as a receiving solvent, which has lower density, compared to the density of water. Dichloromethane, which has a higher density than the water density, was used for the top-down extraction. The concentration of particles in the extracted suspensions was 10–15 g L^{-1}. The mass ratio of NH_2R' /oxide particles and R''-CHO /oxide particles was 0.2–0.3.

For the fabrication of supercapacitor electrodes, the suspensions of extracted MnO_2 in 1-butanol or dichloromethane were separated from the aqueous phase and then MWCNT were added. After ultrasonication of the mixed suspensions, the solution of PVB binder in ethanol was added. The mass ratio of MnO_2:MWCNT:PVB was 80:20:3. Obtained suspensions were used to fabricate MnO_2-MWCNT supercapacitor electrodes by impregnating the Ni foam current collectors. The active mass loading of the electrodes was 35 mg cm^{-2}. Titania suspensions in 1-butanol obtained by liquid-liquid extraction were mixed with 2 g L^{-1} PVB solution in 1-butanol for the deposition of coatings on stainless steel foils by dip coating method[23, 24].

Electron microscopy investigations were performed using a JEOL JSM-7000F scanning electron microscope (SEM). X-ray diffraction (XRD) studies were performed using a powder diffractometer (Nicolet I2, monochromatized CuKα radiation). FTIR studies were performed on Bruker Vertex 70 spectrometer. Dynamic light scattering (DLS, DelsaMax Pro: Beckman Coulter) was used for the particle size distribution analysis.

Cyclic voltammetry and impedance spectroscopy investigations were performed using a potentiostat (PARSTAT 2273, Princeton Applied Research, USA). The capacitive behavior of the electrodes was studied in three-electrode cells using 0.5 M Na_2SO_4 aqueous solutions. The area of the working electrode was 1 cm^2. The counter electrode was a platinum gauze, and the reference electrode was a standard calomel electrode (SCE). Cyclic voltammetry (CV) studies were performed at scan rates of 2–100 mV s^{-1}. The integral capacitances $C_S = Q/\Delta VS$ and $C_m = Q/\Delta Vm$ were calculated using half the integrated area of the CV curve to obtain the charge Q, and subsequently dividing the charge Q by the width of the potential window ΔV and electrode area S or active mass m. The alternating current measurements of complex impedance $Z^* = Z' - iZ''$were performed in the frequency range of 10 mHz to 100 kHz at the amplitude of the signal of 5 mV. The complex differential capacitance $C_S^* = C_S' - iC_S''$ was calculated[25, 26] from the impedance data as $C_S' = Z''/\omega|Z|^2S$ and $C_S'' = Z'/\omega|Z|^2S$, where $\omega = 2\pi f$ (f-frequency).

5.4 Results and discussion

MnO_2 and titania, precipitated in the aqueous phases were washed with water, filtrated and dried. X-ray diffraction studies of the MnO_2 powder showed (Figure 5.1) relatively small peaks of the birnessite phase. The formation of poorly crystallized MnO_2 birnessite phase by precipitation was also reported in other investigations[27]. However, the material also contained an amorphous phase. The as-precipitated titania was amorphous (Figure 4.4b).

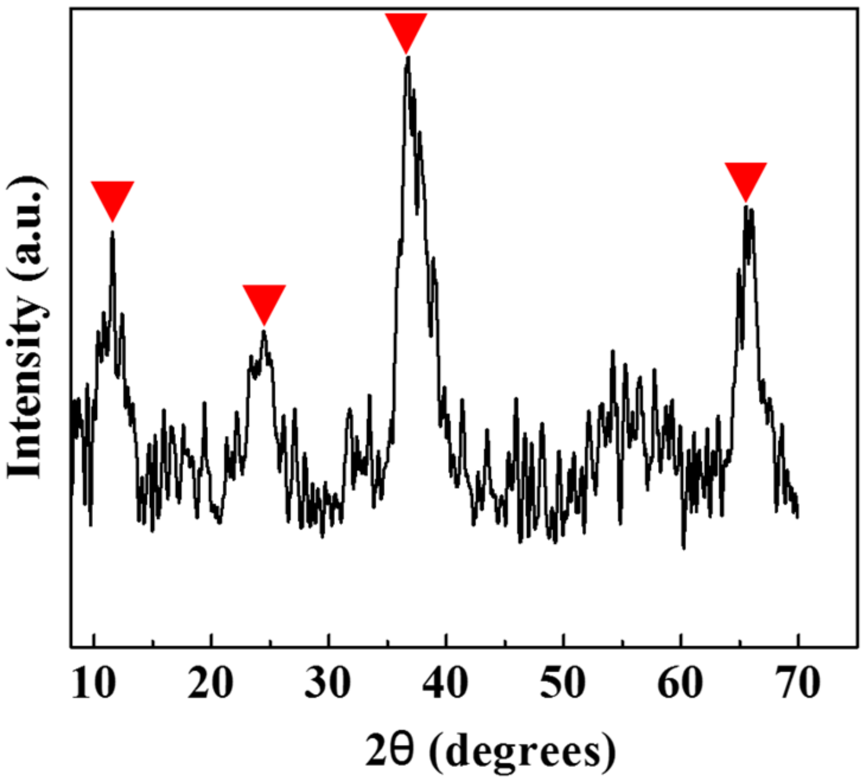

Figure 5.1 X-ray diffraction pattern of manganese dioxide (▼- JCPDS file 87-1497).

Figure 5.2 shows SEM images of the MnO_2 and titania powders after drying. The MnO_2 powders contained submicron particles and large agglomerates with a typical size of 1–5 µm. The SEM images of titania showed a large number of agglomerates with a typical size of 10–100 µm.

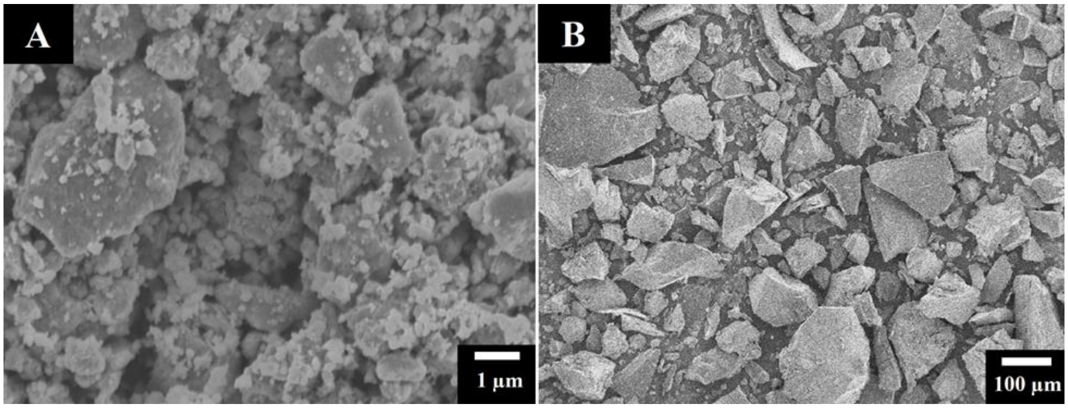

Figure 5.2 SEM images of (A) manganese dioxide and (B) titania powders.

With a desire to reduce agglomeration, we developed extraction methods (EM) for MnO_2 and titania. In this investigation 1-butanol was used as a reducing agent for the synthesis of MnO_2. After the synthesis, a two-phase mixture was obtained, which contained MnO_2 in the bottom aqueous phase, separated from the 1-butanol top phase. Figure 5.3A shows a chemical structure of NH_2R', which was used as an extractor. NH_2R' is a typical head-tail surfactant, containing a hydrophilic NH_2 group and a hydrophobic hydrocarbon group.

Figure 5.4A shows a schematic of the bottom-up EM1. The particles, precipitated in the aqueous phase (Figure 5.4A(a)) were extracted to the 1-butanol phase after the addition of NH_2R'. It is suggested that similar to other head-tail surfactants, NH_2R' accumulated at the liquid-liquid interface with hydrophilic groups exposed to water and hydrophobic tail extended out of the water phase into the 1-butanol phase. The accumulation and orientation of the NH_2R' molecules at the liquid-liquid interface promoted their adsorption on the inorganic particles and extraction (Figure 5.4 A (b and c)). Fig. 3B shows the possible mechanisms of the NH_2R' adsorption, such as chemisorption[28] (Figure 5.3B(a)) or an electrostatic interaction, involving surface OH groups[29] (Figure 5.3B(b)). Fig. 4B shows

MnO_2 suspension before and after extraction. Practically all MnO_2 material was extracted to the 1-butanol phase. The results indicate that EM1 allows for the use of relatively concentrated suspensions. In this bottom-up method the particles were transferred to the top 1-butanol phase against the force of gravity. The stirring and ultrasonic agitation promoted interaction of NH_2R' with the particles and facilitated the phase transfer.

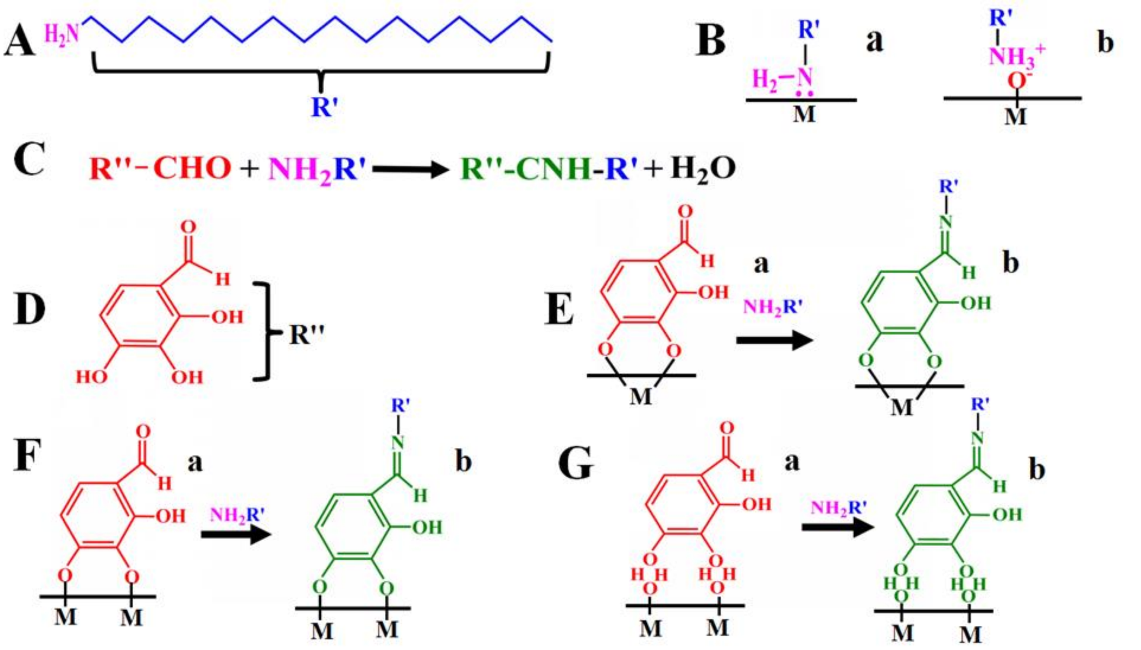

Figure 5.3 (A) Chemical structure of NH_2R', (B) adsorption mechanisms of NH_2R' on oxide surface: (a) chemisorption and (b) electrostatic interactions, involving surface OH groups (C) Schiff base reaction of R″-CHO and NH_2R', (D) chemical structure of R″-CHO, (E-G) schematics of the Schiff base reaction for R″-CHO, adsorbed on particle surface by different mechanism: (E) chelation, (F) bridging inner sphere complex and (E) bridging outer sphere complex.

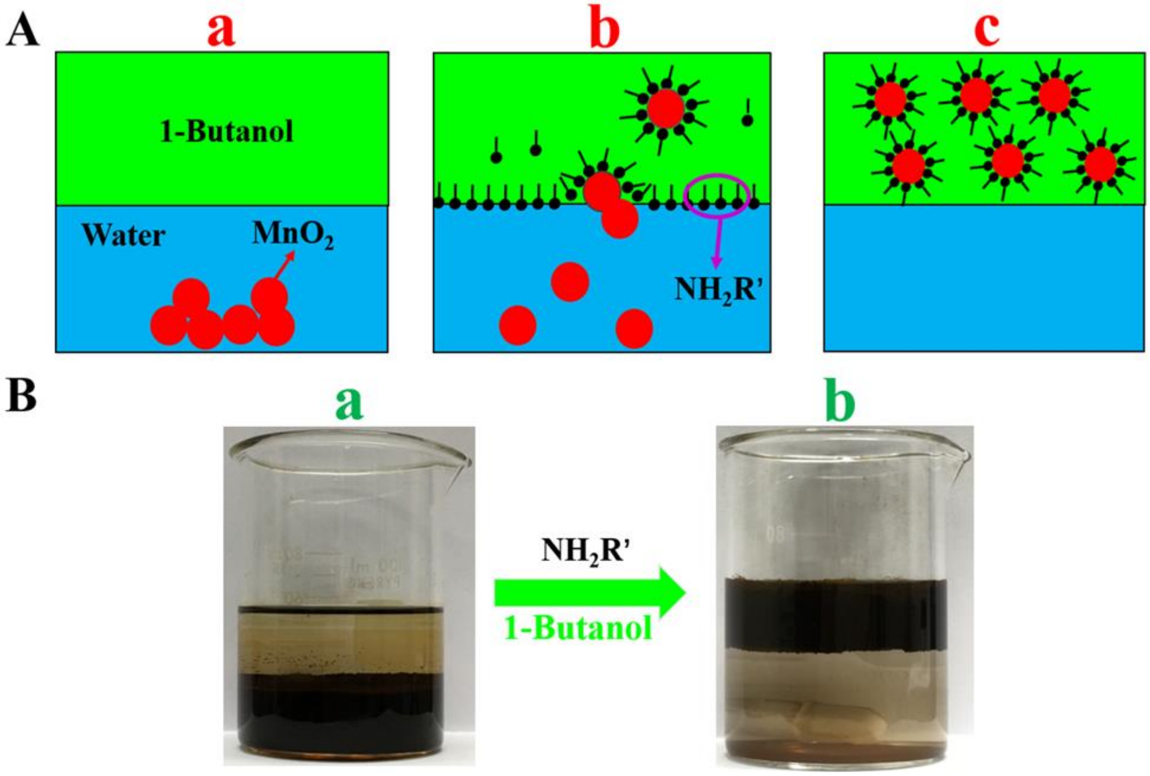

Figure 5.4 (A) Schematic of (a) precipitation and different steps in extraction in EM1, (B) manganese dioxide suspension (a) before and (b) after extraction.

Figure 5.5A shows a schematic of the top-down EM2 process. Prior to the extraction, the aqueous phase was separated from the 1-butanol phase and then dichloromethane was added. The top aqueous phase, containing MnO_2, and bottom dichloromethane phases showed a separation (Figure 5.5A(a) and B(a)). The MnO_2 particles remained in the aqueous phase. After addition of NH_2R' solution in dichloromethane to the dichloromethane phase the extraction of MnO_2 was achieved. The accumulation and orientation of the NH_2R' molecules at the liquid-liquid interface and sedimentation of the MnO_2 in the aqueous phase under the force of gravity promoted surface modification of the MnO_2 particles and their extraction to the 1-butanol phase. However, stirring and ultrasonic agitation accelerated the extraction process. The MnO_2 particles were practically completely extracted to the dichloromethane solvent (Figure 5.5A and B).

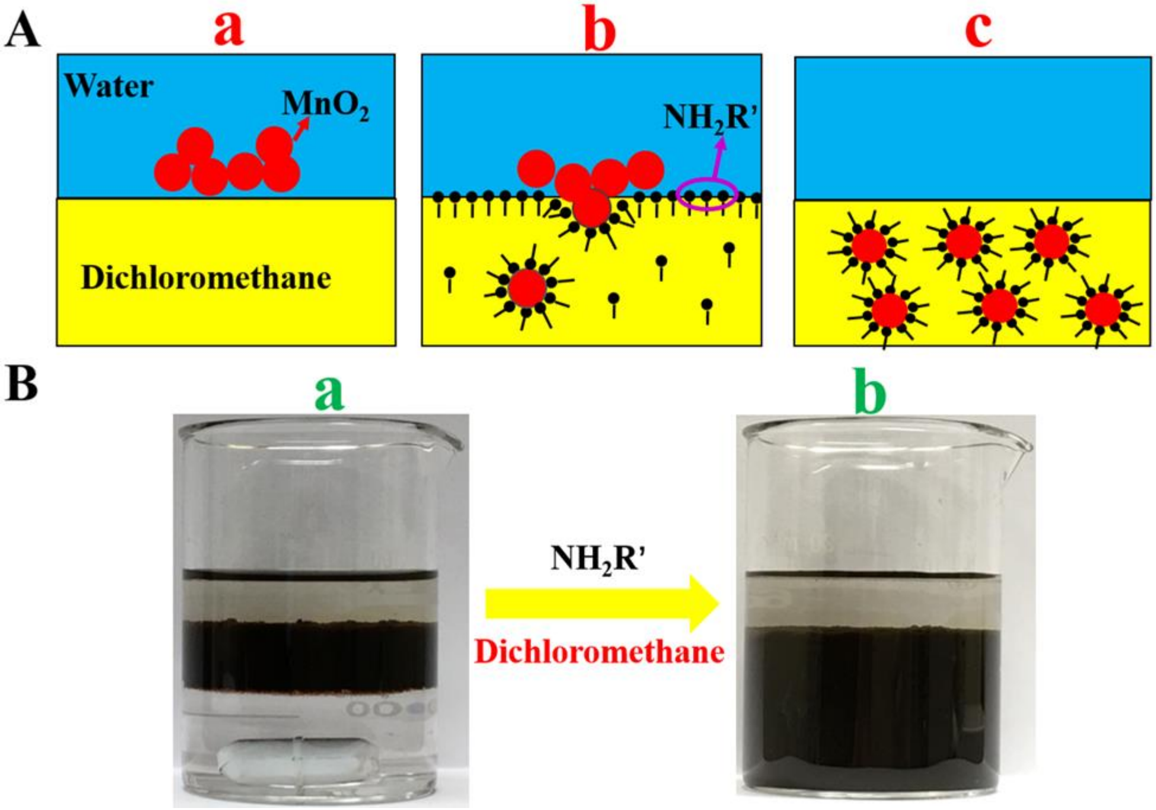

Figure 5.5 (A) Schematic of (a) precipitation and (b,c) different steps in extraction in EM2, (B) manganese dioxide suspension (a) before and (b) after extraction

The suggested extraction mechanism was confirmed by the results of the FTIR studies of the extracted materials. Figure 5.6(a–c) compares the FTIR spectra of as-received NH_2R' and extracted MnO_2 particles. The FTIR spectrum of NH_2R' (Figure 5.6(a)) shows absorptions at 2851, 2916 and 2955 cm^{-1}, which resulted from the CH_2 symmetric stretching, CH_2 asymmetric stretching and CH_3 out-of-plane stretching, respectively[30, 31]. Similar absorptions were observed in the spectra of MnO_2 particles, extracted by EM1 and EM2 (Figure 5.6(b and c)). Therefore, the results of FTIR studies confirmed that NH_2R' was adsorbed on the MnO_2 particles. The adsorbed NH_2R' allowed for particle extraction.

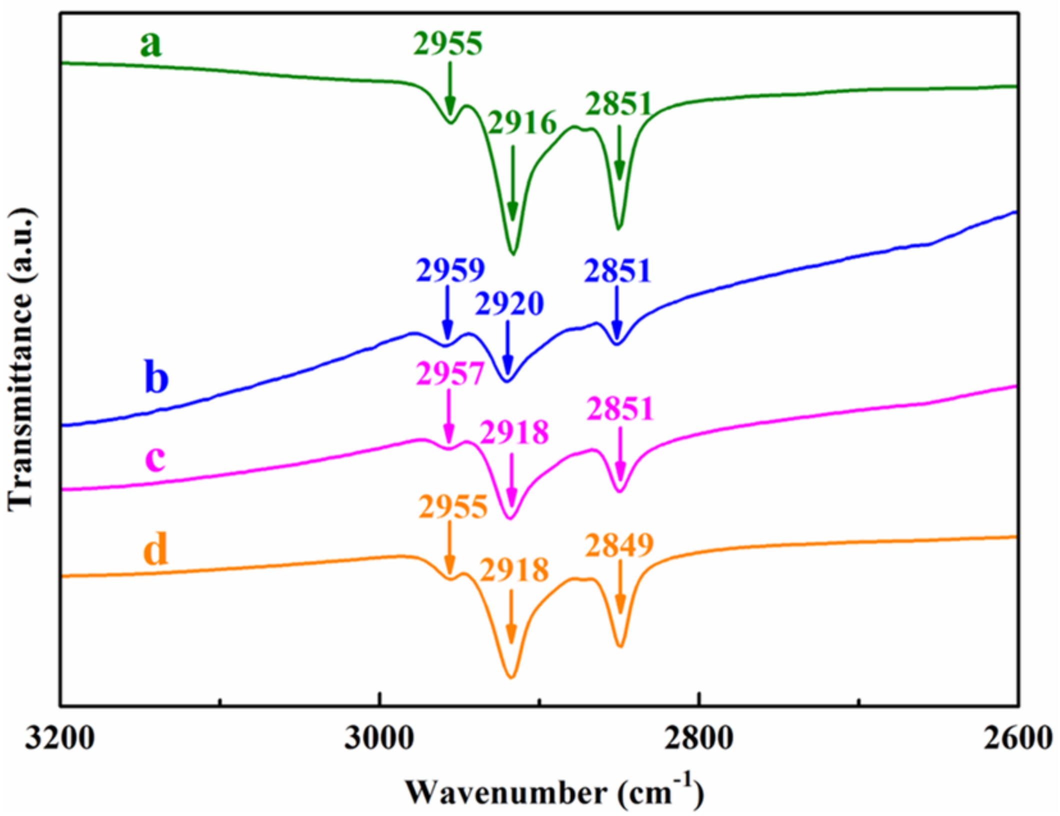

Figure 5.6 FTIR spectra of (a) as-received NH_2R' and (b-d) particles, extracted by methods (a) EM1, (b) EM2 and (c) EM3

The analysis of extracted powders in non-aqueous suspensions by the dynamic light scattering method (Figure 5.7A and B) showed smaller size of the particles, prepared by EM1. The radius of the particles extracted in EM1 was generally below 100 nm. The suspensions, prepared using EM2, contained many particles with radii in the 100–150 nm range. As discussed above, the particle extraction in the EM1 is achieved against the force of gravity. Therefore, EM1 favors the extraction of smaller particles. As also pointed out above, the adsorption of extractor molecules on particles at the liquid-liquid interface can provide partial particle de-agglomeration[22]. These particles can be extracted to the top organic phase. In contrast, during the EM2 process, the force of gravity facilitates the penetration of the liquid-liquid interface by the larger particles. However, for both methods the size of the extracted particles was significantly lower, as compared to the size of the dried agglomerates, shown in Figure 5.2A.

The reduced agglomeration of the MnO_2 particles is beneficial for applications in the electrodes of electrochemical supercapacitors. The non-agglomerated particles provide larger surface area for the electrochemical charge storage reactions. However, it is important to note that BET surface area usually does not correlate[32-35] with capacitance, because very small pores can become inaccessible to the electrolyte.

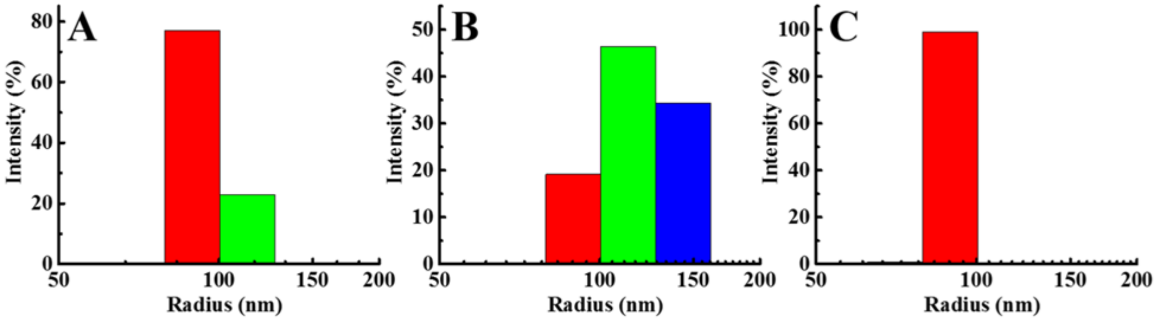

Figure 5.7 Particles size distributions for (a) manganese dioxide particles, extracted by EM1, (b) manganese dioxide particles, extracted by EM2, (c) titania particles, extracted by EM3.

Figure 5.8(A and B) shows CVs for the MnO_2-MWCNT electrodes, prepared using EM1 and EM2. The reduction of particle agglomeration was beneficial for fabricating electrodes that had an active mass as high as 35 mg cm^{-2}. The electrodes, prepared using EM1 showed larger CV areas, compared to the electrodes, prepared using EM2. The larger CV area indicated higher capacitance. The CVs for electrodes, prepared using EM1 were of nearly ideal box shape (Figure 5.8A). The capacitances were calculated from the CV data at different scan rates (Figure 5.8C). The electrodes, prepared using EM1 showed capacitance of 5.48 F cm^{-2} (152.5 F g^{-1}) at a scan rate of 2 mV s^{-1} and capacitance retention of 38.3% at 100 mV s^{-1}. The obtained capacitance was significantly higher than that reported in the literature[36] The electrodes, prepared using EM2, showed a capacitance of 5.13 F cm^{-2} (141.8 F g^{-1}) and capacitance retention of 21.4% at 100 mV s^{-1}. Fig. 8C indicates that EM1 allowed for superior capacitive performance at scan rates above 20 mV s^{-1}. The capacitance of 2.1 F cm^{-2}, obtained at 100 mV s^{-1} and mass loading of 35 mg cm^{-2} was two times higher, compared to the capacitance[37] obtained at the same scan rate at mass loading of 40 mg cm^{-2} by the method, based on the use of co-dispersants for MnO_2 and MWCNT. It is suggested that the reduced agglomeration of the particles allowed for improved mixing of MnO_2 and MWCNT, which resulted in better electrolyte access to the MnO_2 surface and improved electronic conductivity, which led to enhanced capacitance.

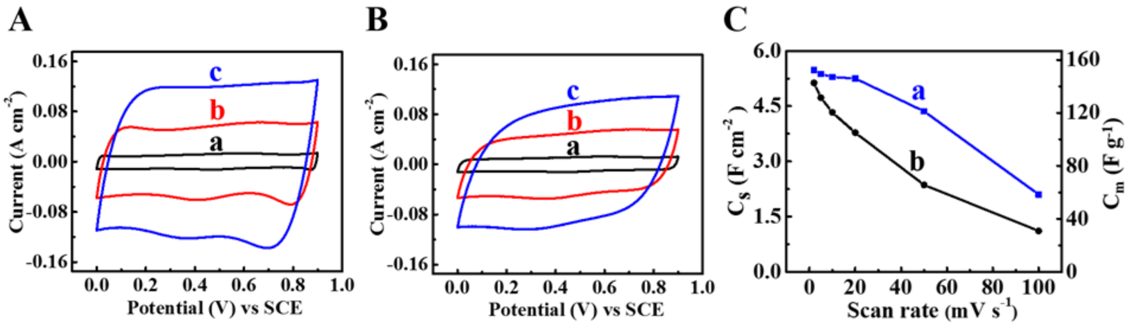

Figure 5.8 (A,B) CVs for manganese dioxide-MWCNT electrodes, prepared using (A) EM1 and (B) EM2 at scan rates of (a) 2, (b) 10 and (c) 20 mV s^{-1}, (C) C_S and C_m for manganese dioxide-MWCNT electrodes, prepared using (a) EM1 and (b) EM2.

The analysis of the impedance data (Figure 5.9A), presented in the Nyquist plot showed lower resistance R = Z′ of the electrode, prepared by EM1. Analysis of the differential capacitances, calculated from the impedance data showed a relaxation type dispersion[38], as indicated by the reduction of the real part C_S' of capacitance (Figure 5.9B) with frequency and relaxation maxima (Figure 5.9C) in the frequency dependences of the imaginary C_S'' components. The relaxation frequencies, corresponding to the C_S'' maxima were 63 and 40 Hz for electrodes, prepared using EM1 and EM2, respectively. The higher relaxation frequency for the electrodes, prepared by EM1 indicates better capacitive performance at high charge-discharge rates, which is in agreement with the CV data. The improved capacitive performance of the electrodes prepared using EM1 correlates with smaller size of the extracted particles. However, EM1 did not permit titania extraction due to poor adsorption of NH_2R' on the titania particles. This problem was addressed in EM3 by the chemical modification of titania prior to its extraction.

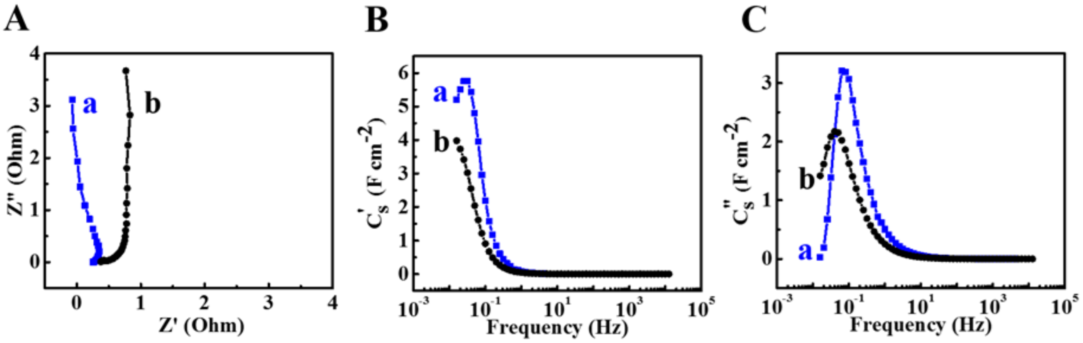

Figure 5.9 (A) Nyquist plot of complex impedance, (B,C) frequency dependences of (B) C_S' and (C) C_S'' for manganese dioxide-MWCNT electrodes, prepared using (a) EM1 and (b) EM2.

In EM3 we used NH_2R' as an extractor for titania particles, which were modified with R″-CHO. Using this strategy, R″-CHO was added to the $TiOSO_4$ solutions prior to the titania precipitation. The addition of the alkali resulted in the formation of a dark-red suspension, containing titania particles with adsorbed R″-CHO (Figure 5.10A(a) and B(a)). The Schiff base reaction (Figure 5.3C) at the liquid-liquid interface linked the extractor molecules to the modified particles and allowed for the extraction (Figure 5.10A(b) and B(b)). The extracted particles had a red color.

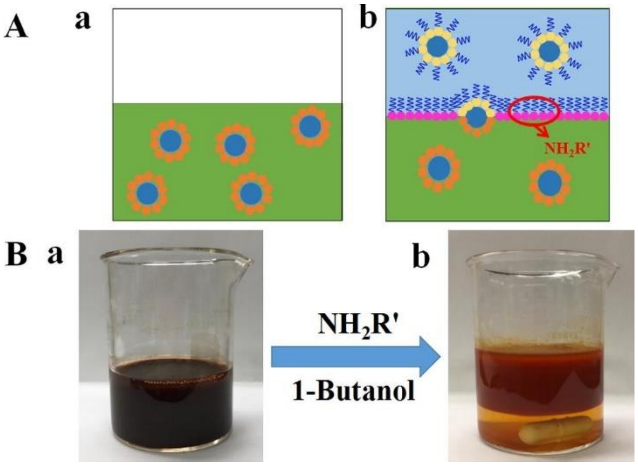

Figure 5.10 (A) Schematic of (a) precipitation in the presence of R″-CHO, involving R″-CHO adsorption on particles (b) particle extraction in EM3, involving Schiff base reaction at the liquid-liquid interface, (B) titania suspension (a) before and (b) after extraction

Figure 5.3D shows the chemical structure of R″-CHO. It contains an aldehyde group, which allows for the chemical bonding of this molecule to the amino group of the NH_2R' extractor in the Schiff base reaction. The OH groups, which bonded to the aromatic ring allowed for adsorption of R″- CHO on the titania surface. It is important to note that molecules with similar structure, such as catecholates and gallates, containing phenolic OH groups bonded to adjacent carbon atoms of the aromatic rings, exhibit unique adsorption properties. The interest in catecholate and gallate adhesives resulted from the fundamental investigations [39-41] of mechanisms of strong mussel adhesion to different surfaces in seawater, which involved protein macromolecules, containing catecholic amino acid, L-3,4-dihydroxyphenylalanine. Further investigations of catecholates and gallates resulted in the development of advanced capping and dispersing agents[42] for the synthesis and dispersion of inorganic nanoparticles. Figure 5.3(E–G) illustrates Schiff base reactions for different adsorption mechanisms of R″-CHO, involving chelation, inner sphere and outer sphere bonding mechanisms, suggested in the literature for the catecholate-type bonding[42].

It is important to note that titania particles, prepared without R″-CHO showed poor colloidal stability. The addition of R″-CHO allowed for the formation of stable suspensions. This is not surprising, because various catecholates and gallates were used as efficient dispersing and capping agents for inorganic particles[42]. The color change from white to red resulted from the adsorption of R″-CHO on the particle surface. A similar color change was observed for the colloidal titania particles, modified with catecholates[42, 43]. The improved colloidal stability of the titania particles, as well as accumulation and orientation of NH_2R' at the liquid-liquid interface, was beneficial for the modification of the particles with the extractor molecules in the Schiff base reaction and extraction. The results of the FTIR studies confirmed the suggested extraction mechanism. The FTIR spectrum (Figure 5.6(d)) of the extracted titania particles showed absorption at 2849, 2918 and 2955 cm^{-1}, attributed to CH_2 symmetric stretching, CH_2 asymmetric stretching and CH_3 out-of-plane stretching. Similar absorptions were observed in the spectrum of pure NH_2R' (Figure 5.6(a)).

The radii of the particles, extracted by EM3 were below 100 nm (Figure 5.7C). The sizes of the extracted particles were significantly smaller than the sizes of the agglomerates shown in Figure 5.2B. The SEM images of the composite titania-PVB films showed a smooth morphology, without agglomerates (Figure 5.11). The ability to avoid particle agglomeration can also be beneficial for the deposition of other oxide materials by various colloidal techniques. EM1 offers the advantage of a simple one-step extraction, but EM3 allows the particles to be modified during synthesis. In this approach R″-CHO and other molecules can potentially reduce the particle growth during synthesis.

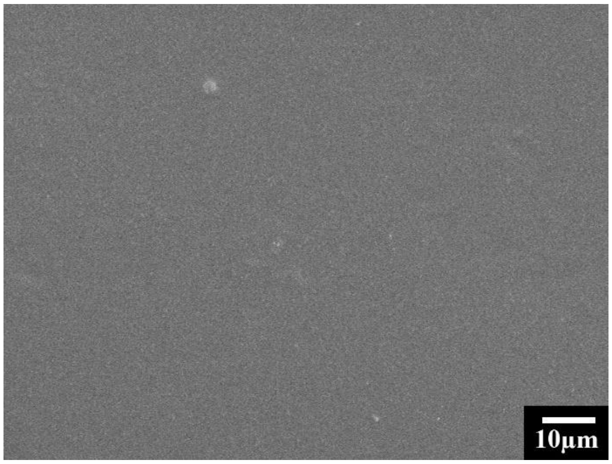

Figure 5.11 SEM image of a titania–PVB film.

5.5 Conclusions

Advanced extractors and PELLI strategies, developed in this investigation allowed for the extraction of MnO_2 and titania particles, which were synthesized in aqueous phases, into organic phases. Thus particle agglomeration during the drying stage can be avoided. In contrast to previous investigations[14, 18, 44] focused on the use of dilute suspensions, these findings open practical PELLI applications for concentrated suspensions of oxide particles. New PELLI strategies allowed the reduction of particle size, enhanced co-dispersion and mixing of MnO_2 and MWCNT. The important outcome of this study was the fabrication of supercapacitor electrodes with active mass loading as high as 35 mg cm^{-2}, which showed excellent electrochemical performance. The bottom-up EM1 produced smaller particle sizes, compared to the top-down EM2. As a result, the MnO_2-MWCNT electrodes, prepared by EM1 showed an improved capacitive behavior. The electrodes showed a capacitance of 5.48 F cm^{-2} at a scan rate of 2 mV s^{-1}, good capacitance retention at high scan rates and low resistance. In another conceptually new bottom-up strategy, colloidal titania particles were modified during synthesis with R″-CHO, which has strong catecholate-type bonding to the Ti atoms on the particle surface. The Schiff base reaction with hexadecylamine at the liquid-liquid interface allowed for particle extraction. This strategy can potentially reduce particle growth during synthesis and extract smaller particles. Further development of PELLI techniques will facilitate the colloidal processing of advanced nanomaterials and nanocomposites for application in energy storage devices and films with enhanced performance.

5.6 References

[1] S. Yamada, Z. Wang, E. Mouri, and K. Yoshinaga, "Crystallization of titania ultra-fine particles from peroxotitanic acid in aqueous solution in the present of polymer and incorporation into poly (methyl methacylate) via dispersion in organic solvent," *Colloid and Polymer Science*, vol. 287, pp. 139-146, 2009.

[2] J. Kim, H. Yang, and P. F. Green, "Tailoring the refractive indices of thin film polymer metallic nanoparticle nanocomposites," *Langmuir*, vol. 28, pp. 9735-9741, 2012.

[3] X. Zhao, C. Hinchliffe, C. Johnston, P. J. Dobson, and P. S. Grant, "Spray deposition of polymer nanocomposite films for dielectric applications," *Materials Science and Engineering: B*, vol. 151, pp. 140-145, 2008.

[4] F. Mauvy, P. Lenormand, C. Lalanne, F. Ansart, J.-M. Bassat, J.-C. Grenier*, et al.*, "Electrochemical characterization of YSZ thick films deposited by dip-coating process," *Journal of Power Sources,* vol. 171, pp. 783-788, 2007.

[5] I. Zhitomirsky and L. Gal-Or, "Formation of hollow fibers by electrophoretic deposition," *Materials Letters*, vol. 38, pp. 10-17, 1999.

[6] S. Jaiser, L. Funk, M. Baunach, P. Scharfer, and W. Schabel, "Experimental investigation into battery electrode surfaces: The distribution of liquid at the surface and the emptying of pores during drying," *Journal of colloid and interface science*, vol. 494, pp. 22-31, 2017.

[7] K. Wu, Y. Wang, and I. Zhitomirsky, "Electrophoretic deposition of TiO_2 and composite TiO_2–MnO_2 films using benzoic acid and phenolic molecules as charging additives," *Journal of colloid and interface science*, vol. 352, pp. 371-378, 2010.

[8] I. Zhitomirsky and A. Petric, "Electrophoretic deposition of ceramic materials for fuel cell applications," *Journal of the European Ceramic Society*, vol. 20, pp. 2055-2061, 2000.

[9] I. Zhitomirsky, "Cathodic electrodeposition of ceramic and organoceramic materials. Fundamental aspects," *Advances in colloid and interface science,* vol. 97, pp. 279-317, 2002.

[10] G. P. Ojha, B. Pant, S.-J. Park, M. Park, and H.-Y. Kim, "Synthesis and characterization of reduced graphene oxide decorated with CeO_2-doped MnO_2 nanorods for supercapacitor applications," *Journal of colloid and interface science,* vol. 494, pp. 338-344, 2017.

[11] Y. Wang, X. Zhang, X. Li, X. Li, Y. Zhao, H. Wei, *et al.*, "Highly dispersed ultrasmall $Ni(OH)_2$ aggregated particles on a conductive support as a supercapacitor electrode with superior performance," *Journal of colloid and interface science,* vol. 490, pp. 252-258, 2017.

[12] C. Yuan, H.-g. Wang, J. Liu, Q. Wu, Q. Duan, and Y. Li, "Facile synthesis of Co_3O_4-CeO_2 composite oxide nanotubes and their multifunctional applications for lithium ion batteries and CO oxidation," *Journal of colloid and interface science,* vol. 494, pp. 274-281, 2017.

[13] P. Bhattacharjee, D. Naskar, T. K. Maiti, D. Bhattacharya, and S. C. Kundu, "Non-mulberry silk fibroin grafted poly (Є-caprolactone)/nano hydroxyapatite nanofibrous scaffold for dual growth factor delivery to promote bone regeneration," *Journal of colloid and interface science,* vol. 472, pp. 16-33, 2016.

[14] W. Cheng and E. Wang, "Size-dependent phase transfer of gold nanoparticles from water into toluene by tetraoctylammonium cations: a wholly electrostatic interaction," *The Journal of Physical Chemistry B,* vol. 108, pp. 24-26, 2004.

[15] H. Yao, O. Momozawa, T. Hamatani, and K. Kimura, "Phase transfer of gold nanoparticles across a water/oil interface by stoichiometric ion-pair formation on particle surfaces," *Bulletin of the Chemical Society of Japan,* vol. 73, pp. 2675-2678, 2000.

[16] N. Gaponik, D. V. Talapin, A. L. Rogach, A. Eychmüller, and H. Weller, "Efficient phase transfer of luminescent thiol-capped nanocrystals: from water to nonpolar organic solvents," *Nano Letters,* vol. 2, pp. 803-806, 2002.

[17] M. Karg, N. Schelero, C. Oppel, M. Gradzielski, T. Hellweg, and R. von Klitzing, "Versatile phase transfer of gold nanoparticles from aqueous media to different organic media," *Chemistry–A European Journal,* vol. 17, pp. 4648-4654, 2011.

[18] A. Kumar, H. Joshi, R. Pasricha, A. Mandale, and M. Sastry, "Phase transfer of silver nanoparticles from aqueous to organic solutions using fatty amine molecules," *Journal of Colloid and Interface Science,* vol. 264, pp. 396-401, 2003.

[19] B. Hu, Y. Nakahiro, and T. Wakamatsu, "The effect of organic solvents on the recovery of fine mineral particles by liquid-liquid extraction," *Minerals engineering,* vol. 6, pp. 731-742, 1993.

[20] X. Feng, H. Ma, S. Huang, W. Pan, X. Zhang, F. Tian, *et al.*, "Aqueous− organic phase-transfer of highly stable gold, silver, and platinum nanoparticles and new route for fabrication of gold Nanofilms at the oil/water Interface and on solid supports," *The Journal of Physical Chemistry B,* vol. 110, pp. 12311-12317, 2006.

[21] A. Otsuki, G. Dodbiba, A. Shibayama, J. Sadaki, G. Mei, and T. Fujita, "Separation of rare earth fluorescent powders by two-liquid flotation using organic solvents," *Japanese Journal of Applied Physics,* vol. 47, p. 5093, 2008.

[22] J. Erler, S. Machunsky, P. Grimm, H.-J. Schmid, and U. A. Peuker, "Liquid–liquid phase transfer of magnetite nanoparticles—evaluation of surfactants," *Powder technology,* vol. 247, pp. 265-269, 2013.

[23] H. Tikkanen, C. Suciu, I. Wærnhus, and A. C. Hoffmann, "Dip-coating of 8YSZ nanopowder for SOFC applications," *Ceramics International,* vol. 37, pp. 2869-2877, 2011.

[24] H. Tikkanen, C. Suciu, I. Wærnhus, and A. C. Hoffmann, "Examination of the co-sintering process of thin 8YSZ films obtained by dip-coating on in-house produced NiO–YSZ," *Journal of the European Ceramic Society,* vol. 31, pp. 1733-1739, 2011.

[25] P. Taberna, P. Simon, and J.-F. Fauvarque, "Electrochemical characteristics and impedance spectroscopy studies of carbon-carbon supercapacitors," *Journal of The Electrochemical Society,* vol. 150, pp. A292-A300, 2003.

[26] M. J. Barmi and M. Minakshi, "Tuning the redox properties of the nanostructured $CoMoO_4$ electrode: effects of surfactant content and synthesis temperature," *ChemPlusChem,* vol. 81, pp. 964-977, 2016.

[27] L. Coustan, A. Le Comte, T. Brousse, and F. Favier, "MnO_2 as ink material for the fabrication of supercapacitor electrodes," *Electrochimica Acta,* vol. 152, pp. 520-529, 2015.

[28] M. H. Wood, R. J. Welbourn, T. Charlton, A. Zarbakhsh, M. Casford, and S. M. Clarke, "Hexadecylamine Adsorption at the Iron Oxide–Oil Interface," *Langmuir,* vol. 29, pp. 13735-13742, 2013.

[29] R. Müller, M. Knapp, K. Heckmann, M. von Ruthendorf, and G. Boden, "Protecting nanoscaled non-oxidic particles from oxygen uptake by coating with nitrogen-containing surfactants," *Langmuir,* vol. 20, pp. 2598-2606, 2004.

[30] W. Chen, J. Peng, L. Mai, Q. Zhu, and Q. Xu, "Synthesis of vanadium oxide nanotubes from V_2O_5 sols," *Materials letters,* vol. 58, pp. 2275-2278, 2004.

[31] H.-H. Lee, Z. Ruzele, L. Malysheva, A. Onipko, A. Gutés, F. Björefors, *et al.*, "Long-chain alkylthiol assemblies containing buried in-plane stabilizing architectures," *Langmuir,* vol. 25, pp. 13959-13971, 2009.

[32] W. Dong, D. R. Rolison, and B. Dunna, "Electrochemical properties of high surface area vanadium oxide aerogels," *Electrochemical and Solid-State Letters,* vol. 3, pp. 457-459, 2000.

[33] W. Dong, J. S. Sakamoto, and B. Dunn, "Electrochemical properties of vanadium oxide aerogels," *Science and Technology of Advanced Materials,* vol. 4, p. 3, 2003.

[34] Y. Jeong and A. Manthiram, "Nanocrystalline manganese oxides for electrochemical capacitors with neutral electrolytes," *Journal of the Electrochemical Society,* vol. 149, pp. A1419-A1422, 2002.

[35] R. N. Reddy and R. G. Reddy, "Sol–gel MnO_2 as an electrode material for electrochemical capacitors," *Journal of Power Sources,* vol. 124, pp. 330-337, 2003.

[36] M. M. Sundaram, A. Biswal, D. Mitchell, R. Jones, and C. Fernandez, "Correlation among physical and electrochemical behaviour of nanostructured electrolytic manganese dioxide from leach liquor and synthetic for aqueous asymmetric capacitor," *Physical Chemistry Chemical Physics,* vol. 18, pp. 4711-4720, 2016.

[37] Y. Wang, Y. Liu, and I. Zhitomirsky, "Surface modification of MnO_2 and carbon nanotubes using organic dyes for nanotechnology of electrochemical supercapacitors," *Journal of Materials Chemistry A,* vol. 1, pp. 12519-12526, 2013.

[38] K. Shi and I. Zhitomirsky, "Polypyrrole nanofiber–carbon nanotube electrodes for supercapacitors with high mass loading obtained using an organic dye as a co-dispersant," *Journal of Materials Chemistry A,* vol. 1, pp. 11614-11622, 2013.

[39] B. P. Lee, P. B. Messersmith, J. N. Israelachvili, and J. H. Waite, "Mussel-inspired adhesives and coatings," *Annual review of materials research,* vol. 41, pp. 99-132, 2011.

[40] H. Lee, S. M. Dellatore, W. M. Miller, and P. B. Messersmith, "Mussel-inspired surface chemistry for multifunctional coatings," *science,* vol. 318, pp. 426-430, 2007.

[41] H. Lee, B. P. Lee, and P. B. Messersmith, "A reversible wet/dry adhesive inspired by mussels and geckos," *Nature,* vol. 448, p. 338, 2007.

[42] M. Ata, Y. Liu, and I. Zhitomirsky, "A review of new methods of surface chemical modification, dispersion and electrophoretic deposition of metal oxide particles," *Rsc Advances,* vol. 4, pp. 22716-22732, 2014.

[43] I. A. Jankovic, Z. V. Saponjic, M. I. Comor, and J. M. Nedeljkovic, "Surface modification of colloidal TiO_2 nanoparticles with bidentate benzene derivatives," *The Journal of Physical Chemistry C,* vol. 113, pp. 12645-12652, 2009.

[44] A. Kumar, P. Mukherjee, A. Guha, S. Adyantaya, A. Mandale, R. Kumar, *et al.*, "Amphoterization of colloidal gold particles by capping with valine molecules and their phase transfer from water to toluene by electrostatic coordination with fatty amine molecules," *Langmuir,* vol. 16, pp. 9775-9783, 2000.

6 Effect of extractors and active mass loading on the electrochemical performance of electrochemical capacitors

This chapter is reproduced from *MnO_2-carbon nanotube electrodes for supercapacitors with high active mass loadings, 164(9), A1673-A167, 2017, Journal of Electrochemical Society, **Ri Chen**, Ryan Poon, Rakesh P. Sahu, Ishwar K. Puri and Igor Zhitomirsky, doi: 10.1149/2.1491707jes, Copyright 2019, with permission from ECS -- The Electrochemical Society*. The author of this thesis is the first author and the main contributor of this publication.

6.1 Abstract

MnO_2-carbon nanotube electrodes with high active mass loadings for supercapacitors have been fabricated with the goal of achieving a high area normalized capacitance, low impedance and enhanced capacitance retention at high charge-discharge rates. Interface synthesis and liquid-liquid extraction of MnO_2 particles produced non-agglomerated MnO_2 particles which allowed the fabrication of electrodes with good dispersion of carbon nanotubes in the MnO_2 matrix. This strategy was used to fabricate electrodes with active mass loadings in the range of 21–50 mg cm^{-2} and mass ratios of active material to the nickel foam current collector of 0.33–0.78. The comparison of the experimental data for different extractor molecules provided an insight into the influence of the molecular structure, adsorption mechanism and interface phenomena on particle size and electrode performance. The analysis of capacitance data at different charge-discharge rates and different mass

loadings was utilized to optimize electrode performance. The highest capacitance of 7.52 F cm^{-2} was achieved at a scan rate of 2 mV s^{-1} and active mass loading of 47 mg cm^{-2}. Electrodes with mass loading of 35 mg cm^{-2} showed improved capacitance retention at high scan rates and the highest capacitance of 2.63 F cm^{-2} at a scan rate of 100 mV s^{-1}.

6.2 Introduction

Electrochemical supercapacitors[1-5] are being developed for novel applications in electric and hybrid vehicles, buses, aircrafts and various electronic devices. The success of the supercapacitor technology will depend largely on the ability to utilize high specific capacitance of advanced charge storage materials in the electrodes with high active mass loadings[6, 7]. MnO_2 is one of the most promising materials for charge storage[8-13] due to its high theoretical specific capacitance of 1400 F g^{-1} in a relatively large voltage window. However, due to the low electronic conductivity of MnO_2 and poor electrolyte access to the material surface, the specific capacitance decreased drastically[14] with increasing active mass loading, particularly at high charge-discharge rates. The investigation of charge-discharge behavior by the cavity microelectrode technique highlighted the importance of electrode porosity and conductive additives for the manufacturing of efficient electrodes with enhanced performance at high cycling rates[15]. Hence, MnO_2 is usually mixed with conductive additives in order to increase the electronic conductivity[14]. The gravimetric capacitance of composite MnO_2-carbon nanotube electrodes[16-19] with mass loading in the range of 0.2–4.2 mg cm^{-2} was typically 150–200 F g^{-1}. The important task is to achieve good electrochemical performance at a high ratio of the active material mass to the current collector mass (M_r). Metallic current collectors offer the benefits of high conductivity and low contact resistance[20]. However, the typical M_r values for 1 mg cm^{-2} films of active materials, deposited on metal foil current collectors lie below 0.01–0.02. Significantly higher active mass loadings and M_r values are required for practical applications[7]. The area normalized capacitance is another important parameter for the characterization of capacitor electrodes with high active mass loadings[7]. A high area normalized capacitance must be achieved with low electrical resistance of the electrodes.

The development of advanced microstructures that provide good electrolyte access to the active material is a promising basis for the fabrication of efficient electrodes with high active mass loading. Previous investigations[21-24] have shown that the specific capacitance does not correlate with the BET surface area, since some very small pores are inaccessible by the electrolyte. However, small particle sizes, low agglomeration and good mixing of active materials with conductive additives are of critical importance for fabricating advanced electrodes with high active mass loadings, high capacitance, good capacitance retention at high charge-discharge rates and low impedance.

MnO_2 particles are typically prepared by precipitation from aqueous solutions. The synthesized particles are dried and then re-dispersed in an organic solvent, containing conductive additives and dissolved organic binder, which is insoluble in water. However, MnO_2 particles agglomerate during drying. The reduction of surface energy and condensation of surface OH groups are major driving forces of particle agglomeration. This problem can be addressed by the particle extraction from an aqueous phase directly into an organic phase, thus avoiding the drying stage and related particle agglomeration. This strategy can potentially result in improved mixing of MnO_2 with conductive additives.

Particle extraction through liquid-liquid interface (PELLI) is emerging as a method of technological and scientific interest. The selection of extractor molecules that can be strongly adsorbed on the particle surface is of critical importance for the development of PELLI methods. Previous investigations have successfully extracted metals[25, 26] and quantum dots[27]. Various interactions between the inorganic particles and extractor molecules were utilized for the extraction, such as electrostatic[25], covalent[28, 29] and ion-pair interactions[26]. The extraction efficiency was enhanced in the presence of co-solvents[27, 30]. Extraction can also be triggered by the temperature changes[31], where a temperature increase reduces the solubility of the polymer extractor in an aqueous phase and promotes the particle transfer to an organic phase.

Previous PELLI research has been mainly focused on the extraction of metals and quantum dots from dilute suspensions. The selection of new extractor molecules with strong adsorption on oxide particle surfaces is a promising strategy for the further development of PELLI and its application to supercapacitor technology.

In a previous investigation[32], 1-hexadecylamine was used as an extractor for MnO_2 and TiO_2 particles. It was found that extraction of MnO_2 can be performed by bottom-up or top-down methods, using different organic solvents as receiving liquids. The bottom-up method allowed for smaller particle size and higher capacitance of the MnO_2 based electrodes. However, 1-hexadecylamine did not allow for extraction of TiO_2. Therefore, TiO_2 particles were modified with 2,3,4-trihydroxybenzaldehyde, which provided strong catecholate-type bonding to Ti atoms on the particle surface. The Schiff base reaction of 2,3,4-trihydroxybenzaldehyde, adsorbed on the TiO_2 surface, with 1-hexadecylamine at the liquid-liquid interface allowed for particle extraction. These studies highlighted the importance of the investigation of new extractor molecules with different sizes and different bonding mechanisms.

The goal of this investigation was to fabricate MnO_2-multiwalled carbon nanotube (MWCNT) electrodes for supercapacitors using advanced PELLI strategies and analyze the influence of extractor molecules on the morphology and performance of the resulting composite electrodes. We investigated decylphosphonic acid (DPA) and tetradecylamine (TDA) as new extractors for MnO_2. Testing results provided an insight into the influence of the functional groups of the extractor molecules on the extraction mechanism and capacitive performance. The use of TDA as an extractor allowed for significant increase in capacitance and capacitance retention at high scan rates, compared to DPA and 1-hexadecylamine at similar active mass loadings. The use of TDA allowed the fabrication of electrodes with high active mass loading in the range of 21–50 mg cm^{-2} and mass ratios of active material to the nickel foam current collector of 0.33–0.78. Another important finding was the possibility of variation of particle sizes of the extracted MnO_2 by variation of the ratio of the extractor mass to the mass of $NaMnO_4$ precursor. We provided detailed analysis of the influence of active mass loading on the capacitive behavior at different scan rates. It was found that electrolyte diffusion limitations in thick MnO_2-MWCNT electrodes can result in reduction of area normalized capacitance with increasing active mass, especially at high charge-discharge rates. The results indicate that the use of TDA as a new extractor for the PELLI method allowed the fabrication of electrodes with high area normalized capacitance, relatively high ratio of active mass to current collector mass, low impedance and good capacitance retention at high charge-discharge rates.

6.3 Experimental procedures

Decylphosphonic acid (DPA), tetradecylamine (TDA), $NaMnO_4$, n-butanol, poly(vinyl butyral-co-vinyl alcohol-co-vinyl acetate) (PVB, average Mw = 50,000-80,000), Na_2SO_4 (Aldrich), multiwalled carbon nanotubes (MWCNT, ID 4 nm, OD 13 nm, length 1–2 μm, Bayer, Germany) were used. Ni foams with 95% porosity were provided by Vale Limited. In this work, n-butanol was used as a reducing agent for Mn^{7+} in the MnO_2 synthesis and a water immiscible solvent in the extraction procedure.

Aqueous solutions, containing 200 mg of $NaMnO_4$ in 40 ml of water (concentration C_m = 5 g L^{-1}) were prepared. After addition of 10 ml of n-butanol and stirring, the precipitation of MnO_2 in the aqueous phase was observed (Figure 6.1Aa, 1Ba, 1Ca). In this procedure, the reduction of Mn^{7+} was achieved at the liquid-liquid interface.

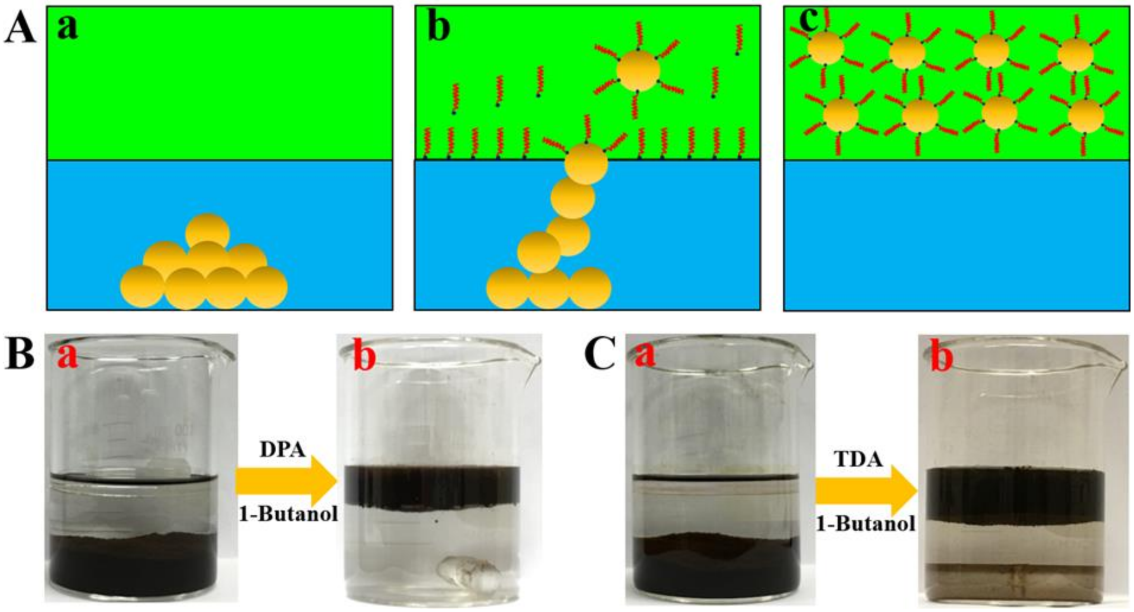

Figure 6.1 (A) Schematic of (a) precipitation and (b,c) different steps in extraction, (B) MnO_2 suspensions (a) before and (b) after extraction using DPA and (C) MnO_2 suspensions (a) before and (b) after extraction using TDA for C_m = 5 g L^{-1} and Rep = 0.25.

50 mg of TDA or DPA were dissolved in 10 ml of n-butanol and added to the two-phase mixture, containing precipitated MnO_2 as a bottom phase below a top n-butanol phase. After stirring, the extraction of MnO_2 into the n-butanol phase was observed (Figure 6.1Ab,c, 1Bb, 1Cb). In order to investigate the influence of C_m on particle size of synthesized MnO_2, C_m was varied in the range of 0.5–5 g L^{-1} and the corresponding ratio (Rep) of the extractor mass to the mass of $NaMnO_4$ precursor was 0.25–2.5.

The material, shown in Figure 6.1Ba was filtrated, washed with water and dried. The obtained powder was used for the X-ray diffraction and electron microscopy analysis of unmodified MnO_2.

The MnO_2 materials for the electrochemical testing experiments were prepared from solutions with $C_m = 5$ g L^{-1}, and Rep = 0.25. For the fabrication of supercapacitor electrodes, the suspensions of extracted MnO_2 in n-butanol were separated from the aqueous phase and then MWCNT were added. After ultrasonication of the mixed suspensions, the PVB binder solution in ethanol was added. The mass ratio of MnO_2:MWCNT:PVB was 80:20:3. The resulting suspensions were used to fabricate MnO_2-MWCNT supercapacitor electrodes by impregnating the Ni foam current collectors. The impregnated Ni foams were pressed in order to achieve thickness of 0.34 mm. The active mass loadings of the electrodes after drying and corresponding M_r factors were in the ranges of 21–50 mg cm^{-2} and 0.33–0.78, respectively.

Electron microscopy investigations were performed using a JEOL JSM-7000F scanning electron microscope (SEM). X-ray diffraction (XRD) studies were performed using a powder diffractometer (Nicolet I2, monochromatized CuKα radiation). FTIR studies were performed on Bruker Vertex 70 spectrometer. Dynamic light scattering (DLS, DelsaMax Pro: Beckman Coulter) was used for the particle size distribution analysis.

Cyclic voltammetry and impedance spectroscopy investigations were performed using a potentiostat (PARSTAT 2273, Princeton Applied Research, USA). The capacitive behavior of the electrodes was studied in three-electrode cells using 0.5 M Na_2SO_4 aqueous solutions. The area of the working electrode was 1 cm^2, both sides of the electrode were in contact with the electrolyte. The counter electrode was a platinum gauze, and the reference electrode was a standard calomel electrode (SCE). Cyclic voltammetry (CV) studies were performed at scan rates of 2–100 mV s^{-1}. The integral capacitances $C_S = Q/\Delta VS$ and $C_m =$

$Q/\Delta V_m$ were calculated using half the integrated area of the CV curve to obtain the charge Q, and subsequently dividing the charge Q by the width of the potential window ΔV and electrode area S or active mass m. Alternating current measurements of complex impedance $Z^* = Z' - iZ''$ were performed in the frequency range of 10 mHz - 100 kHz at the amplitude of the signal of 5 mV. The complex differential capacitance $C_S^* = C_S' - iC_S''$ was calculated[33] from the impedance data as $C_S' = Z''/\omega|Z|^2S$ and $C_S'' = Z'/\omega|Z|^2S$, where $\omega = 2\pi f$ (f-frequency).

6.4 Results and discussion

In this investigation, n-butanol was used as a reducing agent for the synthesis of MnO_2 from the $NaMnO_4$ solutions. The XRD pattern of as-precipitated MnO_2 showed relatively small peaks of the birnessite phase (Figure 6.2). However, the precipitated material also contained an amorphous phase. The XRD analysis indicated the formation of preferentially a not well crystallized powder. Similar XRD test results were reported for the MnO_2 powders, prepared using other alcohols as reducing agents for $KMnO_4$ solutions[34, 35]. Precipitation of MnO_2 by other methods[36] is also known to result in poorly crystallized MnO_2 materials. The SEM studies of the MnO_2 powder showed the formation of agglomerates with a typical size in the range of 1–3 microns (Figure 6.3A), but larger agglomerates were also observed (Figure 6.3B). The agglomerates contained submicrometer primary particles. The formation of such agglomerates is detrimental for the fabrication of supercapacitor electrodes, due to poor electrolyte access to the active MnO_2 material. Moreover, MnO_2 agglomeration generates problems with the formation of conductive composites with good dispersion of MWCNT in the MnO_2 matrix. Therefore, PELLI methods were investigated to reduce particle agglomeration.

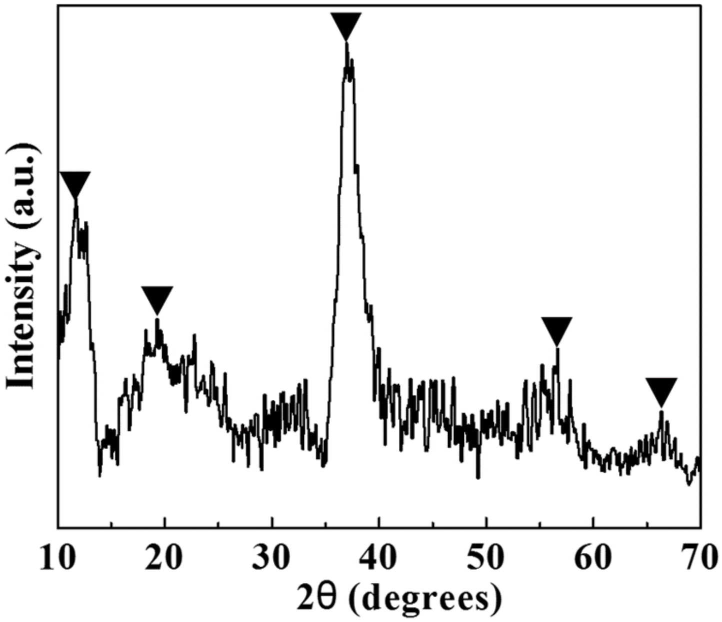

Figure 6.2 X-ray diffraction pattern of precipitated MnO_2 (▼- JCPDS file 87-1497).

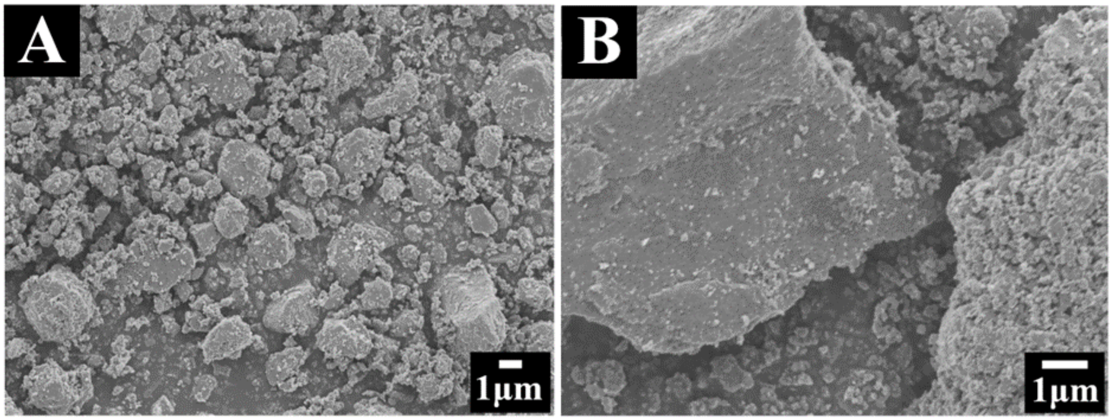

Figure 6.3 (A,B) SEM images of MnO_2 powder.

The PELLI strategies used in this investigation were based on the application of DPA and TDA molecules as extractors. Both molecules are insoluble in water, but are soluble in n-butanol. Figure 6.4 shows the chemical structures of the molecules and their adsorption mechanisms. DPA and TDA are typical head-tail surfactants, containing hydrophobic hydrocarbon tails. The hydrophilic properties of DPA and TDA are related to their PO_3H_2 and NH_2 groups, respectively. The PO_3H_2 groups of DPA can be adsorbed on oxide particles by bridging (Figure 6.4Ba,b) or chelation (Figure 6.4Bc,d) mechanisms[37]. TDA can be adsorbed on particle surfaces through different mechanisms, such as chemisorption[38] (Figure 6.4Da) or an electrostatic interaction[39] (Figure 6.4Db), involving surface OH groups.

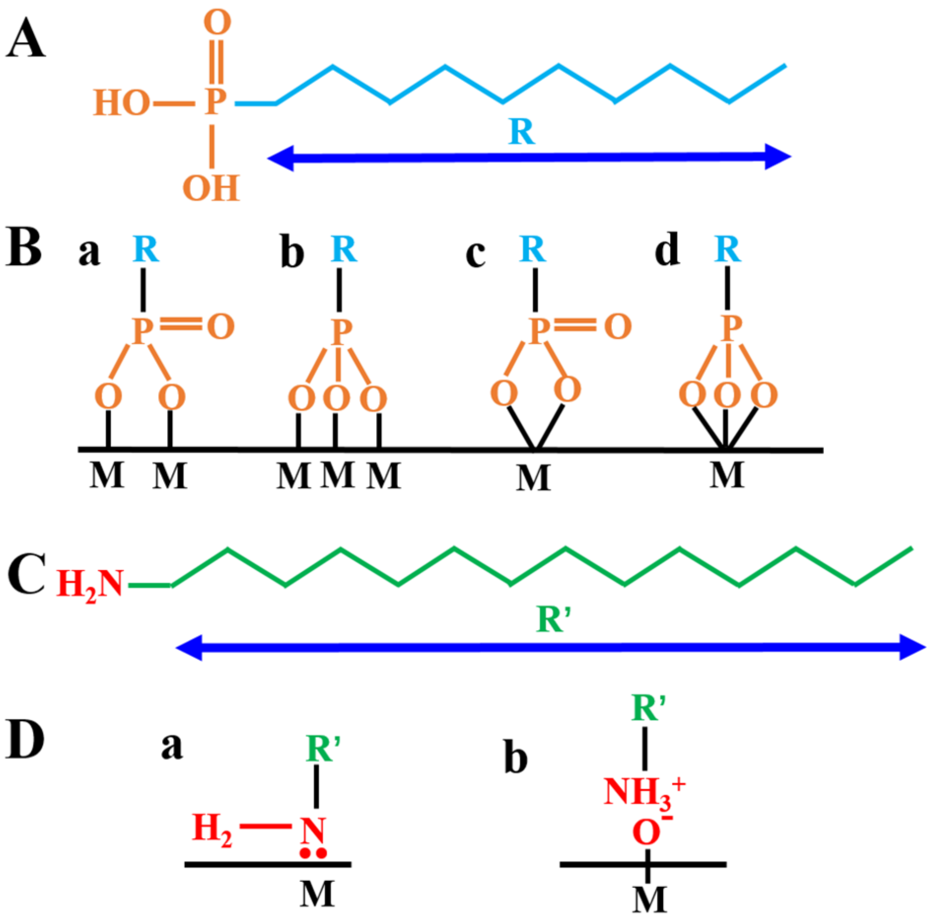

Figure 6.4 (A) Chemical structure of DPA, (B) DPA adsorption on particle surface: (a,b) bridging, (c,d) chelation of metal atoms (M) on the particle surface, (C) chemical structure of TDA, (D) TDA adsorption mechanisms: (a) chemisorption and (b) electrostatic interaction, involving a surface OH group.

It was found that, using DPA and TDA molecules as extractors, the precipitated MnO_2 particles can be transferred from water into the n-butanol phase. The extracted MnO_2 particles were studied by the FTIR method. Figure 6.5 compares FTIR spectra of as-received DPA and TDA with the spectra of extracted MnO_2 particles. The absorption peaks at 2849, 2918 and 2957 cm^{-1} in the spectrum of DPA (Figure 6.5a) and at 2849, 2916 and 2955 cm^{-1} in the spectrum of TDA (Figure 6.5c) resulted from the CH_2 symmetric stretching, CH_2 asymmetric stretching and CH_3 out-of-plane stretching[40, 41], respectively. Similar absorption peaks were observed in the spectra of MnO_2 particles, extracted using DPA (Figure 6.5b) and TDA (Figure 6.5d). Therefore, the results of the FTIR studies confirmed the adsorption of the extractor molecules on the particles.

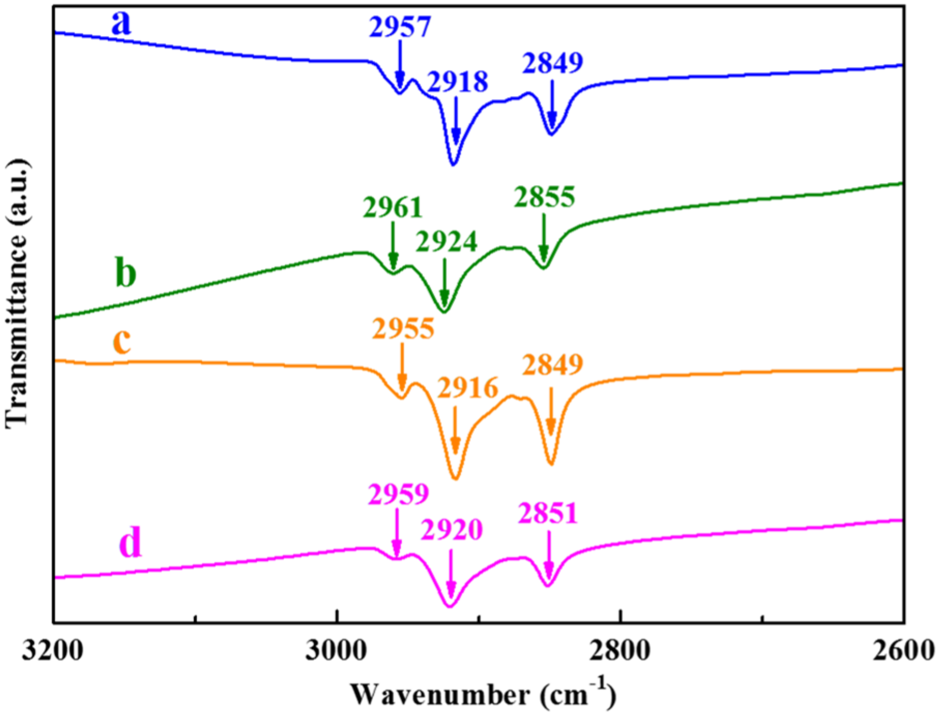

Figure 6.5 FTIR spectrum of (a) DPA, (b) MnO_2, extracted using DPA, (c) TDA and (d) MnO_2, extracted using TDA.

Figure 6.6 shows particle size distribution of the extracted particles for Rep = 0.25. The size of the particles was significantly smaller than the size of agglomerates, shown in Figure 6.3. Examination of the data shown in Figure 6.6A, 6B indicated that the use of TDA allowed smaller particle sizes. The material extracted using TDA primarily contained particles with radii below 60 nm, whereas the material, extracted using DPA mainly contained particles with the radii in the range of 60–80 nm. The sizes of the extracted MnO_2 particles were larger than the sizes of metallic particles, prepared previously through aqueous synthesis and PELLI[25, 29, 42]. However, the concentrations of the precursors used in the literature[25, 29, 42] were significantly lower than the $NaMnO_4$ concentration in our experiments. The relatively high concentration of $NaMnO_4$ in the solutions allowed for high concentration of synthesized particles in suspensions, which was beneficial for the impregnation of the Ni foam current collectors and fabrication of supercapacitor electrodes with high active mass loadings. However, the method used in this investigation can also be potentially used for the fabrication of smaller particles. Decreasing the $NaMnO_4$ concentration in the solutions from 5 to 0.5 g L^{-1} and a corresponding increase of Rep from 0.25 to 2.5 resulted in significantly smaller sizes of the extracted MnO_2 particles.

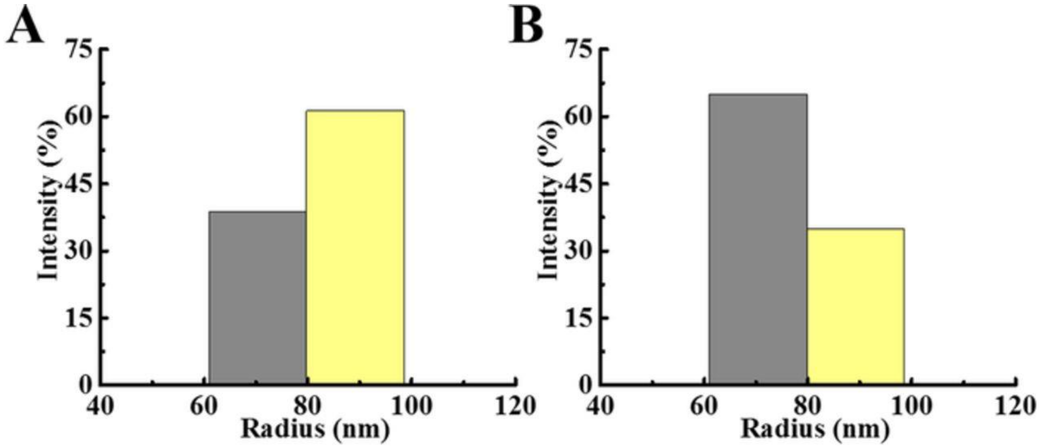

Figure 6.6 Particle size distribution for MnO_2 particles, extracted using (A) DPA and (B) TDA for $C_m = 5$ g L^{-1} and Rep = 0.25.

Figure 6.7 shows the particle size distribution for MnO_2 prepared from 0.5–3.75 g L^{-1} $NaMnO_4$ solutions and extracted into the n-butanol phase using TDA. The analysis of the data indicated that particles size decreased with decreasing concentration of $NaMnO_4$. The radii of MnO_2, prepared from 0.5 g L^{-1} $NaMnO_4$ solutions (Rep = 2.5) were in the range of 40–60 nm. It is important to note that in our experiments the DPA and TDA molecules were added after MnO_2 synthesis. Small particles of other materials are usually prepared using organic capping agents[42, 43], which limit particle growth during synthesis. However, many organic molecules cannot be used as capping agents for MnO_2 synthesis from $NaMnO_4$ solutions, because $NaMnO_4$ is a strong oxidant that reacts with organic materials.

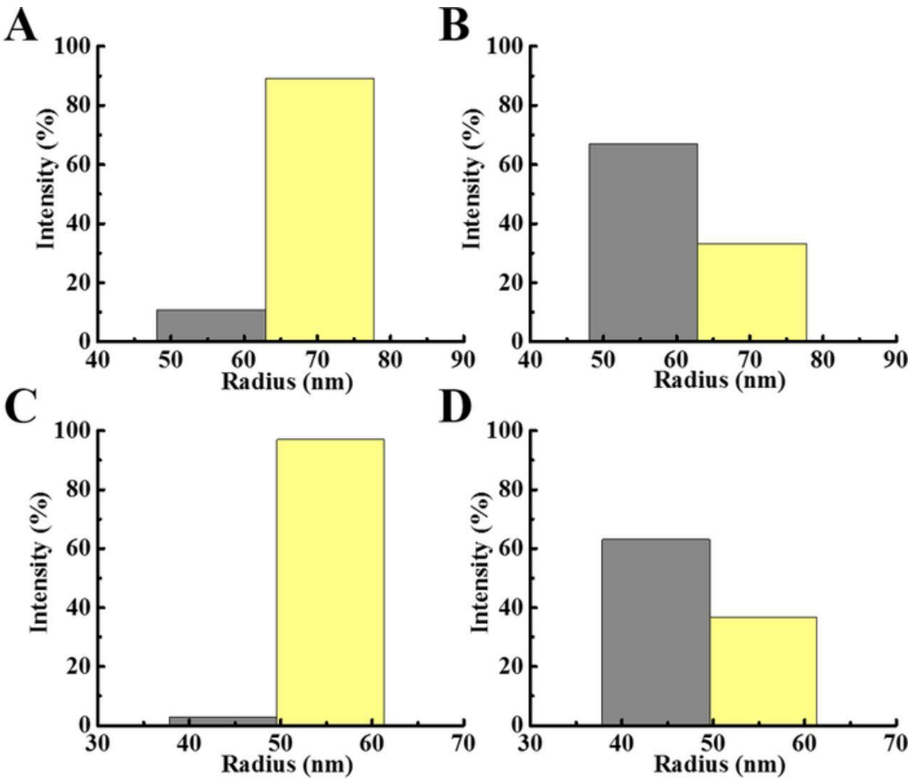

Figure 6.7 Particle size distribution for MnO_2 particles, extracted using TDA for different Rep: (A) 0.33, (B) 0.5, (C) 1.0 and (D) 2.5.

The PELLI methods, developed in this investigation were beneficial for reducing agglomeration of MnO_2 and improving the mixing of MnO_2 with MWCNT. The as–received MWCNT contained large agglomerates with typical sizes of 0.5–1 mm. However, the SEM investigation (Figure 6.8) of the MnO_2-MWCNT composites impregnated into the Ni foam current collector showed well dispersed MWCNT in the MnO_2 matrix. This was achieved by avoiding MnO_2 agglomeration in the PELLI method, and through co-dispersion and mixing of MnO_2 and MWCNT in the organic phase. The reduced agglomeration and improved mixing of these individual components allowed good electrochemical performance of electrodes at high active mass loadings.

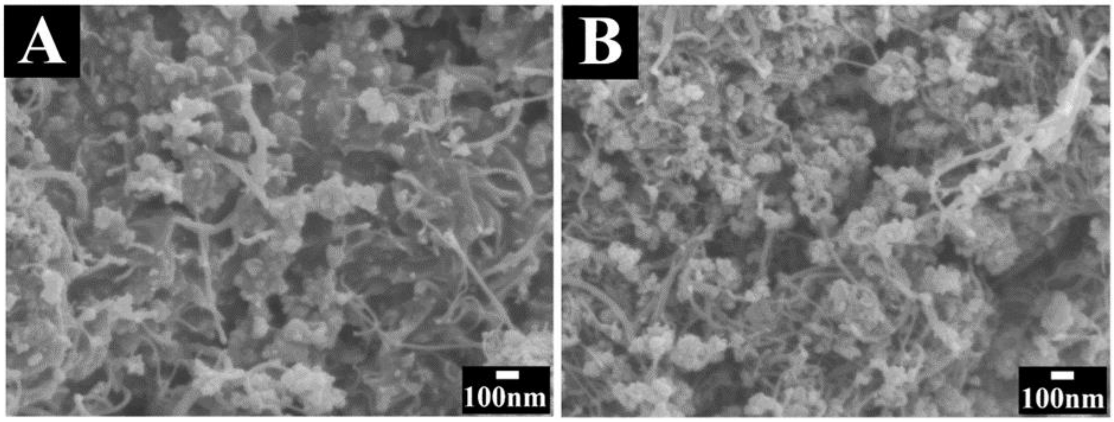

Figure 6.8 SEM images of the MnO_2-MWCNT composites, prepared by the extraction methods using (A) DPA and (B) TDA for $C_m = 5$ g L^{-1} and Rep = 0.25.

Figure 6.9A, 9B shows CVs for the electrodes with a mass loading of 35 mg cm^{-2}. The nearly box shapes of the CVs indicated good capacitive behavior. The area normalized capacitance of the electrodes, prepared using DPA and TDA was 5.81 F cm^{-2} at a scan rate of 2 mV s^{-1}. The capacitance decreased with increasing scan rate. The capacitance retention at 100 mV s^{-1} was 27 and 45%, for the electrodes, prepared using DPA and TDA, respectively. Electrodes prepared using TDA showed a remarkably high capacitance of 2.63 F cm^{-2} at a scan rate of 100 mV s^{-1}.

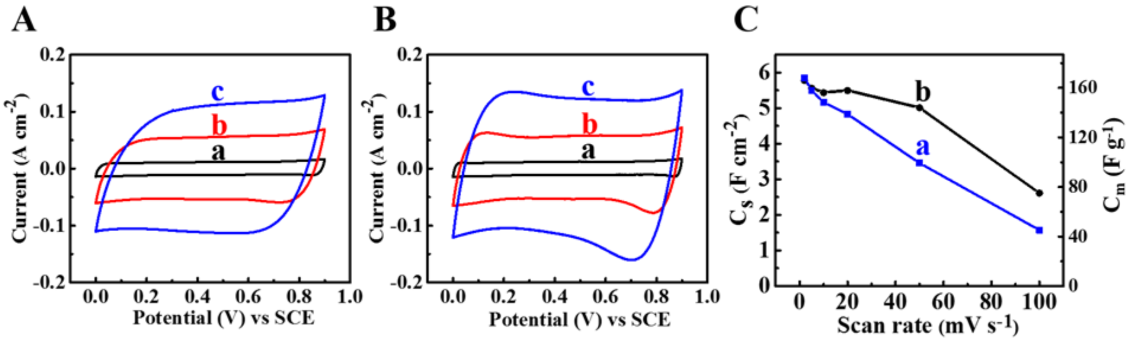

Figure 6.9 (A,B) CVs for MnO_2-MWCNT electrodes with active mass loading of 35 mg cm^{-2}, prepared using (A) DPA and (B) TDA at scan rates of (a) 2, (b) 10 and (c) 20 mV s^{-1}, (C) C_S and C_m for MnO_2-MWCNT electrodes, prepared using (a) DPA and (b) TDA.

Figure 6.10A shows the electrochemical impedance data, presented in the Nyquist plot. The electrodes, showed relatively low resistance R = Z′, which was below 0.5 Ohm. The slope of the curves was close to 90°, indicating good capacitive behavior. The low resistance, achieved at high active mass loadings indicated good utilization of conductive properties of MWCNT due to the reduced agglomeration and good mixing of MnO_2 and MWCNT. The frequency dependence of the components of the complex capacitance (Figure 6.10B,10C) showed a relaxation type dispersion[44]. The real components of the complex capacitance decreased with frequency and the corresponding imaginary components showed maxima. The relaxation frequencies, corresponding to the maxima of the imaginary components were found to be 50 and 79 mHz for electrodes, prepared using DPA and TDA, respectively. The test results presented in Figure 6.9 and Figure 6.10 showed that electrodes, prepared using TDA performed better as compared to those, prepared using DPA. The electrodes, fabricated with TDA showed improved capacitance retention at high scan rates, higher relaxation frequency and lower resistance. This difference likely resulted from the smaller size of the MnO_2 particles, prepared using TDA. It was suggested that larger size of the TDA molecules or stronger interaction of NH_2 groups of TDA with MnO_2 allowed for reduced particle agglomeration and improved electrode performance. Therefore, further investigations were focused on the application of TDA for the fabrication of electrodes with higher active mass loadings.

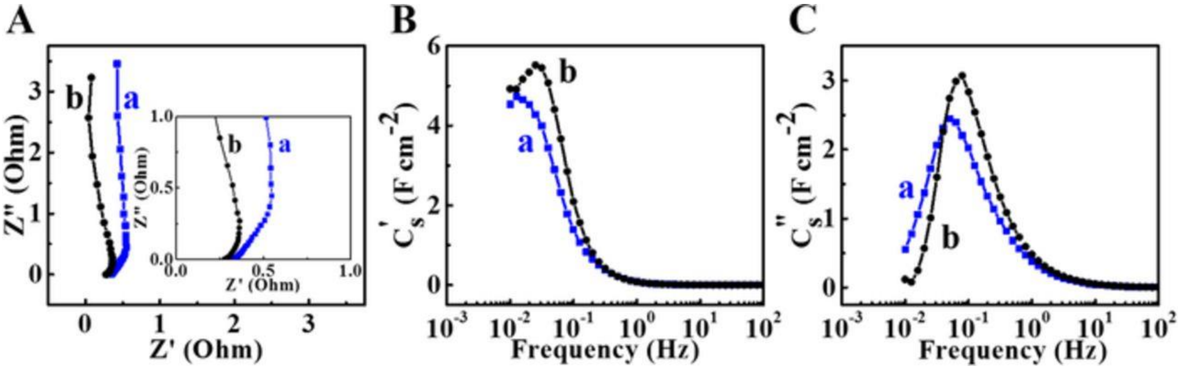

Figure 6.10 (A)Nyquist plot of complex impedance, inset shows a high frequency range, (B) C_S' versus frequency and (C) C_S'' versus frequency for MnO_2-MWCNT electrodes with active mass loading of 35 mg cm^{-2}, prepared using (a) DPA and (b) TDA.

Figure 6.11A shows CVs for the electrodes with active mass loading of 47 mg cm^{-2}. Nearly box shapes of CV were observed at such high active mass loading. A capacitance of 7.52 F cm^{-2} was achieved at a scan rate of 2 mV s^{-1}. However, the capacitance retention (Figure 6.11B) at 100 mV s^{-1} was only 17%. It is important to note that the increase in active mass loading from 35 to 47 mg cm^{-2} allowed for significant increase in capacitance at 2 mV s^{-1}. However, the increase in the active mass loading resulted in the lower capacitance at 100 mV s^{-1}, which was found to be 1.3 F cm^{-2}.

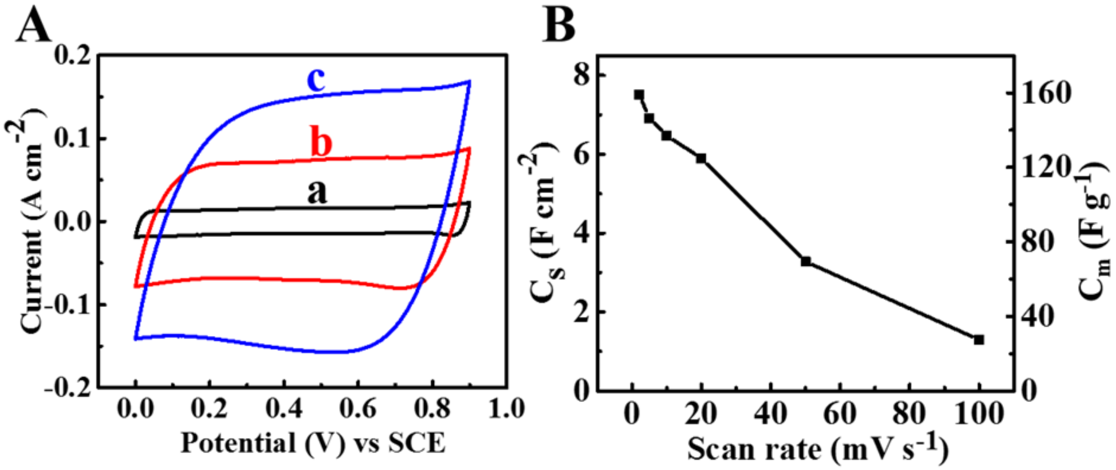

Figure 6.11 (A) CVs at scan rates of (a) 2, (b) 10 and (c) 20 mV s^{-1} and (B) capacitance versus scan rate for MnO_2-MWCNT electrodes with active mass loading of 47 mg cm^{-2}, prepared using TDA.

Figure 6.12A shows impedance data for the 47 mg cm^{-2} electrode, presented in the Nyquist plot. The electrode showed relatively low resistance, the slope of the curve was close to 90°, thus indicating good capacitive behavior. The real and imaginary components of complex capacitance showed a relaxation type dispersion (Figure 6.12B,12C). The relaxation frequency was found to be 40 mHz. The comparison with the data for the 35 mg cm^{-2} electrode indicated that the increase in electrode mass resulted in decreasing relaxation frequency.

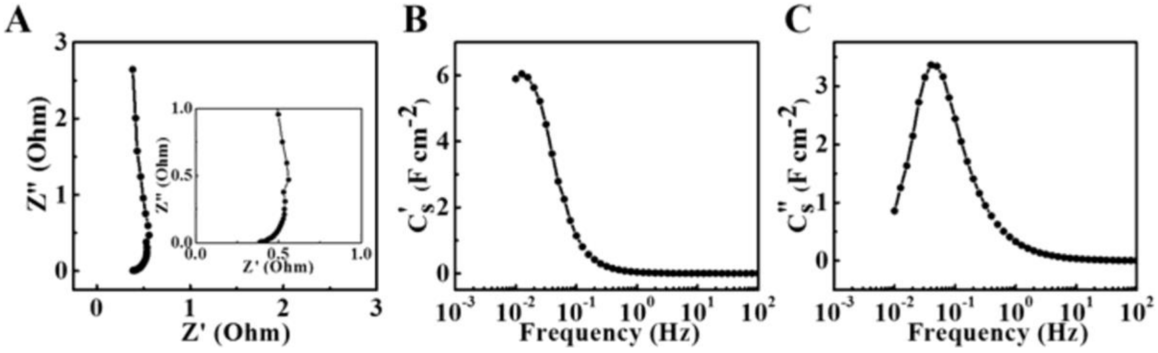

Figure 6.12 (A) Nyquist plot of complex impedance, inset shows a high frequency range, (B) C_S' versus frequency and (C) C_S'' versus frequency for MnO_2-MWCNT electrodes with active mass loading of 47 mg cm^{-2}, prepared using TDA.

The experimental data presented in Figure 6.13 provided additional information on the influence of active mass loading on the electrochemical capacitance of the electrodes. The data was presented for mass loadings in the range of 21–50 mg cm^{-2} (M_r in the range of 0.33–0.78). The area normalized capacitance, calculated from the CV data at 2 and 5 mV s^{-1} increased with increasing active mass loadings from 21 to 47 mg cm^{-2} and slightly decreased at higher active mass loadings. The capacitances, measured at 50 and 100 mV s^{-1} showed maxima at a mass loading of 35 mg cm^{-2}. It was suggested that the diffusion limitations of electrolytes in pores at high charge-discharge rates resulted in poor electrolyte access to the bulk of the active material. In this case the bulk material behaved as a capacitor with low capacitance that was connected in series with a highly capacitive surface layer, and reduced the total capacitance of the electrode material. Testing results indicated that the active mass loading for electrodes, prepared by the PELLI method, can be optimized at 35 mg cm^{-2} (M_r = 0.55) in order to achieve good performance at high charge-discharge rates. However, the highest capacitance of 7.52 F cm^{-2} can be achieved at a scan rate of 2 mV s^{-1} and active mass loading of 47 mg cm^{-2} (M_r = 0.74).

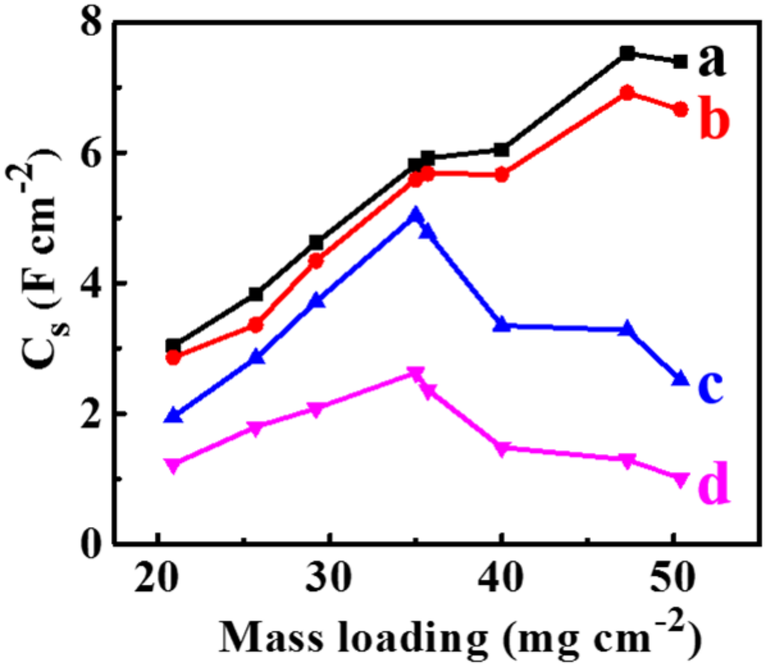

Figure 6.13 Capacitance versus active mass loading for MnO_2-MWCNT electrodes at scan rates of (a) 2, (b) 5, (c) 50 and (d) 100 mV s^{-1}.

6.5 Conclusions

The results of this investigation indicated that DPA and TDA can be used as extractors for MnO_2 particles. The PELLI method facilitated the fabrication of MnO_2-MWCNT composites with reduced agglomeration and improved mixing of the individual components. The use of TDA allowed for smaller MnO_2 particle sizes and improved electrode performance. The enhanced mixing of the individual components of the composite materials facilitated the formation of electrodes with high capacitance and low impedance at high active mass loadings in the range of 21–50 mg cm^{-2} and M_r of 0.33–0.78. The capacitance increased with increasing mass loading in the range of 21–35 mg cm^{-2} at scan rates of 2–100 mV s^{-1}. At higher mass loadings the capacitance behavior was strongly influenced by scan rate due to diffusion limitations of the electrolyte in the electrode material. The highest capacitance of 7.52 F cm^{-2} was achieved at a scan rate of 2 mV s^{-1} and active mass loading of 47 mg cm^{-2}. Electrodes with mass loading of 35 mg cm^{-2} showed improved capacitance retention at high scan rates and the highest capacitance of 2.63 F cm^{-2} at a scan rate of 100 mV s^{-1}.

6.6 References

[1] A. Balducci, "Electrolytes for high voltage electrochemical double layer capacitors: A perspective article," *Journal of Power Sources,* vol. 326, pp. 534-540, 2016.

[2] L. Demarconnay, E. Raymundo-Pinero, and F. Béguin, "Adjustment of electrodes potential window in an asymmetric carbon/MnO_2 supercapacitor," *Journal of Power Sources,* vol. 196, pp. 580-586, 2011.

[3] H.-S. Kim, J. B. Cook, S. H. Tolbert, and B. Dunn, "The development of pseudocapacitive properties in nanosized-MoO_2," *Journal of The Electrochemical Society,* vol. 162, pp. A5083-A5090, 2015.

[4] N. Goubard-Bretesché, O. Crosnier, G. Buvat, F. Favier, and T. Brousse, "Electrochemical study of aqueous asymmetric $FeWO_4$/MnO_2 supercapacitor," *Journal of Power Sources,* vol. 326, pp. 695-701, 2016.

[5] M. B. Sassin, S. G. Greenbaum, P. E. Stallworth, A. N. Mansour, B. P. Hahn, K. A. Pettigrew, *et al.*, "Achieving electrochemical capacitor functionality from nanoscale $LiMn_2O_4$ coatings on 3-D carbon nanoarchitectures," *Journal of Materials Chemistry A,* vol. 1, pp. 2431-2440, 2013.

[6] V. Augustyn, P. Simon, and B. Dunn, "Pseudocapacitive oxide materials for high-rate electrochemical energy storage," *Energy & Environmental Science,* vol. 7, pp. 1597-1614, 2014.

[7] Y. Gogotsi and P. Simon, "True performance metrics in electrochemical energy storage," *Science,* vol. 334, pp. 917-918, 2011.

[8] S. Devaraj and N. Munichandraiah, "High capacitance of electrodeposited MnO_2 by the effect of a surface-active agent," *Electrochemical and Solid-State Letters,* vol. 8, pp. A373-A377, 2005.

[9] T. Brousse, P.-L. Taberna, O. Crosnier, R. Dugas, P. Guillemet, Y. Scudeller*, et al.*, "Long-term cycling behavior of asymmetric activated carbon/MnO_2 aqueous electrochemical supercapacitor," *Journal of Power Sources,* vol. 173, pp. 633-641, 2007.

[10] F. Grote, R.-S. Kühnel, A. Balducci, and Y. Lei, "Template assisted fabrication of free-standing MnO_2 nanotube and nanowire arrays and their application in supercapacitors," *Applied Physics Letters,* vol. 104, p. 053904, 2014.

[11] V. Khomenko, E. Raymundo-Pinero, and F. Béguin, "Optimisation of an asymmetric manganese oxide/activated carbon capacitor working at 2 V in aqueous medium," *Journal of Power Sources,* vol. 153, pp. 183-190, 2006.

[12] E. Machefaux, T. Brousse, D. Bélanger, and D. Guyomard, "Supercapacitor behavior of new substituted manganese dioxides," *Journal of Power Sources,* vol. 165, pp. 651-655, 2007.

[13] C. A. Beasley, M. B. Sassin, and J. W. Long, "Extending electrochemical quartz crystal microbalance techniques to macroscale electrodes: Insights on pseudocapacitance mechanisms in MnO_x-coated carbon nanofoams," *Journal of The Electrochemical Society*, vol. 162, pp. A5060-A5064, 2015.

[14] Y. Wang, Y. Liu, and I. Zhitomirsky, "Surface modification of MnO_2 and carbon nanotubes using organic dyes for nanotechnology of electrochemical supercapacitors," *Journal of Materials Chemistry A*, vol. 1, pp. 12519-12526, 2013.

[15] L. Athouel, P. Arcidiacono, C. Ramirez-Castro, O. Crosnier, C. Hamel, Y. Dandeville, *et al.*, "Investigation of cavity microelectrode technique for electrochemical study with manganese dioxides," *Electrochimica Acta*, vol. 86, pp. 268-276, 2012.

[16] J. Li and I. Zhitomirsky, "Electrophoretic deposition of manganese dioxide–carbon nanotube composites," *Journal of Materials Processing Technology*, vol. 209, pp. 3452-3459, 2009.

[17] R. Jiang, T. Huang, Y. Tang, J. Liu, L. Xue, J. Zhuang, *et al.*, "Factors influencing MnO2/multi-walled carbon nanotubes composite's electrochemical performance as supercapacitor electrode," *Electrochimica acta*, vol. 54, pp. 7173-7179, 2009.

[18] H. Xia and C. Huo, "Electrochemical properties of MnO_2/CNT nanocomposite in neutral aqueous electrolyte as cathode material for asymmetric supercapacitors," *International Journal of Smart and Nano Materials*, vol. 2, pp. 283-291, 2011.

[19] M. S. Ata, P. Wojtal, and I. Zhitomirsky, "Electrophoretic deposition of materials using humic acid as a dispersant and film forming agent," *Colloids and Surfaces A: Physicochemical and Engineering Aspects,* vol. 493, pp. 74-82, 2016.

[20] Y. Lei, B. Daffos, P.-L. Taberna, P. Simon, and F. Favier, "MnO_2-coated Ni nanorods: Enhanced high rate behavior in pseudo-capacitive supercapacitor," *Electrochimica Acta,* vol. 55, pp. 7454-7459, 2010.

[21] W. Dong, J. S. Sakamoto, and B. Dunn, "Electrochemical properties of vanadium oxide aerogels," *Science and Technology of Advanced Materials,* vol. 4, p. 3, 2003.

[22] W. Dong, D. R. Rolison, and B. Dunn, "Electrochemical properties of high surface area vanadium oxide aerogels," *Electrochemical and Solid State Letters,* vol. 3, pp. 457-459, Oct 2000.

[23] Y. U. Jeong and A. Manthiram, "Nanocrystalline manganese oxides for electrochemical capacitors with neutral electrolytes," *Journal of the Electrochemical Society,* vol. 149, pp. A1419-A1422, Nov 2002.

[24] R. N. Reddy and R. G. Reddy, "Sol-gel MnO_2 as an electrode material for electrochemical capacitors," *Journal of Power Sources,* vol. 124, pp. 330-337, Oct 1 2003.

[25] W. L. Cheng and E. Wang, "Size-dependent phase transfer of gold nanoparticles from water into toluene by tetraoctylammonium cations: A wholly electrostatic interaction," *Journal of Physical Chemistry B,* vol. 108, pp. 24-26, Jan 8 2004.

[26] H. Yao, O. Momozawa, T. Hamatani, and K. Kimura, "Phase transfer of gold nanoparticles across a water/oil interface by stoichiometric ion-pair formation on

particle surfaces," *Bulletin of the Chemical Society of Japan,* vol. 73, pp. 2675-2678, Dec 2000.

[27] N. Gaponik, D. V. Talapin, A. L. Rogach, A. Eychmuller, and H. Weller, "Efficient phase transfer of luminescent thiol-capped nanocrystals: From water to nonpolar organic solvents," *Nano Letters,* vol. 2, pp. 803-806, Aug 2002.

[28] M. Karg, N. Schelero, C. Oppel, M. Gradzielski, T. Hellweg, and R. von Klitzing, "Versatile Phase Transfer of Gold Nanoparticles from Aqueous Media to Different Organic Media," *Chemistry-a European Journal*, vol. 17, pp. 4648-4654, Apr 2011.

[29] A. Kumar, H. Joshi, R. Pasricha, A. B. Mandale, and M. Sastry, "Phase transfer of silver nanoparticles from aqueous to organic solutions using fatty amine molecules," *Journal of Colloid and Interface Science,* vol. 264, pp. 396-401, Aug 15 2003.

[30] B. Hu, Y. Nakahiro, and T. Wakamatsu, "The Effect of Organic-Solvents on the Recovery of Fine Mineral Particles by Liquid-Liquid-Extraction," *Minerals Engineering,* vol. 6, pp. 731-742, Jul 1993.

[31] X. L. Feng, H. Y. Ma, S. X. Huang, W. Pan, X. K. Zhang, F. Tian*, et al.*, "Aqueous-organic phase-transfer of highly stable gold, silver, and platinum nanoparticles and new route for fabrication of gold nanofilms at the oil/water interface and on solid supports," *Journal of Physical Chemistry B,* vol. 110, pp. 12311-12317, Jun 29 2006.

[32] R. Chen, M. S. Ata, X. Y. Zhao, A. Clifford, I. Puri, and I. Zhitomirsky, "Strategies for liquid-liquid extraction of oxide particles for applications in supercapacitor

electrodes and thin films," *Journal of Colloid and Interface Science,* vol. 499, pp. 1-8, Aug 1 2017.

[33] P. L. Taberna, P. Simon, and J. F. Fauvarque, "Electrochemical characteristics and impedance spectroscopy studies of carbon-carbon supercapacitors," *Journal of the Electrochemical Society,* vol. 150, pp. A292-A300, Mar 2003.

[34] G. M. Jacob, Q. M. Yang, and I. Zhitomirsky, "Electrodes for electrochemical supercapacitors," *Materials and Manufacturing Processes,* vol. 24, pp. 1359-1364, 2009.

[35] J. Li, Q. M. Yang, and I. Zhitomirsky, "Composite Electrodes for Electrochemical Supercapacitors," *Nanoscale Research Letters,* vol. 5, pp. 512-517, Mar 2010.

[36] L. Coustan, A. Le Comte, T. Brousse, and F. Favier, "MnO_2 as ink material for the fabrication of supercapacitor electrodes," *Electrochimica Acta,* vol. 152, pp. 520-529, Jan 10 2015.

[37] M. S. Ata, S. Ghosh, and I. Zhitomirsky, "Electrostatic assembly of composite supercapacitor electrodes, triggered by charged dispersants," *Journal of Materials Chemistry A,* vol. 4, pp. 17857-17865, 2016.

[38] M. H. Wood, R. J. L. Welbourn, T. Charlton, A. Zarbakhsh, M. T. Casford, and S. M. Clarke, "Hexadecylamine Adsorption at the Iron Oxide-Oil Interface," *Langmuir,* vol. 29, pp. 13735-13742, Nov 12 2013.

[39] R. Muller, M. Knapp, K. Heckmann, M. von Ruthendorf, and G. Boden, "Protecting nanoscaled non-oxidic particles from oxygen uptake by coating with nitrogen-containing surfactants," *Langmuir,* vol. 20, pp. 2598-2606, Mar 30 2004.

[40] H. H. Lee, Z. Ruzele, L. Malysheva, A. Onipko, A. Gutes, F. Bjorefors, *et al.*, "Long-Chain Alkylthiol Assemblies Containing Buried In-Plane Stabilizing Architectures," *Langmuir,* vol. 25, pp. 13959-13971, Dec 15 2009.

[41] W. Chen, J. F. Peng, L. Q. Mai, Q. Y. Zhu, and Q. Xu, "Synthesis of vanadium oxide nanotubes fromV(2)O(5) sols," *Materials Letters,* vol. 58, pp. 2275-2278, Jul 2004.

[42] A. Kumar, P. Mukherjee, A. Guha, S. D. Adyantaya, A. B. Mandale, R. Kumar, *et al.*, "Amphoterization of colloidal gold particles by capping with valine molecules and their phase transfer from water to toluene by electrostatic coordination with fatty amine molecules," *Langmuir,* vol. 16, pp. 9775-9783, Dec 12 2000.

[43] K. S. Mayya and F. Caruso, "Phase transfer of surface-modified gold nanoparticles by hydrophobization with alkylamines," *Langmuir,* vol. 19, pp. 6987-6993, Aug 19 2003.

[44] K. Y. Shi and I. Zhitomirsky, "Polypyrrole nanofiber-carbon nanotube electrodes for supercapacitors with high mass loading obtained using an organic dye as a co-dispersant," *Journal of Materials Chemistry A,* vol. 1, pp. 11614-11622, 2013.

7 Multifunctional extractor for liquid-liquid extraction of oxide particles and applications in supercapacitors, electrophoretic deposition and screen printing

This chapter is reproduced from *Influence of molecular structure of extractor molecules on liquid-liquid extraction of oxide particles and properties of composites, 44, 15714-15720, 2018, Ceramics International,* ***Ri Chen****, Zhengzheng Wang, Rakesh P. Sahu, Ishwar K. Puri and Igor Zhitomirsky, https://doi.org/10.1016/j.ceramint.2018.05.244, Copyright 2019, with permission from Elsevier*. The author of this thesis is the first author and the main contributor of this publication.

7.1 Abstract

Interest in particle extraction through liquid-liquid interface (PELLI) technology is motivated by the need to transfer particles directly from the synthesis medium to the device processing medium. This method avoids the difficulty encountered by conventional re-dispersion methods where particles agglomerate during the drying stage. We develop PELLI strategies to transfer MnO_2, ZnO and CeO_2 particles that are synthesized in aqueous media into 1-butanol using extractors containing phosphonate and carboxylic groups. We demonstrate that, in addition to head-tail (HT) surfactants, molecules containing two hydrophilic end groups (HTH) can also be employed as extractors, a finding that opens new PELLI applications. We demonstrate this new approach using multifunctional HTH molecules as both PELLI extractors and charged dispersing agents for the electrophoretic

deposition (EPD) of particles that are transferred to an EPD processing medium. Using the HTH extractors for PELLI, we fabricate MnO_2-based bulk electrodes for electrochemical supercapacitors (ES) that exhibit superior electrochemical performance. These high active mass loading ES electrodes have a capacitance of $5.7\ F\ cm^{-2}$ ($157\ F\ g^{-1}$) and $2.5\ F\ cm^{-2}$ ($67\ F\ g^{-1}$) at 2 and $100\ mV\ s^{-1}$ scan rates, respectively, with low impedance. In another strategy, the use of HTH extractor for particle transfer to screen printing processing medium facilitates the fabrication of efficient thin film SC electrodes. Measurements provide insight into the influence of anchoring groups and extractor molecule structure on the extraction efficiency and electrochemical performance.

7.2 Introduction

While many important methods of inorganic particle synthesis are based on aqueous processing, non-aqueous solvents are necessary to produce moisture-stable films and coatings. Moreover, organic solvents are required to manufacture functional devices that can operate reliably in aqueous media, such as aqueous batteries and supercapacitors[1-4]. During device fabrication, the particles must be dispersed in organic solvents that contain water insoluble binders, film forming agents and other organic components. Therefore, particles that are synthesized in aqueous media are typically dried and then re-dispersed in organic solvents.

Particle extraction through liquid-liquid interface (PELLI)[5] has gained considerable attention recently because the technique allows direct particle transfer from a synthesis medium to a device processing medium, thus eliminating the particle drying process that often results in irreversible agglomeration of the inorganic particles. The agglomeration occurs because of surface condensation reactions and a reduction in particle surface energy. Particle agglomeration must be strictly avoided for many applications, such as energy storage devices, catalysis and printed electronics.

Progress has been made in applying PELLI, to extract metals[6-9] and quantum dots[10]. Organic molecules have been used as reducing agents to synthesize metal particles at the liquid-liquid interface and subsequently transfer the particles to an organic phase[11]. It is possible to extract metal oxides and hydroxide particles from an aqueous synthesis medium into an organic phase[11-15]. Bottom-up[5, 16] and top-down [5, 15] techniques have been developed. This work generated interest in the agglomerate-free processing of advanced ceramic materials. The extraction of titania, Mn_3O_4 and $Al(OH)_3$ particles based on a two-step procedure has involved particle modification during synthesis, and subsequent Schiff base reaction with an extractor at the liquid-liquid interface[12, 17]. Phase transfer can be facilitated in one-step PELLI procedures by adsorbing extractor molecules on the titania and Mn_3O_4 particles that converge at the liquid-liquid interface[12]. HT extractors containing hydrocarbon tails and hydrophilic anchoring head groups have been used, such as lauryl gallate[11-13], phosphonic acids[13, 14, 18, 19], fatty amines[5, 18], fatty acids[15, 20] and octanohydroxamic acid[16] to extract hydroxyapatite, MnO_2 and iron oxides. Organic solvents used as particle-receiving liquids include 1-butanol[17], dichloromethane[5], toluene[20] and ionic liquids[14].

Since PELLI applications are yet limited to a few materials thus far, the important challenge is to further develop PELLI methods for the agglomerate-free processing of functional ceramic materials. Oxide extraction requires extractors containing anchoring groups that have affinity for specific metal atoms. Thus, understanding extraction mechanisms and searching for new extractors are critical factors for the development and application of PELLI methods.

The goal of this investigation was the development of efficient extractors and PELLI strategies to process ZnO, CeO_2 and MnO_2. We analyzed and compared different extractors, i.e., octadecylphosphonic acid (ODPA) containing phosphonate anchoring groups, stearic acid (SA) containing carboxylic groups, and 16-phosphonohexadecanoic acid (16PHA) containing both: phosphonate and carboxylic acid end groups. Test results provided insight into the influence of the structure of the extractor molecules on particle extraction from an aqueous synthesis medium to an organic processing medium. We demonstrated the benefits of PELLI for the agglomerate free processing of materials for three applications. The particles were prepared in aqueous solutions and transferred by PELLI to different processing media, such as suspensions for the electrophoretic deposition (EPD) of thin films, slurries for impregnation of porous current collectors and fabrication of bulk ES electrodes, and slurries for screen printing of thin film ES electrodes. An important finding was that particle extraction using 16PHA is possible, which is a fundamentally different extractor from those used in previous investigations. This allows the development of advanced extractors that have enhanced functionality. For instance, we have developed a conceptually new approach to fabricate suspensions for EPD using 16PHA as the extractor for PELLI, as well as the dispersing and charging agent for EPD. We analyzed the influence of the extractor molecule structures on the charge storage properties of extracted MnO_2, where MnO_2–multiwalled carbon nanotube (MWCNT) bulk composite electrodes with high active mass loading were fabricated and tested for energy storage in ES. These electrodes, prepared using 16PHA as an extractor for PELLI, showed superior capacitive performance compared to other electrodes. We also demonstrated the benefits of PELLI for screen printing of advanced ES thin film electrodes.

7.3 Experimental procedures

$KMnO_4$, $Zn(NO_3)_2$, $Ce(NO_3)_3 \cdot 6H_2O$, Na_2SO_4, 1-butanol, NaOH, 16-phosphonohexadecanoic acid (16PHA), octadecylphosphonic acid (ODPA), stearic acid (SA), poly(vinyl butyral-co-vinyl alcohol-co-vinyl acetate) (PVB, average Mw = 50,000–80,000) (Aldrich), carbon black (CB, average particle size 15 nm, Cabot) and multiwalled carbon nanotubes (MWCNT, ID 4 nm, OD 13 nm, length 1–2 μm, Bayer) were used. Ni foams with 95% porosity were provided by Vale Company.

MnO_2 was obtained by reducing aqueous 0.06 M $KMnO_4$ solution with 1-butanol [11], where stirring facilitated the reduction reaction at the liquid-liquid interface. ZnO was prepared by a chemical precipitation method from 0.26 M $Zn(NO_3)_2$ solutions in water at a temperature of 70 °C. The pH of the solutions was adjusted to pH = 8 using NaOH. CeO_2 was prepared through the hydrothermal method using a Teflon-lined stainless-steel autoclave. An aqueous 0.06 M $Ce(NO_3)_3$ solution was prepared and the pH of the solutions was adjusted to pH = 12 using NaOH. Synthesis was performed at 100 °C for 24 h.

1-butanol was used as a particle-receiving organic liquid for the PELLI method. The mass ratio of extractor:oxide was in the range extending from 1:3 to 1:1. The concentration of the extracted particles in the 1-butanol suspensions was 5.5 g L^{-1}. Electrophoretic deposition (EPD) experiments were performed using suspensions of these extracted oxide particles. The deposition voltage was 50 V, and the distance between stainless steel substrates and Pt counter electrodes was 15 mm. A powder diffractometer (Nicolet I2, CuKα radiation) was used for X-ray diffraction (XRD) investigations. Scanning electron microscopy (SEM) studies were performed using a JEOL JSM-7000F microscope. A Bruker Vertex 70 spectrometer was used for the FTIR studies.

The MnO_2 suspensions, prepared by PELLI were used to fabricate bulk and thin film electrodes for ES. For bulk electrodes, the slurry containing MnO_2, MWCNT and PVB was impregnated into Ni foam current collectors. The total mass of the impregnated material after drying was 36.6 mg cm^{-2}. The mass ratio of MnO_2 and MWCNT in the composite electrodes was 4:1. The electrodes contained 3% PVB as a binder. The fabrication of thin film electrodes was performed by screen printing on stainless steel substrates using a plain weave mesh (mesh count – 156; mesh opening – 90 μm), purchased from Ryonet Corporation. The mass ratio of MnO_2:CB:PVB was 65:30:5. The screen printed film mass was 0.3 mg cm^{-2}.

A potentiostat (PARSTAT 2273, Princeton Applied Research, USA) was used for cyclic voltammetry (CV) studies at scan rates of 2–100 mV s^{-1} and impedance spectroscopy studies in the frequency range of 10 Hz–100 kHz in 0.5 M Na_2SO_4 aqueous electrolyte. The three-electrode cell contained a working electrode with a 1 cm^2 area, a platinum gauze counter electrode and a saturated calomel electrode (SCE) as a reference. The areal C_S = $Q/\Delta VS$ and gravimetric C_m = $Q/\Delta Vm$ capacitances were obtained using half of the integrated area under the CV curve to calculate the charge Q in the potential window ΔV for electrodes with area S and mass m of the impregnated material. The complex differential capacitance $C_S^* = C_S' - iC_S''$ at AC voltage amplitude of 5 mV was calculated[1, 21] from the impedance data as $C_S' = Z''/\omega|Z|^2S$ and $C_S'' = Z'/\omega|Z|^2S$, where $\omega = 2\pi f$ and f denotes the frequency.

7.4 Results and discussion

Figure 7.1 shows X-ray diffraction patterns of the as-prepared powders after they were dried in air. MnO_2 showed broad diffraction peaks corresponding to the JCPDS file 87-1497, but the material also contained an amorphous phase. The X-ray diffraction pattern of CeO_2 showed peaks matching JCPDS file 34-0394. The XRD data for ZnO showed peaks corresponding to JCPDS file 36-1451.

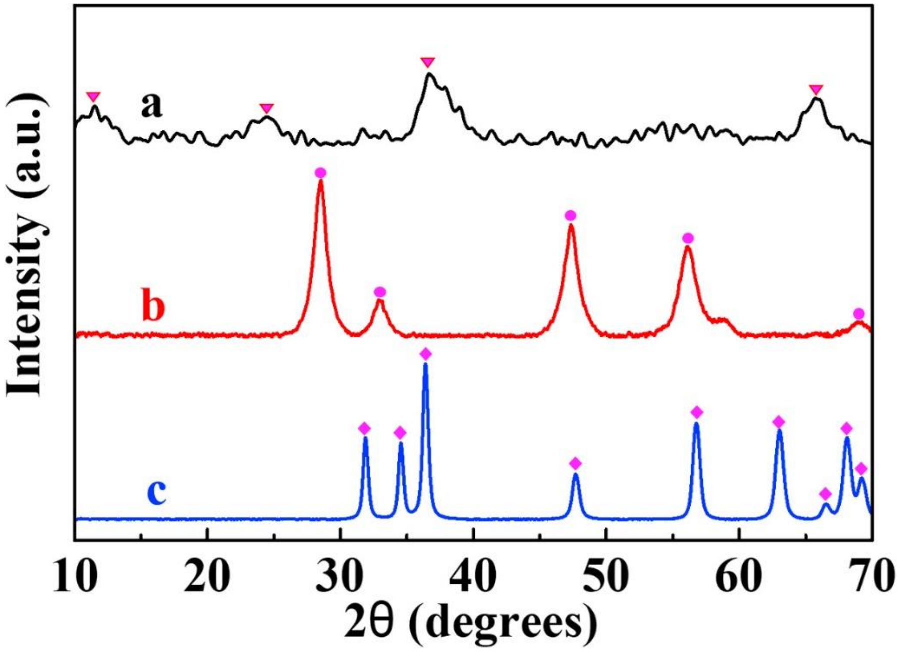

Figure 7.1 X-ray diffraction pattern of as-precipitated (a) MnO_2 (▼- JCPDS file 87-1497), (b) CeO_2 (•-JCPDS file 34-0394) and (c) ZnO (♦ -JCPDS file 36-1451).

The oxide particles prepared in aqueous solutions were transferred to 1-butanol using the PELLI method and different extractor molecules, 16PHA, ODPA and SA, were employed. Figure 7.2A–C shows the chemical structures of the extractor molecules. The chemical structures of ODPA and SA contain PO_3H_2 and COOH groups, respectively, and long hydrocarbon chains. The chemical structure of 16PHA contains PO_3H_2 and COOH end groups as well as a hydrocarbon chain. Fig. 2D(a–d) shows different mechanisms[22] for ODPA adsorption on particle surfaces involving the PO_3H_2 groups of ODPA and metal atoms (M) on the particle surface. The adsorption can be based on either bridging (Figure 7.2D(a and b)) or chelation (Figure 7.2D(c and d)) mechanisms. The adsorption of SA involved bridging (Figure 7.2D(e)) or chelation (Figure 7.2D(f)) of COOH groups[23, 24].

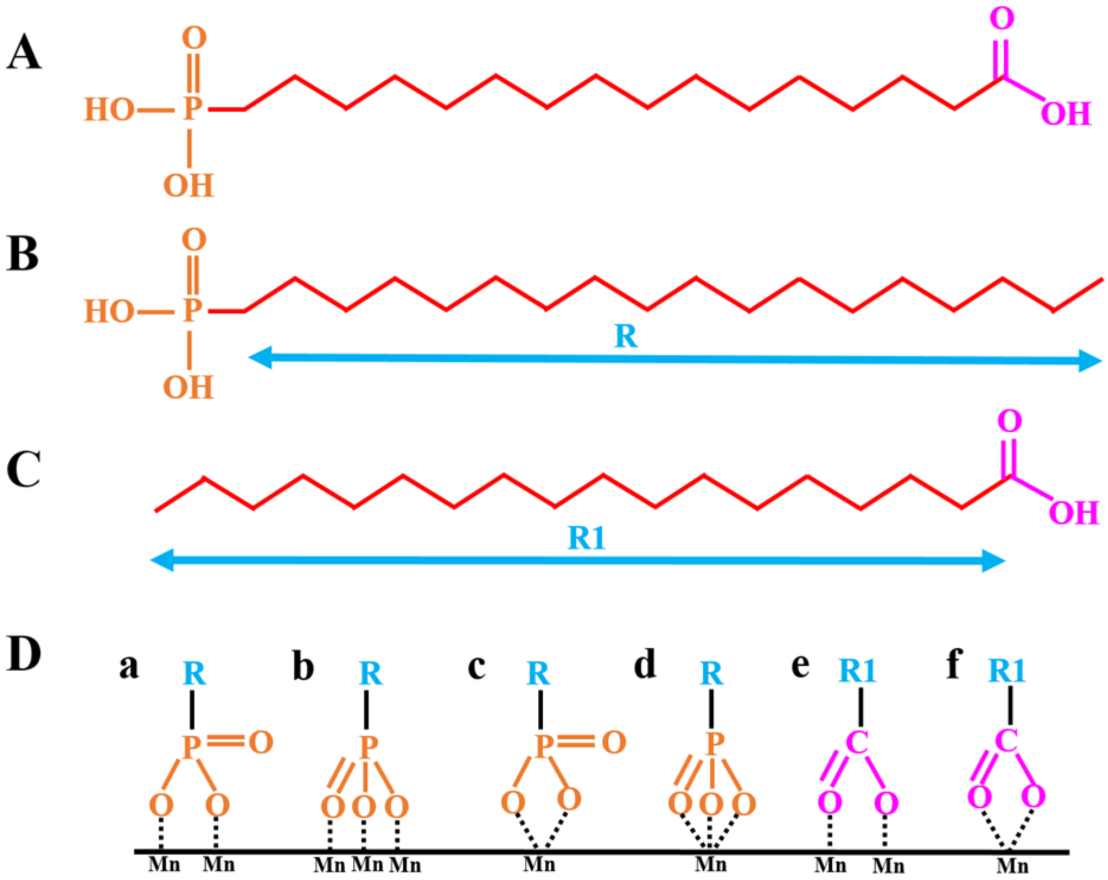

Figure 7.2 (A–C) Chemical structures of (A) 16PHA, (B) ODPA and (C) SA; (D) adsorption mechanisms, involving metal (M) atoms on the particle surface and (a–d) phosphonic acid group of ODPA or (e, f) carboxylic acid group of SA: (a, b, e) bridging, (c, d, f) chelation.

Previous PELLI investigations have focused on the use of HT surfactants containing a hydrophilic anchoring head group and a hydrophobic hydrocarbon tail. It is conceivable that, similar to other HT surfactants, the ODPA and SA molecules also accumulated at the liquid-liquid interface with the hydrophilic groups exposed to water and hydrophobic hydrocarbon chains extending into the 1-butanol phase. Such an accumulation and orientation of the molecules facilitated their adsorption on inorganic particles at the liquid-liquid interface, as well as the particle transfer from water to the 1-butanol phase (Figure

7.3A–C). However, the structure of 16PHA contains two end hydrophilic groups (HTH structure, Figure 7.2A), both of which can potentially be involved in 16PHA adsorption on particles at the liquid-liquid interface.

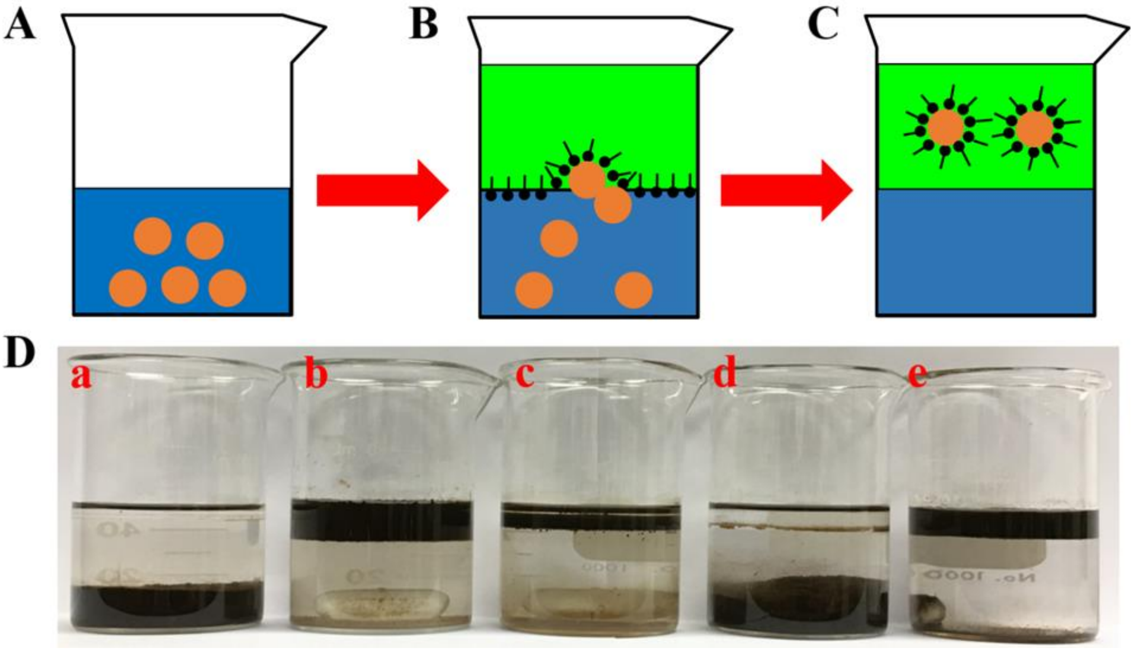

Figure 7.3 Schematic of PELLI method: (A) particles, precipitated in aqueous phase, (B) transfer through liquid-liquid interface, (C) formation of a stable suspension of particles in n-butanol, (D) (a) as-prepared MnO_2, (b–e) extraction of MnO_2 to the 1-butanol solvent, using (b) 16PHA, (c) ODPA, (d, e) SA for mass ratio of extractor:MnO_2 of (b, c, d) 1:3 and (e) (1:1).

It was found that 16PHA and ODPA extracted MnO_2, CeO_2 and ZnO from water to 1-butanol efficiently when the mass ratio of extractor:oxide was 1:3. However, the oxide particles remained in aqueous phase for a SA:oxide mass ratio of 1:3. It was found that the particle extraction also occurs with an SA:oxide mass ratio of 1:1. Fig. 3D illustrates an extraction experiment with MnO_2 particles. Similar results were obtained for CeO_2 and ZnO particles. The differences in extraction efficiency can result from stronger adsorption of PO_3H_2 groups on the particle surface as compared to COOH groups.

The adsorption of 16PHA, ODPA and SA on oxide particles was confirmed by FTIR studies of the extracted particles. Figure 7.4 compares FTIR spectra of as-received extractor molecules and extracted particles. The absorptions at 2849 and 2916 cm^{-1} in the spectrum of 16PHA, 2851 and 2918 cm^{-1} in the spectrum of ODPA, 2851 and 2918 cm^{-1} in the spectrum of SA were attributed to CH_2 symmetric and asymmetric stretching, respectively [18]. Similar absorptions were observed in the spectra of extracted MnO_2, CeO_2 and ZnO particles, which all indicated that extracted particles contained adsorbed 16PHA, ODPA and SA.

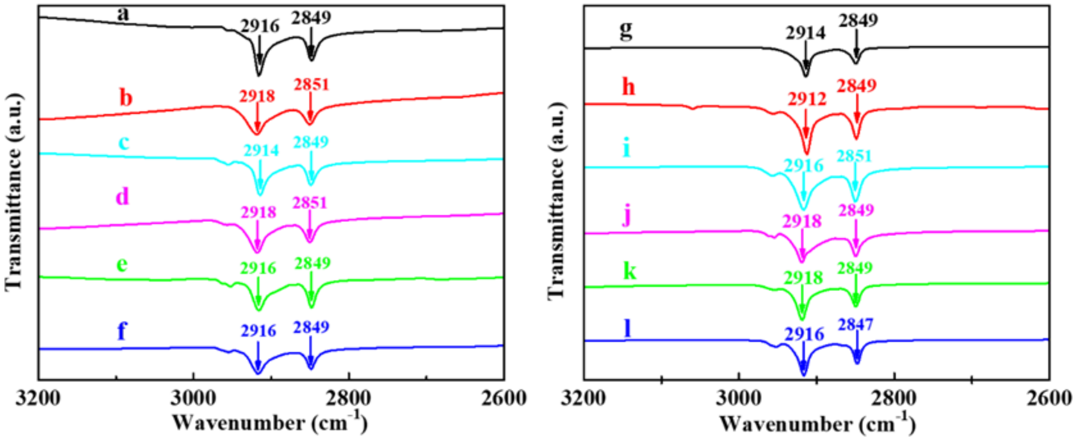

Figure 7.4 (a–l) FTIR spectra for (a) 16PHA, (c) ODPA, (e) SA, (b, d, f) MnO_2, extracted using 16PHA, ODPA and SA, respectively, (g, h, i) CeO_2, extracted using 16PHA, ODPA, and SA, respectively, (j, k, l) ZnO, extracted using 16PHA, ODPA, and SA, respectively.

The feasibility of particle extraction with 16PHA indicates that HTH molecules can be used as extractors in addition to HT surfactants for PELLI. Therefore, the search for extractors should be focused on molecules of other types with advanced functionality that can advance

PELLI applications. Hence, we employed 16PHA not only as an extractor for PELLI, but also as a dispersing and charging agent for EPD. With this conceptually new approach, the particles extracted into the organic phase using 16PHA as an extractor, were electrophoretically deposited from the organic phase by also using 16PHA as a dispersing and charging agent. The formation of stable suspensions of charged non-agglomerated particles is critical for EPD[25-28], where organic solvents offer advantages due to the reduced gas evolution at the electrode.

The particles extracted with 16PHA had enhanced suspension stability in the 1-butanol phase, compared to the same particles extracted using ODPA and SA. It is reasonable to suggest that 16PHA adsorption occurs via bonding of the PO_3H_2 groups whereas dissociated COOH end groups impart a negative charge to the particles and facilitate their electrostatic dispersion. However, the dispersion is also attributed to the steric effect. EPD experiments confirmed that MnO_2, CeO_2 and ZnO particles extracted with 16PHA were negatively charged and deposited on the anode surface. Figure 7.5 shows SEM images of the deposited films, which are relatively smooth, dense and agglomerate-free.

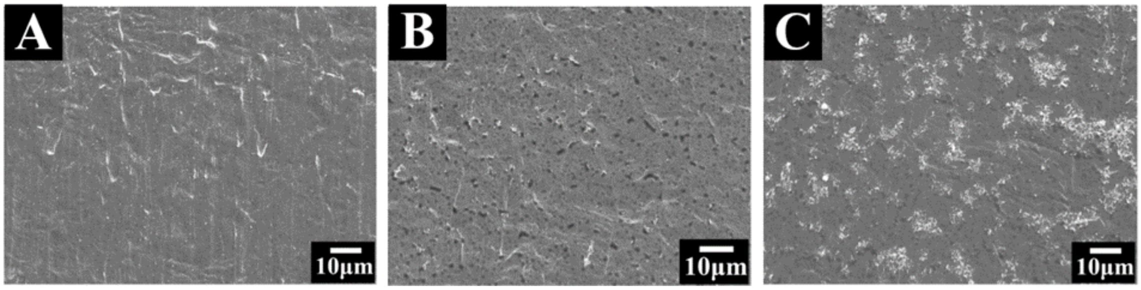

Figure 7.5 SEM images of (A) MnO_2, (B) CeO_2 and (C) ZnO films, which were electrophoretically deposited from suspensions, prepared using PELLI and 16PHA extractor.

The use of PELLI facilitated the fabrication of advanced slurries to impregnate Ni-foam current collectors and develop MnO_2-MWCNT bulk electrodes with high active mass loadings and good electrochemical performance. It is challenging[29-31] to obtain high C_m and C_S at high mass loadings due to poor electrolyte access to the active material surface and the increasing electrode electrical resistance with increasing mass. The agglomerate-free processing of MnO_2 was a key factor for improving material utilization at high active mass loading and enhanced mixing of MnO_2 with MWCNTs, which were used as a conductive additive. Measurements of C_m and C_S, coupled with impedance spectroscopy data showed significant improvement in the performance of electrodes prepared using PELLI.

Figure 7.6 compares CV data for MnO_2-MWCNT bulk electrodes, prepared without PELLI and using PELLI with different extractors. The electrodes, prepared without PELLI showed poor capacitive behavior, as indicated by low CV areas. The CVs were tilted and deviated significantly from the ideal box shape. In contrast, the electrodes, prepared using PELLI showed significant increase in CV area. Nearly ideal box-shape CVs were obtained at different scan rates. The box shape CVs and increase in current with increasing scan rate indicated good capacitive behavior. The larger area of CVs for electrodes prepared using 16PHA was attributed to the higher capacitance. The capacitances of the electrodes were calculated from the CV data and presented in Figure 7.7.

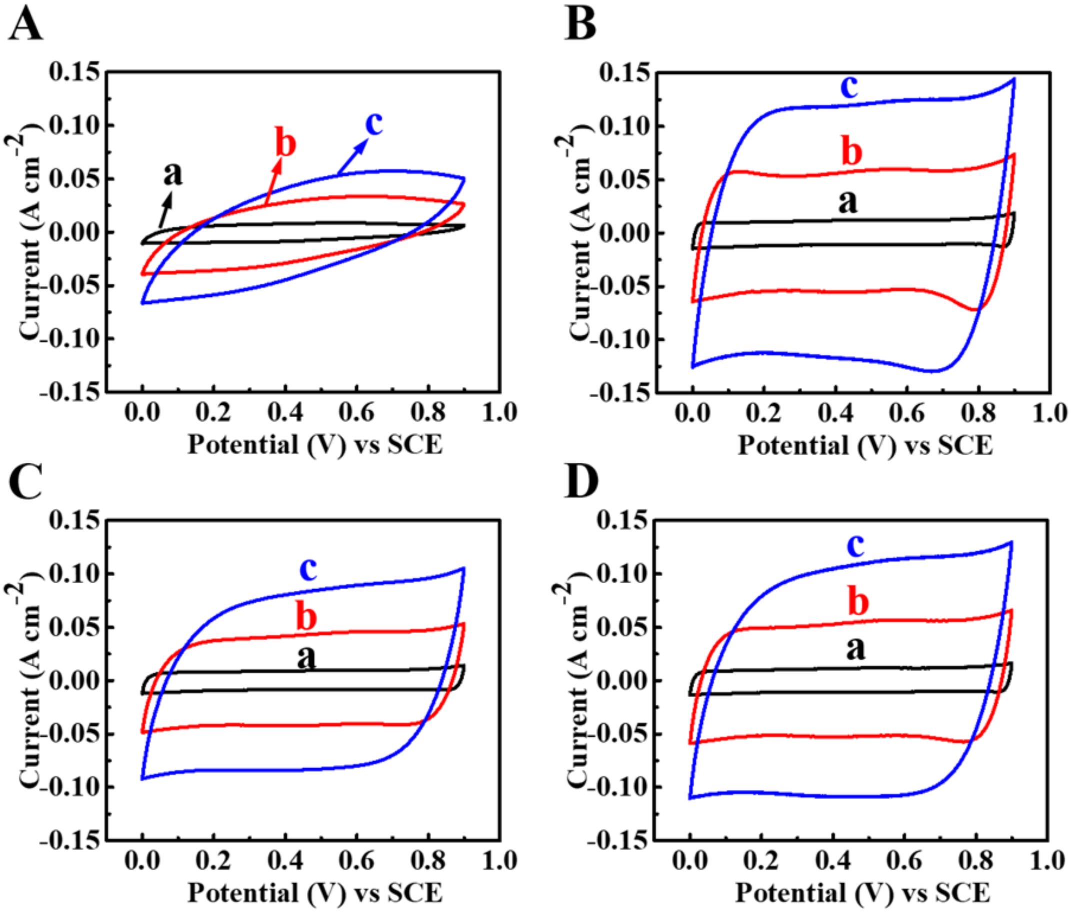

Figure 7.6 CVs at scan rates of (a) 2, (b) 10 and (c) 20 mV s^{-1} for bulk MnO_2-MWCNT electrodes, prepared (A) without extraction, and (B–D) by PELLI using (B) 16PHA, (C) ODPA and (D) SA extractors.

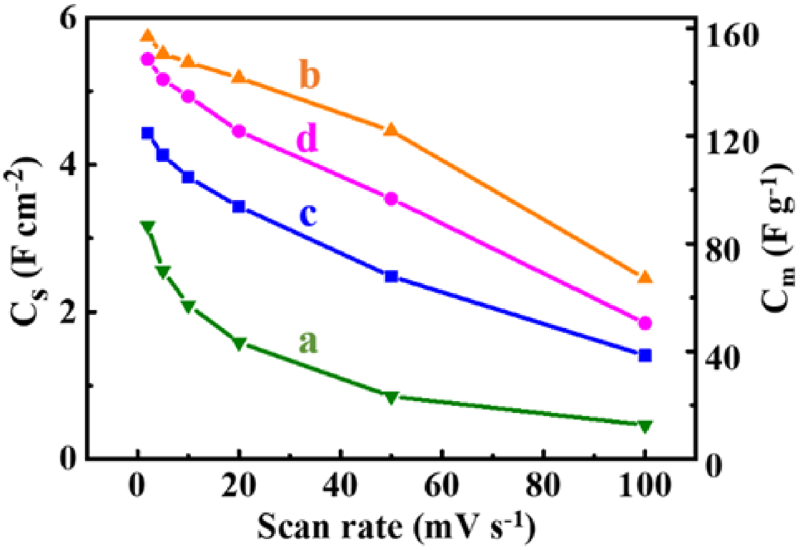

Figure 7.7 Capacitances C_S and C_m calculated from the CVs for bulk MnO_2-MWCNT electrodes, prepared (a) without extraction, and (b–d) by PELLI using (b) 16PHA, (c) ODPA and (d) SA extractors.

The electrodes, prepared without PELLI showed capacitances of 3.2 F cm^{-2} (87 F g^{-1}) and 0.5 F cm^{-2} (13 F g^{-1}) at scan rates of 2 and 100 mV s^{-1}, respectively. The electrodes showed significant decrease in capacitance with increasing scan rate, which resulted in capacitance retention of 15% at a scan rate of 100 mV s^{-1}. The low capacitance of the electrodes and their low capacitance retention indicated poor active material utilization[32]. In contrast, the use of PELLI resulted in a significant increase in capacitance with the highest capacitance achieved using 16PHA as an extractor. The use of PELLI and 16PHA as an extractor allowed the fabrication of electrodes with capacitances of 5.7 F cm^{-2} (157 F g^{-1}) and 2.5 F cm^{-2} (67 F g^{-1}) at scan rates of 2 and 100 mV s^{-1}, respectively. The capacitance retention at a scan rate of 100 mV s^{-1} was 43%. The difference in C_S and C_m for electrodes, prepared with different extractors, can be attributed to influence of the molecular structure of the extractors on particle dispersion. It is in this regard that molecules with PO_3H_2 groups showed enhanced adsorption on particles, which was beneficial for particle dispersion. Moreover, 16PHA molecules of the HTH type with two anionic groups provided better dispersion, compared to the molecules of HT type.

Figure 7.8A shows Nyquist plots of complex impedance for the MnO_2-MWCNT bulk electrodes. The electrodes, prepared without PELLI showed relatively high resistance $R = Z'$, which can explain the tilted CVs in Figure 7.6A. In contrast, the electrodes prepared using PELLI showed significantly lower resistance, where the slopes of the Nyquist plots were close to 90° and indicated good capacitive behavior. The components of complex capacitance were calculated from the CV data and plotted in Figure 7.8B and C. The frequency dependences of complex capacitance showed a relaxation type dispersion, as indicated by the reduction of C_S' with frequency and relaxation maxima in the frequency dependencies of C_S''. The electrodes prepared using 16PHA as an extractor for PELLI showed the highest C_S' in agreement with the corresponding CV data. Moreover, the use of PELLI resulted in the highest relaxation frequency, corresponding to the maximum in the frequency dependence of C_S''. This indicated improved capacitance retention at high frequencies.

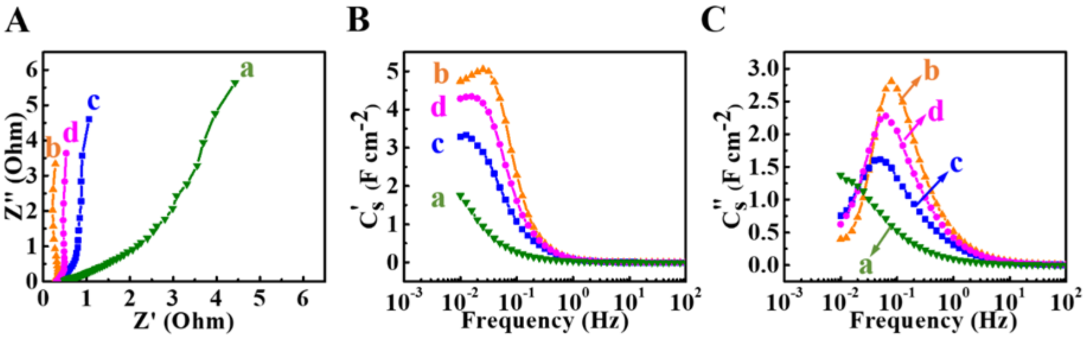

Figure 7.8 (A) Nyquist plots of complex impedance and frequency dependences of (B) real C_S' and (C) imaginary C_S'' components of complex capacitance, calculated from the impedance data for MnO_2-MWCNT electrodes, prepared (a) without extraction and (b–d) by PELLI using (b) 16PHA, (c) ODPA and (d) SA extractors.

Figure 7.9 contains an SEM image of the electrode, prepared using 16PHA, showing MWCNTs were well mixed with non-agglomerated MnO_2. The use of PELLI facilitated good mixing of non-agglomerated MnO_2 particles with MWCNT and the fabrication of these advanced electrodes that have good performance at high active mass loadings.

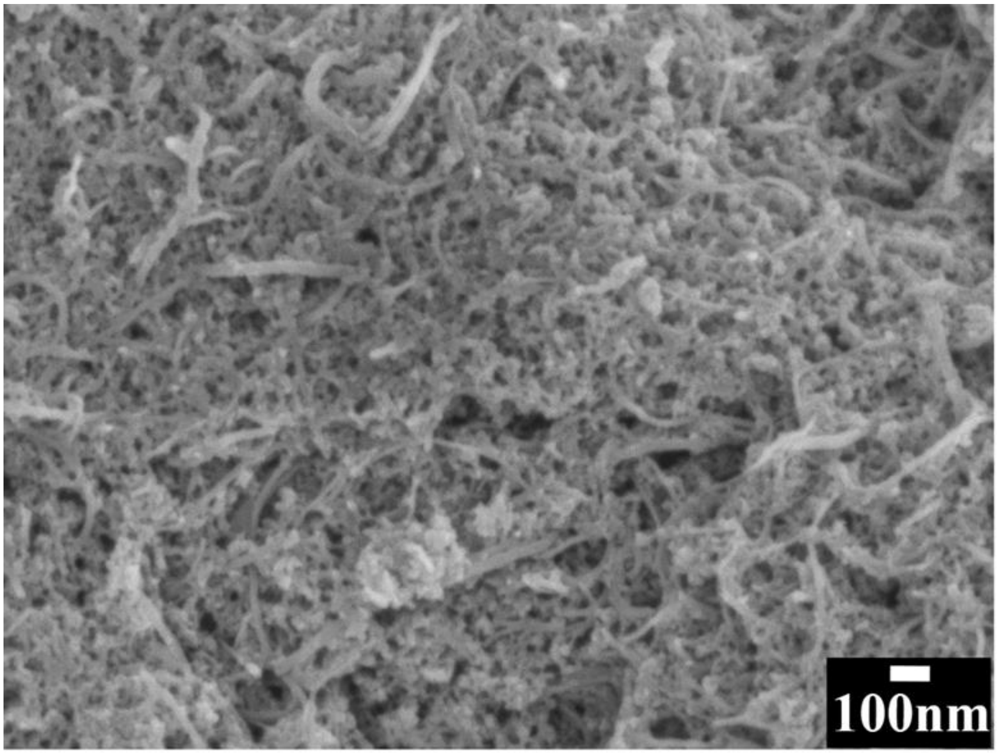

Figure 7.9 SEM image of MnO_2-MWCNT composite, prepared by PELLI using 16PHA extractor.

The use of PELLI facilitated the fabrication of inks containing non-agglomerated MnO_2 particles for the deposition of thin film ES electrodes using screen printing. Figure 7.10 shows CVs at different scan rates and capacitance data for the fabricated MnO_2-CB electrodes with a mass loading of 0.3 mg cm^{-2}. The capacitance of 35 mF cm^{-2} (137 F g^{-1}) was obtained at a scan rate of 2 mV s^{-1}. The capacitance retention at a scan rate of 100 mV s^{-1} was 34%. Figure 7.11 shows impedance spectroscopy data for the thin film electrodes. The Nyquist plot showed higher resistance as compared to the bulk electrodes. The lower resistance of the Ni-foam based electrodes can result from the improved contact of the Ni foam with the active material and the lower amount of binder required for electrode fabrication. The real component of capacitance C_S' calculated from the impedance data at low frequencies was close to the C_S values measured at low scan rates. The imaginary part showed a relaxation maximum at a frequency of 30 mHz.

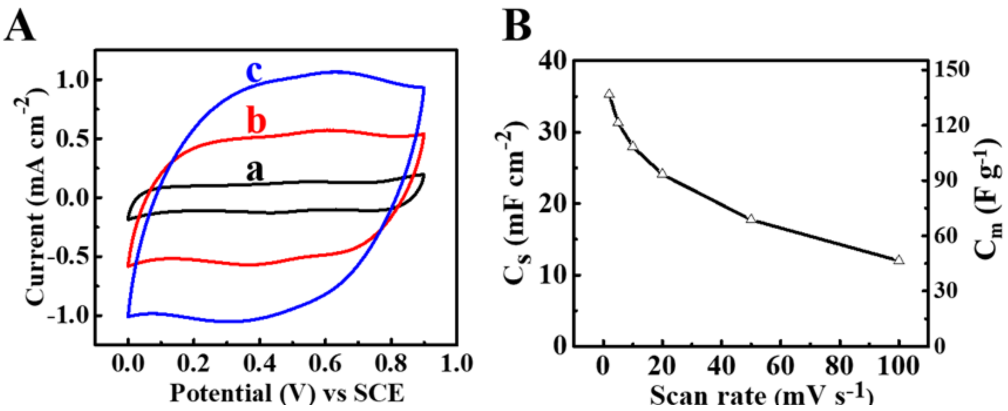

Figure 7.10 (A) CVs at scan rates of (a) 2, (b) 10 and (c) 20 mV s^{-1}, (B) C_S and C_m for thin film MnO_2-CB electrode, prepared by screen printing.

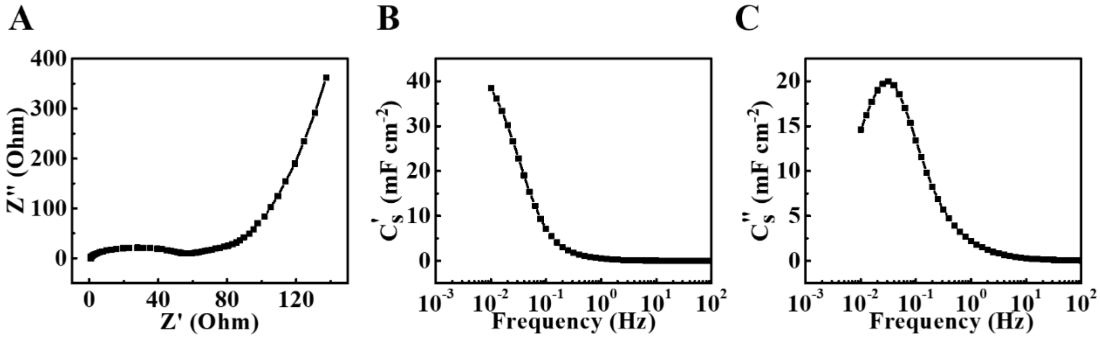

Figure 7.11 (A) Nyquist plot of complex impedance, (B) C_S' and (C) C_S'' versus frequency for thin film MnO_2-CB electrodes, prepared using screen printing method.

7.5 Conclusions

16PHA, ODPA and SA allowed extraction of ZnO, CeO_2 and MnO_2 particles from the aqueous synthesis media to the 1-butanol phase in the PELLI method. The ability to extract oxide particles using 16PHA paves the way for application of extractor molecules of new types that do not belong to the HT surfactant category. Therefore, it is expected that further investigations will create a larger pool of extractor molecules suitable for PELLI applications. The use of extractor molecules with advanced functionality opens new and unexplored PELLI applications. Therefore, we have developed a conceptually new approach based on the use of multifunctional 16PHA molecules not only as extractors, but also as dispersing and charging agents for EPD of particles that are transferred to the EPD processing medium. The use of 16PHA as an extractor for PELLI allowed superior electrochemical performance of MnO_2 based bulk electrodes for ES. Good electrochemical performance resulted from the phase transfer of non-agglomerated MnO_2 particles and their improved mixing with MWCNT. We have fabricated ES bulk electrodes with high active mass loading, which showed a capacitance of $5.7\,F\,cm^{-2}$ ($157\,F\,g^{-1}$) and $2.5\,F\,cm^{-2}$ ($67\,F\,g^{-1}$) at scan rates of 2 and $100\,mV\,s^{-1}$, respectively, and low impedance. The use of PELLI for developing an ink for screen printing facilitated the fabrication of efficient thin film SC electrodes.

7.6 References

[1] K. Y. Shi and I. Zhitomirsky, "Influence of current collector on capacitive behavior and cycling stability of Tiron doped polypyrrole electrodes," *Journal of Power Sources*, vol. 240, pp. 42-49, Oct 15 2013.

[2] D. Bélanger, L. Brousse, and J. W. Long, "Manganese oxides: battery materials make the leap to electrochemical capacitors," *The Electrochemical Society Interface*, vol. 17, p. 49, 2008.

[3] L. Liu, F. H. Tian, M. Zhou, H. P. Guo, and X. Y. Wang, "Aqueous rechargeable lithium battery based on polyaniline and $LiMn_2O_4$ with good cycling performance," *Electrochimica Acta,* vol. 70, pp. 360-364, May 30 2012.

[4] P. Simon and Y. Gogotsi, "Materials for electrochemical capacitors," *Nature Materials,* vol. 7, pp. 845-854, Nov 2008.

[5] R. Chen, M. S. Ata, X. Y. Zhao, A. Clifford, I. Puri, and I. Zhitomirsky, "Strategies for liquid-liquid extraction of oxide particles for applications in supercapacitor electrodes and thin films," *Journal of Colloid and Interface Science,* vol. 499, pp. 1-8, Aug 1 2017.

[6] M. Karg, N. Schelero, C. Oppel, M. Gradzielski, T. Hellweg, and R. von Klitzing, "Versatile Phase Transfer of Gold Nanoparticles from Aqueous Media to Different Organic Media," *Chemistry-a European Journal,* vol. 17, pp. 4648-4654, Apr 2011.

[7] A. Kumar, P. Mukherjee, A. Guha, S. D. Adyantaya, A. B. Mandale, R. Kumar, *et al.*, "Amphoterization of colloidal gold particles by capping with valine molecules and their phase transfer from water to toluene by electrostatic coordination with fatty amine molecules," *Langmuir,* vol. 16, pp. 9775-9783, Dec 12 2000.

[8] K. S. Mayya and F. Caruso, "Phase transfer of surface-modified gold nanoparticles by hydrophobization with alkylamines," *Langmuir,* vol. 19, pp. 6987-6993, Aug 19 2003.

[9] A. Kumar, H. Joshi, R. Pasricha, A. B. Mandale, and M. Sastry, "Phase transfer of silver nanoparticles from aqueous to organic solutions using fatty amine

molecules," *Journal of Colloid and Interface Science,* vol. 264, pp. 396-401, Aug 15 2003.

[10] N. Gaponik, D. V. Talapin, A. L. Rogach, A. Eychmuller, and H. Weller, "Efficient phase transfer of luminescent thiol-capped nanocrystals: From water to nonpolar organic solvents," *Nano Letters,* vol. 2, pp. 803-806, Aug 2002.

[11] C. Wallar, T. Zhang, K. Shi, and I. Zhitomirsky, "Synthesis of metal and metal oxide nanoparticles, liquid-liquid extraction and application in supercapacitors," *Colloids and Surfaces a-Physicochemical and Engineering Aspects,* vol. 500, pp. 195-202, Jul 5 2016.

[12] R. Poon, X. Zhao, M. S. Ata, A. Clifford, and I. Zhitomirsky, "Phase transfer of oxide particles for application in thin films and supercapacitors," *Ceramics International*, vol. 43, pp. 8314-8320, Aug 1 2017.

[13] A. Clifford, M. S. Ata, and I. Zhitomirsky, "Synthesis, liquid - Liquid extraction and deposition of hydroxyapatite nanorod composites," *Materials Letters,* vol. 201, pp. 140-143, Aug 15 2017.

[14] R. Bhandary, J. G. Alauzun, P. Hesemann, A. Stocco, M. In, and P. H. Mutin, "Phase transfer of TiO_2 nanoparticles from water to ionic liquid triggered by phosphonic acid grafting," *Soft Matter*, vol. 13, pp. 8023-8026, Nov 28 2017.

[15] J. Erler, S. Machunsky, P. Grimm, H. J. Schmid, and U. A. Peuker, "Liquid-liquid phase transfer of magnetite nanoparticles - Evaluation of surfactants," *Powder Technology,* vol. 247, pp. 265-269, Oct 2013.

[16] J. Milne and I. Zhitomirsky, "Application of octanohydroxamic acid for liquid-liquid extraction of manganese oxides and fabrication of supercapacitor electrodes," *Journal of Colloid and Interface Science,* vol. 515, pp. 50-57, Apr 1 2018.

[17] T. Zhang, X. Zhao, R. Poon, A. Clifford, R. Mathews, and I. Zhitomirsky, "Synthesis and liquid-liquid extraction of non-agglomerated Al(OH)($_3$) particles for deposition of cellulose matrix composite films," *Journal of Colloid and Interface Science,* vol. 508, pp. 49-55, Dec 15 2017.

[18] R. Chen, R. Poon, R. P. Sahu, I. K. Puri, and I. Zhitomirsky, "MnO_2-Carbon Nanotube Electrodes for Supercapacitors with High Active Mass Loadings," *Journal of the Electrochemical Society,* vol. 164, pp. A1673-A1678, 2017.

[19] R. Chen, M. S. Ata, X. Y. Zhao, I. Puri, and I. Zhitomirsky, "Liquid-liquid extraction of oxide particles and application in supercapacitors," *Journal of Materials Research,* vol. 32, pp. 3242-3250, Sep 2017.

[20] Y. Hou, C. X. Hou, Y. Q. Fan, F. Dang, and B. W. Li, "Biphasic liquid interface derived magnetite nanocrystals: synthesis, properties and growth mechanism," *Materials Research Express,* vol. 4, Dec 2017.

[21] Y. Su and I. Zhitomirsky, "Asymmetric electrochemical supercapacitor, based on polypyrrole coated carbon nanotube electrodes," *Applied Energy,* vol. 153, pp. 48-55, Sep 1 2015.

[22] R. Boissezon, J. Muller, V. Beaugeard, S. Monge, and J. J. Robin, "Organophosphonates as anchoring agents onto metal oxide-based materials: synthesis and applications," *Rsc Advances,* vol. 4, pp. 35690-35707, 2014.

[23] K. D. Dobson and A. J. McQuillan, "In situ infrared spectroscopic analysis of the adsorption of aliphatic carboxylic acids to TiO_2, ZrO_2, Al_2O_3, and Ta_2O_5 from aqueous solutions," *Spectrochimica Acta Part a-Molecular and Biomolecular Spectroscopy,* vol. 55, pp. 1395-1405, Jul 1999.

[24] K. D. Dobson and A. J. McQuillan, "In situ infrared spectroscopic analysis of the adsorption of aromatic carboxylic acids to TiO_2, ZrO_2, Al_2O_3, and Ta_2O_5 from aqueous solutions," *Spectrochimica Acta Part a-Molecular and Biomolecular Spectroscopy,* vol. 56, pp. 557-565, Feb 15 2000.

[25] A. R. Boccaccini, C. Kaya, and K. K. Chawla, "Use of electrophoretic deposition in the processing of fibre reinforced ceramic and glass matrix composites: a review," *Composites Part a-Applied Science and Manufacturing,* vol. 32, pp. 997-1006, 2001.

[26] A. R. Boccaccini, J. Cho, J. A. Roether, B. J. C. Thomas, E. J. Minay, and M. S. P. Shaffer, "Electrophoretic deposition of carbon nanotubes," *Carbon,* vol. 44, pp. 3149-3160, Dec 2006.

[27] L. Besra and M. Liu, "A review on fundamentals and applications of electrophoretic deposition (EPD)," *Progress in Materials Science,* vol. 52, pp. 1-61, Jan 2007.

[28] M. Cheong and I. Zhitomirsky, "Electrophoretic deposition of manganese oxide films," *Surface Engineering,* vol. 25, pp. 346-352, Jul 2009.

[29] Y. Gogotsi and P. Simon, "True Performance Metrics in Electrochemical Energy Storage," *Science,* vol. 334, pp. 917-918, Nov 18 2011.

[30] W. T. Gu and G. Yushin, "Review of nanostructured carbon materials for electrochemical capacitor applications: advantages and limitations of activated carbon, carbide-derived carbon, zeolite-templated carbon, carbon aerogels, carbon nanotubes, onion-like carbon, and graphene," *Wiley Interdisciplinary Reviews-Energy and Environment*, vol. 3, pp. 424-473, Sep-Oct 2014.

[31] L. Wei and G. Yushin, "Nanostructured activated carbons from natural precursors for electrical double layer capacitors," *Nano Energy*, vol. 1, pp. 552-565, Jul 2012.

[32] B. E. Conway and W. G. Pell, "Power limitations of supercapacitor and capacitance distribution operation associated with resistance in porous electrode devices," *Journal of Power Sources*, vol. 105, pp. 169-181, Mar 20 2002.

8 High areal capacitance of FeOOH-carbon nanotube negative electrodes for asymmetric supercapacitors

This chapter is reproduced from *High areal capacitance of FeOOH-carbon nanotube negative electrodes for asymmetric supercapacitors, 44, 18007-18015, 2018, Ceramics International,* ***Ri Chen****, Ishwar K. Puri and Igor Zhitomirsky, https://doi.org/10.1016/j.ceramint.2018.07.002, Copyright 2019, with permission from Elsevier*. The author of this thesis is the first author and the main contributor of this publication.

8.1 Abstract

The relatively low capacitance of negative electrodes, as compared to the capacitance of advanced positive electrodes, poses a serious problem, since this limits the development of asymmetric supercapacitor (SC) devices with a large voltage window and enhanced power-energy characteristics. We fabricate negative SC electrodes with a high capacitance that match the capacitance of advanced positive electrodes at similar active mass loadings, as high as 37 mg cm^{-2}. Cyclic voltammetry, impedance spectroscopy, galvanostatic charge-discharge data and the power-energy characteristics of the asymmetric SC device exhibit good electrochemical performance for a voltage window of 1.6 V. Our approach involves the development and application of particle extraction through liquid-liquid interface (PELLI) methods, new extraction mechanisms and efficient extractors to synthesize α-FeOOH and β-FeOOH electrode materials. The use of PELLI allows agglomerate-free processing of powders, which facilitates their efficient mixing with multiwalled carbon

nanotubes (MWCNT) and allows improved electrolyte access to the particle surface. Experiments to determine the properties of FeOOH-MWCNT composites provided insight into the influence of the electrode material and the structure of extractor molecules on the composite properties. The highest capacitance of 5.86 F cm^{-2} for negative electrodes and low impedance were achieved using α-FeOOH-MWCNT composites and a 16-phosphonohexadecanoic acid (16PHA) extractor. This extractor allows adsorption on particles, not only at the liquid-liquid interface, but also in the bulk aqueous phase and can potentially be used as a capping agent for particle synthesis and as an extractor in the PELLI method.

8.2 Introduction

The development of efficient electrode materials that work in a negative potential range is a serious challenge for the fabrication of asymmetric aqueous supercapacitors (SC). The capacitances of negative electrodes are typically lower than those of positive electrodes at similar active mass loadings. Therefore, the important task is to match the capacitive performance of cathodes and anodes and enhance device performance over an enlarged voltage window.

There is substantial interest in investigating FeOOH and composite materials for negative electrodes. Recent studies have focused on crystalline α-FeOOH[1-3], β-FeOOH[4-6] and γ-FeOOH[7, 8] phases, as well as amorphous FeOOH[9, 10] materials. The capacitive behavior of individual electrodes and cells has been studied in different electrolytes, such as KOH[1, 9, 11], NaOH[9, 12], LiOH[13], Li_2SO_4[14], Na_2SO_4[2], Na_2SO_3[9] and others

[15, 16]. Investigations have emphasized advantages[2] of a mild Na_2SO_4 electrolyte for the fabrication of individual electrodes and asymmetric devices. Particular attention was focused on the synthesis and application of particles with nanorod shapes[1, 4, 17], which allow improved capacitive performance. Various conductive additives, such as carbon black[1, 18], polypyrrole[19], carbon nanotubes[20]and graphene[15, 20-22] have facilitated the fabrication of electrodes with high capacitance and reduced impedance. Improved capacitive performance can also be achieved using doped FeOOH[17].

It is important to note that FeOOH electrodes were tested in positive[11, 23-25] and negative voltage windows[26]. The highest capacitances in negative voltage windows were achieved using KOH and Na_2SO_4 electrolytes. A capacitance of $463.18\,\mathrm{F\,g^{-1}}$ was reported[1] in a KOH electrolyte with a relatively narrow voltage window from -0.6 to $-1.0\,\mathrm{V}$ versus a saturated calomel electrode (SCE). The charge-discharge characteristics in the KOH electrolyte deviated significantly from ideal capacitive behavior[1, 6]. Improved capacitive behavior was also observed for FeOOH-graphene composites[22]. A capacitance of $160\,\mathrm{F\,g^{-1}}$ was reported for FeOOH electrodes in Na_2SO_4 electrolyte[2]. These investigations of electrodes with low active mass loadings indicated that FeOOH is a promising material for negative electrodes.

An important challenge is to achieve good performance of electrodes with high active mass loadings[27]. The mass normalized capacitance (C_m) of various electrode materials[27] decreased drastically with increasing active mass due to poor electrolyte access to the active material and low electronic conductivity of the electrodes. The critical requirement for practical applications[27] is good active material performance at mass loadings above 10–

$20\ mg\ cm^{-2}$. An important characteristic of electrodes with high active mass loadings is the areal capacitance (C_S). The increase in active material loading[28] allowed the fabrication of negative FeOOH electrodes with $C_S = 6.5\ F\ cm^{-2}$ in KOH electrolyte. The highest C_S of $3.3\ F\ cm^{-2}$ in a Na_2SO_4 electrolyte in the negative potential range was obtained using Ti doped FeOOH composites containing quantum dots and bacterial cellulose[21].

Despite the impressive progress in the development of FeOOH and its composite materials, further advances in synthesis and electrode fabrication can result in better utilization of FeOOH properties in the SC devices. The use of water insoluble binders facilitates the fabrication of electrodes for stable operation in aqueous electrolytes. During a typical electrode fabrication procedure, the binder must be well dissolved in an organic solvent in order to facilitate mixing with FeOOH and to minimize the binder content in the electrode. FeOOH particles, synthesized in an aqueous phase are usually dried and then re-dispersed in an organic solvent, containing a water insoluble binder. However, particle drying results in the formation of hard agglomerates, which is driven by the reduction of total particle surface energy and surface condensation reactions. Particle agglomeration is detrimental for their mixing with conductive additives and for electrolyte access to the particle surface.

The goal of this investigation was the fabrication of efficient FeOOH-multiwalled carbon nanotube (MWCNT) negative electrodes with high active mass loadings for application in advanced asymmetric SC devices. Agglomerate-free processing of FeOOH particles was achieved by particle extraction through the liquid-liquid interface (PELLI) technique. In this approach, the FeOOH particles synthesized in an aqueous phase were directly transferred to an organic solvent. Therefore, the drying procedure and related agglomeration were avoided. We developed and tested efficient extractors for FeOOH, which contained phosphonic or/and carboxylic anchoring groups. Two extraction methods have been developed, which involve particle modification at the liquid-liquid interface or in an aqueous phase. We compared the electrochemical performance of α-FeOOH-MWCNT and β-FeOOH-MWCNT electrodes at high active mass loading. The test results presented below indicated that C_S as high as $5.86\ \mathrm{F\ cm^{-2}}$ can be achieved at a low impedance in a wide negative voltage window using α-FeOOH-MWCNT electrodes and Na_2SO_4 electrolyte. The capacitance of α-FeOOH-MWCNT negative electrodes matched the capacitance of advanced MnO_2-MWCNT positive electrodes at the same active mass loading of $37\ \mathrm{mg\ cm^{-2}}$. As a result, the asymmetric SC device showed improved capacitive performance.

8.3 Experimental procedures

$FeCl_3{\cdot}6H_2O$, NaOH, Na_2SO_4, 16-phosphonohexadecanoic acid (16PHA), hexadecylphosphonic acid (HDPA), palmitic acid (PA), poly(vinyl butyral-co-vinyl alcohol-co-vinyl acetate) (PVB, Mw = 50,000–80,000), 1-butanol (Aldrich), MWCNT (4 nm ID, 13 nm OD, 1–2 μm length, Bayer, Germany), and Ni foams (95% porosity, Vale Canada) were used.

Chemical precipitation of FeOOH was performed from aqueous $FeCl_3$ solutions, which were adjusted to pH = 7 using NaOH. The synthesis of α-FeOOH was performed at room temperature, whereas reaction at 70 °C resulted in the formation of β-FeOOH. In the PELLI-1 method, the solutions of 16PHA, HDPA and PA in 1-butanol were added to the aqueous phases containing precipitated particles. The stirring of the mixtures resulted in particle transfer to the 1-butanol phase. In the PELLI-2 method, a solution of 16PHA in NaOH was added to the $FeCl_3$ solution. The precipitation was performed at $pH = 7$. The addition of 1-butanol resulted in the FeOOH extraction to the 1-butanol phase. The mass ratio of FeOOH: extractor was 3:1 in both methods.

To fabricate supercapacitor electrodes, suspensions of the extracted FeOOH in 1-butanol were separated from the aqueous phase and then MWCNT were added. After ultrasonication of the mixed suspensions, a solution of PVB binder in ethanol was added. The mass ratio of FeOOH:MWCNT:PVB was 80:20:3. The suspensions thus obtained were used to fabricate FeOOH-MWCNT supercapacitor electrodes by impregnating the Ni foam current collectors. The active mass loading of the electrodes was 37 mg cm^{-2}. The MnO_2-MWCNT electrodes of similar mass were prepared using PELLI by the method described by us previously[29].

Electron microscopy investigations were performed using a JEOL JSM-7000F scanning electron microscope (SEM). X-ray diffraction (XRD) studies were performed using a powder diffractometer (Nicolet I2, monochromatized CuKα radiation). FTIR studies were performed on Bruker Vertex 70 spectrometer. Thermogravimetric analysis (TGA) was performed using a NETZSCH STA-409 thermoanalyser in air at a heating rate of 5 °C min^{-1}.

Cyclic voltammetry and impedance spectroscopy investigations were performed using a potentiostat (PARSTAT 2273, Princeton Applied Research, USA). The capacitive behavior of the electrodes was studied in three-electrode cells using 0.5 M Na_2SO_4 aqueous solution.

The area of the working electrode was 1 cm^2. The counter electrode was a platinum gauze and the reference electrode was a standard calomel electrode (SCE). Cyclic voltammetry (CV) studies were performed at scan rates of 2–100 $mV\ s^{-1}$. FeOOH–MWCNT negative electrodes were combined with MnO_2-MWCNT positive electrodes for the fabrication of asymmetric cells, which offer the advantage of an enlarged voltage window in aqueous solutions. The electrodes were separated by a porous polyethylene membrane with an average pore size of 0.4 μm.

The capacitances $C_S = Q/\Delta VS$ and $C_m = Q/\Delta Vm$ were calculated using half the integrated area of the CV curve to obtain the charge Q, and subsequently dividing the charge Q by the width of the potential window ΔV and electrode area S or active mass m of an electrode or device. The alternating current measurements of complex impedance $Z^* = Z'-iZ''$ were performed in the frequency range of 10 mHz to 100 kHz with a signal amplitude of 5 mV. The complex differential capacitance $C_S^* = C_S'-iC_S''$ was calculated from the impedance data as $C_S' = Z''/\omega|Z|^2S$ and $C_S'' = Z'/\omega|Z|^2S$, where $\omega = 2\pi f$ (f-frequency). The charge–discharge behavior of the cells was investigated using battery analyzers BST8-MA and BST8-3 (MTI corporation, USA) at current densities of 3–50 $mA\ cm^{-2}$.

8.4 Results and discussion

X-ray diffraction studies of the powders, precipitated at room temperature and at 70 °C, showed the X-ray diffraction peaks of α-FeOOH (Figure 8.1a) and β-FeOOH (Figure 8.1b), respectively. Thermogravimetric analysis revealed mass loss of 22% and 16% related to the dehydration of α-FeOOH and β-FeOOH, respectively (Figure 8.2). The dehydration reaction resulted in the release of water and formation of Fe_2O_3. Both materials showed higher mass loss, compared to the theoretical mass loss of 10%. The additional mass loss resulted from the adsorbed water. The higher mass loss of α-FeOOH compared to that of β-FeOOH was attributed to larger amount of adsorbed water. The difference can be attributed to different structures and synthesis conditions of the α-FeOOH and β-FeOOH phases.

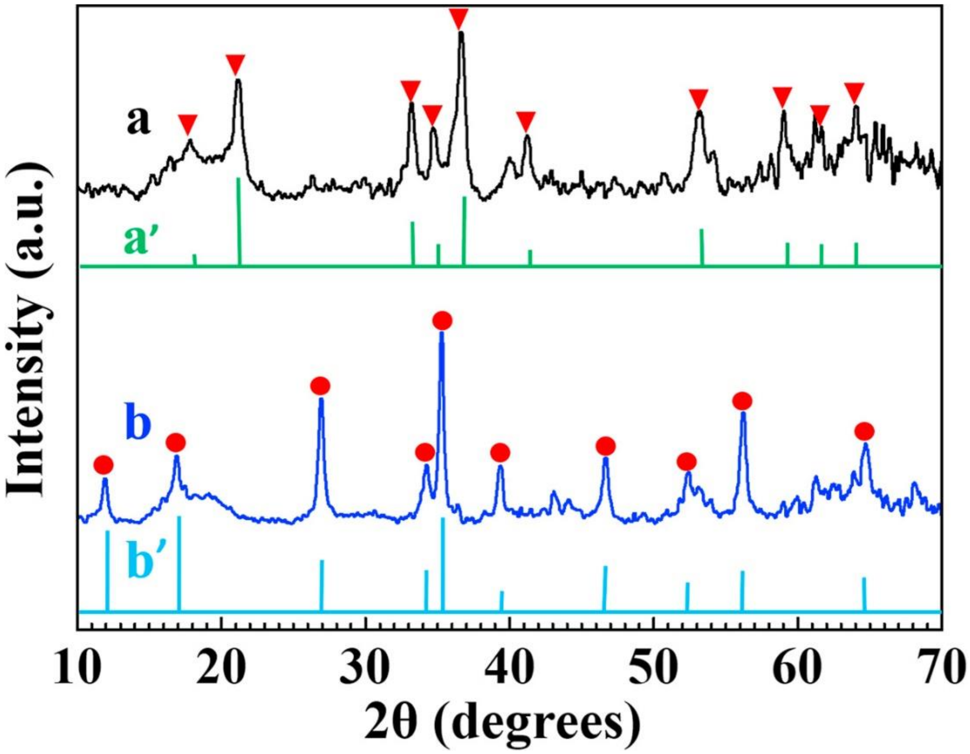

Figure 8.1 X-ray diffraction patterns of as-precipitated (a) α-FeOOH (▼- peaks corresponding to JCPDS file 29–713, a′ - diagram of standard peaks of JCPDS file 29–713), and (b) β-FeOOH (•- peaks, corresponding to JCPDS file 34–1266, b′ - diagram of standard peaks of JCPDS file 34–1266).

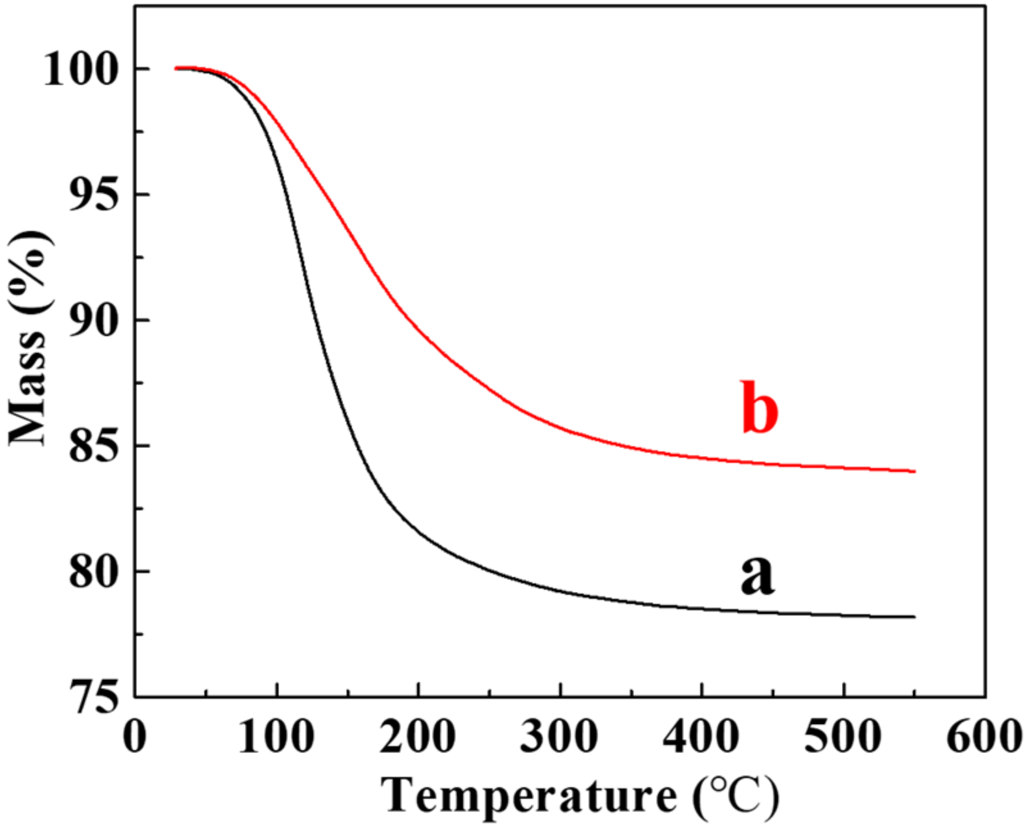

Figure 8.2 TGA data for (a) α-FeOOH and (b) β-FeOOH.

SEM studies (Figure 8.3) of the dried powders showed significant agglomeration of α-FeOOH and β-FeOOH particles. The typical size of the agglomerates was about 2–6 μm. The formation of such agglomerates must be avoided in order to improve FeOOH mixing with MWCNT and facilitate electrolyte access to the FeOOH surface. Therefore, PELLI strategies have been developed to transfer the particles precipitated in an aqueous phase directly to an organic phase and avoid particle agglomeration due to drying.

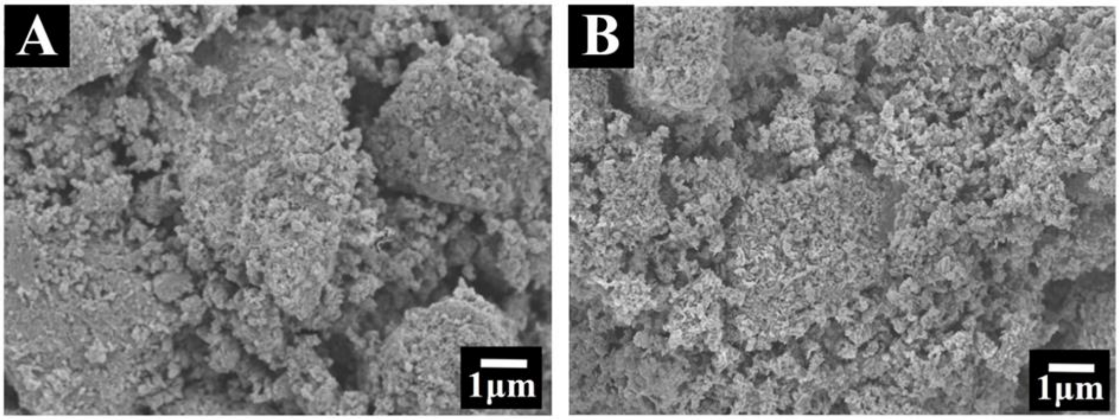

Figure 8.3 SEM images of (A) α-FeOOH and (B) β-FeOOH powders.

PELLI is a relatively new technique for surface modification and agglomerate-free processing of oxide and hydroxide materials[30]. Current PELLI research is focused on the development of fundamental extraction mechanisms and analysis of phenomena at the liquid-liquid interface[30, 31]. Of particular importance is finding efficient extractor molecules for specific oxide and hydroxide materials and understanding particle-extractor interactions, which facilitate extractor adsorption on the particle surface[30, 31].

In this investigation we developed a PELLI technique for the extraction of FeOOH, prepared by chemical precipitation methods. We found that extractor molecules with phosphonic and carboxylic groups strongly adsorbed on the particle surface and facilitated extraction. Figure 8.4 shows chemical structures of the extractor molecules and suggested adsorption mechanisms. The chemical structures of 16PHA, HDPA and PA include a long hydrocarbon chain as well as phosphonic or/and carboxylic groups. The suggested adsorption mechanisms involved bridging or chelation of Fe atoms on the particle surface. The selected molecules allowed good extraction of α-FeOOH and β-FeOOH with extraction method 1. As an example, Figure 8.5 shows that α-FeOOH particles were transferred from the aqueous phase to 1-butanol after addition of the extractor solutions in 1-butanol. The adsorption of 16PHA, HDPA and PA on α-FeOOH particles facilitated phase transfer. Figure 8.6 compares FTIR spectra of as-received 16PHA, HDPA and PA with the spectra of extracted particles. The absorptions in the range of 2800–3000 cm^{-1} in the spectra of 16PHA, HDPA and PA were attributed to symmetric and asymmetric CH_2 vibrations. The FTIR spectra of the extracted particles showed similar absorptions, indicating that 16PHA, HDPA and PA were adsorbed on the particles.

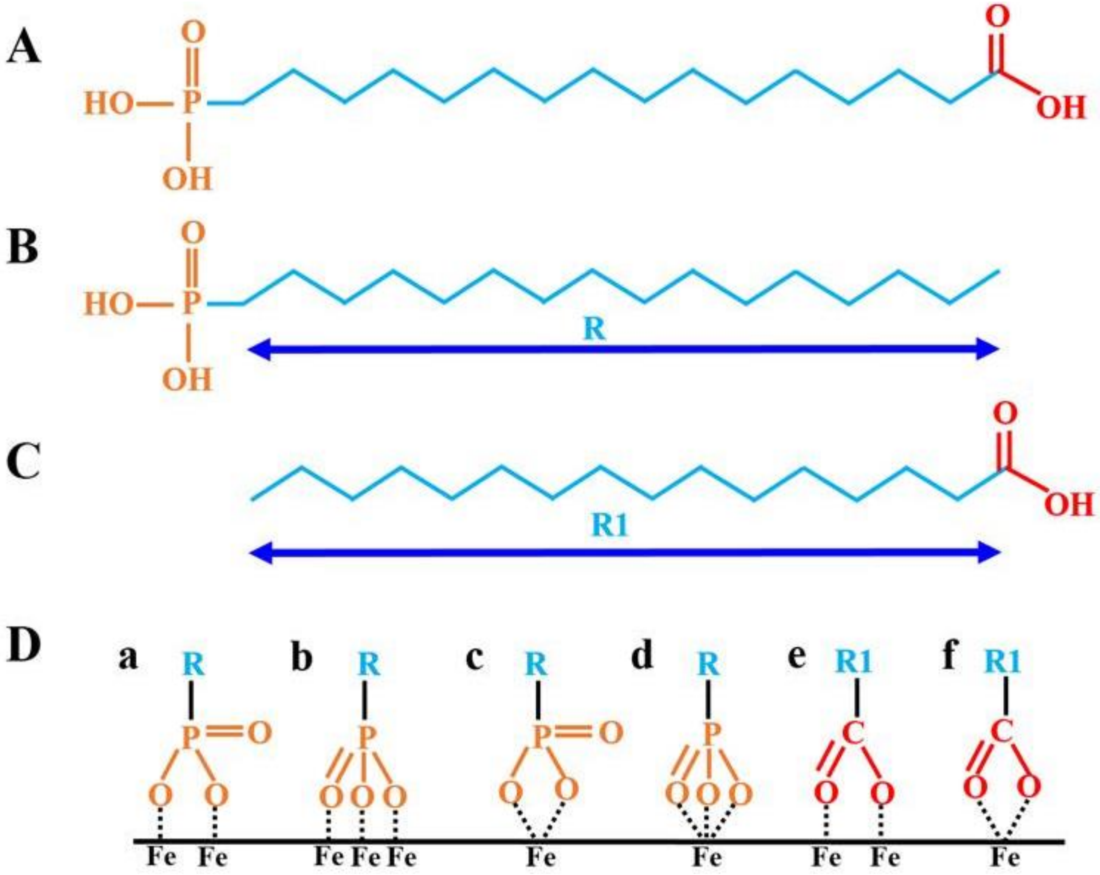

Figure 8.4 (A–C) Chemical structures of (A) 16PHA, (B) HDPA and (C) PA; (D) adsorption mechanisms, involving Fe atoms on the particle surface and (a–d) phosphonic acid group of HDPA or (e, f) carboxylic acid group of PA: (a, b,e) bridging, (c,d,f) chelation.

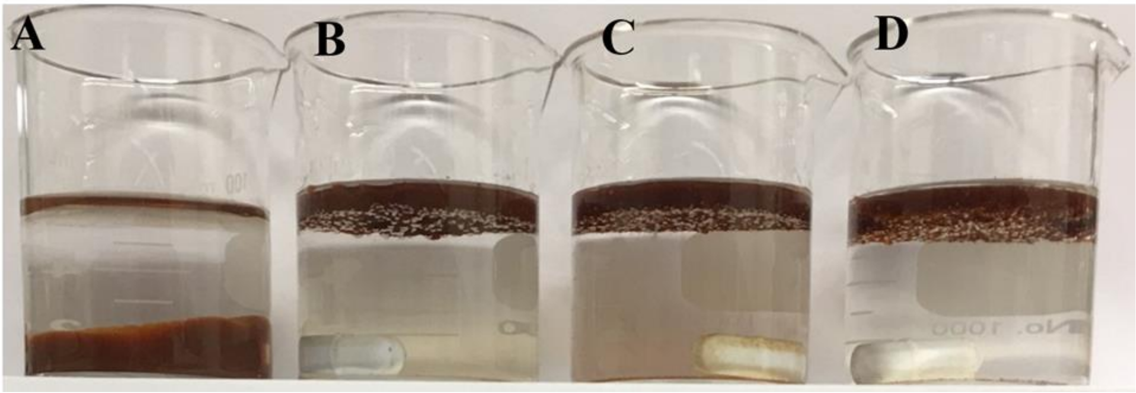

Figure 8.5 (A) as-prepared α-FeOOH, (B–D) extraction of α-FeOOH to the 1-butanol solvent, using (B) 16PHA, (C) HDPA and (D) PA.

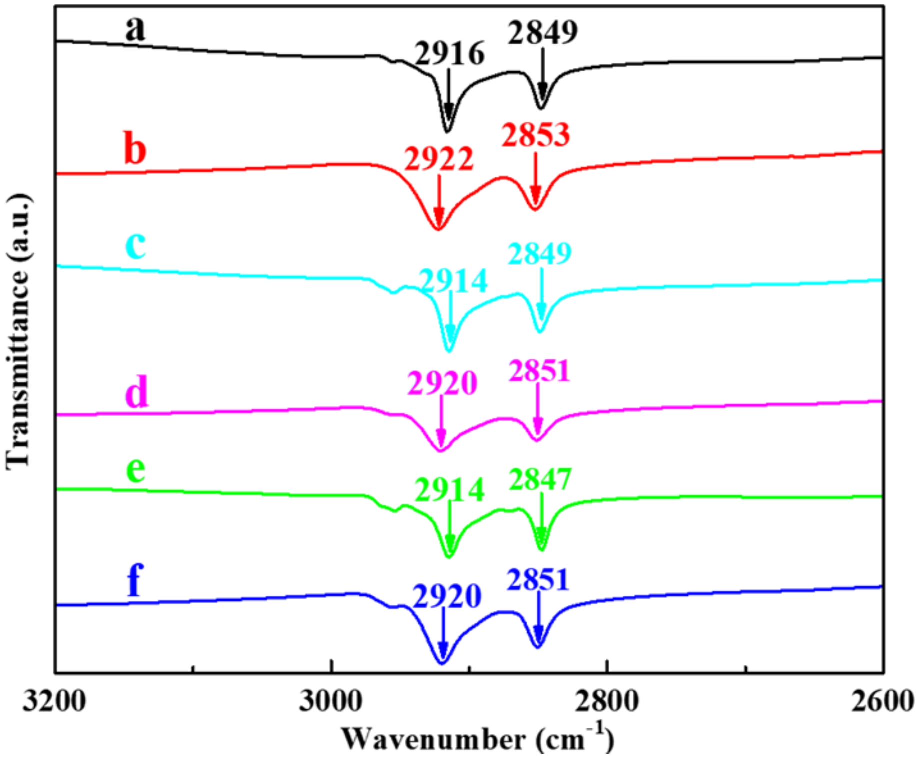

Figure 8.6 FTIR spectra of (a) 16PHA, (b) α-FeOOH, extracted using 16PHA, (c) HDPA and (d) α-FeOOH, extracted using HDPA, (e) PA, (f) α-FeOOH, extracted using PA.

The behavior of particles at the liquid-liquid interface is of fundamental importance for the understanding of PELLI mechanisms. It is known[32] that small particles with homogeneous surface chemical composition and properties can spontaneously accumulate at the interface of two immiscible liquids. The particle behavior at the liquid-liquid interface is influenced by particle weight, interfacial tension and hydrostatic pressure forces. Modeling results[32] have confirmed that, under thermodynamically favorable conditions, small colloidal particles with chemically homogeneous surfaces can spontaneously attach to the liquid interfaces. Moreover, it was found that colloidal particles can form two-dimensional ordered structures, containing non-agglomerated particles at the liquid-liquid interface. It was demonstrated[32] that particle interactions at the interface are significantly different from their interactions in the bulk. Experimental data and modeling revealed long-range repulsion forces, which facilitate particle de-agglomeration at the interface. The minimum energy required to detach a spherical particle with radius R from the interface of two immiscible liquids is proportional to R^2. As a result, small non-agglomerated particles showed preferred detachment from the interface. The energy of particle detachment into organic solvent is smaller for hydrophobic particles, while the opposite is true for hydrophilic particles[32].

Extractor molecules can accumulate at the liquid-liquid interface and become adsorbed on the particle surfaces. HDPA and PA are typical head-tail surfactants, containing hydrophilic phosphonic (HDPA) or carboxylic (PA) groups and long hydrophobic hydrocarbon chains. It is suggested that, similar to other head-tail surfactants, the HDPA and PA molecules accumulate at the liquid-liquid interface with hydrophilic groups exposed to water and hydrophobic hydrocarbon chains extending into the 1-butanol phase. The HDPA and PA molecules were adsorbed on the FeOOH particles at the liquid-liquid interface. Stirring promoted interaction between the extractor molecules and FeOOH particles. We cannot exclude the possibility that the accumulation of HDPA and PA at the liquid-liquid interface changed the interfacial surface tension, which, in turn, promoted particle accumulation. It is in this regard that the interfacial tension is one of the decisive factors for particle accumulation at the liquid-liquid interface[32]. The HDPA and PA adsorption imparted hydrophobic properties to the particles, and facilitated their detachment from the interface and transfer to the 1-butanol phase. Figure 8.7 shows a schematic of synthesis and extraction method 1. The mechanism A-B1-B2-D involved (A) particle precipitation in an aqueous phase, (B1) extractor molecule accumulation at the liquid-liquid interface, (B2) extractor molecule adsorption on the particles and (D) particle transfer to 1-butanol.

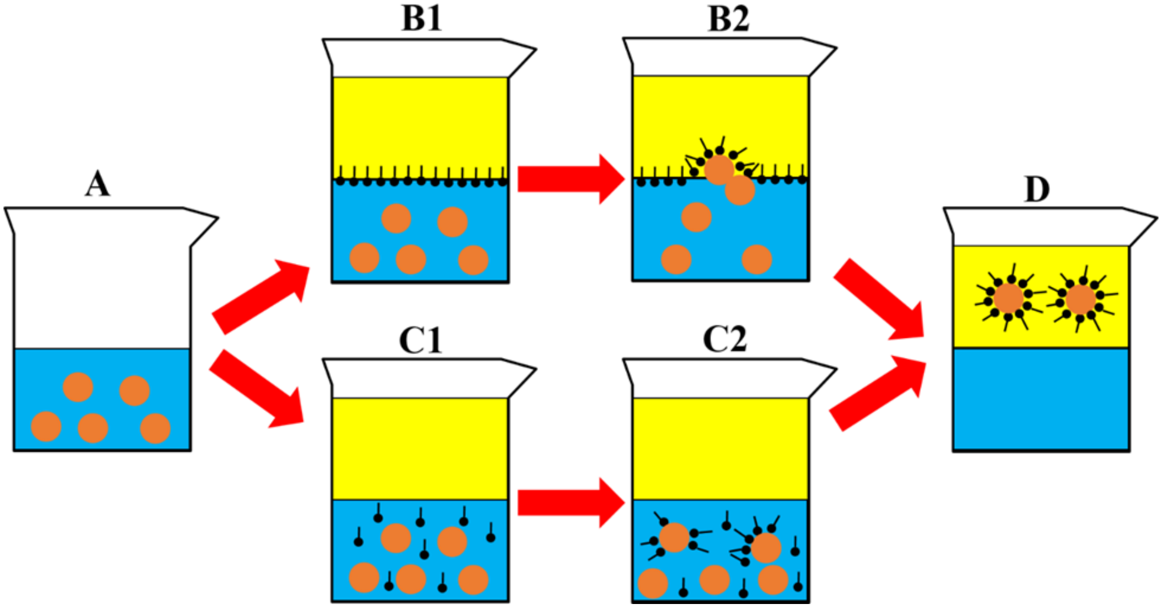

Figure 8.7 Schematic of the extraction mechanisms A-B1-B2-D and A-C1-C2-D in the extraction method 1: (A) as-prepared FeOOH particles in an aqueous phase, (B1,C1) the solution of extractor molecules in 1-butanol is added and extractor molecules (B1) accumulated at or (C1) penetrated the liquid-liquid interface, (B2,C2) extractor molecules

are adsorbed on the particles (B2) at the liquid-liquid interface or (C2) in the bulk of an aqueous phase, (D) particles are extracted to 1-butanol.

It is important to note that HDPA and PA are water insoluble molecules. In contrast, 16PHA is slightly soluble in water at pH = 7 and shows significant increase in solubility with pH increase. The chemical structure of 16PHA is different from the structures of HDPA and PA. It includes hydrophilic phosphonate and carboxylic end groups, which facilitate 16PHA solubility in water at high pH. Both end groups can be involved in the 16PHA adsorption on the particles. The FeOOH particles can potentially be extracted to the 1-butanol phase by the A-B1-B2-D mechanism using 16PHA. However, we suggest that 16PHA partially dissolved in water (Figure 8.7C1) and adsorbed on the particle surface (Figure 8.7C2). The bonding of 16PHA to the Fe atoms resulted in the formation of water-insoluble surface complexes and facilitated the transfer of the FeOOH particles, containing adsorbed 16PHA to the 1-butanol phase. In order to confirm the feasibility of the A-C1-C2-D mechanism (Figure 8.7), we developed an extraction method 2, which is schematically shown in Figure 8.8. In this method (Figure 8.8), (A) 16PHA was dissolved in alkali and added to (B) $FeCl_3$ solution to form (C) a suspension of FeOOH particles in water, which (D) were then spontaneously extracted to the added 1-butanol solvent. The feasibility of particle extraction in method 2 confirmed that 16PHA can be adsorbed on the FeOOH particles in aqueous phase and then transformed to the organic phase. Therefore, 16PHA can be used not only as an extractor in the PELLI method, but also as a capping agent for the FeOOH synthesis.

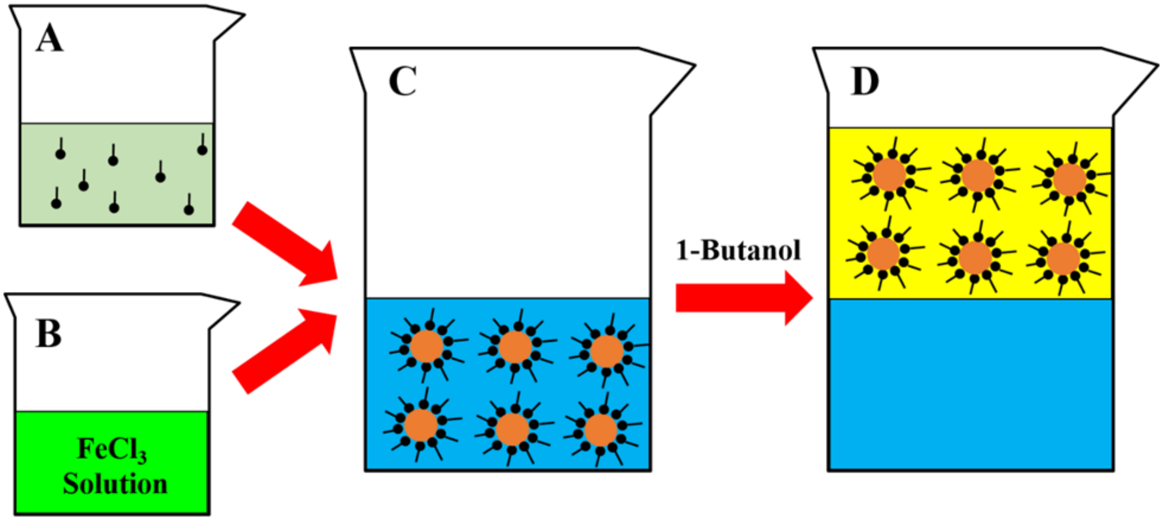

Figure 8.8 Schematic of the extraction method 2: (A) 16PHA is dissolved in alkali and added to (B) $FeCl_3$ solution, (C) FeOOH particles, modified with 16PHA are formed and (D) after addition of 1-butanol the modified particles are transferred to the 1-butanol phase.

The extracted α-FeOOH and β-FeOOH particles were used to fabricate composite FeOOH-MWCNT electrodes, which were tested in the negative potential range. Figure 8.9A,B show CVs for α-FeOOH-MWCNT and β-FeOOH-MWCNT electrodes prepared by the extraction method 1 using 16PHA as an extractor. The CVs for the β-FeOOH-MWCNT electrodes (Figure 8.9A) deviated significantly from the ideal box shape and relatively low current was observed in the range of − 0.25–0 V. The α-FeOOH-MWCNT electrodes (Figure 8.9B) showed enhanced capacitive behavior, as indicated by an improved CV shape, higher currents and larger CV area, which resulted from higher capacitance. The α-FeOOH-MWCNT electrodes, prepared by method 2 showed a similar behavior (Figure 8.9C). The capacitances of the electrodes calculated from the CV data at different scan rates are presented in Figure 8.9D. The α-FeOOH-MWCNT electrodes prepared by method 1 showed significantly higher capacitance, compared to the capacitance of β-FeOOH-

MWCNT electrodes at the same electrode mass. The capacitance of β-FeOOH-MWCNT electrodes decreased from 2.84 to 1.36 F cm^{-2} with increasing scan rate from 2 to 100 mV s^{-1}. The capacitance of α-FeOOH-MWCNT electrodes decreased from 5.34 to 1.98 F cm^{-2} in the same scan rate range. This result is surprising taking into account TGA data, which showed lower Fe content in the α-FeOOH material. It is in this regard that capacitive behavior of FeOOH resulted from the reduction of Fe^{3+} species. The difference in the capacitive behavior of α-FeOOH-MWCNT and β-FeOOH-MWCNT can be attributed to the different ionic conductivities and particle morphologies of α-FeOOH and β-FeOOH. It is important to note that the detailed analysis of the particle morphology presented difficulties, because drying procedure was avoided and particles were directly transferred to the 1-butanol phase for the fabrication of electrodes. The α-FeOOH-MWCNT electrodes prepared using extraction method 2 showed a capacitance of 5.86 F cm^{-2} at a scan rate of 2 mV s^{-1}. The capacitance decreased to 1.51 F cm^{-2} with an increase in the scan rate to 100 mV s^{-1}. Comparison with literature data on the capacitance of FeOOH based electrodes, presented above in the Introduction, indicated that use of PELLI provides the highest capacitance in Na_2SO_4 electrolyte.

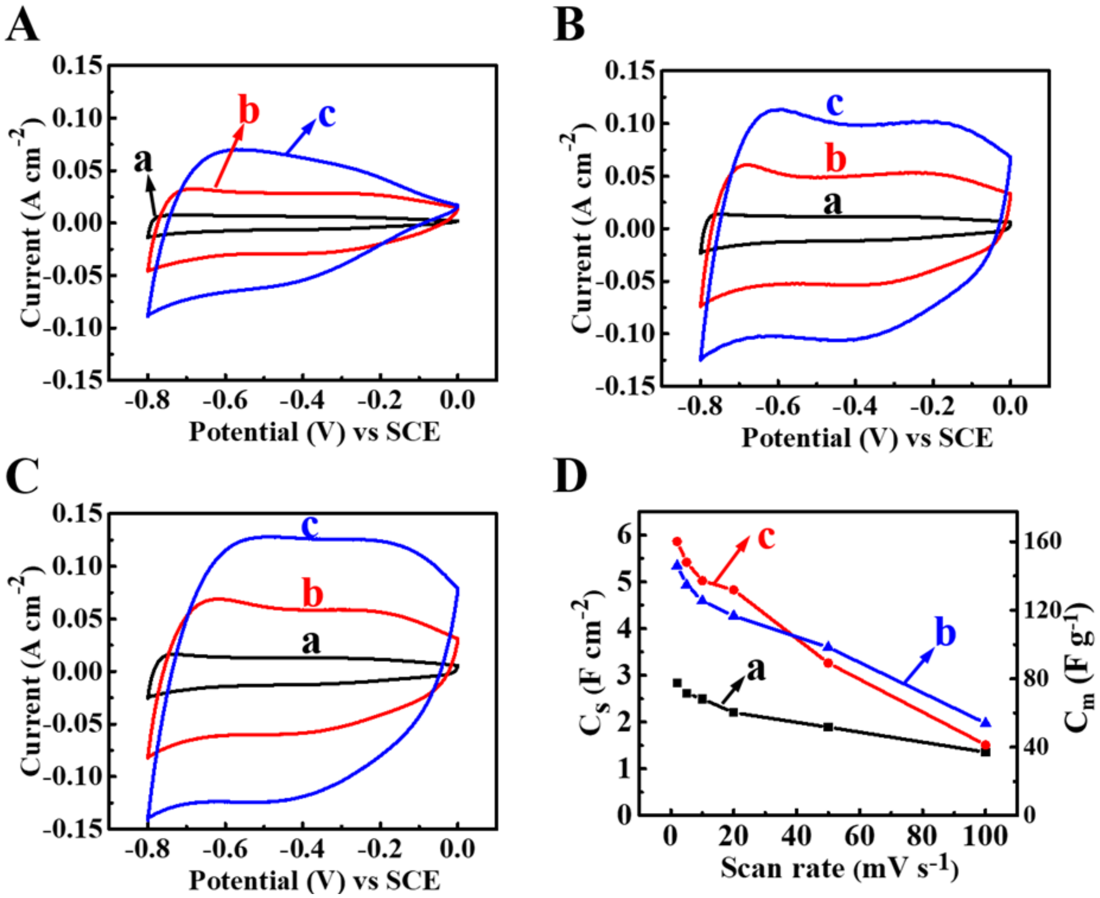

Figure 8.9 (A–C) CVs at scan rates of (a) 2, (b) 10 and (c) 20 mV s^{-1} and (D) C_S and C_m for (A, D(a)) β-FeOOH-MWCNT, prepared using 16PHA and extraction method 1, (B, D(b)) α-FeOOH-MWCNT, prepared using 16PHA and extraction method 1, (C, D(c)) α-FeOOH-MWCNT, prepared using 16PHA and extraction method 2.

The analysis of the impedance data, presented in the Nyquist plot in Figure 8.10A revealed a relatively low resistance (Z′=R), which is critically important for SC applications. The AC capacitance, calculated from the impedance data, showed a relaxation type dispersion[33], as indicated by the reduction of C_S' with increasing frequency(Figure 8.10B) and relaxation maxima in the frequency dependences of C_S'' (Figure 8.10C). The investigations at low frequencies revealed higher C_S' of α-FeOOH-MWCNT electrodes as compared to β-FeOOH-MWCNT electrodes (Figure 8.10B(a,b)), in agreement with the corresponding capacitances calculated from the CV data. The α-FeOOH-MWCNT electrodes, prepared using the PELLI method 2 showed the highest capacitance at low frequencies (Figure 8.10B(c)). The higher frequency of the relaxation maximum for α-FeOOH-MWCNT electrodes, prepared using PELLI-1 method, indicated better capacitance retention at higher frequencies (Figure 8.10C (b,c)).

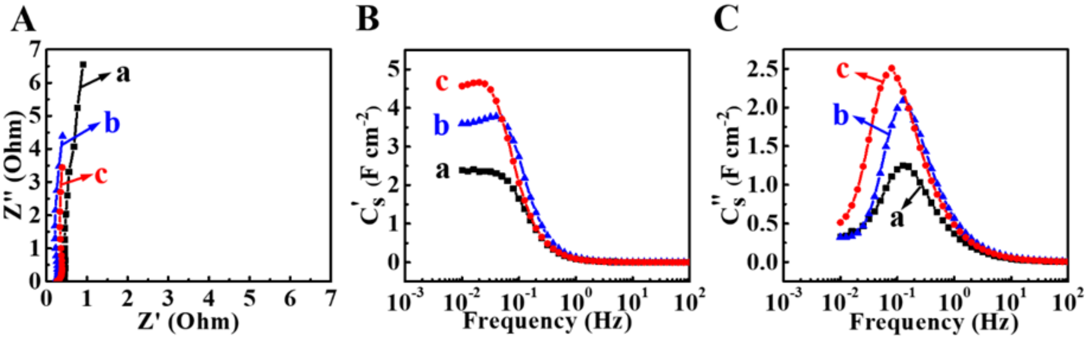

Figure 8.10 (A) Nyquist plot of complex impedance and frequency dependences of (B) real C_S' and (C) imaginary C_S'' components of complex capacitance, calculated from the impedance data for (a) β-FeOOH-MWCNT, prepared using 16PHA and extraction method 1, (b) α-FeOOH-MWCNT, prepared using 16PHA and extraction method 1, (c) α-FeOOH-MWCNT, prepared using 16PHA and extraction method 2.

The use of PELLI methods allowed significant improvement in the capacitive behavior of α-FeOOH-MWCNT electrodes. Fig. 11A shows CVs for α-FeOOH-MWCNT electrodes prepared by a traditional method, which involved drying of α-FeOOH and re-dispersion in alcohol. The CV data showed low currents, especially in the range from − 0.3–0 V, which resulted from low capacitance. The use of PELLI with HDPA and PA extractors allowed improved capacitive behavior, as indicated by higher currents and larger CV area (Figure 8.11B,C). However, the highest capacitance was obtained using PELLI with the 16PHA extractor. The capacitances of the α-FeOOH-MWCNT electrodes prepared without PELLI

(Figure 8.11D(a)), using PELLI and HDPA extractor (Figure 8.11D(b)) and using PELLI and PA extractor (Figure 8.11D(c)) were lower than the capacitances obtained using PELLI with 16PHA extractor (Figure 8.9D(b)). The use of PELLI significantly reduced the electrode resistance (Figure 8.12A) and improved capacitive behavior, especially at frequencies between 10 mHz – 1 Hz (Figure 8.12B,C).

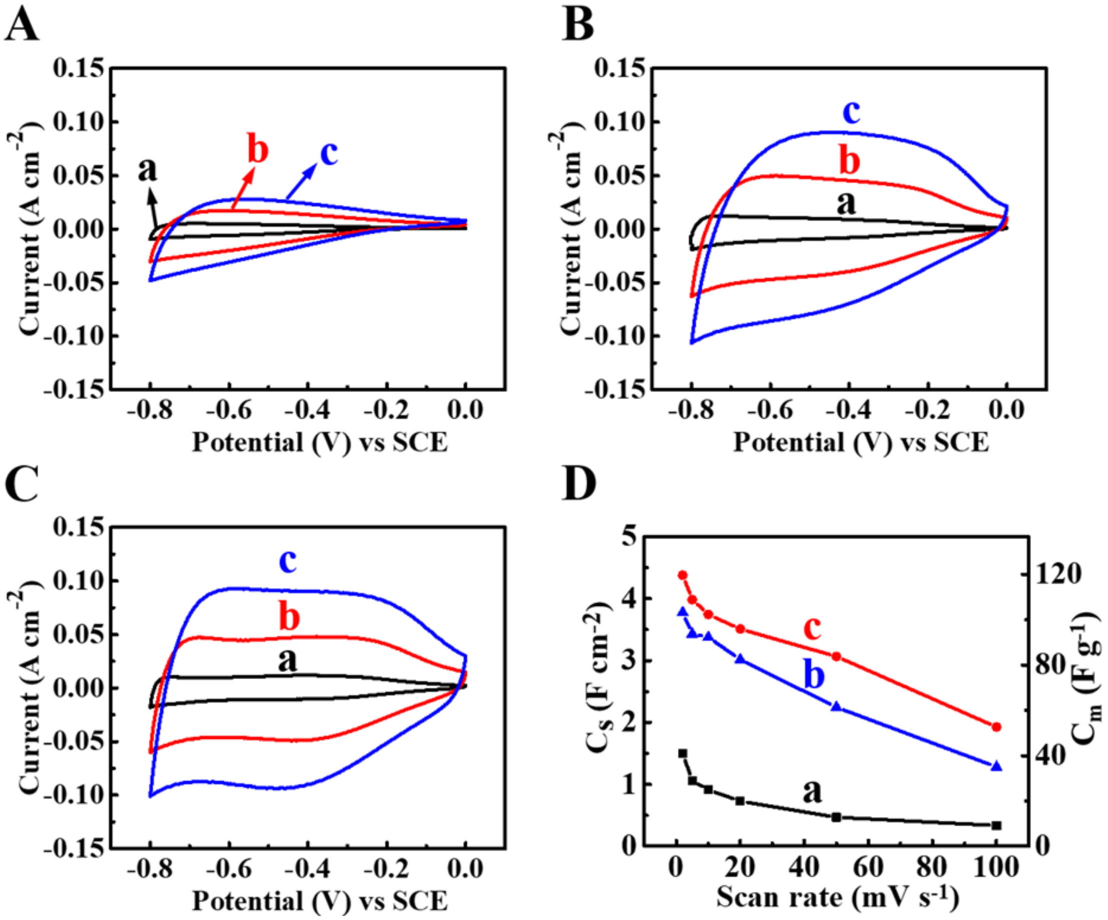

Figure 8.11 (A–C) CVs at scan rates of (a) 2, (b) 10 and (c) 20 mV s^{-1} and (D) C_S and C_m for α-FeOOH-MWCNT, prepared (A, D(a)) without extraction, (B, D(b)) using HDPA and extraction method 1, (C, D(c)) using PA and extraction method 1.

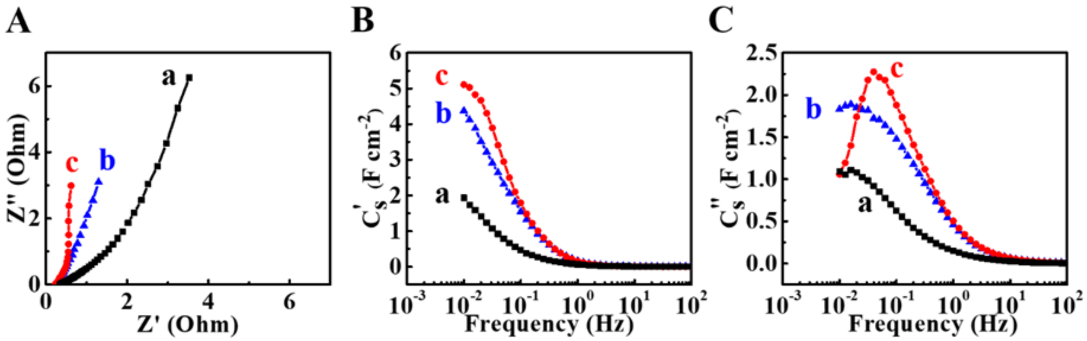

Figure 8.12 (A) Nyquist plot of complex impedance and frequency dependences of (B) real C_S' and (C) imaginary C_S'' components of complex capacitance, calculated from the impedance data for α-FeOOH-MWCNT, prepared (a) without extraction, (b) using HDPA and extraction method 1, (c) using PA and extraction method 1.

This investigation provides evidence that PELLI facilitated the fabrication of FeOOH-MWCNT electrodes with enhanced electrochemical performance at high active mass loadings. The ability to avoid powder drying by phase transfer allowed for reduced particle agglomeration. It is known[34] that drying often leads to the complete loss of the ability to re-disperse particles. Moreover, the literature data for particle behavior at liquid-liquid interfaces[32], discussed above, indicated that particle transfer through the interface can promote de-agglomeration of soft agglomerates formed in an aqueous phase. The reduced agglomeration facilitated FeOOH mixing with conductive MWCNT. Figure 8.13 compares microstructures of the α-FeOOH-MWCNT electrodes prepared without PELLI and using the PELLI method 1 and 16PHA as an extractor. The analysis of the SEM image of the composite, prepared without PELLI showed large agglomerates and poor mixing of the components. In contrast, SEM studies indicated that good mixing of α-FeOOH and MWCNT can be achieved using PELLI. The reduced α-FeOOH agglomeration allowed efficient mixing with MWCNT and facilitated electrolyte access to the particle surface. As a result, we achieved a relatively high capacitance for a negative α-FeOOH-MWCNT electrode in Na_2SO_4 electrolyte, which matched the capacitance of advanced positive MnO_2-MWCNT electrodes[29] in the same electrolyte and at similar active mass loadings. Therefore, the results of this investigation illustrate a way to fabricate advanced asymmetric devices. Such devices showed nearly ideal box shape CVs in enlarged voltage window of 1.6 V (Figure 8.14A). The capacitance was calculated from the CV data at different scan rates, from impedance data at different frequencies and from galvanostatic discharge data at different current densities. The integral capacitance C_S in the voltage window of 1.6 V, calculated from the CV data was 2.64 F cm^{-2}. The capacitance decreased with increasing scan rate due to electrolyte diffusion limitations in the electrodes and a membrane (Figure 8.14B). The C_S at a scan rate of 100 mV s^{-1} was found to be 0.58 F cm^{-2}.

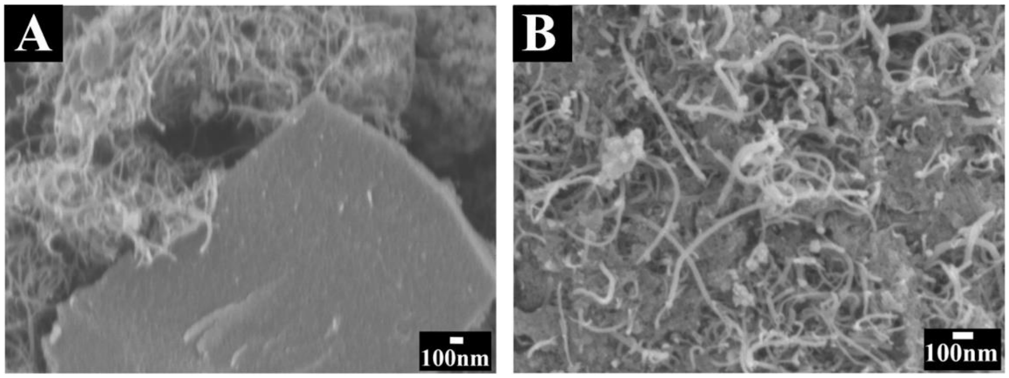

Figure 8.13 SEM image of α-FeOOH-MWCNT composite, prepared (A) without PELLI and (B) by the PELLI method 1 using 16PHA.

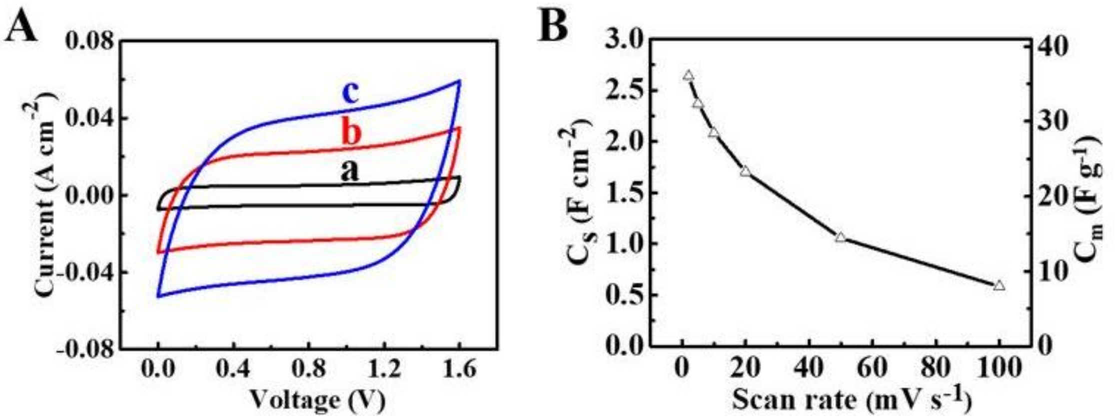

Figure 8.14 (A) CVs at scan rates of (a) 2, (b) 10 and (c) 20 mV s^{-1} (B) C_S and C_m versus scan rate for an asymmetric supercapacitor cell, containing MnO_2-MWCNT positive electrode and α-FeOOH-MWCNT negative electrode.

Figure 8.15A shows impedance data, presented in a Nyquist plot. The resistance $R = Z'$ of the device was higher than of the individual electrodes. It included the resistances of the individual electrodes and the resistance of the electrolyte in the pores of the membrane material. The frequency dependencies of the components of the complex AC capacitance showed (Figure 8.15B,C) a relaxation type[33] dispersion. The real part of the capacitance at 10 mHz was found to be 1.80 F cm^{-2}. The lower relaxation frequency, corresponding to the C_S'' maximum (Figure 8.15C), compared to the relaxation frequency of the individual electrodes can result from a larger cell resistance[35].

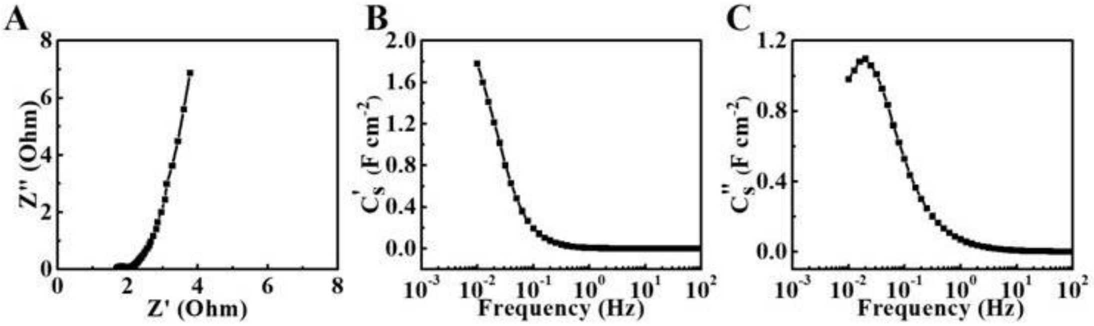

Figure 8.15 (A)Nyquist plot of complex impedance, and frequency dependences of (B) real C_S' and (C) imaginary C_S'' components of complex capacitance, calculated from the impedance data for an asymmetric supercapacitor cell, containing MnO$_2$-MWCNT positive electrode and α-FeOOH-MWCNT negative electrode.

The charge-discharge behavior of the SC device was analyzed at different current densities in the range from 3 to 50 mA cm^{-2} and at a cell voltage of 1.6 V. The galvanostatic charge-discharge curves (Figure 8.16A) were of nearly ideal symmetric triangular shape, which indicated good capacitive behavior. The capacitance (Figure 8.16B) decreased with increasing current density in the range from 2.91 to 2.19 F cm^{-2}. Testing results indicated that the differential AC capacitance measured at a voltage of 5 mV was lower than the integral capacitance calculated from the CV or galvanostatic charge-discharge data in the voltage window of 0–1.6 V. The difference in the differential and integral capacitances can be attributed to various factors discussed in the literature[36-38] [36], such as poor access of ions to redox sites at low voltages, physical heterogeneity of the electrodes and other factors. The galvanostatic discharge data was used for the analysis of power-energy characteristics of the SC device at different current densities in the range of 3–50 mA cm^{-2}. The device showed (Figure 8.16C) areal energy density of 0.62–0.97 mW h cm^{-2} and power density of 2.2–31.8 mW cm^{-2}.

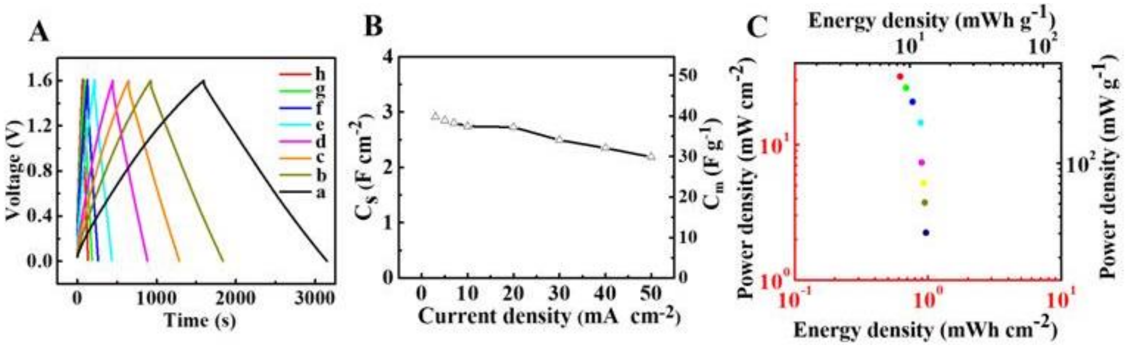

Figure 8.16 (A) Charge-discharge curves at current densities of (a) 3, (b) 5, (c)7, (d) 10, (e) 20, (f) 30, (g) 40 and (h) 50 mA cm^{-2}, (B) C_S and C_m calculated from the charge-discharge curves versus current density and (C) Ragone plot for an asymmetric supercapacitor cell, containing MnO_2-MWCNT positive electrode and α-FeOOH-MWCNT negative electrode.

8.5 Conclusions

PELLI strategies have been developed for the fabrication of α-FeOOH and β-FeOOH for energy storage in negative SC electrodes. PELLI allowed agglomerate-free processing of powders, which facilitated their efficient mixing with MWCNT and improved electrolyte access to the particle surface. 16PHA, HDPA and PA showed strong adsorption on particle surface and allowed for efficient extraction. Two different extraction methods have been developed, which involved extractor adsorption on particles at the liquid-liquid interface or in an aqueous phase. The use of PELLI allowed for significant improvement in capacitive properties. The important finding was the ability to achieve high electrochemical performance of negative electrodes at active mass loadings as high as 37 mg cm^{-2}. α-FeOOH-MWCNT electrodes showed higher capacitance, compared to β-FeOOH-MWCNT electrodes. The highest capacitance of 5.86 F cm^{-2} for negative electrodes and low impedance were achieved using α-FeOOH-MWCNT and 16PHA as an extractor. The capacitance of negative α-FeOOH-MWCNT electrodes matched the capacitance of advanced MnO_2-MWCNT positive electrodes at similar active mass loading. This opened a way for the fabrication of advanced asymmetric SC devices for operation in a voltage window of 1.6 V. Cyclic voltammetry, impedance spectroscopy and galvanostatic charge-discharge data showed high capacitance, low impedance and good power-energy characteristics. The approach, developed in this investigation is promising for agglomerate-free processing of other powder materials and their application in advanced composites.

8.6 References

[1] R. Barik, B. K. Jena, and M. Mohapatra, "Metal doped mesoporous FeOOH nanorods for high performance supercapacitors," *Rsc Advances,* vol. 7, pp. 49083-49090, 2017.

[2] R. Barik, B. K. Jena, A. Dash, and M. Mohapatra, "In situ synthesis of flowery-shaped alpha-FeOOH/Fe_2O_3 nanoparticles and their phase dependent supercapacitive behaviour," *Rsc Advances,* vol. 4, pp. 18827-18834, 2014.

[3] Z. C. Li, S. S. Chen, A. J. Gu, Z. X. Wang, and X. H. Chen, "Facile hydrothermal synthesis and electrochemical properties of hollow urchin-like α-FeOOH," *Micro & Nano Letters,* vol. 7, pp. 757-761, 2012.

[4] K. F. Chen, X. Chen, and D. F. Xue, "Hydrothermal route to crystallization of FeOOH nanorods via $FeCl_3$ center dot 6H($_2$)O: effect of Fe^{3+} concentration on pseudocapacitance of iron-based materials," *Crystengcomm,* vol. 17, pp. 1906-1910, 2015.

[5] L. Cheng, H. Q. Li, and Y. Y. Xia, "A hybrid nonaqueous electrochemical supercapacitor using nano-sized iron oxyhydroxide and activated carbon," *Journal of Solid State Electrochemistry,* vol. 10, pp. 405-410, Jun 2006.

[6] R. Sahoo, A. Pal, and T. Pal, "Proportion of composition in a composite does matter for advanced supercapacitor behavior," *Journal of Materials Chemistry A,* vol. 4, pp. 17440-17454, 2016.

[7] Y. C. Chen, Y. G. Lin, Y. K. Hsu, S. C. Yen, K. H. Chen, and L. C. Chen, "Novel Iron Oxyhydroxide Lepidocrocite Nanosheet as Ultrahigh Power Density Anode Material for Asymmetric Supercapacitors," *Small,* vol. 10, pp. 3803-3810, Sep 24 2014.

[8] K. K. Lee, R. W. Y. Ng, K. K. She, W. S. Chin, and C. H. Sow, "Vertically aligned iron (III) oxyhydroxide/oxide nanosheets grown on iron substrates for electrochemical charge storage," *Materials Letters,* vol. 118, pp. 150-153, Mar 1 2014.

[9] V. S. Jamadade, V. J. Fulari, and C. D. Lokhande, "Supercapacitive behavior of electrosynthesized marygold-like structured nickel doped iron hydroxide thin film," *Journal of Alloys and Compounds,* vol. 509, pp. 6257-6261, May 26 2011.

[10] Q. Lu, L. Liu, S. L. Yang, J. Liu, Q. Y. Tian, W. J. Yao*, et al.*, "Facile synthesis of amorphous FeOOH/MnO_2 composites as screen-printed electrode materials for all-printed solid-state flexible supercapacitors," *Journal of Power Sources,* vol. 361, pp. 31-38, Sep 1 2017.

[11] M. Y. Zhu, Y. Wang, and X. Zhang, "Hydrothermal Synthesis of Akaganeite Nanorods and Their Supercapacitance Property," *Journal of Inorganic and Organometallic Polymers and Materials*, vol. 25, pp. 982-985, Jul 2015.

[12] J. S. Sagu, K. G. U. Wijayantha, M. Bohm, S. Bohm, and T. K. Rout, "Anodized Steel Electrodes for Supercapacitors," *Acs Applied Materials & Interfaces,* vol. 8, pp. 6277-6285, Mar 9 2016.

[13] J. Yang, H. Wang, and R. F. Wang, "Facile synthesis of core-shell FeOOH@MnO_2 nanomaterials with excellent cycling stability for supercapacitor electrodes," *Journal of Materials Science-Materials in Electronics,* vol. 28, pp. 6481-6487, May 2017.

[14] S. N. Yang, Y. J. Li, T. F. Xu, Y. G. Li, H. Q. Fu, K. Cheng, *et al.*, "FeOOH electrodeposited on Ag decorated ZnO nanorods for electrochemical energy storage," *Rsc Advances,* vol. 6, pp. 39166-39171, 2016.

[15] F. X. Wang, Y. X. Zeng, D. Z. Zheng, C. Li, P. Liu, X. H. Lu, *et al.*, "Three-dimensional iron oxyhydroxide/reduced graphene oxide composites as advanced electrode for electrochemical energy storage," *Carbon,* vol. 103, pp. 56-62, Jul 2016.

[16] N. Li, C. Y. Zhi, and H. Y. Zhang, "High-performance Transparent and Flexible Asymmetric Supercapacitor based on Graphene-wrapped Amorphous FeOOH Nanowire and Co(OH)($_2$) Nanosheet Transparent Films Produced at air-water interface," *Electrochimica Acta,* vol. 220, pp. 618-627, Dec 1 2016.

[17] L. F. Chen, Z. Y. Yu, J. J. Wang, Q. X. Li, Z. Q. Tan, Y. W. Zhu, *et al.*, "Metal-like fluorine-doped beta-FeOOH nanorods grown on carbon cloth for scalable high-performance supercapacitors," *Nano Energy,* vol. 11, pp. 119-128, Jan 2015.

[18] W. H. Jin, G. T. Cao, and J. Y. Sun, "Hybrid supercapacitor based on MnO_2 and columned FeOOH using Li2SO4 electrolyte solution," *Journal of Power Sources,* vol. 175, pp. 686-691, Jan 3 2008.

[19] X. F. Gong, S. H. Li, and P. S. Lee, "A fiber asymmetric supercapacitor based on FeOOH/PPy on carbon fibers as an anode electrode with high volumetric energy density for wearable applications," *Nanoscale,* vol. 9, pp. 10794-10801, Aug 14 2017.

[20] H. W. Chang, C. L. Dong, Y. R. Lu, Y. C. Huang, J. L. Chen, C. L. Chen, *et al.*, "X-ray Absorption Spectroscopic Study on Interfacial Electronic Properties of FeOOH/Reduced Graphene Oxide for Asymmetric Supercapacitors," *Acs Sustainable Chemistry & Engineering,* vol. 5, pp. 3186-3194, Apr 2017.

[21] R. Liu, L. N. Ma, G. D. Niu, X. L. Li, E. Y. Li, Y. Bai, *et al.*, "Flexible Ti-Doped FeOOH Quantum Dots/Graphene/Bacterial Cellulose Anode for High-Energy Asymmetric Supercapacitors," *Particle & Particle Systems Characterization,* vol. 34, Oct 2017.

[22] Y. X. Wei, R. M. Ding, C. H. Zhang, B. L. Lv, Y. Wang, C. M. Chen, *et al.*, "Facile synthesis of self-assembled ultrathin alpha-FeOOH nanorod/graphene oxide composites for supercapacitors," *Journal of Colloid and Interface Science,* vol. 504, pp. 593-602, Oct 15 2017.

[23] Y. M. Lv, H. W. Che, A. F. Liu, J. B. Mu, C. X. Dai, X. L. Zhang, *et al.*, "Urchin-like alpha-FeOOH@MnO$_2$ core-shell hollow microspheres for high-performance supercapacitor electrode," *Journal of Applied Electrochemistry,* vol. 47, pp. 433-444, Apr 2017.

[24] G. J. Wei, K. Du, X. X. Zhao, C. Li, J. Q. Li, K. K. Ren, *et al.*, "Integrated FeOOH nanospindles with conductive polymer layer for high-performance supercapacitors," *Journal of Alloys and Compounds,* vol. 728, pp. 631-639, Dec 25 2017.

[25] Z. C. Li, M. Y. Guan, Z. S. Lou, and T. M. Shang, "Facile hydrothermal synthesis and electrochemical properties of flowerlike alpha-FeOOH," *Micro & Nano Letters,* vol. 7, pp. 33-36, Jan 2012.

[26] P. M. Hallam, M. Gomez-Mingot, D. K. Kampouris, and C. E. Banks, "Facile synthetic fabrication of iron oxide particles and novel hydrogen superoxide supercapacitors," *Rsc Advances,* vol. 2, pp. 6672-6679, 2012.

[27] Y. Gogotsi and P. Simon, "True Performance Metrics in Electrochemical Energy Storage," *Science,* vol. 334, pp. 917-918, Nov 18 2011.

[28] K. A. Owusu, L. B. Qu, J. T. Li, Z. Y. Wang, K. N. Zhao, C. Yang, *et al.*, "Low-crystalline iron oxide hydroxide nanoparticle anode for high-performance supercapacitors," *Nature Communications,* vol. 8, Mar 6 2017.

[29] R. Chen, M. S. Ata, X. Y. Zhao, I. Puri, and I. Zhitomirsky, "Liquid-liquid extraction of oxide particles and application in supercapacitors," *Journal of Materials Research*, vol. 32, pp. 3242-3250, Sep 2017.

[30] R. Chen, M. S. Ata, X. Y. Zhao, A. Clifford, I. Puri, and I. Zhitomirsky, "Strategies for liquid-liquid extraction of oxide particles for applications in supercapacitor electrodes and thin films," *Journal of Colloid and Interface Science,* vol. 499, pp. 1-8, Aug 1 2017.

[31] J. Erler, S. Machunsky, P. Grimm, H. J. Schmid, and U. A. Peuker, "Liquid-liquid phase transfer of magnetite nanoparticles - Evaluation of surfactants," *Powder Technology,* vol. 247, pp. 265-269, Oct 2013.

[32] B. P. Binks and T. S. Horozov, *Colloidal particles at liquid interfaces*: Cambridge University Press, 2006.

[33] K. Y. Shi and I. Zhitomirsky, "Influence of current collector on capacitive behavior and cycling stability of Tiron doped polypyrrole electrodes," *Journal of Power Sources,* vol. 240, pp. 42-49, Oct 15 2013.

[34] M. Brust, M. Walker, D. Bethell, D. J. Schiffrin, and R. Whyman, "Synthesis of Thiol-Derivatized Gold Nanoparticles in a 2-Phase Liquid-Liquid System," *Journal of the Chemical Society-Chemical Communications,* pp. 801-802, Apr 7 1994.

[35] Y. Su and I. Zhitomirsky, "Asymmetric electrochemical supercapacitor, based on polypyrrole coated carbon nanotube electrodes," *Applied Energy,* vol. 153, pp. 48-55, Sep 1 2015.

[36] X. M. Ren and P. G. Pickup, "The Origin of the Discrepancy between the Low-Frequency Ac Capacitances and Voltammetric Capacitances of Conducting Polymers," *Journal of Electroanalytical Chemistry,* vol. 372, pp. 289-291, Jul 18 1994.

[37] J. Tanguy, N. Mermilliod, and M. Hoclet, "Capacitive Charge and Noncapacitive Charge in Conducting Polymer Electrodes," *Journal of the Electrochemical Society*, vol. 134, pp. 795-802, Apr 1987.

[38] B. J. Feldman, P. Burgmayer, and R. W. Murray, "The Potential Dependence of Electrical-Conductivity and Chemical Charge Storage of Poly(Pyrrole) Films on Electrodes," *Journal of the American Chemical Society*, vol. 107, pp. 872-878, 1985.

9 Polypyrrole-carbon nanotube-FeOOH composites for negative electrodes of asymmetric supercapacitors

This chapter is reproduced from *Polypyrrole-carbon nanotube-FeOOH composites for negative electrodes of asymmetric supercapacitors, 166 (6), A935-A940, 2019, Journal of Electrochemical Society,* ***Ri Chen****, Ishwar K. Puri and Igor Zhitomirsky, doi: 10.1149/2.0281906jes, Copyright 2019, with permission from ECS -- The Electrochemical Society*. The author of this thesis is the first author and the main contributor of this publication.

9.1 Abstract

For the first time, polypyrrole (PPy) coated carbon nanotubes (CNT) were combined with FeOOH to fabricate negative supercapacitor (SC) electrodes. The synergistic effects of PPy-CNT and FeOOH resulted in enhanced electrochemical performance at high active mass loading of 37 mg cm^{-2} in a voltage window of −0.8 – +0.1 V versus a saturated calomel electrode. Particle extraction through liquid-liquid interface (PELLI) was utilized for the agglomerate-free processing of FeOOH, which improved FeOOH mixing with PPy-CNT and contributed to the enhanced capacitive behavior of the composite. Tetradecylamine (TDA) was found to be an efficient extractor for FeOOH. Cyclic voltammetry and impedance spectroscopy data at different electrode potentials provided an insight into the synergistic effects of PPy-CNT and FeOOH, and influence of PELLI on electrode performance. An areal capacitance of 4.5 F cm^{-2} and nearly ideal capacitive behavior were achieved at a low electrode impedance. The important finding was that

capacitances of the negative PPy-CNT-FeOOH and positive MnO_2-CNT electrodes can be matched in different voltage windows to fabricate advanced asymmetric devices, which exhibited promising electrochemical performance in a voltage window of 1.6 V at high active mass.

9.2 Introduction

PPy - metal oxide (MO) and PPy - metal hydroxide (MOH) composites combine advanced functional properties of PPy, MO and MOH. Various PPy-MO composites have been developed, containing individual MO components, such as Fe_3O_4[1], SnO_2[2], TiO_2[3], V_2O_5[4], NiO[5], ZnO[6], MnO_2[7], CuO and Cu_2O[8]. Complex oxides, such as $MnCo_2O_4$[9], $NiCo_2O_4$[10], $LiCoO_2$[11] and $ZnFe_2O_4$[12] have also been used to develop advanced PPy-MO composites. PPy-MOH composites have been fabricated with $Co(OH)_2$[13] FeOOH[14] and $Ni(OH)_2$[15]. Of particular interest are materials, containing PPy and various iron oxides and hydroxides that have been investigated to fabricate actuators[16], batteries[17], magnetic and microwave absorption devices[1], drug delivery systems[18], electrocatalytic[19] and water purification devices[20], tumor targeting biomaterials[14], imaging guided photothermal cancer therapy devices[21], sensors[22] and supercapacitors (SC)[23].

The use of PPy has also facilitated the fabrication of flexible devices[24]. The high conductivity and redox-active properties of PPy are being explored to manufacture functional composites[25].The use of PPy as a conductive binder and film forming agent offers advantages for various energy storage devices and thin film applications. A number of studies have examined the synergistic effect[16, 26, 27] of PPy, MO and MOH. Major focus areas include improvement in microstructure, formation of hierarchical materials, design of composite particles and fibers[4, 11, 17, 28]. Investigation revealed the crucial need in efficient dispersion of MO and MOH particles in the PPy matrix[26]. Emphasis was placed on the development of advanced dispersion techniques, new colloidal and surface modification technologies[29].

The high conductivity, flexibility and redox properties of PPy have been utilized for energy storage in the positive electrodes of SC[30, 31]. Many attempts have been made to enhance electrochemical performance using fibrous, nanowire, nanotube and nanorod composite materials[32-34]. A wire-shaped flexible SC[30], containing PPy-MnO_2 positive electrodes displayed a capacitance of 0.613 F cm^{-2}. RuO_x particles were deposited on PPy nanorods[31] and obtained electrodes showed a capacitance of 0.419 F cm^{-2}. Electrochemical performance was enhanced using carbon nanotube additives[35].

PPy-Fe_2O_3 composites have also been developed to fabricate negative SC electrodes[36], where a capacitance of 0.382 F cm^{-2} was achieved. PPy was utilized to fabricate binderless negative electrodes[37]. PPy-FeOOH-carbon fiber[38] negative electrodes showed relatively high specific capacitance for low mass loading and high resistance. Many recent investigations have been limited to very low mass loadings (below 1–3 mg cm^{-2}), which are not suitable for practical SC applications[39]. Therefore, an emphasis has been placed[40, 41] on the electrode performance at practical mass loadings above 10–20 mg cm^{-2} and the fabrication of electrodes with high areal capacitance and high power.

The high active mass loading is beneficial to obtain low relative mass of current collectors and other passive components of the SC devices. An increase in the active mass loading from 1–3 mg cm^{-2} to 10–20 mg cm^{-2} requires a proportionally larger amount of charge to be delivered over a significantly larger electrode thickness[39]. As a result of limited electrolyte access to the active material and low electronic conductivity, the mass normalized capacitance decreases drastically with increasing active mass. Reducing particle agglomeration and improving the mixing of the components of an electrode can potentially enhance electrolyte access to the active material and improve electrode performance.

The capacitances of negative electrodes are usually significantly lower than the capacitances of positive electrodes, limiting the capacitance and energy storage properties of the asymmetric SC. Further progress in the development of negative electrodes is crucial for improving asymmetric SC technology.

The goal of this investigation was to develop advanced negative electrodes with high active mass loading for the fabrication of asymmetric SC devices and improve capacitance matching of positive and negative electrodes at similar active mass. In order to improve the capacitive behavior of PPy and widen the working voltage window, we developed composite PPy-CNT-FeOOH electrodes. The fabrication of FeOOH involved particle extraction through liquid-liquid interface (PELLI)[42] method which reduced agglomeration and improved mixing of the components. Tetradecylamine (TDA) was found to be an efficient extractor for FeOOH. The analysis of capacitive behavior gives insight into the synergistic effects provided by each component of the composite electrodes.

It was found that impedance analysis of differential capacitance and resistance at different electrode potentials is an important tool for investigating of the synergistic effects of PPy and FeOOH. The results presented below show that an areal capacitance of 4.5 F cm^{-2} and nearly ideal capacitive behavior were achieved at active mass loading of 37 mg cm^{-2}. Efforts to enhance the performance of PPy-CNT-FeOOH electrodes allowed better capacitance matching of the negative and positive electrodes. The asymmetric devices, based on negative PPy-CNT-FeOOH electrodes and positive MnO_2-CNT electrodes showed promising electrochemical performance at high active mass.

9.3 Experimental procedures

$FeCl_3 \cdot 6H_2O$, NaOH, Na_2SO_4, tetradecylamine (TDA), sulfonazo III sodium salt (SF), pyrrole (Py), poly(vinyl butyral) (PVB), 1-butanol (Aldrich), ammonium peroxydisulfate (AP, Fisher Scientific), and carbon nanotubes (CNT, multiwalled, inner and outer diameters of ~4 and 13 nm, respectively, and lengths in the range of 1–2 μm, Bayer, Germany) were used. Ni foam current collectors (thickness 1.6 mm, porosity 95%) were supplied by Vale (Canada).

The synthesis of PPy coated CNT (PPy-CNT) was performed by a chemical polymerization method[43] using SF as a dopant for polymerization of PPy and as a dispersant for CNT. In this process, CNT were dispersed by SF under ultrasonication in ethanol to achieve a homogeneous CNT suspension. The mass ratio of CNT:SF was 2:1. The suspension was stirred in an ice bath for 1 h and then 310 mg Py was added. The mass ratio of Py:CNT was 4:1. Then 1.275g AP was dissolved in 10ml DI water and the AP solution was added to the

CNT suspension, containing Py. The reaction was performed during 24 h using ice–water bath. The precipitate was filtered and dried in an oven at 70°C.

The FeOOH synthesis procedure involved chemical precipitation from $FeCl_3$ solutions at pH = 7. The solution pH was adjusted using an aqueous NaOH. TA was used as an extractor and 1-butanol was utilized as a receiving solvent for PELLI. The concentration of FeOOH particles in the extracted suspensions was 15 g L^{-1}. The mass ratio of extractor: particles was 1:3.

For the fabrication of PPy-CNT-FeOOH, the suspensions of extracted FeOOH in 1-butanol were separated from the aqueous phase and then CNT were added. After ultrasonication of the mixed FeOOH-CNT suspensions, the PPy-CNT powder and the solution of PVB binder in ethanol were added. The mass ratio of PPy:FeOOH was 1:1.

The CNT content in all electrodes was 20%. The content of PVB was 3% of total electrode mass. The obtained suspensions were used to fabricate the supercapacitor electrodes by impregnating of the Ni foam current collectors, which were then calendered to 30% of original thickness. The active mass loading of the working electrode (WE) was 37 mg cm^{-2}, which is close to upper practical limit for given thickness of the calendered Ni foam. The fabrication of positive MnO_2-CNT electrodes was described previously[44].

The phase content of the materials was tested by XRD with a Nicolet I2 diffractometer (CuKα radiation). A Bruker Vertex 70 spectrometer was used for FTIR studies.

All electrochemical measurements were performed using a potentiostat (PARSTAT model 2273, Ametek, USA) and BST8 battery analyzers (MTI, USA). A three electrode cell contained a WE (area 1 cm^2), a saturated calomel electrode (SCE) and a Pt counter electrode. The two electrode cells consisted of positive MnO_2-CNT and negative PPy-CNT-FeOOH electrodes. An aqueous 0.5 M Na_2SO_4 solution was used as an electrolyte. Cyclic voltammetry (CV) studies at scan rates of 2–100 mV s^{-1} were used to calculate the integral capacitances $C_S = Q/\Delta VS$ and $C_m = Q/\Delta Vm$ of individual electrodes and devices, where Q, ΔV, S and m are charge, potential window (or cell voltage), electrode area and total active mass (individual electrodes or devices), respectively. The AC complex impedance $Z^* = Z'$ $-iZ''$ of individual electrodes and devices was measured at the signal amplitude of 5 mV in the frequency (f) range of 0.01 Hz-100 kHz. The impedance of individual electrodes was measured at different applied potentials. The complex differential capacitance $C_S^* = C_S'$-iC_S'' was obtained as $C_S' = Z''/2\pi f\ |Z|^2 S$ and $C_S'' = Z'/2\pi f\ |Z|^2 S$. The integral capacitances of devices were also calculated from the galvanostatic discharge data as $C_S = It/\Delta VS$ and $C_m = It/\Delta Vm$ where I denoted discharge current and t the discharge time.

9.4 Results and discussion

Figure 8.1a presents the X-ray diffraction pattern of a dried FeOOH powder, where the peaks corresponded to JCPDS file 29–713 for α-FeOOH. A major issue in the development of FeOOH nanocomposites is particle agglomeration resulting from the drying of precipitated particles, which generates difficulties in particle re-dispersion in organic solvents for device fabrication. To avoid drying, PELLI was used for the particle extraction from the aqueous suspension of as-prepared FeOOH particles to the 1-butanol phase. PELLI is a convenient means for improving the mixing of non-agglomerated FeOOH particles with CNT or PPy-CNT in the organic solvent, which is necessary for the dissolution of the PVB binder. The ability of PELLI to extract particles depends on the availability of efficient extractors, which must be adsorbed on the particle surface. Figure 9.1A shows the chemical structure of TA used as an extractor. The long hydrocarbon chain facilitates TA dissolution in 1-butanol. The TA adsorption on FeOOH can result from Ref.[44] chemisorption or electrostatic attraction (Figure 9.1B(a,b)). Figure 9.1C-F shows the FeOOH suspensions before and after extraction and also presents a schematic of the extraction mechanism, which involved phase transfer of FeOOH particles, containing adsorbed TA, from water to 1-butanol. The TA adsorption on FeOOH was confirmed by the FTIR spectrum of extracted FeOOH particles, which shows absorptions at 2851, 2920 and 2957 cm^{-1}, resulting from the vibrations of CH_2 and CH_3 groups of adsorbed TDA. Similar absorptions at slightly lower wavenumbers were observed in the spectrum of as-received TDA (Figure 9.2).

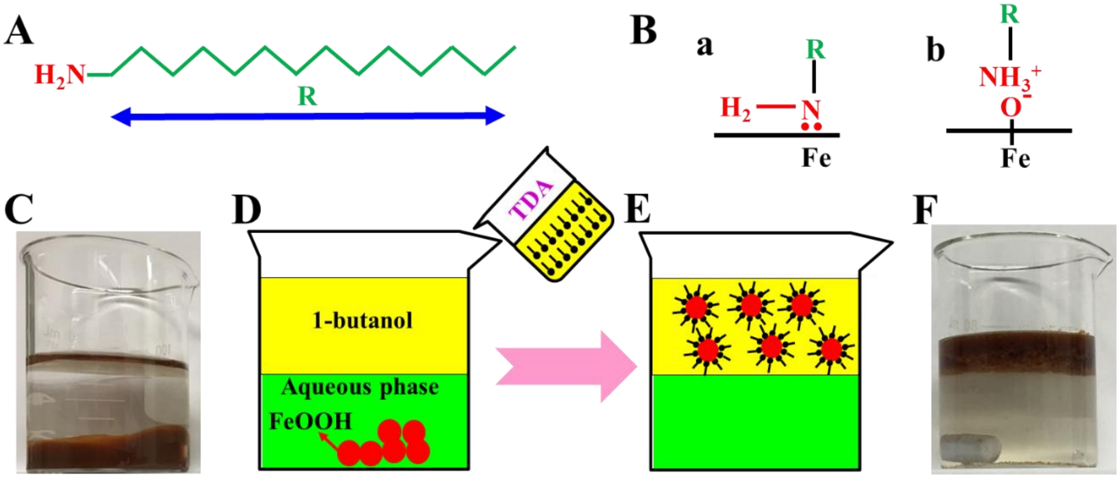

Figure 9.1 (A) Chemical structure of TDA, (B) TDA adsorption mechanisms involving a surface OH group: (a) chemisorption and (b) electrostatic interaction, (C) precipitated

FeOOH (D,E) schematic of extraction: (D) addition of TDA extractor to precipitated FeOOH, (E) extraction of FeOOH to n-butanol phase, (F) extracted FeOOH.

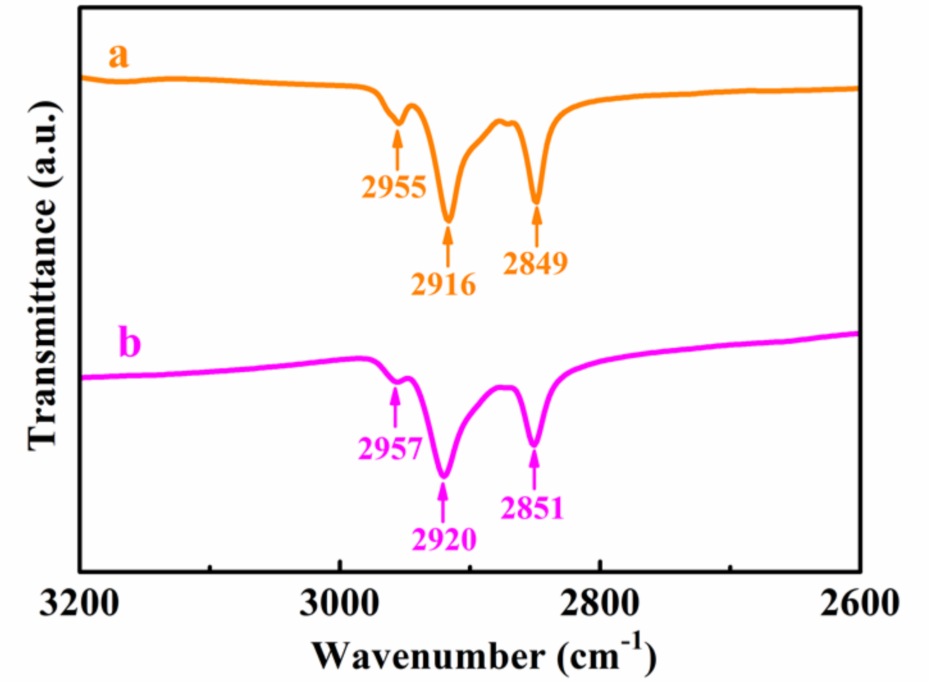

Figure 9.2 FTIR spectrum of (a) TDA, (b) FeOOH, extracted using TDA.

The extracted FeOOH particles were mixed with CNT or PPy-CNT and the resulting mixtures were used to impregnate the Ni foam current collectors. Figure 9.3A shows CVs for the PPy-CNT electrodes. The capacitive properties of PPy are related to doping/de-doping behavior[45]. The PPy reduction resulted in the compensation of positive charges and reversible de-doping[46]. Relatively high currents were obtained in the potential range of −0.4 to +0.1 V versus SCE. The currents decreased significantly in the range from −0.8 to −0.4 V due to the poor charge storage properties of PPy-CNT in this potential range. The FeOOH-CNT electrodes, prepared without PELLI (Figure 9.3B), showed poor electrochemical performance, especially in the range from −0.2 to + 0.1 V. The use of

PELLI allowed significant improvement in the charge storage properties of FeOOH-CNT (Figure 9.3C), as indicated by the significant increase in currents and large CV areas at potentials below −0.2 V. However, the currents remained low at higher potentials. Figure 9.3D shows the synergistic effect of PPy-CNT and FeOOH materials. The nearly box shapes of the CVs indicated good capacitive behavior in the potential range of −0.8–+0.1 V.

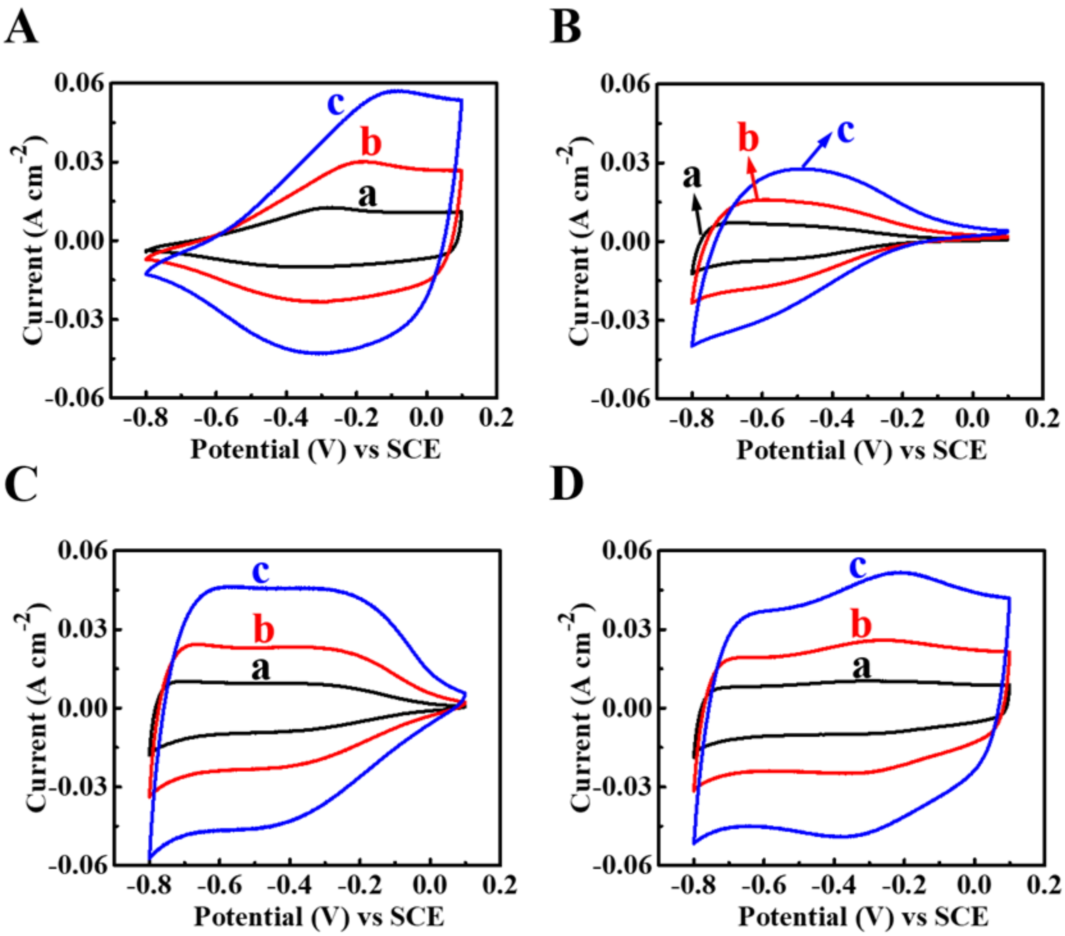

Figure 9.3 CVs at scan rates of (a) 2, (b) 5 and (c) 10 mV s^{-1} for different electrodes: (A) PPy-CNT, (B) FeOOH-CNT, prepared without PELLI, (C) FeOOH-CNT, prepared using PELLI, and (D) PPy-CNT-FeOOH, prepared using PELLI.

The synergistic effect of PPy-CNT and FeOOH-CNT was also confirmed by the analysis of the integral capacitances of the electrodes in the same potential window. The PPy-CNT electrodes showed (Figure 9.4Figure 9.4) the highest capacitance of 3.7 F cm^{-2} at a scan rate of 2 mV s^{-1}. The capacitance decreased with increasing scan rate from 2 to 100 mV s^{-1}. The FeOOH-CNT electrodes, prepared without PELLI, showed the highest capacitance of 1.9 F cm^{-2}. The use of PELLI allowed significant increase in the capacitance of FeOOH-CNT electrodes, which showed a capacitance of 3.5 F cm^{-2} at a scan rate of 2 mV s^{-1} and significant improvement in capacitance retention at high scan rates. The PPy-CNT-FeOOH electrodes, prepared using PELLI, showed higher capacitances, compared to PPy-CNT and FeOOH-CNT. The integral capacitance of 4.5 F cm^{-2} was obtained at 2 mV s^{-1}.

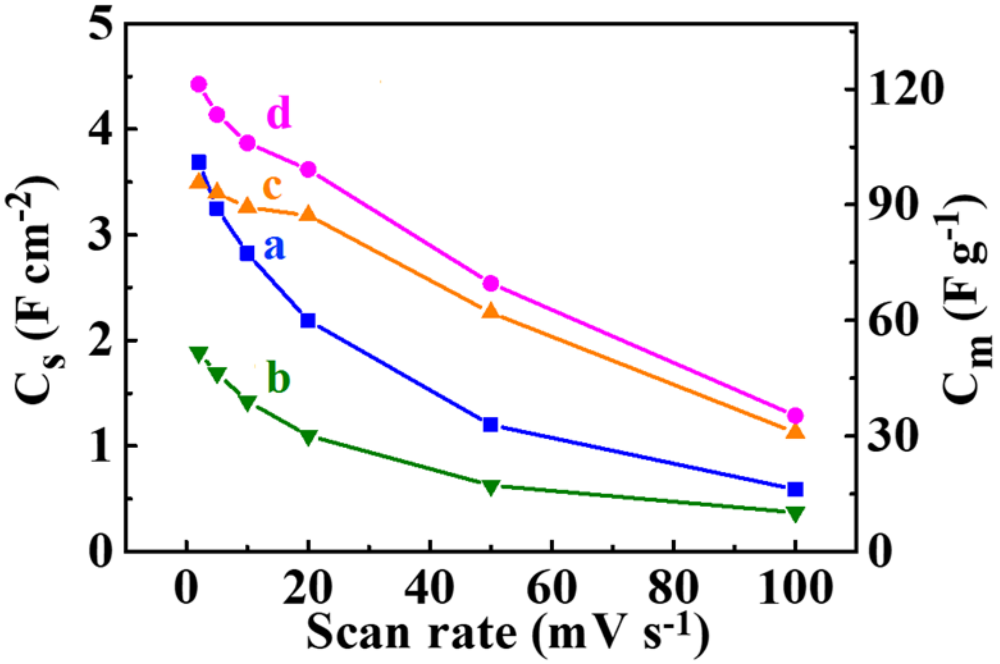

Figure 9.4 C_S and C_m for different electrodes: (a) PPy-CNT, (b) FeOOH-CNT, prepared without PELLI, (c) FeOOH-CNT, prepared using PELLI and (d) PPy-CNT-FeOOH, prepared using PELLI.

The CV data provided integral capacitance in the potential window of −0.8–+0.1 V. Additional information was obtained from measurements of AC impedance and differential capacitance at different electrode potentials. Figure 9.5 presents impedance data in the Nyquist plot for PPy-CNT electrodes. The slopes of the Nyquist plots at +0.1 and −0.2 V were close to 90° and the real part of the impedance Z' was below 1 Ohm. Therefore, the Nyquist plots indicated good capacitive behavior. The reduction of electrode potential resulted in decreasing slopes of the Nyquist plots and significant increase in Z'. At electrode potential of −0.8 V the slope of the curve was close to 45° at high frequencies. This behavior can be due to significant contribution of Warburg impedance[45]. The analysis of the differential capacitance C' showed that the highest capacitance of about 4 F cm^{-2} was obtained at −0.2 V. In contrast, C' was below 0.1 F cm^{-2} for an electrode potential of −0.8 V. The decrease in C' with increasing frequency and maxima in the frequency dependences of C'' are in agreement with the relaxation model for PPy electrodes[45].

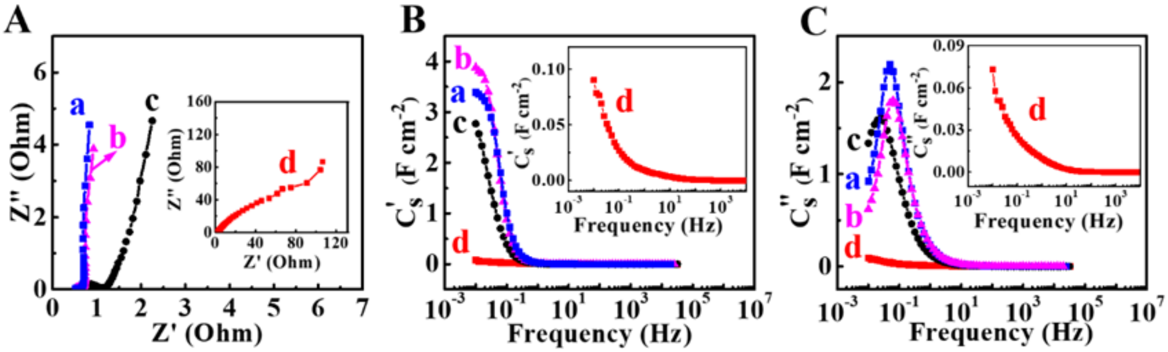

Figure 9.5 (A) Nyquist plot of complex impedance, (B) C_S' versus frequency and (C) C_S'' versus frequency for PPy-CNT at different electrode potentials: (a) 0.1, (b) −0.2, (c) −0.5 and (d) −0.8 V.

Test results revealed the enhanced electrochemical performance of the composite electrodes, prepared using PELLI. Figure 9.6 compares impedance spectroscopy data for FeOOH-CNT electrodes prepared with and without PELLI. The Nyquist plots at +0.1 V showed relatively large impedances. However, the use of PELLI resulted in the reduction in Z′ and Z″, which indicated minor improvement in the capacitive behavior. The slope of the Nyquist plot at −0.2V was close to 45° for the electrode prepared without PELLI. In contrast, this slope increased significantly for the electrode prepared using PELLI. Moreover, a significant reduction in Z′ was observed. The use of PELLI improved the capacitive behavior at −0.5 and −0.8 V, as indicated by the reduction in Z′ and increasing slopes of the Nyquist plots, which were close to 90°. The analysis of differential capacitances derived from the impedance data showed relatively poor capacitive behavior at 0.1 V. The highest capacitance of 0.15 F cm^{-2} was obtained at 0.1 V and 10 mHz frequency for electrodes prepared using PELLI. The capacitance increased with decreasing electrode potential. Electrodes prepared using PELLI showed higher capacitances at all electrode potentials. The highest capacitance of 6 F cm^{-2} was obtained at an electrode potential of −0.8 V at a frequency of 10 mHz. The electrode prepared using PELLI displayed relaxation type dispersions, which resulted in a C′ decrease and a maximum in C″.

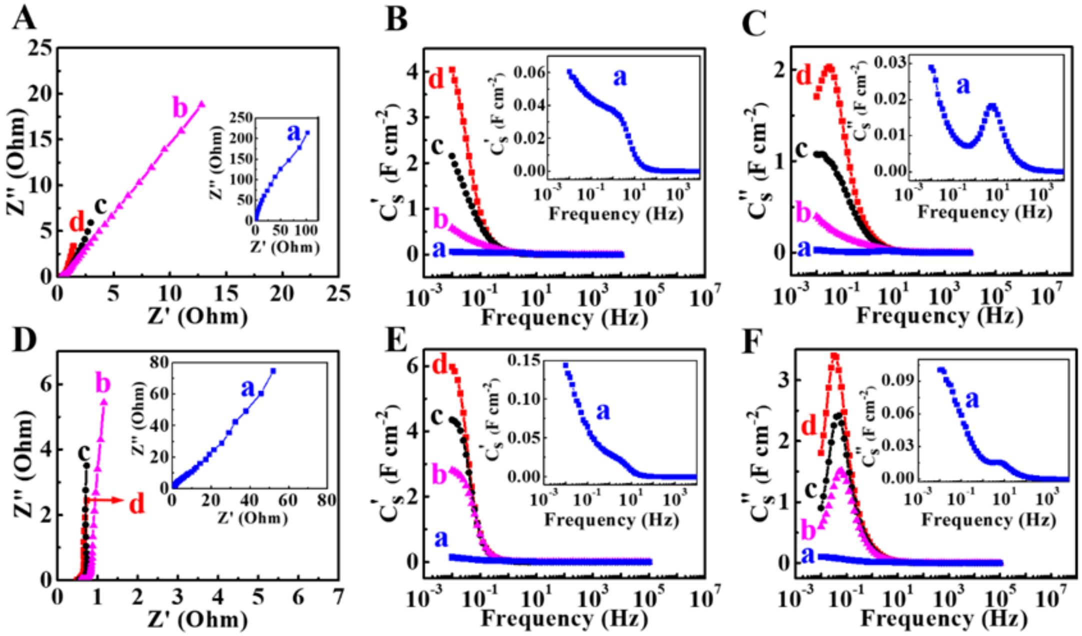

Figure 9.6 (A) Nyquist plot of complex impedance, (B) C_S' versus frequency and (C) C_S'' versus frequency for FeOOH-CNT, prepared without PELLI, (D) Nyquist plot of complex impedance, (E) C_S' versus frequency and (F) C_S'' versus frequency for FeOOH-CNT, prepared using PELLI at different electrode potentials: (a) 0.1, (b) −0.2, (c) −0.5 and (d) −0.8 V.

The improved capacitive behavior of electrodes prepared using PELLI resulted from reduced agglomeration of FeOOH particles, which facilitated their mixing with CNT. The charge-discharge behavior of FeOOH is described in Ref.[47] by Eq. 9-1:

$$\mathrm{Fe(III)OOH+Na^{+}+e^{-}\leftrightarrow NaFe(II)OOH} \qquad (9\text{-}1)$$

Therefore, the reduced agglomeration of FeOOH particles and their improved mixing with CNT facilitated transfer of Na^+ and electrons to the particle surface and resulted in higher capacitance.

The reduced agglomeration of FeOOH particles was also beneficial for the fabrication of PPy-CNT-FeOOH composites. Figure 9.7 shows AC impedance data for PPy-FeOOH-

CNT electrodes, prepared using PELLI. The PPy-CNT-FeOOH composites showed enhanced performance at potentials −0.8 – −0.5 V, compared to PPy-CNT and at potentials −0.2 – +0.1 compared to FeOOH-CNT. Indeed, Figure 9.7A indicates reduced Z' and a higher slope of the Nyquist plots, whereas Figure 9.7B shows increased capacitance. The PPy-CNT-FeOOH electrodes showed reduced variation in Z^*, C_S^* and relaxation frequencies, corresponding to maxima in C'' at different electrode potentials (Figure 9.7C).

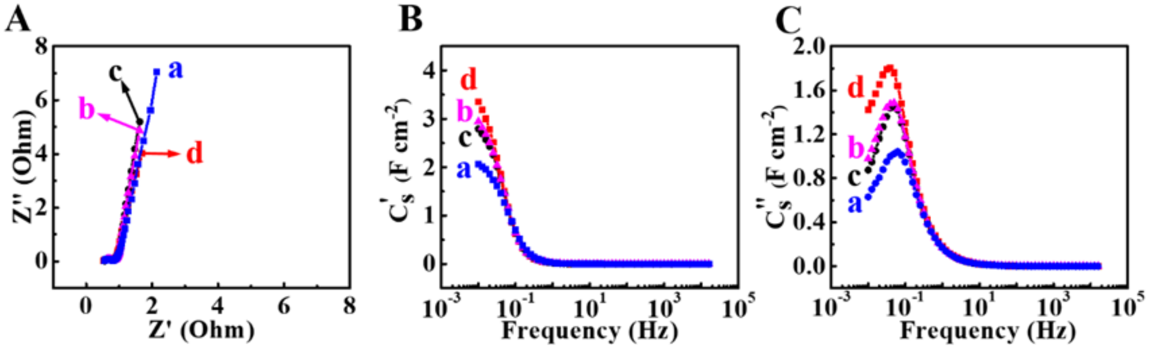

Figure 9.7 (A) Nyquist plot of complex impedance, (B) C_S' versus frequency and (C) C_S'' versus frequency for PPy-CNT-FeOOH, prepared using PELLI at different electrode potentials: (a) 0.1, (b) −0.2, (c) −0.5 and (d) −0.8 V.

Use of the PPy-CNT-FeOOH composites addressed the need in advanced negative electrodes for SC. The design of asymmetric SC is usually based on the development of positive and negative electrodes, which show comparable charge storage properties in partially overlapping voltage windows and in the same electrolyte[48, 49]. We developed composites for negative electrodes that have enhanced performance in the voltage window of −0.8 – +0.1 V, which partially overlap with a voltage window of 0 – +0.9 V for MnO_2-CNT positive electrodes (Figure 9.8). The asymmetric device containing PPy-FeOOH-CNT negative electrodes and MnO_2-CNT positive electrodes with mass loadings of 37 mg cm^{-2} of individual electrodes showed box shape CVs in a voltage window of 1.6 V (Figure 9.9A). The device showed a capacitance of 2.6 F cm^{-2} at a scan rate of 2 mV s^{-1} (Figure 9.9B) and relatively low impedance (Figure 9.10A). The differential capacitance, calculated from the impedance data (Figure 9.10) was lower compared to the integral capacitance, as calculated from the CV data (Figure 9.9).

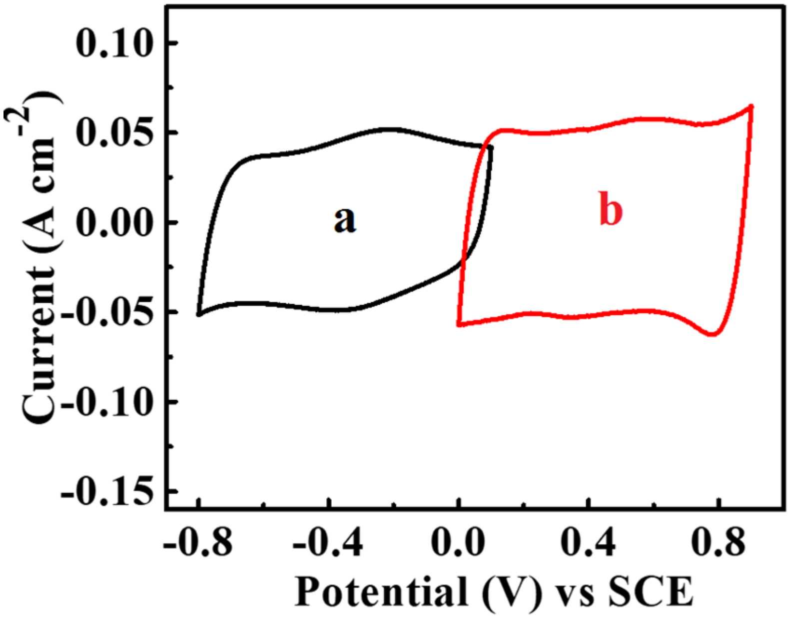

Figure 9.8 CVs for (a) negative PPy-CNT-FeOOH electrodes and (b) positive MnO_2-CNT electrodes at a scan rate of 10mV s^{-1}.

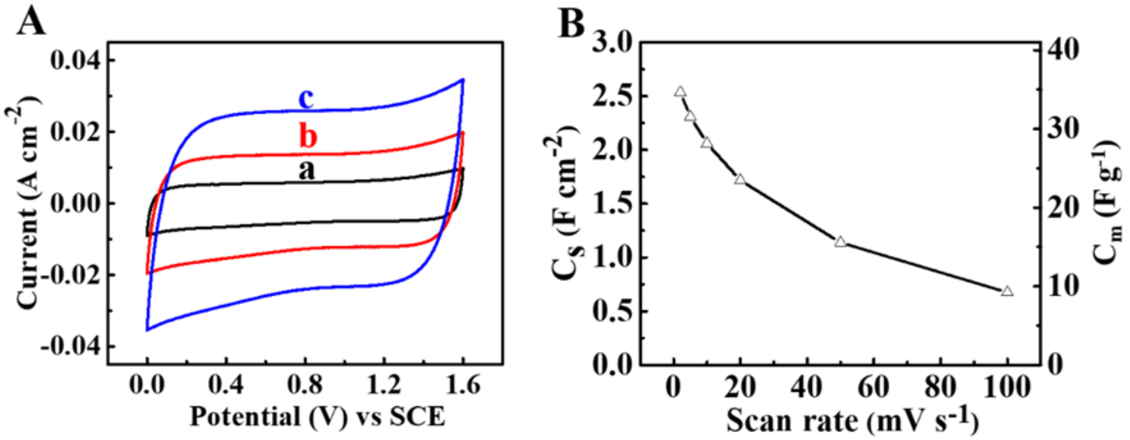

Figure 9.9 (A) CVs at scan rates of (a) 2, (b) 5 and (c) 10 mV s^{-1} (B) C_S and C_m versus scan rate for an asymmetric supercapacitor cell, containing a negative PPy-CNT-FeOOH electrode and a positive MnO_2-CNT electrode.

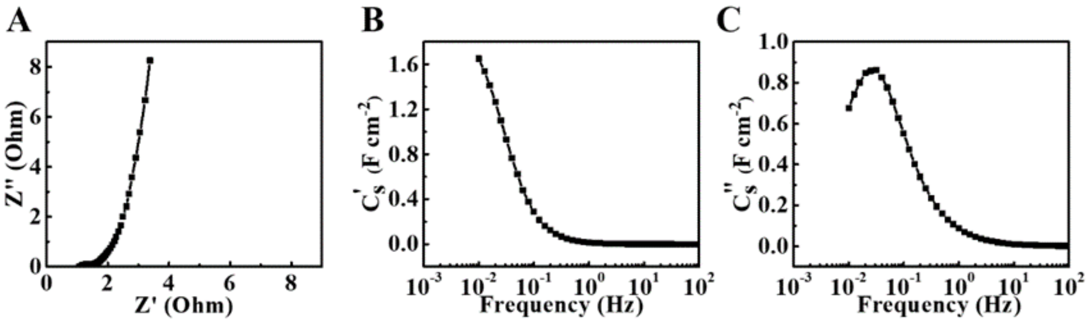

Figure 9.10 (A) Nyquist plot of complex impedance, (B) C_S' versus frequency and (C) C_S'' versus frequency for an asymmetric supercapacitor cell, containing a negative PPy-CNT-FeOOH electrode and a positive MnO_2-CNT electrode.

The triangular shape of the galvanostatic charge-discharge curves (Figure 9.11A) at different current densities indicated good capacitive behavior. The capacitance, calculated from the discharge data (Figure 9.11B) was close to the capacitance calculated from the CVs (Figure 9.9).

The PPy-FeOOH-CNT negative electrodes, developed in this investigation showed significantly higher areal capacitance, compared to PPy-V_2O_5 and PPy-MoO_3 negative electrodes[50-52]. We achieved good capacitive performance at high active mass loading due to the use of PPy coated CNT and by the development of PELLI method for FeOOH. It is important to note that resistance of our electrodes with high active mass was typically by 2–3 order of magnitude lower, compared to resistance of PPy-V_2O_5 and PPy-MoO_3 with low active mass[50, 53]. The capacitive properties of the asymmetric SC device achieved at high active mass are promising for practical applications.

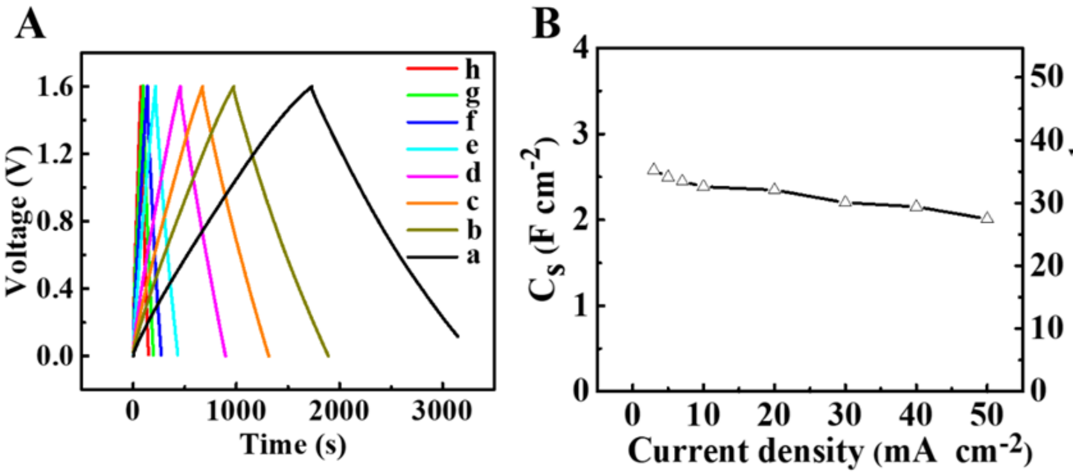

Figure 9.11 (A) Charge-discharge curves at currents of (a) 3, (b) 5, (c) 7, (d) 10, (e) 20, (f) 30, (g) 40 and (h) 50 mA cm^{-2}, (B) C_S and C_m calculated from the charge-discharge data versus current density for an asymmetric supercapacitor cell, containing a negative PPy-CNT-FeOOH electrode and a positive MnO_2-CNT electrode.

9.5 Conclusions

PPy-CNT-FeOOH composites have been developed for the application in the negative electrodes of SC. The use of PELLI allowed for reduced FeOOH agglomeration and facilitated FeOOH mixing with CNT. TA was found to be an efficient extractor for FeOOH. This strategy allowed improved electrolyte access to FeOOH and also improved electronic conductivity, which resulted in significant improvement in the capacitance of FeOOH-CNT composites. Moreover, the use of PELLI allowed the fabrication of advanced PPy-CNT-FeOOH composites, which have good performance in a voltage window of −0.8 – +0.1 V versus SCE. The analysis of cyclic voltammetry and impedance spectroscopy data at different electrode potentials revealed synergistic effects of PPy-CNT and FeOOH. Good electrochemical performance was achieved at high active mass loading of 37 mg cm^{-2}. An areal capacitance of 4.5 F cm^{-2} and nearly ideal capacitive behavior were achieved at low electrode impedance. The important finding was the possibility of matching of capacitances of the negative PPy-CNT-FeOOH and positive MnO_2-CNT electrodes. The asymmetric devices showed promising electrochemical performance in a voltage window of 1.6 V at high active mass. The devices showed a capacitance of 2.6 F cm^{-2} at high active mass loadings of the individual electrodes.

9.6 Reference

[1] Y. B. Li, G. Chen, Q. H. Li, G. Z. Qiu, and X. H. Liu, "Facile synthesis, magnetic and microwave absorption properties of Fe3O4/polypyrrole core/shell nanocomposite," *Journal of Alloys and Compounds,* vol. 509, pp. 4104-4107, Mar 10 2011.

[2] D. H. Nam, S. J. Lim, M. J. Kim, and H. S. Kwon, "Facile synthesis of SnO_2-polypyrrole hybrid nanowires by cathodic electrodeposition and their application to Li-ion battery anodes," *Rsc Advances*, vol. 3, pp. 16102-16108, 2013.

[3] F. Deng, Y. X. Li, X. B. Luo, L. X. Yang, and X. M. Tu, "Preparation of conductive polypyrrole/TiO_2 nanocomposite via surface molecular imprinting technique and its photocatalytic activity under simulated solar light irradiation," *Colloids and*

Surfaces a-Physicochemical and Engineering Aspects, vol. 395, pp. 183-189, Feb 5 2012.

[4] O. Y. Posudievsky, O. A. Kozarenko, V. S. Dyadyun, S. W. Jorgensen, J. A. Spearot, V. G. Koshechko, *et al.*, "Effect of host-guest versus core-shell structure on electrochemical characteristics of vanadium oxide/polypyrrole nanocomposites," *Electrochimica Acta*, vol. 58, pp. 442-448, Dec 30 2011.

[5] N. H. Idris, J. Z. Wang, S. L. Chou, C. Zhong, M. M. Rahman, and H. K. Liu, "Effects of polypyrrole on the performance of nickel oxide anode materials for rechargeable lithium-ion batteries," *Journal of Materials Research*, vol. 26, pp. 860-866, Apr 2011.

[6] W. K. Chee, H. N. Lim, I. Harrison, K. F. Chong, Z. Zainal, C. H. Ng, *et al.*, "Performance of Flexible and Binderless Polypyrrole/Graphene Oxide/Zinc Oxide Supercapacitor Electrode in a Symmetrical Two-Electrode Configuration," *Electrochimica Acta*, vol. 157, pp. 88-94, Mar 1 2015.

[7] J. S. Shayeh, S. O. R. Siadat, M. Sadeghnia, K. Niknam, M. Rezaei, and N. Aghamohammadi, "Advanced studies of coupled conductive polymer/metal oxide nano wire composite as an efficient supercapacitor by common and fast fourier electrochemical methods," *Journal of Molecular Liquids*, vol. 220, pp. 489-494, Aug 2016.

[8] F. H. Meng, W. Shi, Y. N. Sun, X. Zhu, G. S. Wu, C. Q. Ruan, *et al.*, "Nonenzymatic biosensor based on Cu_xO nanoparticles deposited on polypyrrole nanowires for

improving detection range," *Biosensors & Bioelectronics,* vol. 42, pp. 141-147, Apr 15 2013.

[9] R. C. Jin, Y. F. Meng, Y. Q. Ma, H. H. Li, Y. X. Sun, and G. Chen, "Hierarchical $MnCo_2O_4$ constructed by mesoporous nanosheets@polypyrrole composites as anodes for lithium ion batteries," *Electrochimica Acta,* vol. 209, pp. 163-170, Aug 10 2016.

[10] D. Z. Kong, W. N. Ren, C. W. Cheng, Y. Wang, Z. X. Huang, and H. Y. Yang, "Three-Dimensional $NiCo_2O_4$@Polypyrrole Coaxial Nanowire Arrays on Carbon Textiles for High-Performance Flexible Asymmetric Solid-State Supercapacitor," *Acs Applied Materials & Interfaces,* vol. 7, pp. 21334-21346, Sep 30 2015.

[11] J. C. Cao, G. R. Hu, Z. D. Peng, K. Du, and Y. B. Cao, "Polypyrrole-coated $LiCoO_2$ nanocomposite with enhanced electrochemical properties at high voltage for lithium-ion batteries," *Journal of Power Sources,* vol. 281, pp. 49-55, May 1 2015.

[12] X. R. Sun, H. W. Zhang, L. Zhou, X. D. Huang, and C. Z. Yu, "Polypyrrole-Coated Zinc Ferrite Hollow Spheres with Improved Cycling Stability for Lithium-Ion Batteries," *Small,* vol. 12, pp. 3732-3737, Jul 20 2016.

[13] J. S. Lee, D. H. Shin, W. Kim, and J. Jang, "Highly ordered, polypyrrole-coated $Co(OH)(_2)$ architectures for high-performance asymmetric supercapacitors," *Journal of Materials Chemistry A,* vol. 4, pp. 6603-6609, 2016.

[14] T. T. V. Phan, N. Q. Bui, S. W. Cho, S. Bharathiraja, P. Manivasagan, M. S. Moorthy, *et al.*, "Photoacoustic Imaging-Guided Photothermal Therapy with

Tumor-Targeting HA-FeOOH@PPy Nanorods," *Scientific Reports,* vol. 8, Jun 11 2018.

[15] J. Yang, M. Cho, C. Pang, and Y. Lee, "Highly sensitive non-enzymatic glucose sensor based on over-oxidized polypyrrole nanowires modified with Ni(OH)($_2$) nanoflakes," *Sensors and Actuators B-Chemical,* vol. 211, pp. 93-101, May 2015.

[16] M. J. Liu, X. L. Liu, J. X. Wang, Z. X. Wei, and L. Jiang, "Electromagnetic synergetic actuators based on polypyrrole/Fe_3O_4 hybrid nanotube arrays," *Nano Research,* vol. 3, pp. 670-675, Sep 2010.

[17] J. Liu, X. J. Xu, R. Z. Hu, L. C. Yang, and M. Zhu, "Uniform Hierarchical Fe_3O_4@Polypyrrole Nanocages for Superior Lithium Ion Battery Anodes," *Advanced Energy Materials,* vol. 6, Jul 6 2016.

[18] C. Wang, H. Xu, C. Liang, Y. M. Liu, Z. W. Li, G. B. Yang*, et al.,* "Iron Oxide @ Polypyrrole Nanoparticles as a Multifunctional Drug Carrier for Remotely Controlled Cancer Therapy with Synergistic Antitumor Effect," *Acs Nano,* vol. 7, pp. 6782-6795, Aug 2013.

[19] S. Z. Ren, S. B. Ma, Y. Yang, Q. Mao, and C. Hao, "Hydrothermal synthesis of Fe_2O_3/polypyrrole/graphene oxide composites as highly efficient electrocatalysts for oxygen reduction reaction in alkaline electrolyte," *Electrochimica Acta,* vol. 178, pp. 179-189, Oct 1 2015.

[20] J. Chen, J. T. Feng, and W. Yan, "Influence of metal oxides on the adsorption characteristics of PPy/metal oxides for Methylene Blue," *Journal of Colloid and Interface Science,* vol. 475, pp. 26-35, Aug 1 2016.

[21] X. J. Song, H. Gong, S. N. Yin, L. Cheng, C. Wang, Z. W. Li, *et al.*, "Ultra- Small Iron Oxide Doped Polypyrrole Nanoparticles for In Vivo Multimodal Imaging Guided Photothermal Therapy," *Advanced Functional Materials,* vol. 24, pp. 1194-1201, Mar 2014.

[22] S. T. Navale, G. D. Khuspe, M. A. Chougule, and V. B. Patil, "Polypyrrole, alpha-Fe_2O_3 and their hybrid nanocomposite sensor: An impedance spectroscopy study," *Organic Electronics,* vol. 15, pp. 2159-2167, Oct 2014.

[23] G. J. Wei, K. Du, X. X. Zhao, C. Li, J. Q. Li, K. K. Ren, *et al.*, "Integrated FeOOH nanospindles with conductive polymer layer for high-performance supercapacitors," *Journal of Alloys and Compounds,* vol. 728, pp. 631-639, Dec 25 2017.

[24] J. Z. Wang, S. L. Chou, J. Chen, S. Y. Chew, G. X. Wang, K. Konstantinov, *et al.*, "Paper-like free-standing polypyrrole and polypyrrole-$LiFePO_4$ composite films for flexible and bendable rechargeable battery," *Electrochemistry Communications,* vol. 10, pp. 1781-1784, Nov 2008.

[25] Z. M. Zhang, Q. Li, L. M. Yu, Z. J. Cui, L. J. Zhang, and G. A. Bowmaker, "Highly Conductive Polypyrrole/gamma-Fe_2O_3 Nanospheres with Good Magnetic Properties Obtained through an Improved Chemical One-Step Method," *Macromolecules,* vol. 44, pp. 4610-4615, Jun 28 2011.

[26] F. Han, D. Li, W. C. Li, C. Lei, Q. Sun, and A. H. Lu, "Nanoengineered Polypyrrole-Coated Fe_2O_3@C Multifunctional Composites with an Improved Cycle

Stability as Lithium-Ion Anodes," *Advanced Functional Materials,* vol. 23, pp. 1692-1700, Apr 5 2013.

[27] N. M. Dimitrijevic, S. Tepavcevic, Y. Z. Liu, T. Rajh, S. C. Silver, and D. M. Tiede, "Nanostructured TiO_2/Polypyrrole for Visible Light Photocatalysis," *Journal of Physical Chemistry C,* vol. 117, pp. 15540-15544, Aug 1 2013.

[28] J. L. Liu, W. W. Zhou, L. F. Lai, H. P. Yang, S. H. Lim, Y. D. Zhen, *et al.*, "Three dimensionals alpha-Fe_2O_3/Polypyrrole (Ppy) nanoarray as anode for micro lithium ion batteries," *Nano Energy,* vol. 2, pp. 726-732, Sep 2013.

[29] X. C. Cao, W. N. Yan, C. Jin, J. H. Tian, K. Ke, and R. Z. Yang, "Surface modification of $MnCo_2O_4$ with conducting polypyrrole as a highly active bifunctional electrocatalyst for oxygen reduction and oxygen evolution reaction," *Electrochimica Acta,* vol. 180, pp. 788-794, Oct 20 2015.

[30] W. J. Liu, N. S. Liu, Y. L. Shi, Y. Chen, C. X. Yang, J. Y. Tao, *et al.*, "A wire-shaped flexible asymmetric supercapacitor based on carbon fiber coated with a metal oxide and a polymer," *Journal of Materials Chemistry A,* vol. 3, pp. 13461-13467, 2015.

[31] H. Lee, M. S. Cho, I. H. Kim, J. D. Nam, and Y. Lee, "RuO_x/polypyrrole nanocomposite electrode for electrochemical capacitors," *Synthetic Metals,* vol. 160, pp. 1055-1059, May 2010.

[32] J. F. Zang and X. D. Li, "In situ synthesis of ultrafine beta-MnO_2/polypyrrole nanorod composites for high-performance supercapacitors," *Journal of Materials Chemistry,* vol. 21, pp. 10965-10969, 2011.

[33] W. Yao, H. Zhou, and Y. Lu, "Synthesis and property of novel MnO_2@polypyrrole coaxial nanotubes as electrode material for supercapacitors," *Journal of Power Sources*, vol. 241, pp. 359-366, Nov 1 2013.

[34] C. Zhou, Y. W. Zhang, Y. Y. Li, and J. P. Liu, "Construction of High-Capacitance 3D CoO@Polypyrrole Nanowire Array Electrode for Aqueous Asymmetric Supercapacitor," *Nano Letters*, vol. 13, pp. 2078-2085, May 2013.

[35] P. X. Li, Y. B. Yang, E. Z. Shi, Q. C. Shen, Y. Y. Shang, S. T. Wu, *et al.*, "Core-Double-Shell, Carbon Nanotube@Polypyrrole@MnO_2 Sponge as Freestanding, Compressible Supercapacitor Electrode," *Acs Applied Materials & Interfaces*, vol. 6, pp. 5228-5234, Apr 9 2014.

[36] L. B. Wang, H. L. Yang, X. X. Liu, R. Zeng, M. Li, Y. H. Huang, *et al.*, "Constructing Hierarchical Tectorum- like alpha-Fe_2O_3/PPy Nanoarrays on Carbon Cloth for Solid-State Asymmetric Supercapacitors," *Angewandte Chemie-International Edition*, vol. 56, pp. 1105-1110, Jan 19 2017.

[37] A. Moyseowicz, A. Sliwak, E. Miniach, and G. Gryglewicz, "Polypyrrole/iron oxide/reduced graphene oxide ternary composite as a binderless electrode material with high cyclic stability for supercapacitors," *Composites Part B-Engineering*, vol. 109, pp. 23-29, Jan 15 2017.

[38] X. F. Gong, S. H. Li, and P. S. Lee, "A fiber asymmetric supercapacitor based on FeOOH/PPy on carbon fibers as an anode electrode with high volumetric energy density for wearable applications," *Nanoscale*, vol. 9, pp. 10794-10801, Aug 14 2017.

[39] H. M. Cheng and F. Li, "ENERGY STORAGE Charge delivery goes the distance," *Science,* vol. 356, pp. 582-583, May 12 2017.

[40] W. T. Gu and G. Yushin, "Review of nanostructured carbon materials for electrochemical capacitor applications: advantages and limitations of activated carbon, carbide-derived carbon, zeolite-templated carbon, carbon aerogels, carbon nanotubes, onion-like carbon, and graphene," *Wiley Interdisciplinary Reviews-Energy and Environment,* vol. 3, pp. 424-473, Sep-Oct 2014.

[41] Y. Gogotsi and P. Simon, "True Performance Metrics in Electrochemical Energy Storage," *Science,* vol. 334, pp. 917-918, Nov 18 2011.

[42] R. M. E. Silva, R. Poon, J. Milne, A. Syed, and I. Zhitomirsky, "New developments in liquid-liquid extraction, surface modification and agglomerate-free processing of inorganic particles," *Advances in Colloid and Interface Science,* vol. 261, pp. 15-27, Nov 2018.

[43] Y. Su and I. Zhitomirsky, "Asymmetric electrochemical supercapacitor, based on polypyrrole coated carbon nanotube electrodes," *Applied Energy,* vol. 153, pp. 48-55, Sep 1 2015.

[44] R. Chen, R. Poon, R. P. Sahu, I. K. Puri, and I. Zhitomirsky, "MnO_2-Carbon Nanotube Electrodes for Supercapacitors with High Active Mass Loadings," *Journal of the Electrochemical Society,* vol. 164, pp. A1673-A1678, 2017.

[45] J. Tanguy, N. Mermilliod, and M. Hoclet, "Capacitive Charge and Noncapacitive Charge in Conducting Polymer Electrodes," *Journal of the Electrochemical Society,* vol. 134, pp. 795-802, Apr 1987.

[46] T. Schoetz, M. Kurniawan, M. Stich, R. Peipmann, I. Efimov, A. Ispas, *et al.*, "Understanding the charge storage mechanism of conductive polymers as hybrid battery-capacitor materials in ionic liquids by in situ atomic force microscopy and electrochemical quartz crystal microbalance studies," *Journal of Materials Chemistry A,* vol. 6, pp. 17787-17799, Sep 28 2018.

[47] L. Cheng, H. Q. Li, and Y. Y. Xia, "A hybrid nonaqueous electrochemical supercapacitor using nano-sized iron oxyhydroxide and activated carbon," *Journal of Solid State Electrochemistry,* vol. 10, pp. 405-410, Jun 2006.

[48] R. Attias, D. Sharon, A. Borenstein, D. Malka, O. Hana, S. Luski, *et al.*, "Asymmetric Supercapacitors Using Chemically Prepared MnO_2 as Positive Electrode Materials," *Journal of the Electrochemical Society,* vol. 164, pp. A2231-A2237, 2017.

[49] Z. Y. Zhang, K. Chi, F. Xiao, and S. Wang, "Advanced solid-state asymmetric supercapacitors based on 3D graphene/MnO_2 and graphene/polypyrrole hybrid architectures," *Journal of Materials Chemistry A,* vol. 3, pp. 12828-12835, 2015.

[50] T. Qian, N. Xu, J. Q. Zhou, T. Z. Yang, X. J. Liu, X. W. Shen, *et al.*, "Interconnected three-dimensional V_2O_5/polypyrrole network nanostructures for high performance solid-state supercapacitors," *Journal of Materials Chemistry A,* vol. 3, pp. 488-493, 2015.

[51] S. W. Zhang, B. S. Yin, C. Liu, Z. B. Wang, and D. M. Gu, "Self-assembling hierarchical $NiCo_2O_4$/MnO_2 nanosheets and MoO_3/PPy core-shell heterostructured

nanobelts for supercapacitor," *Chemical Engineering Journal*, vol. 312, pp. 296-305, Mar 15 2017.

[52] Y. D. Xu, X. Zhang, Y. Li, Y. J. Zhang, L. J. He, and J. W. Zhao, "Effect of electrolyte cations on the capacitive performance of the hexagonal-MoO_3/polypyrrole hybrid," *Materials Letters*, vol. 210, pp. 314-316, Jan 1 2018.

[53] Y. Liu, B. H. Zhang, Y. Q. Yang, Z. Chang, Z. B. Wen, and Y. P. Wu, "Polypyrrole-coated alpha-MoO_3 nanobelts with good electrochemical performance as anode materials for aqueous supercapacitors," *Journal of Materials Chemistry A*, vol. 1, pp. 13582-13587, 2013.

10 Conclusions and future directions

10.1 Conclusions

Advanced colloidal techniques have been developed to fabricate advanced composite electrodes with high active mass loading and high active material to current collector mass ratio for electrochemical capacitors (ECs). The colloidal technique can also fabricate stable suspensions for electrophoretic deposition of thin films and fabricate advanced printing inks for screen printing applications.

We investigated the bottom-up and top-down particle extraction through liquid-liquid interface (PELLI) to extract MnO_2 particle synthesized in an aqueous phase to the organic phases of 1-butanol and dichloromethane, respectively. The experimental results showed that the MnO_2-multiwalled carbon nanotube (MWCNT) electrodes prepared by bottom-up technique exhibited higher capacitance and lower impedance compared to those prepared by top-down technique, which was attributed to reduced agglomeration of MnO_2 particles by bottom-up technique. Effects of the extractors and active mass loading on the electrodes' performance had been systematically studied at high active mass loadings in the range of 21–50 mg cm^{-2} and mass ratios of active material to the nickel foam current collector of 0.33–0.78.

Multifunctional head-tail-head (HTH) extractors with two functional groups of carboxylic acid and phosphonate at both ends of the hydrophobic tail had been used for extracting MnO_2 particles from the synthesized media to the device processing media to achieve good suspension of MnO_2-MWCNT for fabrication of ECs positive electrodes. Moreover, it was found that the multifunctional HTH surfactants could be used as the PELLI extractors and as the charging and dispersing agents for the fabrication of stable suspensions for electrophoretic deposition of thin films. We also demonstrated that advanced printing inks had been fabricated by use of non-agglomerated MnO_2 particles prepared by these multifunctional HTH molecules for screen printing applications.

For the first time, advanced FeOOH-MWCNT negative electrodes with a high capacitance comparable to MnO_2-MWCNT positive electrodes at a similar high active mass loading had been fabricated by PELLI using multifunctional HTH extractors. Asymmetric ECs devices had been assembled by using FeOOH-MWCNT and MnO_2-MWCNT as negative and positive electrodes respectively. These devices showed good power-energy characteristics with low impedance at wide voltage window of 1.6 V in an aqueous electrolyte.

We also demonstrated that PPy coated MWCNT could be fabricated as advanced negative electrodes operated at a voltage window of -0.8 - +0.1V using FeOOH particles prepared by PELLI techniques. High electrochemical performance ECs devices combining PPy-FeOOH-MWCNT negative electrodes with MnO_2-MWCNT positive electrodes were achieved in a voltage window of 1.6 V at high active mass loading owing to the improving contact between PPy coated MWCNT and the agglomeration-free FeOOH particles.

10.2 Future directions

In this thesis, it has been demonstrated that colloidal particles prepared by PELLI strategies showed promising applications in different fields, such as electrochemical capacitors, electrophoretic deposition and screen printing. Therefore, it is extremely necessary to continue the research for fabrication of agglomeration-free colloidal particles by PELLI techniques. Based on the research in this thesis, promising directions will be proposed as followings: (1) Further development of efficient extractors for fabrication of non-agglomeration particles and homogeneous composites for different applications; (2) Fabrication of stable composite suspension for electrophoretic deposition of multifunctional composite films and (3) Fabrication of stable printing inks for colloidal manufacturing, such as screen printing and inject printing.